TRINITY COLLEGE DUBLIN

DOCTORAL THESIS

Upper mantle structure, intraplate volcanism and the unique anisotropy of the Antarctic Plate from waveform tomography

Author:
Ee Liang CHUA
19338003

Supervisor:
Dr. Sergei LEBEDEV (DIAS)
Dr. David CHEW (TCD)

A dissertation submitted in fulfillment of the degree of Doctor in Philosophy



Trinity College Dublin
Coláiste na Tríonóide, Baile Átha Cliath
The University of Dublin

Submitted
January 21, 2025

Declaration of Authorship

I hereby declare that this thesis has not been submitted as an exercise for a degree at this or any other university.

I consent to the examiner retaining a copy of the thesis beyond the examining period, should they so wish (EU GDPR May 2018).

I agree to deposit this thesis in the University's open access institutional repository or allow the Library to do so on my behalf, subject to Irish Copyright Legislation and Trinity College Library conditions of use and acknowledgement.

Ee Liang Chua	January 21, 2025
Signature	Date

Summary

Upper mantle structure, intraplate volcanism and the unique anisotropy of the Antarctic Plate from waveform tomography

by Ee Liang CHUA

Antarctica's unique geological setting makes it an important location for understanding the Earth's crust and upper mantle, and its connections to the past and future evolution of the Earth. The Antarctic continent has remained relatively stationary at the South Pole over the past 80 million years, and is covered by the largest ice sheet in the world. The ice sheet is a major potential source driving global sea level rise, and is impacted by processes occurring within solid earth that are modulated by the lithospheric and upper mantle parameters. The challenging conditions and remote location has historically limited the direct data sampling of Antarctica, consequently, researchers have been turning to indirect geophysical methods such as seismology to better understand the region.

Over the past two decades, the quantity and quality of seismic stations deployed globally—both permanent and seasonal—have dramatically increased. The significant rise in the the number of temporary deployments have enhanced the station coverage of Antarctica, leading to an increasing number of seismic studies of Antarctica and surroundings. However, the seismic data coverage is still heterogeneous, and our understanding of the Antarctic lithosphere and mantle is still limited. In this work, we present a new anisotropic Sv velocity model of the Antarctic Plate, AP2024, that includes the lithosphere and underlying mantle down to 660 km depth beneath both the continental and oceanic portions of the plate. To augment the limited seismic station coverage of Antarctica, we assemble very large regional and global data sets, comprising all publicly available

broadband seismic data. The model is generated using 785,000 waveform-fitted seismograms from over 27,000 events and 8,700 stations, and constrained by both body and Rayleigh surface waves, ensuring the dense data sampling of the entire upper mantle depth range. We invert the waveforms of S-, multiple S- and surface waves using Automated Multimode Inversion (AMI), producing sets of linearly independent equations with uncorrelated uncertainties for each source-station path. These equations describe the path-averaged perturbations of P- and S-wave velocities along approximate sensitivity kernels. The equations are then combined into a large linear system where the 3-D distributions of P- and S-wave velocities and '2Ψ' azimuthal anisotropy is solved for, to obtain a preliminary model. We then exploit the mutual consistency of data arising from the massive dataset to remove the least mutually consistent measurements. A further manual error identification process, aimed at identifying and removing probable artefacts due to instrumentation errors, completes the process. The tomographic inversion is global but focused on the Antarctic Plate, with the data sampling maximised in the Southern Hemisphere, and with the regularisation tuned for the region. The model is parameterised on a triangular grid with a target lateral inter-knot spacing of 125 km, and is validated via a series of resolution tests.

The model is consistent with previous studies, and reveals that the upper mantle of the Antarctic continent exhibits a bimodal nature. A sharp boundary, along the Transantarctic Mountains divides the cratonic eastern from tectonic western Antarctica. The bimodality also extends to the oceanic part of the plate, with the older oceanic lithosphere beneath the southern Indian Ocean and the Weddell and Enderby basins showing higher shear velocities. The continental lithosphere in East Antarctica shows high velocity anomalies, with significant lateral heterogeneity, similar to those beneath stable cratons elsewhere around the world. Low-velocity anomalies underlie most of West Antarctica at 100 km depth, indicative of thin lithosphere and warm asthenosphere, including a prominent low velocity channel along the southern front of the West Antarctic Rift System. The seismic structure beneath the Antarctic Peninsula, confirms the post-subduction origins of volcanism along the peninsula. The two largest volcanic provinces in West Antarctica—Marie Byrd Land and Erebus—are underlain by prominent low velocity anomalies at asthenospheric depths, indicative of partial melting that feeds the volcanic processes. Combining our observations with whole mantle tomography models, we find strong evidence of deep-mantle origins for West Antarctica. The azimuthal seismic anisotropy reveals interesting fast-propagation directions oriented E-W in the older oceanic lithosphere, in a surprising circular pattern around the continent, in contrast to the younger oceanic lithosphere and elsewhere around the world. We identify com-

plex anisotropy within the cratonic East Antarctica, indicative of the layering of deformation in the course of the craton formation. Strong azimuthal anisotropy associated with the Phoenix-Antarctic and South American-Sandwich subduction zones reveal clues of pressure-driven flow in the oceanic asthenosphere.

Preface

This thesis is based on a collection of one article submitted to and in revision to a peer-reviewed journal (Chapter 3), and two manuscripts in preparation for submission to peer-reviewed journals (Chapters 4 and 5).

The results presented here were generated using programs written mostly in Unix Shell, C, C++, Fortran, and Python. All programs were compiled and run on Ubuntu Linux distributions.

The figures were produced using PyGMT (Tian et al., 2024), a python wrapper of the original Generic Mapping Tools (Wessel et al., 2019), GPlates (Müller et al., 2018) and SubMachine (`http://www.earth.ox.ac.uk/~smachine/cgi/index.php`; Hosseini et al. (2018)).

Statement of co-authorship

Chapter 3 is a manuscript submitted to Geophysical Journal International, and has been accepted for publication. I assembled and processed the newest available data, performed the waveform inversion for the new data, computed the tomographic model, performed the resolution tests and interpretations, created the figures and wrote the manuscript. Sergei Lebedev, my co-supervisor previously from the Dublin Institute for Advanced Studies (DIAS) and currently at the University of Cambridge, provided mentorship and advice on the development of the model, interpretations and the writing of the manuscript.

Chapter 4 is a manuscript in preparation for submission to Geochemistry, Geophysics, Geosystems. I computed the tomographic model, made the interpretations, created the figures and wrote the manuscript. Sergei Lebedev provided valuable input for the interpretations with the writing of the manuscript.

Chapter 5 is a manuscript in preparation for submission to Geophysical Research Letters. I computed the tomographic model, analysed and interpreted the result and data and created the figures. Sergei Lebedev was closely involved in the development of the main hypothesis and provided valuable input in the writing of the manuscript.

"And here, poor fool! With all my lore, I stand no wiser than before"

Goethe/Faust

Acknowledgements

I would like to extend my sincerest gratitude to my supervisor, Sergei Lebedev, without whom I would not have been able to bring this work to fruition. His enthusiasm and passion for science is inspiring. I am always grateful for the insight and experience he brings to our discussions.

I am also grateful to my co-supervisor at Trinity College Dublin (TCD), David Chew, who was always available to assist me with any issues I encountered through my time with TCD.

I would like to thank everyone at DIAS, past and present for making my journey at DIAS an enjoyable one. The atmosphere at DIAS is like no other and I'm grateful for the all the support and friendship through this journey. Thanks to my office mates Nicolas, Bruna, Clara, Janneke and Giuseppe for the random chats and for putting up with my negativity and to Maria who guided me along during my early days at DIAS. Many thanks to Chris, Huda and Emma who have kept everything running smoothly and for always looking out for everyone and helping with the bureaucracy at DIAS. Thanks to Philippe and Jef for always being there to solve any IT issues (including the time I almost got us blacklisted when I tried to download data) and for maintaining the network. Thanks to everyone else who I have not mentioned, I really appreciate the time we've spent together at DIAS, and all the pub nights and parties we've had.

Thanks to all my family and friends for all their support and help. And a special thanks to my parents who have always been supportive of me, and providing the opportunity for my pursuits.

Contents

Declaration of Authorship iii

Summary v

Preface ix

Statement of co-authorship xi

Acknowledgements xv

Table of Contents xix

List of Figures xxii

List of Acronyms xxvi

1 Introduction 1

1.1 Seismic waves . . . 1
1.2 Seismic tomography . . . 3
1.2.1 Early seismic studies . . . 3
1.2.2 Modern tomography . . . 4
1.3 Imaging the Earth's upper mantle . . . 5
1.4 Motivation . . . 7
1.5 Outline . . . 8

2 Theoretical framework 11

2.1 Waveform inversion . . . 11
2.1.1 Waveform fitting . . . 12
2.1.2 Non-linear inversion . . . 13
2.2 Partitioned Waveform Inversion . . . 15
2.3 Automated Multimode Inversion . . . 18
2.3.1 Relating waveforms to Earth structure . . . 19
2.3.2 3-D background model . . . 20

2.3.3 Approximate sensitivity kernels 21
2.3.4 Model parameterisation 22
2.3.5 Linear tomographic inversion 25

3 Waveform tomography of the Antarctic Plate 31
3.1 Abstract 31
3.2 Introduction 32
3.2.1 Tectonic Setting 34
3.2.2 Previous Seismic Studies 37
3.3 Methods 39
3.3.1 Data 39
3.3.2 Inversion 41
3.4 Results 44
3.4.1 The model AP2024 44
3.4.2 Resolution Tests 46
3.4.3 Comparison with other S-wave tomographic models 48
3.5 Discussion 50
3.5.1 East Antarctic Lithosphere 51
3.5.2 West Antarctica 55
3.5.3 Southern and surrounding oceans 60
3.6 Conclusions 61
3.7 Acknowledgements 62

4 Seismic evidence for a deep-mantle origin of the West Antarctic intraplate magmatism 65
4.1 Abstract 65
4.2 Introduction 66
4.2.1 Distribution of intraplate volcanism on the Antarctic Plate . 66
4.3 Methods 69
4.4 Antarctic Mantle Structure 71
4.4.1 Overview of the upper mantle structure 71
4.4.2 Comparison with other tomographic models 73
4.4.3 Resolution tests 77
4.5 Discussion 78
4.5.1 West Antarctica 79
4.5.2 Volcanism in the Southern and surrounding oceans 85
4.6 Conclusions 88

5 The Peculiar Anisotropy of the Antarctic Plate **91**
5.1 Abstract . . . 91
5.2 Introduction . . . 92
5.3 Anisotropic waveform tomography . . . 94
5.3.1 Anisotropy parameterisation . . . 95
5.3.2 Upper mantle anisotropy . . . 96
5.3.3 Resolution testing . . . 99
5.4 Discussion . . . 101
5.4.1 The unique anisotropy of the Antarctic Plate . . . 101
5.4.2 Comparison with shear wave splitting and other observations 104
5.5 Conclusions . . . 110

6 Conclusions **113**
6.1 Lithospheric structure . . . 113
6.2 Intraplate magmatism and hotspots . . . 114
6.3 Azimuthal anisotropy . . . 115
6.4 Future work . . . 115

Bibliography **119**

List of Figures

1.1 Particle motion of the 4 types of elastic waves. 2
1.2 Sensitivity kernels of Rayleigh wave group and phase velocities. . . 3
1.3 Example of a global tomography model, SL2013sv. 6

2.1 Example of a hypothetical parameters of a misfit function. 15
2.2 Background reference models used in AMI. 21
2.3 Path-normal cross section of the kernel, and the approximate sensitivity kernel. 22
2.4 An example of a tomographic model grid and the vertical basis functions used in AMI. 23
2.5 Example of a successful AMI waveform fit. 24

3.1 Bed rock topography and bathymetry of Antarctica and surrounding oceans. 33
3.2 Maps of all stations and events of seismograms successfully fit by AMI. 40
3.3 Data-sampling density of AP2024. 42
3.4 Map views of the S-wave velocity model, AP2024, at twelve depths. 45
3.5 Resolution tests with sparsely distributed spikes at the 3 depth intervals. 47
3.5 A comparison between the AP2024 model and five other S-wave velocity models. 50
3.6 Map views of the model at 110 and 200 km depths. 52
3.7 Synthetic test for the lithosperic structure in East Antarctica. 54
3.8 16 cross sections through the AP2024 model. 57

4.1 Bedrock topography and bathymetry of the Antarctic Plate. 67
4.2 Map views of the S-wave velocity model AP2024 at 4 depths. 72
4.3 A comparison of AP2024 and 3 other velocity models in the upper mantle. 73
4.4 A comparison between 4 whole mantle tomography models in the lower mantle. 75

4.5 Cross sections across the south Pacific and Antarctica generated by SubMachine. 76
4.6 Spike resolution tests at 110 km and 485 km depths. 77
4.7 Resolution test for the leakage of structure. 78
4.8 Upper mantle cross sections through AP2024 in west Antarctica. . . 80
4.9 Vote maps of the 33 whole-mantle global tomography models available on SubMachine. 84
4.10 Intraplate hotspots and hotspot tracks on the Antarctic Plate. 86

5.1 Bed rock topography and bathymetry of the Antarctic Plate. 93
5.2 Age of oceanic lithosphere, sea floor spreading rates and paleo-spreading direction of the Antarctic Plate. 94
5.3 Azimuthal anisotropy of the Antarctic Plate shallow mantle. 97
5.4 Azimuthal anisotropy of the Antarctic Plate mid upper mantle and mantle transition zone. 98
5.5 Anisotropy resolution test of the AP2024 model. 100
5.6 Comparison of azimuthal anisotropy in the oceanic lithosphere and paleo-APM. 102
5.7 Anisotropy, structure and deformation of Antarctica at 56 km and 150 km. 106
5.8 Paleo-APM vectors of 2 different models at different time intervals. 107
5.9 Anisotropy, structure and deformation of the Antarctic upper mantle at 4 depths. 108

List of Acronyms

1-D	1-Dimensional.
3-D	3-Dimensional.
3DLGL	Global upper mantle S-wave velocity model of Debayle et al. (2016).
AAD	Australian-Antarctic-Discordance.
ak135/AK135	1-D seismic reference model of Kennett et al. (1995).
AMI	Automated Multimode Inversion.
AN-1	S-wave velocity model of the Antarctic Plate lithosphere and uppermost mantle of An et al. (2015a).
ANET/POLENET	Seismic array deployed in West Antarctica since 2007 (Accardo et al., 2014).
ANT-20	Voigt average S-wave velocity tomography model of Antarctica of Lloyd et al. (2020).
ANUBIS	Seismic array deployed in West Antarctica in 1998–2001 (Anandakrishnan et al., 2000).
AP	Antarctic Peninsula.
AP2024	Azimuthally anisotropic mode of the Antarctic Plate upper mantle.
APM	Absolute Plate Motion.
CMB	Core-mantle boundary.
CMT	Centroid Moment Tensor.
CPO	Crystallographic preferred orientation.
CRUST1.0	2 degree crustal reference model of Laske et al. (2013).
CRUST2.0	2 degree crustal reference model of Bassin (2000).
DIAS	Dublin Institute for Advanced Studies.

DML	Dronning Maud Land.
EANT	East Antarctica.
ESA	European Space Agency.
EWM	Ellsworth-Whitmore Mountains.
FDSN	International Federation of Digital Seismograph Networks.
GAMSEIS	Seismic array deployed on the Gamburtsev Subglacial Mountains in East Antarctica in 2007–2009 (Hansen et al., 2010).
GFZ	GeoForschungsZentrum, German Research Center for Geosciences.
GHF	Geothermal Heat Flow.
GIA	Glacial Isostatic Adjustment.
GLAD-M25	Global velocity model of of Lei et al. (2020).
Global CMT/GCMT	Global Centroid Moment Tensor Catalogue (Dziewonski et al., 1981; Ekström et al., 2012).
GMT	Generic Mapping Tools (Wessel et al., 2019).
GNSS	Global Navigation Satellite System.
GSM	Gamburtsev Subglacial Mountains.
HIMU	High "μ", where μ is the ratio between ^{238}U and ^{204}Pb isotopes.
IASP91	1-D seismic reference model of Kennett & Engdahl (1991).
IPGP	Institut de Physique du Globe de Paris, Paris Institute of Planetary Physics.
IRIS	Incorporated Research Institutions for Seismology.
IRIS EMC	IRIS Earth Model Collaboration.
JWKB	Jeffreys-Wentzel-Kramers-Brillouin approximation (Dahlen et al., 2000).
LPO	Lattice preferred orientation.
LSQR	An iterative Least Squares algorithm (Paige & Saunders, 1982).

MBL	Marie Byrd Land.
Moho	Mohorovičić discontinuity.
ObsPy	An open-source project dedicated to provide a Python framework for processing seismological data.
ORFEUS	Observatories & Research Facilities for European Seismology.
PAR	Pacific-Antarctic Ridge.
PREM	Preliminary Earth Reference Model, a 1-D seismic reference model (Dziewonski et al., 1981).
PRI-P05	Global P-wave velocity model of Montelli et al. (2006).
PWI	Partitioned Waveform Inversion.
PyGMT	Python interface for the Generic Mapping Tools (Tian et al., 2024).
RIS	Seismic array deployed on the Ross Ice Shelf in West Antarctica in 2014–2017 (Baker et al., 2019).
SEIR	Southeast Indian Ridge.
SEMUCB-WM1	Global whole mantle S-wave velocity model of French et al. (2013).
SEMum2	Global upper mantle S-wave velocity model of French et al. (2013).
SEPA	Seismic array deployed in the Antarctic Peninsula in 1997–1999 (Robertson Maurice et al., 2003).
SKS waves	Seismic waves that travel through the mantle, core and back through the mantle.
SL2013	Global upper mantle Sv velocity tomography model of Schaeffer & Lebedev (2013).
SPiRaL	Global P- and S-wave velocity tomography model of Simmons et al. (2021).
SPO	Shape preferred orientation.
SSCUA	Seismic array deployed in East Antarctica in 2002–2005 (Reading, 2006).
STSE	Support to Science Element.
TAM	Transantarctic Mountains.
TAMNNET	Seismic array deployed on the Transantarctic Mountains in 2012–2015 (Hansen et al., 2015).

TAMSEIS	Seismic array deployed on the Transantarctic Mountains in 2000–2003 (e.g., Lawrence et al., 2006b).
TI	Thurston Island.
TX2019slab-S	Global S-wave velocity model of Lu et al. (2019).
UKANET	Seismic array deployed in West Antarctica in 2016–2018 (O'Donnell et al., 2019a,b).
UU-P07	Global P-wave velocity model of Amaru (2007).
WANT	West Antarctica.
WARS	West Antarctic Rift System.
WINTERC-G	Global thermochemical model of the lithosphere and upper mantle of Fullea et al. (2021).

Chapter 1

Introduction

Seeking a better understanding of the planet Earth that we live on has been an endeavour of humankind for most of our recorded history. Efforts to measure and understand the Earth span millennia, however, it was not until the earth 20th century that the modern study of geophysics began. It was not until the groundbreaking development of the plate tectonics theory, that we were able to reconcile our observations with the processes occurring in the Earth's interior in a self-consistent manner (e.g., Fowler, 2005).

1.1 Seismic waves

Seismology is the study of the propagation of elastic waves in the Earth, and is the best method to study the structure of Earth's deep interior. Seismological observations have been one of the primary methods to study the Earth's interior since the early 20th century. The pioneering work by Robert Mallet in the 19th century laid the foundations for the developments in methodology and instrumentation that ensued in the following decades. Earthquake seismology in particular, is the most effective at studying the deep interior. Mapping the locations of earthquakes provided accurate estimates of the tectonic plate boundaries, and the earthquakes themselves release massive amounts of energy and elastic waves which we can then use to investigate Earth's interior. Elastic waves can be classified into two categories: body and surface waves.

Body waves

Body waves are elastic waves that travel through the Earth and are reflected or transmitted at interfaces. The 2 types of body waves are the P and S waves. P waves, also referred to as primary waves, pressure or compressional waves, involve particle motion in the plane of wave propagation of the and are irrotational

and analogous to sound waves. S waves, also referred to as secondary or shear waves, involve particle motion perpendicular to the wave propagation direction. Shear wave motion can be decomposed into orthogonally polarised components, namely the horizontally polarised (S_H) and and vertically polarised (S_V) waves. The particle motion of the body waves are illustrated in Fig. 1.1.

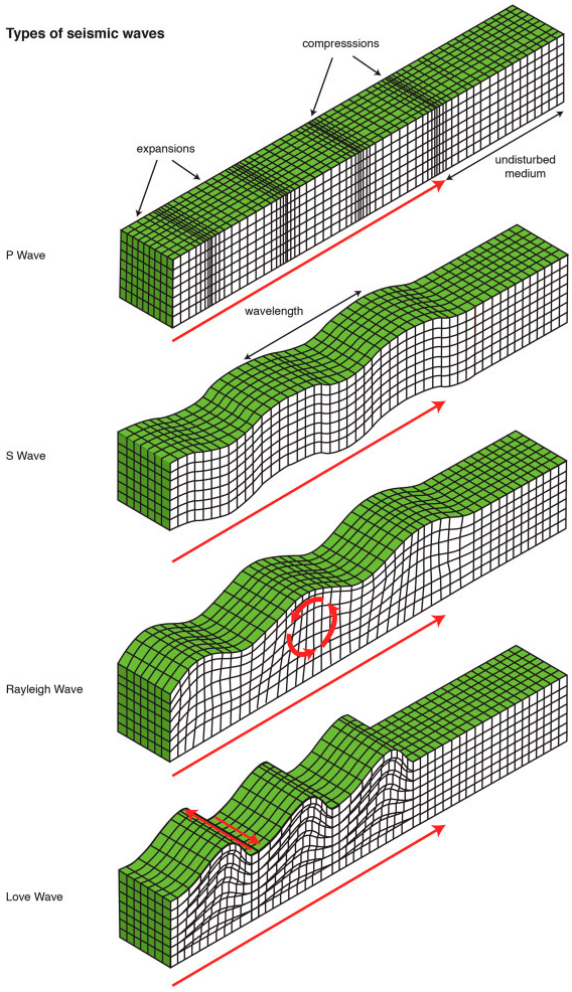


Figure 1.1: Particle motion in the direction of propagation of the 4 types of elastic waves. From top to bottom: P and S waves, the 2 types of body waves, Rayleigh and Love waves, the 2 types of surface waves. From Hersir et al. (2022).

Surface waves

Surface waves are elastic waves that travel along the surface and the near-surface layers of the Earth, and do not penetrate deeply into the interior. Surface waves are higher in amplitudes for most earthquakes, with the exception of those that occur hundreds of kilometre deep and arrive after the first arrivals of P and S waves on the seismograms. There are 2 types of surface waves: Rayleigh and Love waves. The particle motion of Rayleigh waves is restricted to the vertical plane of the direction of wave propagation, and the particles move in a retrograde

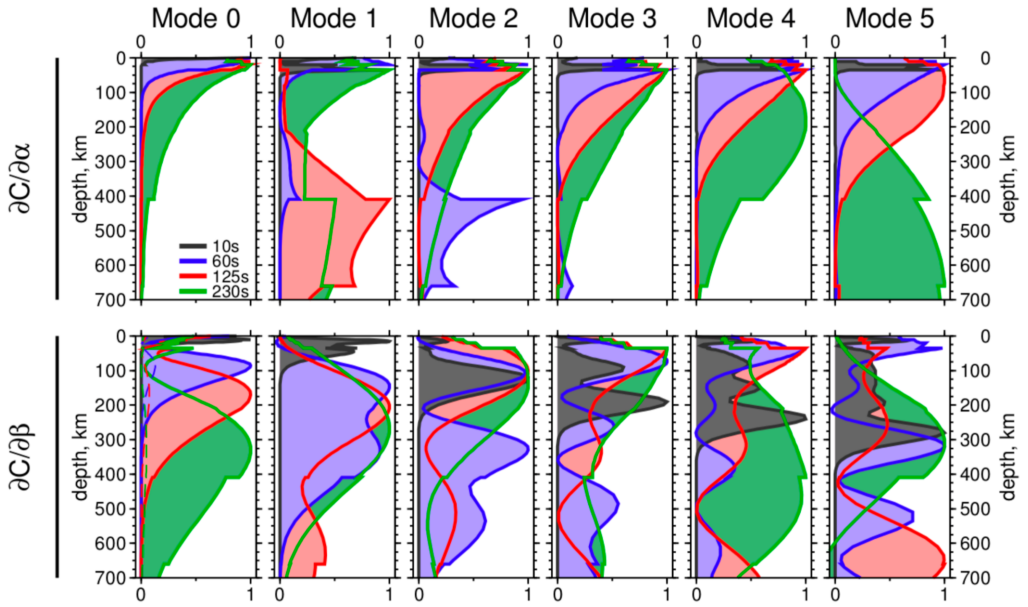


Figure 1.2: Sensitivity of Rayleigh wave phase (top) and group (bottom) velocities with increasing depth, computed for AK135. Each period is differently coloured and the amplitude of each kernel is scaled independently with respect to the maximum at each depth. From Schaeffer & Lebedev (2015).

vertical ellipse. Love wave particle motion is horizontal and perpendicular to to the direction of wave propagation. The particle motion of the surface waves are illustrated in Fig. 1.1.

Rayleigh wave amplitudes decay exponentially with increasing depth. The longer period Rayleigh waves penetrate more deeper into the Earth's surface, and thus, contain more information on the deeper structure. Fig. 1.2 illustrates the depth sensitivity of Rayleigh waves for 4 periods of the fundamental mode and the first 5 odd-numbered higher modes and illustrates the increase in depth sensitivity with increasing period.

1.2 Seismic tomography

1.2.1 Early seismic studies

Variations in the propagation velocities of the elastic waves through the Earth's interior can yield information on the Earth's structure. Seismic velocities can be associated to changes in the temperature and composition in the Earth.

Fundamental features of the Earth, such as the presence of an outer core (Oldham, 1906), the Mohorovičić discontinuity (Moho; Mohorovicic, 1910) and inner core (Lehmann, 1936) were discovered by using data from the early seismograph networks. Subsequent analysis of seismograph data led to the creation of early ra-

dial velocity profiles (Gutenberg & Richter, 1934b,a, 1936, 1939; Jeffreys & Bullen, 1940). They led to the development of 1-D averaged velocity models, including the Preliminary Earth Reference Model (PREM; Dziewonski et al., 1981), IASP91 (Kennett & Engdahl, 1991) and AK135 (Kennett et al., 1995).

Despite the recognition of the usefulness and continued development of 1-D velocity models, such models were commonly acknowledged to be insufficient to reconcile the complex seismic signals recorded as early as in the 1960s. Thus, more advanced techniques were developed, leading to the beginnings of seismic tomography. Seismic tomography is a technique that 'images' the Earth using seismic waves, where the deviations of seismic observations, e.g. P-wave arrival times in the early models, with respect to a reference (or expected) model are visually represented in an image. Pioneering work by Keiti Aki (Aki et al., 1974) who presented the P-wave travel times within a medium in a graphical image led to the development of the field. Subsequent work by Aki & Lee (1976), Sengupta & Toksöz (1976), Dziewonski et al. (1977) and Masters et al. (1982) led the way for the development of techniques that further illuminated the heterogeneous structure of the Earth in the coming decades.

Contemporaneously to the development of these isotropic models, by the 1970s, it was widely recognized that the Earth's upper mantle exhibited anisotropic properties, both radially (i.e. there are differences in propagation velocities of differently polarised seismic waves) and azimuthally (i.e. seismic wave velocities are directionally dependent) (e.g., Anderson, 1961; Kaminuma & Aki, 1963; McEvilly, 1964; Hess, 1964).

The next few decades saw the development of new 3-D tomographic models of the isotropic and anisotropic structure of the Earth (e.g., Forsyth & Uyedat, 1975; Aki et al., 1977; Woodhouse & Dziewonski, 1984; Montagner & Nataf, 1988; Montagner & Tanimoto, 1991; Su et al., 1992; Li & Romanowicz, 1996).

1.2.2 Modern tomography

In the past few decades, the concurrent improvements in computational capabilities and high-quality, broadband seismic data have driven the development of more complex and higher resolution tomographic models.

The models can be broadly classified by the data used to build the models. Body wave travel time models utilise travel time residuals—differences between the observed and expected travel time calculated from a reference model—to map the 3-D variations in seismic wave speeds. Recent models (e.g., Montelli et al., 2004; Amaru, 2007; Li et al., 2008; Simmons et al., 2012) have improved the resolution of the images, with highly sampled regions—the regions where the

density of crossing ray paths is the highest, such as subduction zones or under dense seismic network areas—that are particularly well resolved. Surface-wave and normal-mode models are complementary to body wave models, providing improved resolution where the body wave models are least well resolved (e.g., Shapiro & Ritzwoller, 2002; Zhou et al., 2006; Nettles & Dziewoński, 2008; Ekström, 2011). Furthermore, it is becoming increasingly more common to combine multiple data types to improve the resolution of tomographic models (e.g., Mégnin & Romanowicz, 2000; Masters et al., 2000; Lebedev & van der Hilst, 2008; Lekić & Romanowicz, 2011; Ritsema et al., 2011; Debayle & Ricard, 2013; French & Romanowicz, 2015). These models utilised complementary datasets, e.g. incorporating data from both body and surface waves, allowing them to simultaneously model the lithosphere down to the lower mantle, albeit to varying degrees of success.

With the advances brought about improve data quality and computational capacity, tomographic models have evolved from using simple approximations based on ray theory for body waves or the Jeffreys-Wentzel-Kramers-Brillouin approximation (JWKB; Dahlen & Tromp, 1998) the ray theory equivalent for surface waves, to more sophisticated techniques. More advanced imaging techniques such as finite frequency tomography (Dahlen et al., 2000; Montelli et al., 2004; Sigloch & Nolet, 2006) and full-waveform inversion (Tarantola & Valette, 1982; Fichtner et al., 2009; Tape et al., 2009; Bozdağ et al., 2016; Lei et al., 2020; Cui et al., 2024) were developed in the never ending quest to extract more information from each individual seismogram. The continuous advancements in methods and computational capabilities, along with the increasing number of permanent stations and temporary deployments worldwide, have driven significant progress in the development of tomographic models with increasingly higher resolutions (Fichtner et al., 2024).

1.3 Imaging the Earth's upper mantle

Seismic velocities are our main source of information on the variations of temperature in the Earth's mantle (e.g., Goes et al., 2000; Fullea et al., 2021; Lebedev et al., 2024). Common compositional variations in the upper mantle change seismic velocities by less than 1%, at most 2% (e.g., Sobolev, 1996; Goes et al., 2000; Cammarano et al., 2003; Schutt & Lesher, 2006). By contrast, the total shear-wave speed variations observed in tomographic models are around $\pm$10% at the scales of a few hundred kilometres, with most of that due to temperature variations (Schaeffer & Lebedev, 2015). High seismic velocities in the uppermost mantle (<250 km) indicate low temperatures and are a proxy for the lithospheric thick-

ness, with the highest velocities indicating the thickest, coldest cratonic lithosphere (McKenzie et al., 2005; Fullea et al., 2021; Lebedev et al., 2024). Low seismic velocities at similar depths are most commonly attributed to relatively high temperatures, with partial melting and volatiles also lowering seismic velocities (e.g., Goes et al., 2000; Fullea et al., 2021; Bonadio et al., 2018).

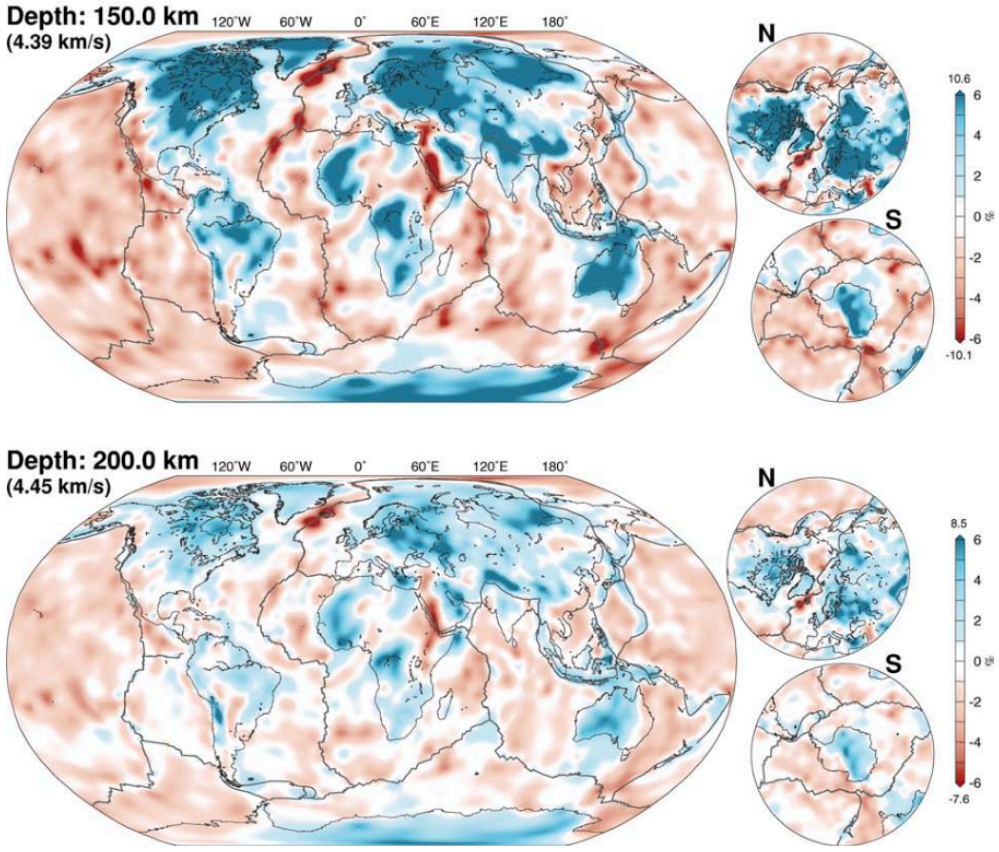


Figure 1.3: Horizontal cross-sections through the SL2013sv model in the uppermost mantle, at 150 and 200 km depths. North and south polar views are shown on the right of each cross-section. Plate boundaries and continental coastlines are indicated. Perturbations with respect to the reference model are shown to the right of each depth cross-section. From Schaeffer & Lebedev (2013).

In Section 1.2.1, we covered the development of early 1-D averaged velocity models, that approximated the Earth's inner structure as a 1-D stratified planet comprising 3 major layers: the crust, mantle and core (e.g., Dziewonski et al., 1981; Kennett & Engdahl, 1991; Kennett et al., 1995). These layers are separated by boundaries or discontinuities—where the seismic properties across the boundaries differ significantly—the Moho between the crust and mantle and the core-mantle boundary (CMB) (e.g., Ammon et al., 2021). The major layers are further subdivided, with velocity discontinuities observed in the mantle at approximately 410 km and 660 km. These mark the boundaries of the mantle transition zone, which separates the upper mantle from the lower mantle at its lower

boundary.

The uppermost mantle is highly heterogeneous, exhibiting significant variations in seismic velocity distributions. These variations are linked to surface tectonic processes such as mantle upwellings, ancient lithosphere, spreading ridges, and subduction zones. Figure 1.3 are two cross-sections through the uppermost mantle (at 150 km and 200 km depths) from the global S-wave velocity tomography model, SL2013sv (Schaeffer & Lebedev, 2013).

Surface tectonic processes can be identified from the model; spreading ridges and mantle upwellings such as the Afar and Iceland plumes are underlain by low seismic velocities in the uppermost mantle (indicated by the red (warm) colours in Fig. 1.3). Continental cratons—ancient and stable portions of continental lithosphere, are generally identified in tomography models as regions where the lithosphere extends beyond 170 km in depth—such as the Amazonian Craton, East European Craton, North American Craton and East Antarctica are underlain by high seismic velocities (indicated by the blue (cool) colours in Fig. 1.3). Subduction zones, though not as clearly identifiable, can be mapped by identifying and tracing the subducted lithosphere—that have significantly higher seismic velocities relative to the surrounding mantle—in the mid-upper mantle. Some prominent examples of subduction zones and subducting slabs identifiable in Fig. 1.3 are the Aleutian, Japan, Sumatra and Tonga Trenches.

1.4 Motivation

Antarctica (also referred to as the Antarctic continent) is a unique location where the present structure of the crust and upper mantle links to processes of particular importance both in the past and in the future of the Earth. Despite being encircled almost entirely by spreading ridges and transform faults, the Antarctic Plate has remained relatively stationary, moving at an average rate of approximately 6 mm/yr since the late Cretaceous (Torsvik et al., 2008). The Antarctic continent, located in the central part of the Antarctic Plate, is encircled by oceanic lithosphere of different ages. The oldest oceanic lithosphere along the Weddell Rift in the Weddell Sea is approximately 183 Ma, while the youngest oceanic lithosphere can be found along the currently spreading ridges at the periphery of the plate. The continent can be subdivided into East Antarctica, composed of mainly ancient Precambrian cratonic blocks, and West Antarctica comprising Phanerozoic terranes.

Located at and around the South Pole, the Antarctic continent is overlain by the largest ice sheet on Earth, making it an integral component of the global climate system, as well as a major risk factor and potential contributor to global sea

level rise (Oppenheimer et al., 2019). The geothermal heat flux (GHF) at the base of ice sheets is a critical yet still poorly constrained parameter modulating the ice dynamics. The heat flux influences basal melting, glacial rheology and erosion rates among other factors, impacting the frictional regime at the base of the ice sheet and potentially increasing ice sheet velocities (e.g., Pollard et al., 2005; Bell, 2008; Golledge et al., 2015; Burton-Johnson et al., 2020; Lösing et al., 2020).

Glacial Isostatic Adjustment (GIA) is the solid Earth response to changes in the ice-sheet surface load over time. A retreating or shrinking ice sheet reduces the load on the solid Earth beneath, which triggers an instantaneous elastic response and a delayed, gradual viscoelastic deformation (Peltier, 1974). This is response of the solid Earth is observable as a topographical change—an uplift of bedrock and, conversely, a decrease in relative the sea levels in the affected regions—consequently negatively affecting the stability of marine ice sheets (e.g., Gomez et al., 2015). GIA responses are modulated by the lithospheric thickness and upper mantle viscosity, which dictate the temporal and spatial scales of the adjustment process (e.g., Konrad et al., 2015; Barletta et al., 2018; Whitehouse, 2018). The properties of the underlying lithosphere and mantle can significantly influence the behaviour of the East and West Antarctic Ice Sheets, affecting the sea level rise.

The challenging conditions and remote location has historically limited the direct data sampling of Antarctica. With most of the continent covered by the ice sheet, geological data is limited to outcrops located primarily along the coastlines, which account for less than 0.2% of Antarctica's total land area (Burton-Johnson et al., 2016). Indirect geophysical methods including seismology, gravimetry, magnetics and geodesy are, thus, particularly important for investigating Antarctica. Seismic imaging is particularly useful in the study of the crust and upper mantle, as we can relate the distribution of seismic velocities to variations in the thermal, compositional, density and viscosity structure at depth.

1.5 Outline

In this thesis, we investigate the structure of the lithosphere and upper mantle beneath the Antarctic Plate. We do so with waveform tomography using the Automated Multimode Inversion (AMI; Lebedev et al., 2005). We use a very large data set of over 1.8 million successfully fit seismograms from events around the Earth. Incorporating new data from the poorly sampled Antarctic region allows us to achieve about the most comprehensive data coverage presently possible. The new AP2024, an azimuthally anisotropic Sv velocity model of the Antarctic Plate upper mantle, is constrained by nearly 0.8 million waveform fits after a

data selection process to reduce computational expense without compromising the sampling density of the model region. The improved sampling and coverage of the Antarctic Plate enables the resolution of structures previously unobserved by other models.

Chapter 2 is a an overview of the theory and background of the AMI methods. We first discuss the concepts of waveform inversion, the set up of Partitioned Waveform Inversion (PWI) of Nolet (1990), and the key components of the waveform inversion and 3-D tomography with AMI.

In **chapter 3**, we present the construction and validation of AP2024 and discuss its isotropic component. We provide an overview of the data used, data selection, methodology and evaluation of the model. We then discuss the heterogeneous cratonic lithosphere present in East Antarctica, the low seismic velocities underlying West Antarctica and their origin and evolution.

Chapter 4 utilises AP2024 to investigate the origins of intraplate magmatism in West Antarctica. In order to do this, we analyse AP2024 alongside several other regional and global-scale upper mantle and whole mantle tomographic models and geochemical datasets. We discuss the post-subduction origin of the current volcanism along the Antarctic peninsula, the two largest volcanic provinces in West Antarctica, Marie Byrd Land and Erebus, and the prominent low seismic velocities underlying the regions in the deep mantle. We then briefly discuss the intraplate volcanism found in the Southern and southern Indian Oceans. Finally, we discuss deep mantle origins and mechanisms of West Antarctic intraplate volcanism.

In **chapter 5** we present the anisotropic component of AP2024, and discuss the peculiar azimuthal anisotropy pattern we find in the oceanic lithosphere. We provide an overview of the anisotropic parameterisation of the model and an overview of the main features of the model. Anisotropy resolution testing is performed. We discuss the key anisotropy patterns and their origins and compare them to those elsewhere around the globe. We also compare the azimuthal anisotropy pattern to splitting measurements, a different method to investigate anisotropy, and discuss how the anisotropy observed in the Antarctic Plate may relate to past and present-day plate motions and mantle deformation.

Chapter 2

Theoretical framework

In this chapter, we discuss the concepts of waveform inversion, the PWI scheme developed by Nolet (1990, 2008) and finally the AMI alogorithm developed by Lebedev et al. (2005) which serves as the theoretical basis for this study.

The equations and derivations presented in this chapter are an overview of the key concepts and equations adopted by AMI, and are not meant to be a rigorous derivation. We refer the reader to the books by Dahlen & Tromp (1998) and Nolet (2008) for a more comprehensive discourse and rigorous derivation of the equations.

2.1 Waveform inversion

A large amount of information is recorded in a seismogram, and that can be utilised to probe the structure that lies along and around the path between the source and receivers. One general approach to constraining the structure along the path involves attempting to fit a synthetically generated seismogram with the observed seismogram. There are three main steps involved in this procedure: forward modelling to generate a seismogram from a synthetic Earth model, a quantitative method to compare and evaluate the synthetic and observed data and finally an algorithm to revise the Earth model to generate better synthetic data. There are various approaches to modelling the structure of the Earth, the approach used in this work utilises surface and reflected shear waves to generate a synthetic Earth model so as to minimise the data-synthetic misfit. .

The forward modelling approach adopted to generate the synthetic seismogram is a frequency-domain mode summation based on the Jeffreys-Wentzel-Kramers-Brillouin approximation (JWKB; Dahlen & Tromp, 1998). The JWKB approximation is the surface-wave counterpart to ray theory; it requires the medium to be smooth the scattering effects—negligible. The waveform comparison and

misfit evaluation are performed in the time domain, using a complex windowing operator designed to identify and weight the portions of the seismogram in the time-frequency plane where the JWKB approximation is valid. This selection, filtering and windowing operator are fully automated and are key components of the Automated Multimode Inversion (AMI) technique developed by Lebedev et al. (2005). A non-linear conjugate gradient method is used to update the synthetic Earth model. Stable convergence to the global minimum of the misfit function is facilitated by the very small data-synthetic misfits within the time-frequency windows selected and used.

2.1.1 Waveform fitting

The displacement spectrum of a synthetic seismogram recorded at a receiver p can be obtained by summing over modes n (Dahlen & Tromp, 1998). We formulate the equation following the approach by Nolet (1990):

$$u_p(\omega) = \sum_n A_{np}(\omega) e^{ik_n(\omega)\Delta_p} \quad , \tag{2.1}$$

where Δ_p is path length and A_{np} is the complex amplitude.

In the JWKB approximation, the total phase measured along the path, $\psi_p(\omega)$, can be expressed as:

$$\psi_p(\omega) = \mathbf{\Phi}_n^{(p)} + k_n(\omega)\Delta_p \quad , \tag{2.2}$$

where $\mathbf{\Phi}_n^{(p)}$ is the initial phase imparted by the source and $k_n(\omega)\Delta_p$ is the accumulated phase along the path.

Assuming the accumulated phase along the path is aggregated between $\Delta = 0$ and the path length, Δ_p, then:

$$k_n(\omega)\Delta_p = \int_0^{\Delta_p} k_n(\omega, \theta, \phi) d\Delta \quad , \tag{2.3}$$

where $k_n(\omega, \theta, \phi)$ is the local wave number for a surface wave in a simple 1-D Earth model. Eq. 2.2 becomes:

$$\psi_p(\omega) = \mathbf{\Phi}_n^{(p)} + \int_0^{\Delta_p} k_n(\omega, \theta, \phi) d\Delta \quad . \tag{2.4}$$

Since the initial phase of the source, $\mathbf{\Phi}_n^{(p)}$, is included in the complex amplitude term, $A_{np}(\omega)$, we can express the displacement spectrum as a function of

the complex amplitude and accumulated phase:

$$u_p(\omega) = \sum_n A_{np}(\omega) exp[i \int_0^{\Delta_p} k_n(\omega, \theta, \phi) d\Delta] \quad . \tag{2.5}$$

Starting at a simple, 1-D initial "best guess" model, heterogeneities along the propagation path perturb the wave number of the starting model:

$$k_n(\omega, \theta, \phi) = k_n(\omega) + \delta k_n(\omega, \theta, \phi) \quad . \tag{2.6}$$

For a multi-dimensional model, we reformulate the model perturbations in a vector, $\delta \boldsymbol{m}(\boldsymbol{r})$, the accumulated phase is then:

$$\int_0^{\Delta_p} k_n(\omega, \theta, \phi) d\Delta = k_n^0(\omega)\Delta_p + \int_0^a \int_0^{\Delta_p} \boldsymbol{G}_n(\omega, r) \cdot \delta \boldsymbol{m}(\boldsymbol{r}) d\Delta dr \quad , \tag{2.7}$$

where the kernel $\boldsymbol{G}_n$ contains the partial derivatives, and we integrate over the radius (or depth), and along the path p.

By exploiting ray theory; applying the JWKB approximation, the kernel $\boldsymbol{G}_n$ is independent of the polar and azimuthal angles, and depends solely on r. Removing the kernel from the path integral yields:

$$\delta k_n(\omega) \equiv \int_0^{\Delta_p} k_n(\omega, \theta, \phi) d\Delta - k_n^0(\omega)\Delta_p = \int_0^a \boldsymbol{G}_n(\omega, r) \cdot \left[\int_0^{\Delta_p} \delta \boldsymbol{m}(\boldsymbol{r}) d\Delta \right] dr \quad . \tag{2.8}$$

Since the path integral only a function of r, it is a simple 1-D model representation for the particular path. Thus, we can parameterise the model with a set of layers that can be expressed in the form of a set of basis functions $\boldsymbol{h}_i(r)$. The path-averaged model can then be expressed as:

$$\frac{1}{\Delta_p} \int_0^{\Delta_p} \delta \boldsymbol{m}(\boldsymbol{r}) d\Delta = \sum_{i=1}^{M} \gamma_i \boldsymbol{h}_i(r) \quad , \tag{2.9}$$

with a set of model parameters M, which we can then invert for by varying δk_n:

$$\delta k_n(\omega) = \sum_{i=1}^{M} \gamma_i \int_0^a \boldsymbol{G}_n(\omega, r) \cdot \boldsymbol{h}_i(r) dr \quad . \tag{2.10}$$

2.1.2 Non-linear inversion

The misfits can be determined in either the time or frequency domains. The time domain is preferred as it allows straightforward time-windowing of the signal. We use transform the synthetic seismogram to the time domain using the inverse

Fourier transform.

We determine the γ_i by minimising the misfit function $F(\boldsymbol{\gamma})$—between the synthetic, u_p, and observed, u_{obs}, data—defined as:

$$F(\boldsymbol{\gamma}) = \int [\boldsymbol{R}u_{obs}(t) - \boldsymbol{R}u_p(t,\boldsymbol{\gamma})]^2 dt + \boldsymbol{\gamma} \cdot \boldsymbol{C}_\gamma^{-1}\boldsymbol{\gamma} \quad , \tag{2.11}$$

where $\boldsymbol{R}$ is a time-frequency windowing operator that identifies and weights the component phases, and $\boldsymbol{C}_\gamma$ is the covariance matrix of the model. The operator $\boldsymbol{R}$ has been adapted and improved upon for AMI by Lebedev et al. (2005), and will be further discussed in Section 2.3.

The optimisation for $\boldsymbol{\gamma}$ is achieved using a fully non-linear parameter space search along optimal directions (Nolet, 1990), as used in PWI and in AMI, and is described in further detail in Nolet et al. (1986) and Nolet (1987). First, the local gradients of $F(\boldsymbol{\gamma})$ are computed numerically, then the non-linear search is performed along the directions of steepest local gradients. The first direction v_0 is the direction of steepest descent, and can be expressed in the following forms:

$$\boldsymbol{v}_0 = -\nabla_\gamma F(\boldsymbol{\gamma}_0) = -\frac{\partial}{\partial\gamma}F(\boldsymbol{\gamma}_0) = -\partial\gamma F(\boldsymbol{\gamma_0}) = -\boldsymbol{g}_0 \quad , \tag{2.12}$$

where $\boldsymbol{g}_k$ is the gradient of the steepest descent for the starting model $\boldsymbol{\gamma}_0$. The subsequent directions of descent are computed recursively (Polak & Ribiere, 1969; Nolet, 2008):

$$\boldsymbol{v}_k = -\boldsymbol{g}_k + \frac{(\boldsymbol{g}_k - \boldsymbol{g}_{k-1}) \cdot \boldsymbol{g}_k}{\boldsymbol{g}_{k-1} \cdot \boldsymbol{g}_{k-1}} \quad , \tag{2.13}$$

where $\boldsymbol{g}_k$ is the gradient of the k^{th} iteration of misfit function $\nabla_\gamma F(\boldsymbol{\gamma}_k)$.

The iterations of $\boldsymbol{g}_k$ are calculated using a finite difference approach around $\boldsymbol{\gamma}_k$. The value of $\nabla_\gamma F(\boldsymbol{\gamma}_k)$ is then evaluated along the line $\boldsymbol{v}_k$ to located the minimum. The next model iteration $\boldsymbol{\gamma}_{k+1}$ is then determined using a quadratic interpolation around the identified minimum value.

In the following sections, we discuss the PWI method introduced by Nolet (1990) and the AMI method developed by Lebedev et al. (2005), which form the foundation of this work. AMI is an efficient and fully automatic implementation of the PWI approach, able to process massive amounts of data, and has been applied on a series of global-, continent- and plate-scale studies (e.g., Schaeffer & Lebedev, 2014; Lebedev et al., 2018; Celli et al., 2020b,a, 2021; de Laat et al., 2023; Dou et al., 2024; Chagas De Melo et al., 2024).

2.2 Partitioned Waveform Inversion

Partitioned Waveform Inversion (PWI), developed by Nolet (1990) decomposes large-scale tomographic inversions into smaller independent problems, thereby reducing computational effort. The partitioning is performed by parameterising the path integrals as perturbations in the model parameters, with respect to a reference model. Non-linear inversion can then be performed over each individual path, j, to obtain the path-averaged perturbations of the model parameters, $\gamma_i^{(j)}$, in the form of linear equations with uncorrelated uncertainties. The resulting independent linear equations from different seismograms are then assembled into a large linear system for the 3D tomographic inversion. This partitioning results in flexibility and computational efficiency, enabling the processing of very large data volumes by inverting each waveform individually.

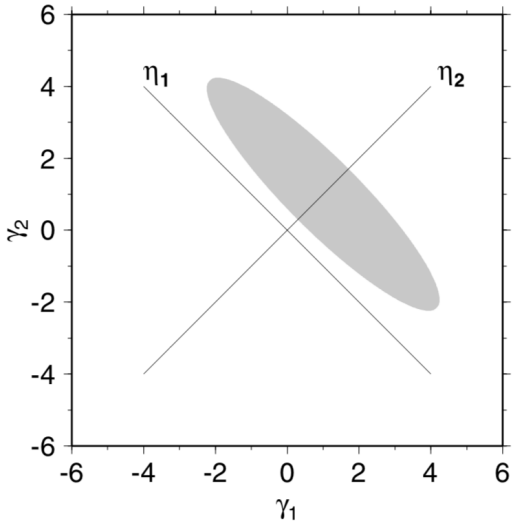


Figure 2.1: Example of two hypothetical parameters, γ_1 and γ_2, of a misfit function. The shaded region represents the zone where the combination of the γ_1 and γ_2 parameters within the misfit function F is within an acceptable threshold. (η_1, η_2) represent a rotated coordinate system where the uncertainties in the parameters can be correctly determined. From Fig. 10.8 of Nolet (2008).

Large-scale linear inversions are, however, not trivially constructed by combining the $\gamma_i^{(j)}$ into a large system. The solutions of the equations for each individual path, $\gamma_i^{(j)}$, are not unique, that is to say that some of the equations, i, are correlated. Constructing the system under the assumption of linear independence would result in a very ill-posed problem. For instance, in Fig. 2.1, uncertainty in the parameter pair (γ_1, γ_2) is strongly correlated. Imposing a coordinate rotation, to one which aligns with the major axes of the shaded ellipse i.e., (η_1, η_2), the errors are now uncorrelated, while the same number of parameters has been retained. This example is applicable to surface waves, as their frequency-

dependent sensitivity is averaged across all layers (e.g., $\gamma_1 + \gamma_2$) and is typically more accurately constrained that their differences ($\gamma_1 - \gamma_2$).

The coordinate rotation is performed using the second derivatives of the misfit function F with respect to $\boldsymbol{\gamma}$ in the optimum value $\boldsymbol{\gamma}_{opt}$:

$$H_{ij} = \frac{\partial^2 F}{\partial \gamma_i \partial \gamma_j} \tag{2.14}$$

.

The misift function at a $\boldsymbol{\gamma}$ close to the optimum value $\boldsymbol{\gamma}_{opt}$ can thus be obtained by a second-order Taylor expansion:

$$F(\boldsymbol{\gamma}) \approx F(\boldsymbol{\gamma}_{opt}) + \frac{1}{2}(\boldsymbol{\gamma} - \boldsymbol{\gamma}_{opt}) \cdot \boldsymbol{H}(\boldsymbol{\gamma} - \boldsymbol{\gamma}_{opt}) \quad . \tag{2.15}$$

Diagonalising the Hessian matrix $\boldsymbol{H}$ results in:

$$\boldsymbol{H} = \boldsymbol{S}\,\boldsymbol{\Lambda}\,\boldsymbol{S}^T \quad , \tag{2.16}$$

where $\boldsymbol{S}$ is the orthogonal transformation matrix of eigenvectors and $\boldsymbol{\Lambda}$ is the diagonal matrix of eigenvalues, which we can use to define the set of orthogonal parameters:

$$\boldsymbol{\eta} = \boldsymbol{S}^T \boldsymbol{\gamma} \quad , \tag{2.17}$$

and the original $\boldsymbol{\gamma}$:

$$\boldsymbol{\gamma} = \boldsymbol{S}\boldsymbol{\eta} \quad . \tag{2.18}$$

We impose an acceptable threshold of misfit ϵ and define the region of confidence of acceptable solutions which allows a deviation of $\Delta\boldsymbol{\gamma} = \boldsymbol{\gamma} - \boldsymbol{\gamma}_{opt}$ from the optimal solution. From eq. 2.15, we obtain the limits of ϵ:

$$\frac{1}{2}\Delta\boldsymbol{\gamma} \cdot \boldsymbol{H}\Delta\boldsymbol{\gamma} = \frac{1}{2}\Delta\boldsymbol{\eta} \cdot \boldsymbol{S}^{\boldsymbol{T}}\boldsymbol{H}\boldsymbol{S}\Delta\boldsymbol{\eta} = \frac{1}{2}\Delta\boldsymbol{\eta} \cdot \boldsymbol{\Lambda}\Delta\boldsymbol{\eta} = \frac{1}{2}\sum_{i=1}^{M} \lambda_i \Delta\eta_i^2 < \epsilon \quad . \tag{2.19}$$

The threshold value for ϵ is typically qualitatively determined and can be based on a number of factors, including misfits, instrumentation errors, anisotropy, unmodelled phases and scattering.

Since the new parameters η_i are independent, the following condition must be satisfied:

$$|\Delta\eta_i| < \sqrt{\frac{2\epsilon}{\lambda_i}} \quad . \tag{2.20}$$

We can then define a new set of basis functions $\boldsymbol{g}_j(r)$:

$$\boldsymbol{g}_j(r) = \sum_{i=1}^{M} S_{ij}\boldsymbol{h}_i(r) \quad , \tag{2.21}$$

where eq. 2.9 is now reformulated as:

$$\begin{aligned} \frac{1}{\Delta_p}\int_p \delta\boldsymbol{m}(\boldsymbol{r})d\Delta &= \sum_{i=1}^{M}\gamma_i\boldsymbol{h}_i(r) \\ &= \sum_{i=1}^{M}\sum_{j=1}^{M} S_{ij}\eta_j\boldsymbol{h}_i(r) \\ &= \sum_{j=1}^{M}\eta_j\boldsymbol{g}_j(r) \quad . \end{aligned} \tag{2.22}$$

The value of the radius r can be arbitrarily defined, indicating an almost infinite set of constraints. The set of equations can be reduced, resolving the issue of non-uniqueness, by introducing a dual basis function $\tilde{\boldsymbol{g}}$ which is orthogonal to $\boldsymbol{g}$, such that:

$$\int_0^a \tilde{\boldsymbol{g}}(r)\cdot\boldsymbol{g}(r)dr = \delta_{ij} \quad . \tag{2.23}$$

Reformulating eq. 2.22, we obtain:

$$\frac{1}{\Delta_p}\int_p\int_0^a \delta\boldsymbol{m}(r)\cdot\tilde{\boldsymbol{g}}_k(r)drd\Delta = \eta_k \pm \Delta\eta_k \quad , \tag{2.24}$$

the final set of constraints describing the path-integrated Earth structure in terms of perturbations with respect to an initial or reference model with uncertainties of $\Delta\eta_k$.

To account for the existence of different background models, we can reformulate the constraints (eq. 2.24), making them independent of the starting model $\boldsymbol{m}_0$. This is done by incorporating the integral over the starting model to eq. 2.24, such that:

$$\frac{1}{\Delta_p}\int_p\int_0^a \delta\boldsymbol{m}(\boldsymbol{r})\cdot\tilde{\boldsymbol{g}}_k(r)drd\Delta = \eta_k \pm \Delta\eta_k + \frac{1}{\Delta_p}\int_p\int_0^a \delta\boldsymbol{m}_0(\boldsymbol{r})\cdot\tilde{\boldsymbol{g}}_k(r)drd\Delta \quad . \tag{2.25}$$

This reformulation allows the use of different starting models for different paths, permitting the use of different models for paths crossing, for example, through oceans versus paths crossing through continental regions. The orthogonality of the constraints (linear equations) extracted from the waveforms and the ability to estimate uncorrelated errors associated with the linear equations is an important advantage of PWI.

2.3 Automated Multimode Inversion

The Automated Multimode Inversion (AMI; Lebedev et al., 2005; Lebedev & van der Hilst, 2008) is a fully-automated algorithm for waveform fitting of surface, S and multiple S wave forms. AMI adopts key components of PWI of Nolet (1990)—the orthogonal decomposition into uncorrelated linear equations, the linear algebra approach and the non-linear optimisation. It combines them with a different approach to the time-frequency windowing and misfit definition and achieves full automation of the signal selection and waveform inversion. We first outline the key advantages of AMI before discussing the AMI method in detail.

1. AMI permits the use of 3-D reference models, an improvement to the 1-D models used in PWI, allowing for more accurate phase-velocity derivatives within the source-station sensitivity volumes.

2. The windowing operator $\boldsymbol{R}$ accommodates numerous time-frequency windows and provides capability to automatically identify waveform components where the theoretical, i.e. JWKB, approximations are valid, while weighting and adjusting the data contributions from different segments of the wave train.

3. The source radiation pattern for each source-station azimuth, frequency and mode is determined and parts or all of the waveform are discarded if the source-station azimuth lies close to a radiation node, for these parts at the frequencies. This is done to avoid the contamination of the signal with the scattered energy, if the azimuth lies near a nodal band, and reduce the complexity of the sensitivity volumes of the waves (Lebedev et al., 2005).

4. AMI allows for the selection of multiple time-frequency windows, spread across multiple narrow-band Gaussian filters and time ranges, that capture only complete wave trains that are not contaminated by scattering effects. The selection of multiple frequency bands enables the extraction of more information from each individual seismograms.

5. The time-frequency windows are selected iteratively, starting by fitting the fundamental-mode wave train with the lowest frequency filter to prevent cycle skipping and then adding progressively higher frequency filters to the set of previously fit time-frequency windows.

6. Balancing the contributions of various types of waves to the misfit function enables AMI to extract more information from each seismogram. The weighting scheme ensures that the misfit of higher mode (body wave) and fundamental mode arrivals have equal contributions, with a correction for the different structural information provided by the fundamental mode at different frequencies. This ensures that the different phases in the fitted time-frequency windows in (5) contribute to the fit equally. This weighting enables the model to resolve structure

within the transition zone; as fundamental mode surface waves (which are sensitive to the shallow-mid mantle depths) normally have the highest amplitudes and tend to overwhelm the misfit function if the contributions are imbalanced.

7. AMI imposes a very strict misfit criterion, i.e. the data-synthetic misfits have to be lesser than 5% of the signal amplitude. The ability to divide large time-frequency windows into multiple smaller segments—on the condition that each segment satisfies the misfit and selection requirements—helps AMI to extract the maximum amount of information from each seismogram despite the strict criterion.

8. The automation of the above windowing and selection process enables AMI to process massive amounts of data. We exploit this very large amount of data, and the data redundancy provided by the massive dataset, to improve the accuracy and resolution of the tomographic models.

2.3.1 Relating waveforms to Earth structure

AMI adopts the JWKB approximation and uses mode summation in the frequency domain to generate synthetic seismograms (Dahlen & Tromp, 1998). We convert the wave number to phase velocity using the relation $k_m(\omega) = \omega / C_m(\omega)$, and rewrite eqs. 2.6 and 2.5 in terms of the local phase velocity:

$$C_n(\omega, \theta, \phi) = C_n^{0,p}(\omega) + \delta C_n^p(\omega, \theta, \phi) \quad , \tag{2.26}$$

and

$$\begin{aligned} u_p(\omega) &= \sum_n A_{np}(\omega) e^{i\omega\Delta_p / C_n(\omega,\theta,\phi)} \\ &= \sum_n A_{np}(\omega) exp[\frac{i\omega\Delta_p}{C_n^{0,p}(\omega) + \delta C_n^p(\omega,\theta,\phi)}] \quad . \end{aligned} \tag{2.27}$$

The dispersion, $C_m^p(\omega)$, along the path p for a P or S ($\alpha(r)$ or $\beta(r)$, respectively) background velocity model can be obtained by integrating eq. 2.26, and approximated using a first order Taylor series expansion:

$$\begin{aligned} \overline{\delta C_n^p(\omega)} &= \frac{1}{\Delta_p} \int_0^{\Delta_p} \delta C_n^p(\omega, \theta, \phi) d\Delta \\ &= \frac{1}{\Delta_p} \int_0^{\Delta_p} C_n(\omega, \theta, \phi) d\Delta - C_n^{(0,p)}(\omega) \\ &= \int_0^a \frac{\partial C_n^{(0,p)}(\omega)}{\partial \beta(r)} \overline{\delta\beta_p(r)} dr + \int_0^a \frac{\partial C_n^{(0,p)}(\omega)}{\partial \alpha(r)} \overline{\delta\alpha_p(r)} dr \quad , \end{aligned} \tag{2.28}$$

where $\partial C_n^{(0,p)}(\omega)/\partial\alpha(r)$ and $\partial C_n^{(0,p)}(\omega)/\partial\beta(r)$ are the Fréchet derivatives of the reference phase velocity, $C_n^{(0,p)}$, along the path p. $\overline{\delta\alpha_p(r)}$ and $\overline{\delta\beta_p(r)}$ are the per-

turbations in the P and S wave velocities with respect to the background velocity model, and can be expressed as:

$$\overline{\delta\alpha_p(r)} = \frac{1}{\Delta_p}\int_0^{\Delta_p}[\alpha(\theta,\phi,r) - \alpha^{(0,p)}(r)]d\Delta \quad , \tag{2.29}$$

$$\overline{\delta\beta_p(r)} = \frac{1}{\Delta_p}\int_0^{\Delta_p}[\beta(\theta,\phi,r) - \beta^{(0,p)}(r)]d\Delta \quad . \tag{2.30}$$

We can thus, relate the path-averaged phase velocities and their perturbations to determine the 3-D structure represented by $\alpha(\theta,\phi,r)$ and $\beta(\theta,\phi,r)$.

2.3.2 3-D background model

A crucial enhancement introduced by AMI is the capability of using 3-D background reference models as a simple 1-D velocity model a crude approximation for the structure of a heterogenous Earth. Significant lateral heterogeneity exists in the Earth, more specifically in the Earth's crust, resulting in large lateral variability in the Fréchet derivatives of phase velocity with respect to the S and P wave velocities.

The 3-D background model is constructed by combining a 1-D global averaged mantle profile and a 3-D crustal model modified from *CRUST2.0* (Bassin, 2000). The 3-D crustal model—modified from Bassin (2000) with added topography and bathymetry—is parameterised on a dense grid of triangular knots (Wang & Dahlen, 1995a) with an approximate inter-knot spacing of 28 km (Lebedev & van der Hilst, 2008; Schaeffer & Lebedev, 2013). Lebedev & van der Hilst (2008) reduced the potentially thousands of possible crust-structure and topography combinations by binning crustal velocity models into 664 1-D velocity models that represent the crustal structure at any point on the Earth with sufficient accuracy. One 1-D crustal model (Fig. 2.2), is then assigned at each knot of the crustal grid (Lebedev & van der Hilst, 2008).

The 1-D mantle profile as a reference for waveform fitting is derived by recomputing the *AK135* (Kennett et al., 1995) at a reference period of 50 s (Fig. 2.2). The 50 s period lies approximately in the middle of the period range of the data used, logarithmically, minimising the errors arising from the un-modelled lateral variations in attenuation.

The phase velocities and their Fréchet derivatives of the 3-D reference model can be directly computed by integrating over coordinates (θ and ϕ) on the Earth's surface:

$$C_n^0(\omega) = \int_\theta\int_\phi \overline{K(\theta,\phi)}C_n(\omega,\theta,\phi)d\phi d\theta \quad , \tag{2.31}$$

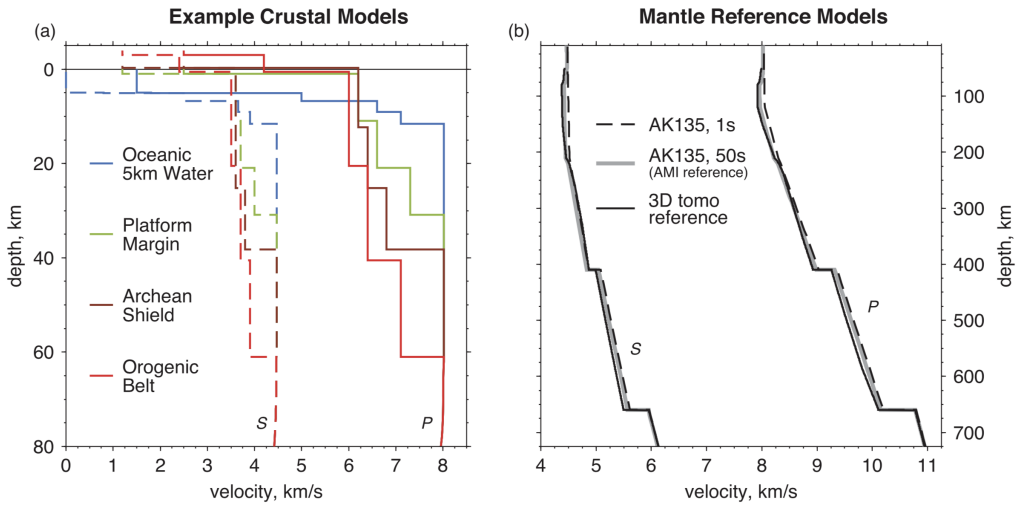


Figure 2.2: Background reference models used in AMI. (a) Four, out of the 664 different, crustal models. (b) Different 1-D mantle reference models. The reference profile used by AMI is plot in grey. The reference profile used in our tomographic inversions is plot as a solid black line, and is modified from a preliminary model by Lebedev & van der Hilst (2008). From Schaeffer & Lebedev (2013).

$$\frac{\partial C_n^0(\omega)}{\partial \alpha(r)} = \int_\theta \int_\phi \overline{K(\theta,\phi)} \frac{\partial C_n(\omega,\theta,\phi)}{\partial \alpha(r)} d\phi d\theta \quad , \tag{2.32}$$

$$\frac{\partial C_n^{(0,p)}(\omega)}{\partial \beta(r)} = \int_\theta \int_\phi \overline{K(\theta,\phi)} \frac{\partial C_n(\omega,\theta,\phi)}{\partial \beta(r)} d\phi d\theta \quad , \tag{2.33}$$

where $\overline{K(\theta,\phi)}$ is a sensitivity kernel of describes the sensitivity between the source-station region averaged over the frequency band of the inversion.

The phase velocities and Fréchet derivatives are then precomputed for each knot of the 3-D reference model and stored. The path-averaged phase velocities and Fréchet derivatives, for any arbitrary path in the model, can then be easily constructed by summing the weighted phase velocities and derivatives—-with weights derived from the sensitivity kernel $\overline{K(\theta,\phi)}$—averaged over the frequency band (Lebedev & van der Hilst, 2008; Schaeffer & Lebedev, 2013).

2.3.3 Approximate sensitivity kernels

The approximate sensitivity kernels, $\overline{K(\theta,\phi)}$, describe the sensitivity volumes of the filtered wave forms. The area on the surface is bounded by the "$\pi/2$" Fresnel zone, encompassing all the knots where the phase shift between the source-point-receiver and source-receiver is less than $\pi/2$. The half-width of the Fresnel zone boundary, δ, is defined by Wang & Dahlen (1995b) as:

$$\delta = \sqrt{\frac{\lambda/2}{|cot\Delta_1 + cot\Delta_2|}} \quad , \tag{2.34}$$

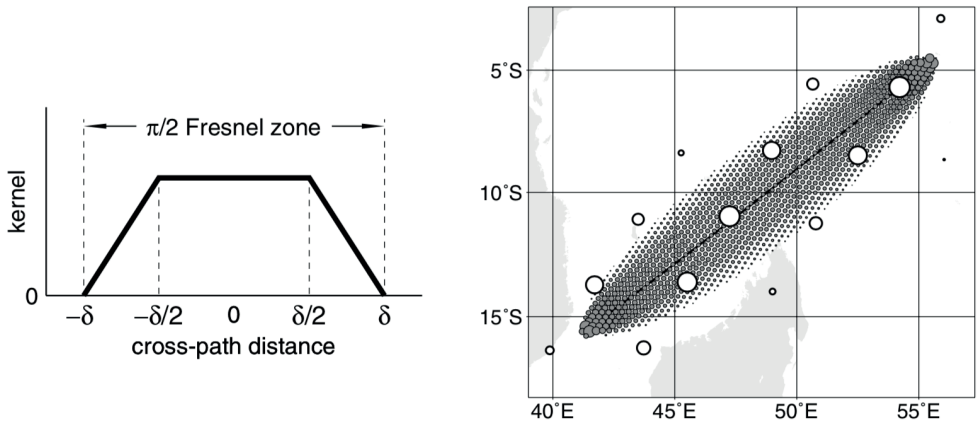


Figure 2.3: Path-normal cross section of the kernel, and the approximate sensitivity kernel, $\overline{K(\theta,\phi)}$, of AMI. Left: Path-normal cross-section of the trapezoidal kernel. Right: Example of an approximate sensitivity volume from Lebedev & van der Hilst (2008). The model grid knots are shown as white circles and the integration grid knots are shown as black circles. The circles are scaled according to the weights applied to the knots. From Lebedev & van der Hilst (2008).

where λ is the average fundamental mode wavelength of the waveform fit, Δ_1 and Δ_2 are the distances between a point, along a great circle path, and the source and receiver, respectively.

The approximate kernels have a path-normal trapezoidal cross-section, with constant weights between $\pm\delta/2$ and a linearly decaying amplitude between $\pm\delta/2$ and $\pm\delta$.

2.3.4 Model parameterisation and non-linear inversion

Vertical parameterisation

The vertical perturbations in S- and P-wave velocities are parameterised on a fixed set of 18 (7, 20, 36, 56, 80, 110, 150, 200, 260, 330, 410-, 410+, 485, 585, 660-, 660+, 809, and 1007 km) and 10 (7, 20, 36, 60, 90, 150, 240, 350, 485, and 585 km) nodes, respectively. Linear interpolation is applied between the knots, creating triangular basis functions (Fig. 2.4). The mantle transition zone discontinuities at 410 and 660 km are accounted for by using half-triangles, located above and below the discontinuities. The shallowest knots guarantees that at least one, and up to four, model nodes are present within the crust.

We can express the volume-averaged perturbations in velocity by combining and reformulating eqs. 2.9 and 2.22; e.g., the S velocity perturbations, $\overline{\delta\beta(r)}$:

$$\overline{\delta\beta(r)} = \sum_{i=1}^{M} \gamma_i \boldsymbol{h}_i(r) \quad , \tag{2.35}$$

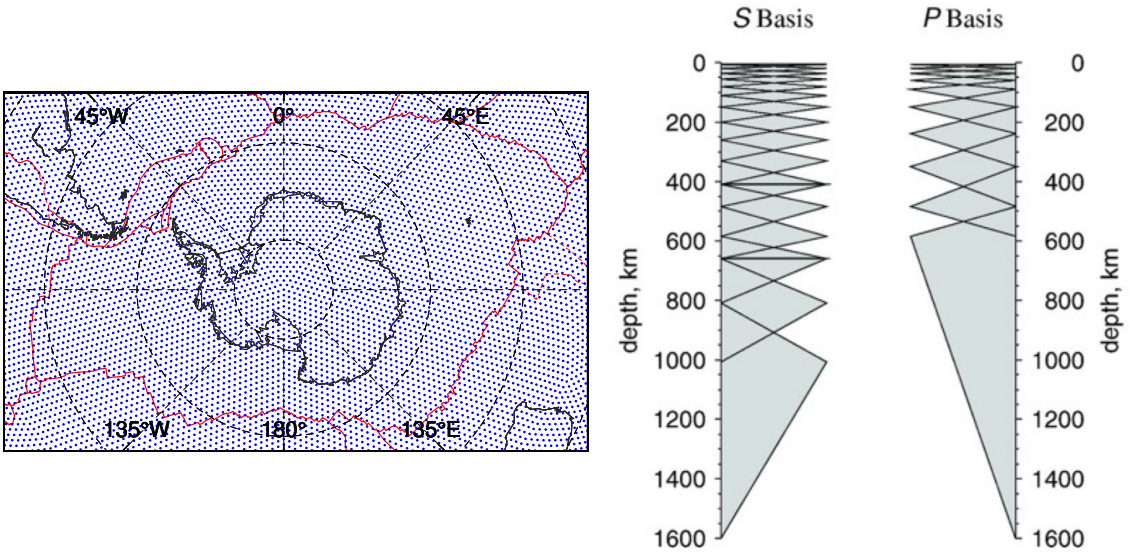


Figure 2.4: Left: Model grid used in a tomographic inversion, shown as blue circles. Right: Triangular basis functions used in the paramterisation of S (left) and P (right) velocities. Discontinuities at 410 km and 660 km in the S velocity parameterisation is accounted for by using two half-triangles, above and below the discontinuity. From Schaeffer & Lebedev (2013).

with M γ_i parameters for each basis function $\boldsymbol{h}_i(r)$. Transforming the original basis functions $\boldsymbol{h}_i(r)$ to a new set of basis functions, $\boldsymbol{g}_i(r)$, with uncorrelated uncertainties yields:

$$\overline{\delta\beta(r)} = \sum_{j=1}^{M} \eta_j \boldsymbol{g}_j(r) \quad , \tag{2.36}$$

where η_j are the new model parameters, related to γ_i by:

$$\eta_j = \sum_{i=1}^{M} S_{ij} \boldsymbol{\gamma}_i \quad . \tag{2.37}$$

The weighted linear equations, including the P velocity perturbations, with uncorrelated uncertainties can be expressed as:

$$\int_{\oplus} G_i^{\beta}(\boldsymbol{r})\delta\beta(\boldsymbol{r}) + G_i^{\alpha}(\boldsymbol{r})\alpha(\boldsymbol{r})d^3\boldsymbol{r} = \eta_i \pm \Delta\eta_i \quad , \tag{2.38}$$

where $G_i^{\alpha}(\boldsymbol{r})$ and $G_i^{\beta}(\boldsymbol{r})$ are the sensitivity volumes of P and S velocities in the Earth ($\oplus$), $\boldsymbol{r} = (\theta, \phi, r)$ and $i = 1, ..., M$. We then combine these M linear equations to form the linear tomographic inverse problem.

We show an example of a waveform fit by AMI in Fig. 2.5.

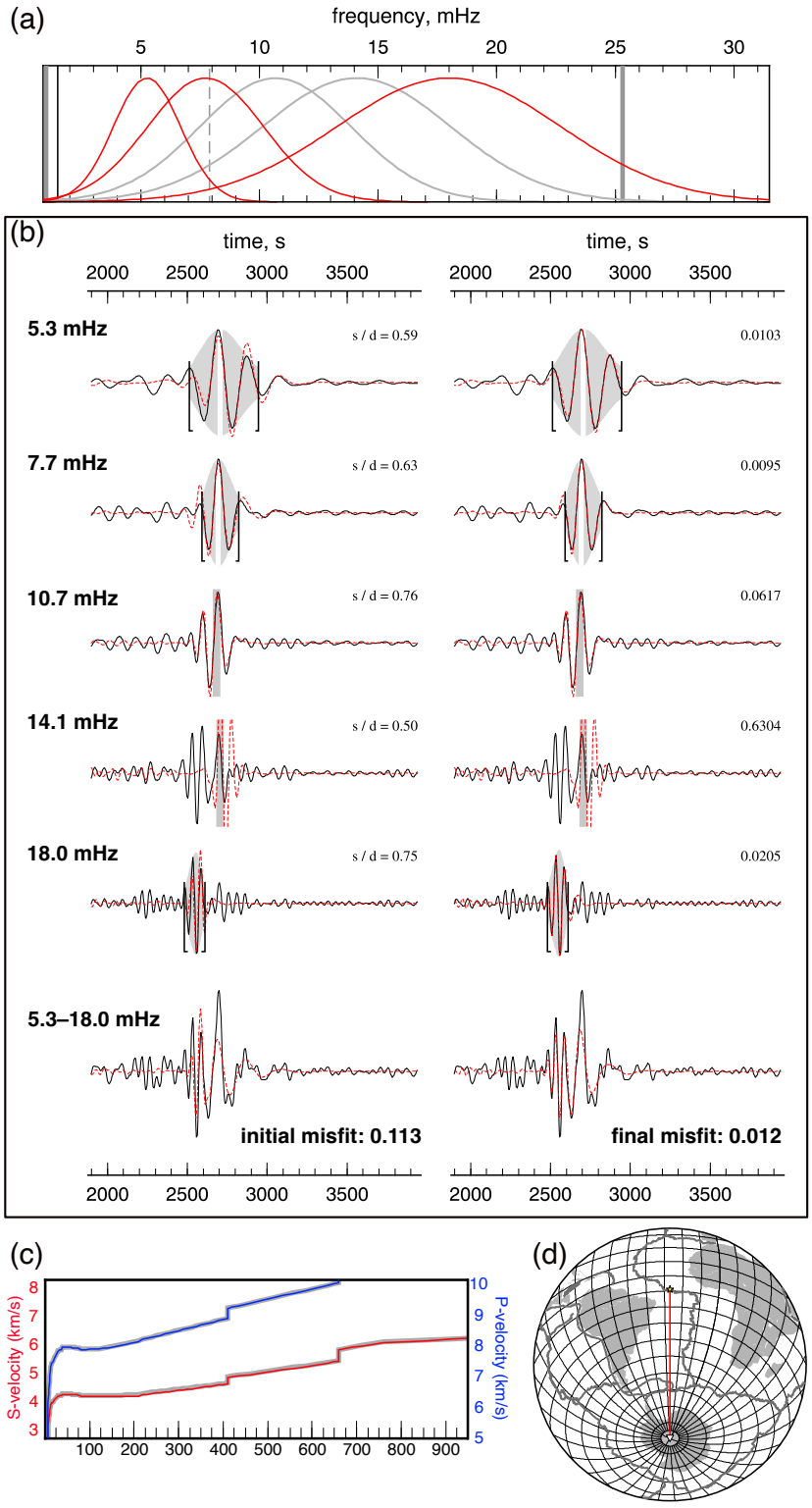


Figure 2.5: Example of a successful AMI waveform fit. The event occurred on 18/09/20 in the South Atlantic and was recorded by the IU.QSPA station located at the South Pole. (a) The Gaussian filters used in the fitting process, successful fits are plot in red. (b) Observed (black) and synthetic (red) seismograms at filtered at the frequency bands shown in (a) for the initial (left) and final fit after the non-linear inversion (right). The brackets highlight the portion of the wavetrain

Figure 2.5: *continued from previous page*
where the successful fit was attempted. The bottom seismogram is the sum of all the frequency bands above. Misfit for each frequency band is indicated on the right of each panel. (c) S (red) and P (blue) wave velocities for the path-averaged 1-D model generated from the inversion. The reference model is plot in grey. (d) Location of the event (star) and station (inverted triangle).

2.3.5 Linear tomographic inversion

The result of the AMI waveform inversion for each path is a set of M equations with uncorrelated uncertainties (eq. 2.38). We can combine any number of sets of equations for individual paths into a large linear tomographic inversion, solving for the distribution of the S and P wave velocities and azimuthal anisotropy of a 3-D Earth model.

In the process of constructing the large linear system, the data (η_i^p) and kernels (G_i^p) for each path p are scaled by their associated uncertainties ($\Delta\eta_i^p$). The scaled data vector is given by $q_i^p = \eta_i^p / \Delta_n^p$, with the same scaling performed for the kernel functions, such that $G_i^{\beta,\alpha}(\boldsymbol{r})$ becomes $\tilde{G}_i^{\beta,\alpha}(\boldsymbol{r})$. Eq. 2.38 is then:

$$\int_{\oplus} \tilde{G}_i^{\beta}(\boldsymbol{r})\delta\beta(\boldsymbol{r}) + \tilde{G}_i^{\alpha}(\boldsymbol{r})\alpha(\boldsymbol{r})d^3\boldsymbol{r} = q_i^p \pm 1 \quad . \tag{2.39}$$

Data vector

Since there are M equations, 18 for S and 10 for P wave velocities, are generated for each path, a large number of equations will be created. However, not all of the equations are critical for the inversion. Thus, we set a minimum threshold for eigenvalues corresponding to the eigenvectors relating to the transformed parameters, below which they are discarded. This results on an average of 3.5 linear equations coming from each seismogram. Typically, more equations are retained if more S waves are included, as there is more independent bits of information from both the fundamental and higher modes than from the fundamental mode alone.

We cast the linear system in a standard form:

$$\boldsymbol{Am} = \boldsymbol{d} \quad , \tag{2.40}$$

where $\boldsymbol{m}$ is the model vector and $\boldsymbol{d}$ data vector, with data from each path:

$$\boldsymbol{d} = d_k = \begin{bmatrix} q_1^1 \\ \vdots \\ q_{M^*}^1 \\ q_1^2 \\ \vdots \\ q_{M_N^*}^N \end{bmatrix} \quad , \tag{2.41}$$

where k is the number of rows, N is the number of seismograms and M^* is the number of retained equations for each seismogram.

Model vector

The model vector, $\mathbf{m}$, is parameterised on a 3-D grid with approximately 125 km lateral knot spacing with 10 and 18 knots radially for P and S waves, respectively. The model is laterally parameterised on a global triangular grid with an approximate inter-knot spacing of 125 km (Fig. 2.4), where the isotropic P-, S-wave and azimuthal perturbations are solved for. A denser integration grid, with approximately 25 km inter-knot spacing, is used to integrate over the approximate sensitivity volumes between the source-receiver pairs (Lebedev & van der Hilst, 2008). The knots of the model and integration grids are deliberately co-located to allow for rapid transformations between the two grids. The vertical parameterisation was discussed in more detail in Section 2.3.4.

The tomographic inversion solves for the perturbations in P-, S-velocities and 2Ψ S-wave azimuthal anisotropy. We include the P-wave terms due to the small, albeit non-negligible, sensitivity of Rayleigh waves to compressional wave speeds. The P-wave terms, however, cannot be resolved on their own and are damped to the S-wave velocity structure (e.g., Lebedev & van der Hilst, 2008).

Azimuthal anisotropy of surface waves in a smooth, and weakly anisotropic medium can be expressed as a series of small π-periodic and $\pi/2$-periodic terms, which describe perturbations from the isotropic-average velocity (Smith & Dahlen, 1973):

$$\begin{aligned} C(\omega, \Psi, \theta, \phi) =& A_0(\omega, \theta, \phi) \\ &+ A_1(\omega, \theta, \phi) cos2\Psi + A_2(\omega, \theta, \phi) sin2\Psi \\ &+ A_3(\omega, \theta, \phi) cos4\Psi + A_4(\omega, \theta, \phi) cos4\Psi \quad , \end{aligned} \tag{2.42}$$

where $C(\omega, \Psi, \theta, \phi)$ is the phase velocity at the azimuth Ψ, $A_0(\omega, \theta, \phi)$ is the isotropic-average phase speed, A_1 and A_2 are the coefficients for the π-periodic

azimuthal variations, A_3 and A_4 are the coefficients for the $\pi/2$-periodic azimuthal variations, ω is the angular frequency, θ is the longitude and ϕ is the latitude. Long-period Rayleigh waves that sample primarily the upper mantle are thought to be sensitive mainly to π-periodic ('2Ψ') anisotropy, described by (A_1, A_2) terms, while Love waves are sensitive to $\pi/2$-periodic ('4Ψ') anisotropy described by (A_3, A_4) terms (e.g., Montagner & Tanimoto, 1991; Trampert & Woodhouse, 2003; Ekström, 2011; Adam & Lebedev, 2012). We thus simplify eq. 2.42 by only parameterising the A_0, A_1 and A_2 terms. We discuss the origin of anisotropy and rationale of this simplification in further detail in Chapter 5.3.

Thus, $\boldsymbol{m}$ is comprises four model parameters, V_P, V_{Sv}, A_1 and A_2, at each knot and is parameterised on a lateral shell of n_{sh} knots, with $n_V^P = 10$ P-wave vertical basis functions and $n_V^S = 18$ vertical S-wave basis functions:

$$\boldsymbol{m} = \begin{bmatrix} V_{Sv}(i,j) \\ A_1(i,j) \\ A_2(i,j) \\ V_P(i,j) \end{bmatrix} = \begin{bmatrix} V_{Sv}(i,j) \\ \vdots \\ V_{Sv}(n_V^S, n_{sh}) \\ A_1(i,j) \\ \vdots \\ A_1(n_V^S, n_{sh}) \\ A_2(i,j) \\ \vdots \\ A_2(n_V^S, n_{sh}) \\ V_P(i,j) \\ \vdots \\ V_P(n_V^P, n_{sh}) \end{bmatrix} , \tag{2.43}$$

with $i = 1, ..., n_V$ and $j = 1, ..., n_{sh}$. The elements in the model vector are arranged by parameter type, across the shell knots for each given depth.

Sensitivity matrix

The weights in the $\boldsymbol{A}$ matrix relate the data and model vectors and are determined by the scaled kernel functions $\tilde{G}_j^(\beta, \alpha)(\boldsymbol{r})$ for each of the j number of paths. The scaled kernels inherit their structure from the transformed basis functions ($\tilde{g}_j^p$) and approximate sensitivity kernels ($\overline{K^P(\theta, \phi)}$). The number of data rows are determined by the number of equations (with additional rows appended for regularisation). The number of columns is determined by the number of knots of the

grid and parameter types per knot. Since each sensitivity kernel is only sensitive to a small portion of the total number of unknowns, the resulting matrix is very sparse. We leverage this sparsity to reduce the memory requirements of the inversion by only storing and indexing the non-zero elements of the matrix in a set of indexing arrays.

Path weighting

In the process of constructing the linear systems, many hundreds of thousands of waveform fits are combined. Thus, many kernel functions ($\overline{K^P(\theta,\phi)}$) will not be unique, due to the similar source-station great-circle paths, for example, between a permanent network recording many events from a seismically active region. The resulting unevenness of the path coverage can bias the inversion, typically with greater anomalies mapped along the highly-sampled paths

It is not possible for these sets of ray-paths to be bundled into "summary rays" as their sensitivity volumes will have different widths due to different depth structure due to their different higher-mode and frequency content. Instead, we introduce a path-similarity score to each seismogram, based on the similarity with all other seismograms. The individual weights of the similarity for each pair of evaluated seismograms are computed using a cosine taper with amplitudes based on the separation distance between the ends of the event-station great-circle path. The path-similarity score is then computed by summing the individual weights for each seismogram.

After the sensitivity matrix $\boldsymbol{A}$ is constructed, the path-similarity score are then computed. The scores are then applied to generate a new data vector ($\boldsymbol{d^s} = di(j)/w_j^{path}$) and sensitivity matrix, such that higher scoring—and thus, more common—paths are down weighted more.

Linear inversion and regularisation

The resulting system of equations is mixed-determined. The inversion has to be regularised to stabilise the inversion. Regularisation is performed in the form of vertical and lateral smoothing, and slight norm damping. The regularisation is imposed onto the sensitivity matrix in the form of a number of operators, such

that:

$$\begin{bmatrix} \boldsymbol{A} \\ a\boldsymbol{I} \\ b\boldsymbol{\Phi} \\ c\boldsymbol{\Gamma} \\ d\boldsymbol{\Pi} \end{bmatrix} \boldsymbol{m} = \begin{bmatrix} \boldsymbol{d^s} \\ 0 \\ 0 \\ 0 \\ 0 \end{bmatrix} \quad , \tag{2.44}$$

where $\boldsymbol{I}$ is the identity matrix, $\boldsymbol{\Phi}$, $\boldsymbol{\Gamma}$ and $\boldsymbol{\Pi}$ are the operators on m to compute the norms and gradients, and a, b, c, d are weights controlling the trade-offs between the misfit, norms and gradient operators.

The operator $\boldsymbol{\Phi}$ penalises differences between dV_P and dV_S, both in m/s. The $\boldsymbol{\Gamma}$ operator controls the radial and lateral gradient damping, penalising the differences between perturbations at neighbouring knots in the radial and lateral direction. The $\boldsymbol{\Pi}$ operator is for lateral smoothing and penalises the difference between the perturbation at a model knot and the average of the perturbation over this and all the neighbouring knots.

We look for a solution $\boldsymbol{m}$ that minimises the weighted sum of the data misfit, model norm and other regularisation terms (Zielhuis & Nolet, 1994; Nolet, 2008):

$$min[(\boldsymbol{Am} - \boldsymbol{d^s})^T(\boldsymbol{Am} - \boldsymbol{d^s})] \quad . \tag{2.45}$$

Due to the large size of the tomographic inversion, a direct least-squares approach to solving eq. 3.3.2 is impractical. We solve it with the computationally efficient iterative least-squares procedure, LSQR, developed by Paige & Saunders (1982).

Outlier analysis

The final step in the tomographic inversion process is the outlier analysis and rejection. We exploit the data redundancy provided by the massive amounts of data identify and remove the least mutually consistent data, which are fit the worst by the 3-D tomographic model. This posteriori outlier analysis ensures that only the most mutually consistent data is retained, discarding the least consistent data that are likely to be affected by the largest errors. A final manual error identification process is then conducted, where a preliminary model is assessed and probable errors and artefacts associated with specific seismograms are removed from the final model dataset.

Chapter 3

Waveform tomography of the Antarctic Plate

3.1 Abstract

We present a new seismic shear wave velocity model of the upper mantle of the Antarctic Plate region, AP2024. It includes the lithosphere and underlying mantle down to 660 km depth beneath both the continental and oceanic portions of the plate. To augment the limited seismic station coverage of Antarctica, we assemble very large regional and global data sets, comprising all publicly available broadband seismic data. The model is built using 785 thousand seismograms from over 27 thousand events and 8.7 thousand stations. It is constrained by both body and Rayleigh surface waves, ensuring the dense data sampling of the entire upper mantle depth range. The tomographic inversion is global but focused on the Antarctic Plate, with the data sampling maximised in the Southern Hemisphere, with elaborate automated and manual outlier analysis and removal performed on the regional data, and with the regularisation tuned for the region. The upper mantle of the Antarctic continent exhibits a bimodal nature. The sharp boundary along the Transantarctic Mountains separates the cratonic eastern from tectonic western Antarctica and shows a shear-velocity contrast of up to 17% at ∼100 km depth. The bimodal pattern is also seen in the oceanic part of the plate, with the older oceanic lithosphere beneath the Indian sector of the Southern Ocean showing higher shear velocities. The continental lithosphere in East Antarctica shows high velocity anomalies similar to those beneath stable cratons elsewhere around the world. It is laterally heterogeneous and exhibits significant thinning in the near-coastal parts of Dronning Maud Land and Wilkes Land. A low velocity channel is observed along the southern front of the West Antarctic Rift System and is probably related to Cenozoic rifting. High seismic velocity

anomalies are detected beneath the Antarctic Peninsula and are likely to indicate fragments of the recently subducted Phoenix Plate Slab. Low velocity anomalies beneath Marie Byrd Land extend into the deep upper mantle and are consistent with a deep mantle upwelling feeding West Antarctica intraplate magmatism.

Keywords: Antarctica, Waveform inversion, Seismic tomography, Cratons, Dynamics of lithosphere and mantle

3.2 Introduction

Antarctica represents a unique region where the present crust and upper mantle structure, comprising ancient Precambrian lithospheric blocks in the east and Phanerozoic terranes in the west, links to processes of significant importance in Earth's past and future. However, thick ice sheets—an integral component of the global climate system and a major potential contributor to global sea level rise (e.g., Oppenheimer et al., 2019)—blanket the continent, leaving the detailed configuration and evolutionary history of the Antarctic crust and upper mantle still unclear. The challenging conditions and remote location have limited the geological sampling of Antarctica. With most of the continent covered by the ice sheet, geological data is limited to outcrops and nunataks primarily located along the coastlines and the Transantarctic Mountains (TAM), which account for less than 0.2% of Antarctica's total land area (Burton-Johnson et al., 2016). Indirect geophysical methods including seismology, gravimetry, magnetics and geodesy are, thus, particularly important for investigating Antarctica.

Among the factors controlling the dynamics and evolution of the Antarctic Ice Sheet, geothermal heat flow (GHF) affects the basal temperature conditions of the Antarctic Ice Sheet and, consequently, the frictional state of the solid earth-ice sheet system. GHF at the base of ice sheets is a critical yet still poorly constrained parameter modulating ice sheet dynamics. The heat flow influences basal melting, englacial rheology and erosion rates among other factors that influence the frictional regime at the base of the ice sheets, potentially resulting in an increase in both ice sheet velocities and ice loss rates (e.g., Pollard et al., 2005; Bell, 2008; Golledge et al., 2015; Burton-Johnson et al., 2020; Lösing et al., 2020). Shrinking ice sheets reduce the load on the solid Earth beneath, triggering an instantaneous elastic response and a delayed, gradual viscoelastic deformation (e.g., Peltier, 1974). Glacial Isostatic Adjustment (GIA) is the viscoelastic solid Earth response to changes in the ice-sheet surface load over time, which affects the evolution of the ice sheet and the sea level (e.g., Peltier, 1976; Konrad et al., 2015; Barletta et al., 2018; Whitehouse, 2018). Topographical uplift caused by the negative buoyancy,

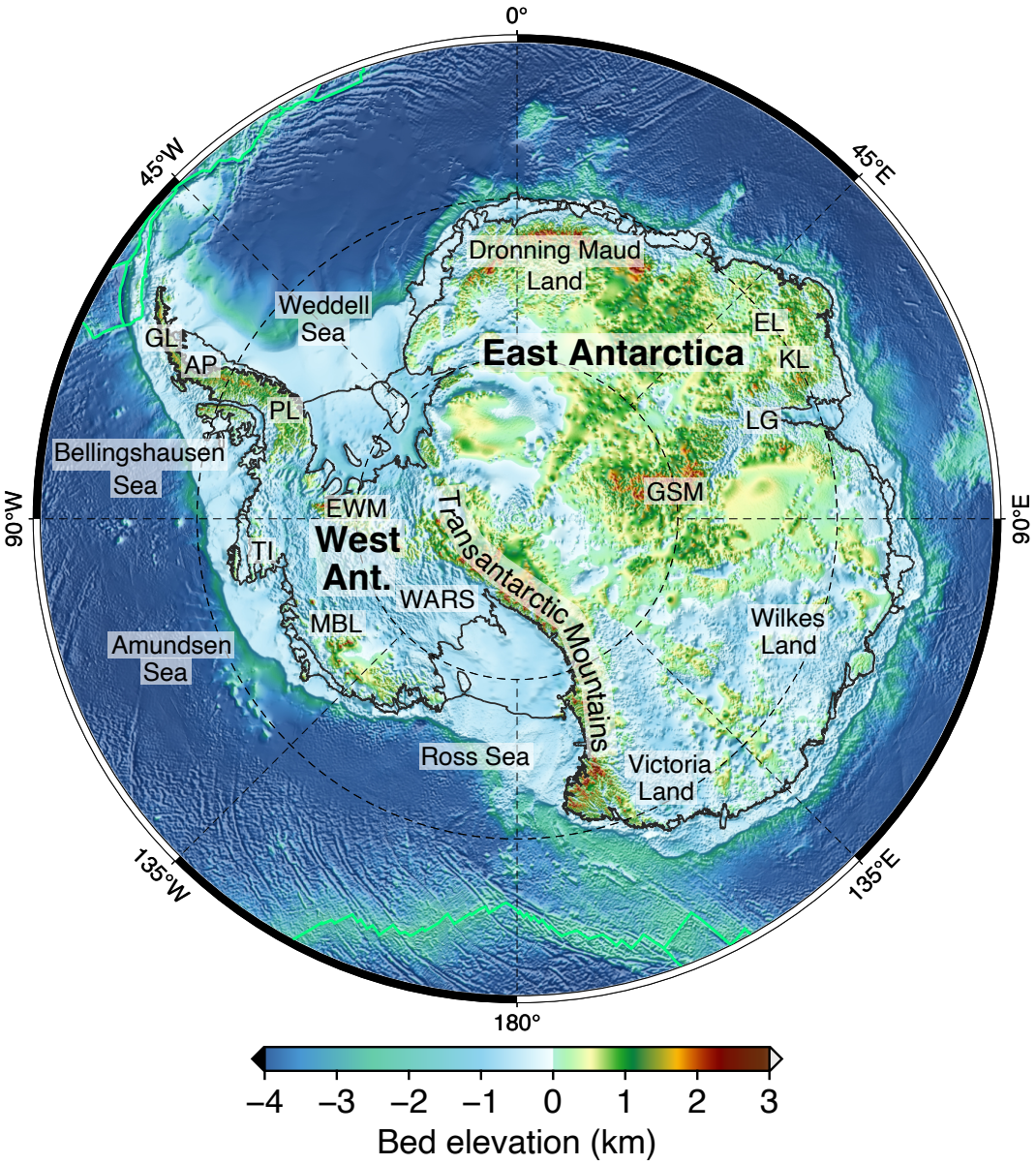


Figure 3.1: Bed rock topography and bathymetry of Antarctica and surrounding oceans (Fretwell et al., 2013) with main geographic features annotated. Abbreviations: AP — Antarctic Peninsula, EL — Enderby Land, EWM — Ellsworth Whitmore Mountains, GL — Graham Land, GSM — Gamburtsev Subglacial Mountains, KL — Kemp Land, LG — Lambert Graben, MBL — Marie Byrd Land, PL — Palmer Land, TI — Thurston Island, WARS — West Antarctic Rift System.

along with the decreased gravitational attraction—both resulting from the loss of ice mass—contributes to a reduction in relative sea levels (e.g., Mitrovica et al., 2001; Gomez et al., 2015). GHF and GIA both depend on the lithospheric thickness and upper mantle temperature, which partly determines the amount of heat transmitted to the Earth's surface and the viscosity of the mantle (e.g., Shen et al., 2020; Ivins et al., 2022). Variations in the lateral viscosity structure of the upper mantle and lithospheric thickness modulate the rate and spatial extents of GIA

(e.g., Kaufmann & Wolf, 2002; Nield et al., 2014, 2018), and the variations are directly related to their thermal properties (e.g., Kuchar & Milne, 2015; Chen et al., 2018). Seismic imaging is particularly useful in the study of the Earth's crust and upper mantle, by relating the distribution of seismic velocities to variations in the thermal, compositional, density and viscosity structure at depth and providing essential constraints to the parameters impacting GHF, GIA and through them, the climate system.

3.2.1 Tectonic Setting

The Antarctic Plate comprises the Antarctica continent, made up of tectonically distinct East Antarctica (EANT) and West Antarctica (WANT), and the oceanic lithosphere under the adjacent Southern Ocean and the southern portions of the Pacific, Atlantic and Indian Oceans. EANT is composed predominantly of Precambrian cratonic units (e.g., Mikhalsky, 2008) that were included in the core of East Gondwana. WANT is an assembly of several Phanerozoic tectonic provinces that were modified throughout the Mesozoic and Cenozoic (Dalziel & Elliot, 1982; Siddoway, 2021).

The Gondwana supercontinent incorporated a number of cratonic blocks, including cratons located in present-day Africa (e.g., Angola, Kalahari, Tanzania and Zimbabwe), Australia (e.g., Gawler and Yilgarn), EANT (e.g., Ruker and Grunehogna) and India (e.g., Dharwar and Bastar) (e.g., Torsvik et al., 2008; Haas et al., 2023). Rifting at what is now the boundaries of EANT began in the Jurassic and proceeded in a primarily eastward direction. Africa-East Antarctic rifting was initiated at the Weddell Sea rift at approximately 175 Ma at relatively low spreading rates (e.g., Svensen et al., 2012; Burgess et al., 2015; Riley et al., 2020b). Rifting between the EANT and East India was initiated at approximately 136 Ma in the eastern Enderby Basin before propagating westward, with similarly low spreading rates (e.g., Gibbons et al., 2013; Davis et al., 2019; Rao & Radhakrishna, 2021; Jokat et al., 2021). Initial Antarctic-Australian rifting began in the Late Jurassic (Powell et al., 1988; Ball et al., 2013), and the continental breakup started at about 83 Ma in the Late Cretaceous (e.g., Royer & Rollet, 1997; Whittaker et al., 2013; Jacob et al., 2014; Jacob & Dyment, 2014; Williams et al., 2019). The opening of the Drake Passage at approximately 50 Ma separated WANT from South America, resulting in the present day configuration of the Antarctic Continent (e.g., Livermore et al., 2005; Eagles et al., 2006; Lagabrielle et al., 2009). The multiple rifting events resulted in the oceanic lithosphere getting younger clockwise (eastward) around the Antarctic Continent (Reeves & De Wit, 2000; Boger, 2011; Williams et al., 2019; Jokat et al., 2021).

The EANT subcontinent can be further divided into several geologically distinct Archean–Proterozoic domains, primarly supported by evidence from the outcrops along the coastlines. The domain encompassing the inland region between Victoria Land, Terre Adelié and the Shackleton Range (Boger, 2011) is probably the largest cratonic block underlying EANT. The exact extent of the region, termed the "Mawson Continent", is not clearly defined, but previous studies have proposed it to include the region spanning the Shackelton Range and Terre Adelié in EANT and the Gawler Craton in southern Australia (e.g., Boger, 2011; Liu et al., 2018; Jordan et al., 2022). The outcrops found along the Terre Adelié coastline show affinities to the ones in the Gawler Craton in southern Australia (Fanning et al., 1988; Flöttmann & Oliver, 1994; Peucat et al., 1999). The Coompana/Albany-Fraser province was the collision zone between the Yilgarn and Gawler cratons in the Mesoproterozoic (Fitzsimons, 2003; Veevers, 2012), located in Wilkes Land, the province was contiguous with the province in southern Australia with the same name.

A separate domain encompasses the region around the Lambert Graben and Pyrdz Bay, including the Napier and Vestfold Complexes and their surroundings, sharing geological similarities to regions of Archean outcrops on the Eastern Ghats Province in India (Phillips et al., 2007; Boger, 2011; Mohanty, 2015; Parmentier, 2015; Chatterjee et al., 2023). Dronning Maud Land (DML) features the Grunehogna Complex that contains the only outcrop of Archean West Gondwana; studies of the region have identified zircons (Marschall et al., 2010), basalts (Faure et al., 1979; Harris et al., 1990; Luttinen & Furnes, 2000) and Jurassic dykes (Riley et al., 2005) that are compositionally and structurally similar to those found in the Kaapvaal Craton in Africa and the Karoo Large Igneous Province.

The remaining Precambrian domain of EANT is bounded by the other three, discussed above, and overlain entirely by ice. The absence of physical samples from the area precludes the determination of any geological similarities with other regions. Despite the traditionally broad characterisation of the geological domains, recent geophysical studies suggest a different and more nuanced separation of different units, comprising a complex assemblage of Precambrian cratons and orogenic belts (e.g., Veevers et al., 2008; Haeger et al., 2019; Pappa, 2019; Pappa & Ebbing, 2022).

The TAM extend across the continent for over 3200 km from the Weddell Sea Embayment to northern Victoria Land, reaching elevations greater than 4500 m. The TAM vary in width, with several regions narrowing to under 200 km, creating a stark topographical and geophysical contrast between the ancient EANT and the younger WANT (ten Brink et al., 1997; Goodge, 2020). Arguments have been made for isostatic (e.g., Studinger et al., 2004; Block et al., 2009), thermal

(Olivetti et al., 2018) and mechanical (Wannamaker et al., 2017) support mechanisms for the Cretaceous–Neogene uplift of the TAM, with alternative mechanisms such as lithospheric delamination in southern TAM (Shen et al., 2018b), but a consensus is yet to be reached (Goodge, 2020).

The West Antarctic part of the continent is an assembly of several tectonic provinces: the Antarctic Peninsula (AP), the Ellsworth-Whitmore Mountains (EWM), Marie Byrd Land (MBL), Thurston Island (TI) and the West Antarctic Rift System (WARS). The oldest rocks in WANT are found in the Weddell Sea sector, and isotopic analyses of outcrops at Haag Nunataks and detrital zircons in the EWM province estimate the terranes to be of Proterozoic in age (Millar & Pankhurst, 1987; Flowerdew et al., 2007). The prevailing theory for the origin of the EWM province suggests that the EWM block was a fragment of Gondwana, located within or near EANT and displaced and rotated during the Jurassic opening of the Weddell Sea (Grunow et al., 1987; Curtis & Storey, 1996; Randall & Mac Niocaill, 2004; Jordan et al., 2013, 2020; Siddoway, 2021).

Arc magmatism along the Gondwanide convergent margins resulted in the amalgamation of the MBL in the Paleozoic (Pankhurst et al., 1998; Mukasa & Dalziel, 2000; Siddoway & Fanning, 2009; Yakymchuk et al., 2015), the AP in the Paleozoic (Millar et al., 2002; Riley et al., 2012, 2023a) and Cretaceous (Garrett, 1990; Leat et al., 1995; Yegorova et al., 2011; Riley et al., 2020a; Bastias et al., 2023), and the TI province in the Mesozoic (Grunow et al., 1991). MBL is principally a topographic dome, housing volcanic systems with past and possibly ongoing volcanic activity (LeMasurier, 1990; Lough et al., 2013; Wilch et al., 2021), with volcano summits up to 4180 m high in its central region (Siddoway, 2021). The elevated topography is relatively recent: the uplift of the MBL region is estimated to have initiated at ∼30–20 Ma due to the arrival of a mantle plume (LeMasurier & Landis, 1996; Spiegel et al., 2016). The AP is the largest tectonic block in WANT and is a complex of several well-preserved Mesozoic to Cenozoic continental magmatic arcs, emplaced when the paleo-Pacific oceanic lithosphere subducted beneath western Gondwana (Garrett, 1990; Leat et al., 1995; Millar et al., 2002; Yegorova et al., 2011; Riley et al., 2012, 2020a, 2023b; Bastias et al., 2023).

The WARS is a broad domain of extended crust (e.g., Winberry & Anandakrishnan, 2004) encompassing the area between the Ross Sea to the Weddell Sea and covering both onshore and offshore regions. WARS extension is broadly distributed across most of WANT, as well as across several extensional episodes. The first major extensional episode at ∼105–85 Ma is attributed to the transition in the stress regime in the region due to opening of a slab window (e.g., Luyendyk, 1995), resulting in widespread extension across the region (Luyendyk et al., 1996; Siddoway et al., 2004; McFadden et al., 2010; Jordan et al., 2020). Approximately

150–200 km extension in the Adare Basin region of the WARS occurred in the early-mid Cenozoic (Cande & Stock, 2004; Wilson & Luyendyk, 2009; Granot & Dyment, 2018), up to the mid-Miocene (e.g., Granot et al., 2010). Subsequent extension in the Ross Sea region is accommodated within the Terror Rift (e.g., Henrys et al., 2007; Fielding et al., 2008), consistent with a change in the relative plate motions (e.g., Granot et al., 2010). Rifting between EANT and WANT ceased at approximately 11 Ma (e.g., Granot & Dyment, 2018).

3.2.2 Previous Seismic Studies

Early seismic studies sampled the crustal structure of Antarctica using surface waves (Press & Dewart, 1959; Evison et al., 1960; Kovach & Press, 1961; Roult et al., 1994) and P-waves (Bentley, 1973; ten Brink et al., 1993). They provided the initial estimates the crustal thicknesses in EANT and WANT, revealing a contrast between East and West Antarctica. Subsequent continent-scale, surface-wave and waveform tomography studies extended the data sampling deeper into the upper mantle (e.g., Danesi & Morelli, 2001; Ritzwoller et al., 2001) and the mantle transition zone (Sieminski et al., 2003). They revealed a sharp transition between the high and low velocity anomalies underlying East and West Antarctica, respectively.

The significant rise in the number of temporary deployments over the past two decades has enhanced the station coverage of Antarctica and the data sampling of its upper mantle. The deployments primarily targetted the more accessible WANT (ANUBIS (Anandakrishnan et al., 2000), SEPA (Robertson Maurice et al., 2003), ANET/ POLENET (Accardo et al., 2014), UKANET (O'Donnell et al., 2019a,b) and the RIS (Baker et al., 2019)) and TAM (TAMSEIS (Lawrence et al., 2006a,b; Watson et al., 2006) and TAMNNET (Hansen et al., 2015)), with fewer deployments in EANT due to logistical limitations (SSCUA (Reading, 2006) and GAMSEIS (Hansen et al., 2010)). Fig. 3.2 shows the distribution of broadband stations with publicly available data (all of which were used to construct the tomographic model presented here). Whereas the station coverage in WANT has significantly improved, EANT remains sparsely covered, with extensive regions in DML and Wilkes Land showing only a few stations.

EANT is characterised by cratonic lithosphere, with high seismic velocities detected beneath the region in many studies. Receiver function and other geophysical studies of EANT found average crustal thicknesses of 40–45 km, typical for Archean cratons, with some variability across EANT (e.g., An et al., 2015a; Shen et al., 2018a; Pappa et al., 2019; Szwillus et al., 2019; Borghi, 2022; Pappa & Ebbing, 2022; Wiens et al., 2023). Thicker crust is observed beneath the Gamburt-

sev Subglacial Mountains (GSM) (55–58 km) (e.g., Hansen et al., 2010) while thinner crust can be found beneath the TAM (35–40 km) (e.g., Bannister et al., 2003; Hansen et al., 2009; Pyle et al., 2010; Ramirez et al., 2017; Shen et al., 2018a) and in the Wilkes Land coast (28–32 km) (e.g., Reading, 2004). Thick cratonic lithosphere underlies most of EANT, observed in regional (e.g., Danesi & Morelli, 2001; Ritzwoller et al., 2001; An et al., 2015a,b; Lloyd et al., 2020) and global (e.g., French et al., 2013; Schaeffer & Lebedev, 2013; Debayle et al., 2016; Simmons et al., 2021; Priestley et al., 2024) tomographic studies, with high-velocity anomalies extending to depths exceeding 200 km and up to 250 km beneath the GSM (Heeszel et al., 2013, 2016; Shen et al., 2018a). A number of studies suggested significant variability in the lithospheric thickness of EANT, with average lithospheric thicknesses decreasing toward the coastline (e.g., An et al., 2015a; Lloyd et al., 2020; Wiens et al., 2023) and regions of thin lithosphere underlying DML (0–20°E), Enderby Land, Kemp Land and Wilkes Land (e.g., Lloyd et al., 2020; Wiens et al., 2023).

WANT is characterised by thinner lithosphere and crust, with average crustal thicknesses between 20 and 30 km (e.g., Chaput et al., 2014; Shen et al., 2018a; Wiens et al., 2023). Thinner, 10–22 km crust was detected in the WARS (e.g., Chaput et al., 2014; Baranov et al., 2021) and thicker, ∼30 km crust—in the EWM (e.g., Baranov et al., 2021). The sharp transition between the lithospheric structure across the WARS-TAM margin and the heterogenous uppermost mantle of the TAM and WARS were mapped by a number of surface wave studies (e.g., Lawrence et al., 2006b; Heeszel et al., 2016; Shen et al., 2018a; O'Donnell et al., 2019a,b). The seismic heterogeneity mapped was interpreted as evidence for ongoing lithospheric delamination in the southern TAM (e.g., Shen et al., 2018a), the absence of thick cratonic lithosphere beneath the adjacent parts of EANT, and their relationship to the uplift and support mechanisms of the TAM (e.g., Shen et al., 2018b; O'Donnell et al., 2019a). Low seismic velocities in the WARS asthenosphere suggested thin, warm lithosphere, interpreted as a consequence of the multiple Mesozoic and Cenozoic extensional events (Wilson & Luyendyk, 2009; Dalziel et al., 2013; Harry et al., 2018; Jordan et al., 2020; Siddoway, 2021). The band of low seismic velocities was reported along the WARS-TAM margin at ∼120–150 km, extending between the Terror Rift and the EWM, and attributed to a Cenozoic rift system (Shen et al., 2018a; O'Donnell et al., 2019a; Lloyd et al., 2020). The deeper upper mantle and lower mantle, across the TAM-WARS margin shows distinctly different seismic velocities underlying the EANT and WANT, extending into the deep upper mantle (>300 km) (Watson et al., 2006; Brenn et al., 2017; White-Gaynor et al., 2019). A deep-seated low seismic velocity anomaly beneath MBL has been reported in a number of studies (Hansen et al., 2014; An et al.,

2015b; Lloyd et al., 2015, 2020; Lucas et al., 2020), with Hansen et al. (2014) imaging low seismic velocities underlying the region in the lower mantle. The presence of the deep-seated low velocity anomalies is consistent with the hypothesis of a mantle plume beneath MBL (e.g., LeMasurier & Landis, 1996; Spiegel et al., 2016).

In this study, we introduce a new S-wave-velocity, upper mantle model of the entire Antarctic Plate. The model is computed using a very large dataset of broadband seismic waveforms, combining both global and regional seismograms in order to maximise the data sampling across the entire plate and its boundaries. By including the waveforms of both the fundamental mode surface waves and body waves (composed of the higher mode surface waves), we resolve the Antarctic crust and upper mantle down to 660 km depth. In the following sections, we present and validate the model, compare it to other recently published models and discuss the inferences it offers on the lithospheric structure and evolution of Antarctica.

3.3 Methods

This study builds on and concludes the series of continent- and plate-scale waveform tomography studies using the automated multimode inversion (AMI) of surface and S-wave waveforms (Lebedev et al., 2005; Lebedev & van der Hilst, 2008), now including North America and the North Atlantic region (Schaeffer & Lebedev, 2014; Celli et al., 2021); the Arctic region (Lebedev et al., 2018); Africa, South America and South Atlantic (Celli et al., 2020a,b; Chagas de Melo et al., 2025); Australia (de Laat et al., 2023) and Asia (Dou et al., 2024). The assembly of all publicly available data from national, global and temporary networks and the meticulous outlier and error analysis amounts to a substantial effort for a continent-scale model.

3.3.1 Data

The model, AP2024, is constrained by 785 thousand vertical component seismograms successfully fit by AMI, which extracts phase information from surface, S- and multiple S-waves (Lebedev et al., 2005). It is computed as a global model but with a focus on the Southern Hemisphere, centred at the South Pole (Fig. 3.2). The data sampling in the hemisphere, including the Antarctic Plate and surroundings, is maximised by including waveform fits of all available seismograms with either the source, the receiver, or both the source and the receiver located within it. The sampling decreases gradually from the Equator northwards but is still

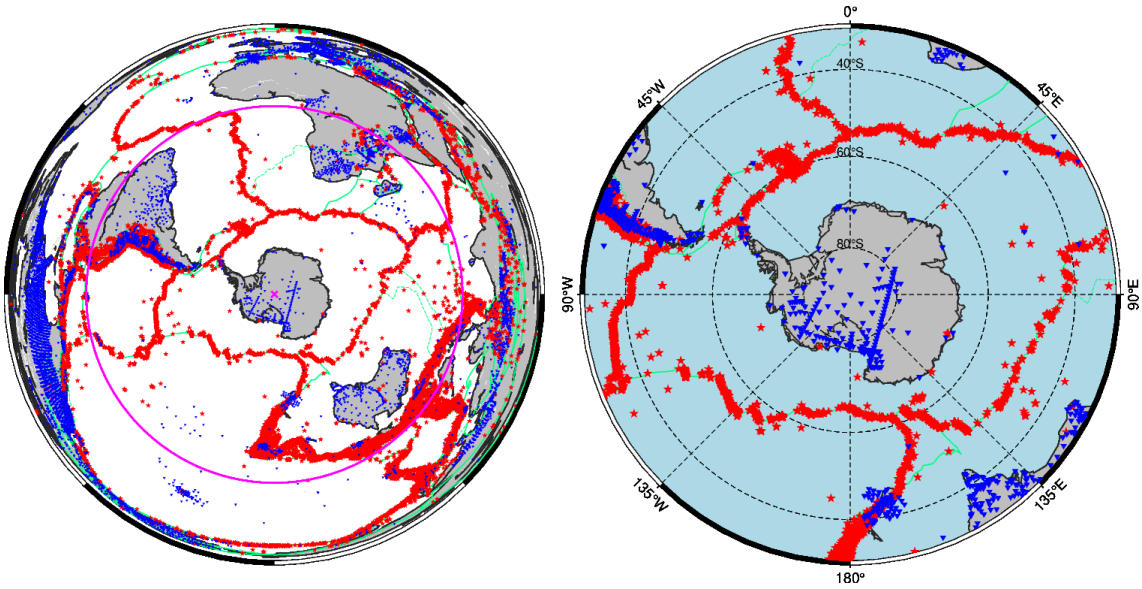


Figure 3.2: Left: Global map of all stations (inverted blue triangles) and events (red stars) of seismograms successfully fit by AMI and included in the tomography. The magenta circle along the equator is the boundary of the Southern Hemisphere within which the data sampling is maximised. Right: A zoom on the stations and events used within the Antarctic Plate, below 30°S.

substantial in the Northern Hemisphere. This data selection approach ensures that the model resolves structure within the antipodal (Northern) hemisphere at a resolution sufficient to prevent erroneous mapping of structures between the hemispheres (Celli et al., 2020b; de Laat et al., 2023).

The 785 thousand waveform-fitted seismograms come from over 27 thousand events recorded between 1982 and 2021 at 8.7 thousand stations. All openly available broad-band seismograms starting with 1994 were requested from the online data centres, including GFZ (`https://geofon.gfz-potsdam.de`), IRIS (`https://www.iris.edu/hq/`), IPGP (`https://datacenter.ipgp.fr`) and ORFEUS (`http://www.orfeus-eu.org`). Seismograms recorded before 1994 were used for stations that stopped operation by 1994 (Lebedev & van der Hilst, 2008). The seismograms were downloaded using ObsPy (Beyreuther et al., 2010) via the FDSN (International Federation of Digital Seismograph Networks) (`https://www.fdsn.org/`) web service. Earthquake source coordinates and moment tensors were obtained from the Global CMT catalogue (Dziewonski et al., 1981; Ekström et al., 2012).

The global data sampling is heterogeneous, with the Antarctic Plate sampled relatively sparsely. The station coverage in Antarctica has expanded recently but is uneven, with most permanent stations and temporary deployments located in WANT and few stations in EANT, with only two permanent stations located along the EANT coast between 5°E and 110°E (Fig. 3.2). The plate is surrounded

by spreading ridges, providing good azimuthal coverage with back azimuths towards events.

The best sampled regions of the model are located in WANT and along some of the boundaries of the Antarctic Plate (Fig. 3.3). The regions with the sparsest sampling are offshore DML, where there are no stations, and the tip of the Antarctic Peninsula, due to the lack of stations along the north-eastern coast of Antarctica (Fig. 3.3). The maps of the sums of the columns of the sensitivity matrix (Fig. 3.3) offer a more quantitative view of how the region is sampled by the data, with the lateral and depth sensitivity of each waveform and their relative weights (Section 3.3.2) taken into account. Radially, the sampling decreases with increasing depth. Laterally, it decreases from the best-sampled WARS eastward towards EANT. Despite the uneven sampling, even the relatively sparsely sampled model knots are sampled by over 7 thousand source-receiver paths, which is sufficient to resolve the structure at the spatial wavelengths presented.

3.3.2 Inversion

The seismograms are pre-processed by removing the instrument responses and converting them to displacement. They are then resampled at 1 Hz. The seismograms include sufficient time before and after the body and surface wave arrivals to estimate the signal-to-noise ratios (Lebedev et al., 2005). Checks for clipping and data gaps are also performed, with the affected seismograms removed.

The model is created via the three step AMI process (Lebedev & Nolet, 2003; Lebedev et al., 2005; Lebedev & van der Hilst, 2008). Firstly, the pre-processed seismograms are inverted using AMI, extracting phase information from the surface, S- and multiple S-waves from the seismograms. AMI produces linearly independent equations with orthogonal basis functions (Nolet, 1990), describing perturbations in P- and S-wave velocities within the sensitivity volumes between the source and receivers with respect to a 3-D reference model (Lebedev & van der Hilst, 2008) for each seismogram.

The reference model used for both non-linear waveform inversion and the following 3-D linear tomography comprises a 1-D mantle profile computed as a global average of a preliminary 3-D model (Lebedev & van der Hilst, 2008) and a 3-D crustal model modified from CRUST2.0 (Bassin, 2000). The crustal model is smoothed at the cell boundaries, and a 1-D global correction is performed to bring the average to the global average of the crust of the Lebedev & van der Hilst (2008) model. The crust is parameterized on a dense triangular grid of knots (Wang & Dahlen, 1995a). The 360 different model types of CRUST 2.0 become many thousands of models once topography and bathymetry are added. Lebe-

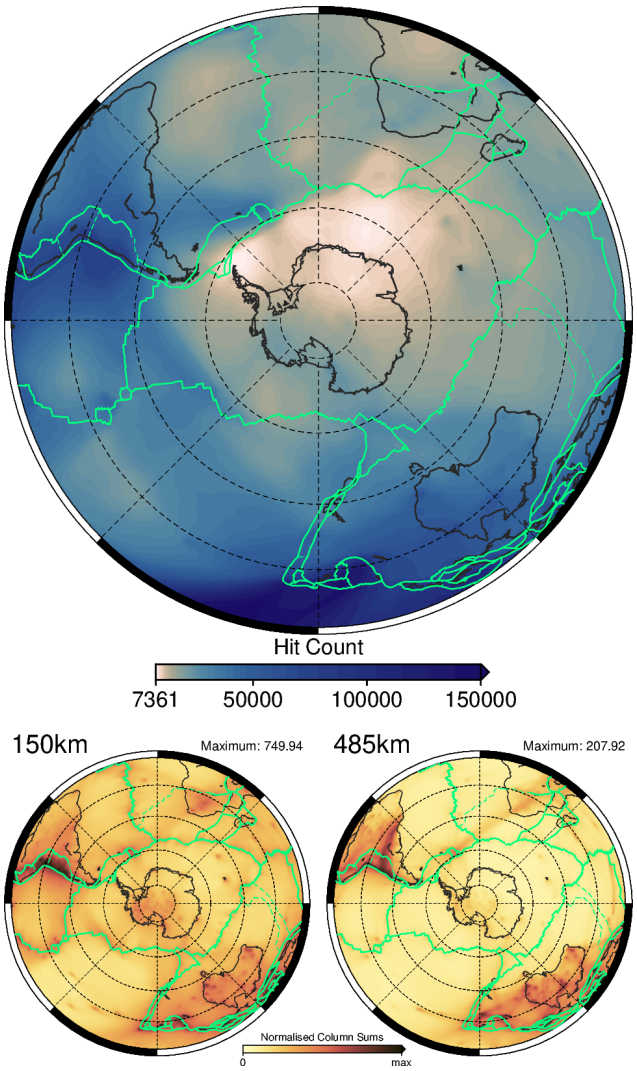


Figure 3.3: Data-sampling density at each knot of the model shown as a hit count map. Bottom: Normalised column sum maps showing the sum of the columns of the sensitivity matrix at each model grid knot for two different depths in the model.

dev & van der Hilst (2008) reduced the number to 664 1-D velocity models that capture the structure at any point with sufficient accuracy. One of the 664 type crustal velocity models was then assigned to each knot of the crustal grid (Lebedev & van der Hilst, 2008). The 1-D mantle model (Lebedev & van der Hilst, 2008) has a Q profile from ak135 (Kennett et al., 1995). The reference period of the reference model—and of the 3-D model presented in this paper—is 50 s, approximately in the middle of the period range of the data used, in the logarithmic sense. This minimizes the errors due to the neglected lateral variations in attenuation.

The linear equations obtained via the waveform inversion of each seismogram are combined into a large system. It is then solved using the conjugate gradient method LSQR (Paige & Saunders, 1982), with norm damping and lateral and ra-

dial smoothing, for the 3-D distribution of perturbations in the isotropic P- and S-wave speeds with respect to the reference model and for the pi-periodic ("2 psi"), S-wave azimuthal anisotropy (Lebedev & van der Hilst, 2008). The model is parametrised using a global triangular grid with an approximate spacing of 125 km, at the knots of which the isotropic P-, S-wave and azimuthal anisotropic perturbations are solved for. An integration grid, with a denser inter-knot spacing of approximately 25 km, is used to integrate over the approximate sensitivity volumes between the source and receiver (Lebedev & van der Hilst, 2008). The knots of the model and integration grids are co-located by design to allow for rapid transformations between the two grids. The model is vertically parameterized using a fixed set of 18 (7, 20, 36, 56, 80, 110, 150, 200, 260, 330, 410-, 410+, 485, 585, 660-, 660+, 809, and 1007 km) and 10 (7, 20, 36, 60, 90, 150, 240, 350, 485, and 585 km) knots for S- and P-wave velocity perturbations, respectively. Linear interpolation is applied between the knots, creating triangular basis functions. The shallowest knots ensure that at least one model node is present in the crust, with continental crust containing up to 4 model nodes. Discontinuities bounding the mantle transition zones at 410 and 660 km are parameterised using two half-triangles just above and just below them, and their depths are fixed in the inversion.

In order to account for the uneven azimuthal path coverage, the equations corresponding to different source-station pairs are weighted. This is achieved by measuring the similarity of a great-circle path with respect to all other paths in the model and assigning lower weights to the equations obtained from more commonly sampled paths. Perturbations of S- and P-wave velocities are damped towards being equal (in m/s) but are not rigidly coupled, allowing deviations if required by the data. The S-wave and P-wave velocity models, however, are very similar, and we limit our discussions to the S-wave velocity model. Regularisation in the form of vertical and lateral smoothing and norm damping is applied to stabilise the inversion. Two forms of smoothing are applied, the first penalizes differences between the anomalies at the node with respect to the average over this and the 6 (or 5) nearest neighbouring nodes. Smoothing in the form of vertical gradient damping, applied to penalize differences between neighbouring model knots, is applied to penalize oscillatory changes with depth. Norm damping penalizes the anomaly amplitudes with respect to the reference model. Smoothing and damping parameters do not vary laterally at each depth but do vary depending on the depth, to take into account the decrease of the data sampling density with depth.

Finally, outlier analysis is applied in order to remove the least mutually consistent data, likely to be affected by the largest errors (Lebedev & van der Hilst,

2008). An automated outlier analysis compares the data with the synthetic data computed from an initial 3-D model. The most inconsistent data showing the largest differences are removed, using an empirical threshold. The new set of equations is then re-inverted to produce a new model. A manual outlier identification procedure is aimed at removing probable artefacts—including errors due to source mislocations or instrumental problems—is then performed as well. 526 thousand waveform fits of the initial set of 785 thousand waveform fits are retained after the automated and manual outlier removals, and are used to constrain the final model.

The tomographic inversion is performed as a global inversion but with a specific focus on the hemisphere including the Antarctic Plate and surroundings, as described in Section 3.3.1. The data sampling is maximised across the Southern Hemisphere, and the parameterization and regularization are fine-tuned specifically for the Antarctic Plate.

3.4 Results

3.4.1 The model AP2024

AP2024 is an azimuthally anisotropic, vertically polarised shear wave (Sv) velocity model of the crust and upper mantle of the Antarctic Plate, down to 660 km depth. We present the isotropic S-wave velocity component (Figs. 3.4 and 3.5) of the model in this paper, plotted as seismic velocity anomalies relative to the reference model (Section 3.3.2). The azimuthally anisotropic component and inferences from it will be discussed in a forthcoming publication.

The model is designed to resolve structure across the Antarctic Plate using all publicly available data and provides new insights into the 3-D shear-wave velocity variations in the upper mantle beneath the region. As observed previously, the Antarctic continent is bimodal at lithospheric depths, with regions of low S-wave velocity prevalent in its western part and high S-wave velocity in its eastern part. The continent is bisected by the major boundary between the two parts, which we observe to be marked by a shear velocity contrast of up to ∼17% (as seen in northern TAM).

The high S-wave velocity anomalies beneath the EANT reach 10% at 110 km depth. The amplitude decreases with depth below 150 km, and the high-velocity anomalies extend down to ∼260 km depth. Low S-wave velocity anomalies underlie most of WANT, with the strongest anomalies exceeding –6% found beneath the MBL dome. The low velocity anomalies beneath different parts of WANT extend continuously across this part of the continent. Low-velocity anomalies are

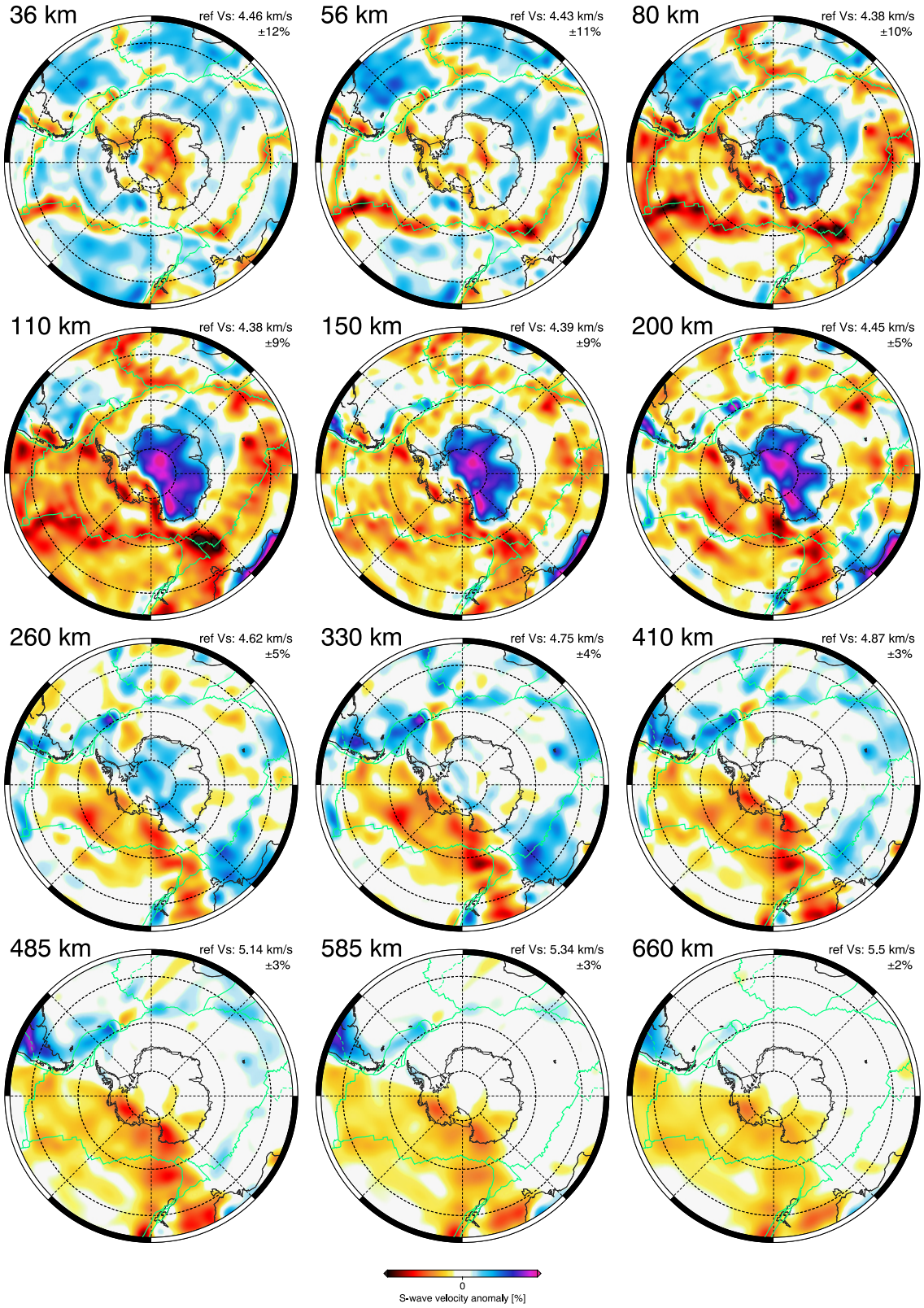


Figure 3.4: Map views of the S-wave velocity model, AP2024, at twelve depths. The anomalies are plotted relative to the reference velocity at each depth, indicated at the top right of each panel. The colour scale limits decrease with increasing depth and are indicated below the reference velocities of each panel. Plate boundaries are shown in green.

also observed in the deep upper mantle beneath WANT and adjacent oceanic areas.

Beneath oceans, the lowest S-wave velocity anomalies lie predominantly along mid ocean ridges that surround the Antarctic Plate and beneath hotspots at asthenospheric depths (80–150 km). The strongest low-velocity anomalies are observed along the Southeast Indian Ridge, just west of the Macquarie Triple Junction and northwest of the Balleny Hotspot (Fig. 3.8). Low velocity anomalies are also found in the deep upper mantle to the west of Antarctica, whereas below the oceanic areas to the east, average or faster than average shear-wave velocity anomalies are seen below ∼300 km depth.

3.4.2 Resolution Tests

We test and validate the model by performing resolution tests using checkerboard patterns of finite-width spikes. Fig. 3.5 displays the results from several tests where we prescribe synthetic disk-like structures of different lateral dimensions across different depth intervals.

Input models comprising alternating perturbations of ±300 m/s for both S- and P-wave velocities were prescribed for 3 different depth intervals, each spanning 3 vertical model knots: 80–150 km, 200–330 km and 485–660 km. The lateral extent of the patterns was 1, 2 and 4 model knots, respectively.

At shallower depths (Fig. 3.5), the input model is resolved with no lateral smearing within the continent, but with lateral elongation and some smearing in parts of the surrounding oceans. The Indian Ocean and its sector of the Southern Ocean anomalies are the least well resolved due to the poorer path sampling in the region. In the deep upper mantle, the location of the anomalies are resolved, but more lateral and vertical smearing occurs. The broadening of the depth extent of the input anomalies in the transition zone is due to the decreasing depth resolution and increasing radial averaging and, also, due to regularisation, which can squeeze deeper anomalies to shallower depths. We note, however, that the amplitude of possible artifacts due to this is small relative to that of the anomalies in shallower upper mantle (Figs. 3.4 and 3.5).

Some regions show pathing effects, indicated by the lateral smearing of neighbouring spikes, in particular between Australia and Antarctica and between the South Sandwich subduction zone and southern Africa. This is due to the abundance of similar source-station paths along some corridors, which can have an effect in spite of the path-weighting factors.

The resolution tests demonstrate the ability of the model to resolve relatively short wavelength structure in the shallow upper mantle, where the retrieved

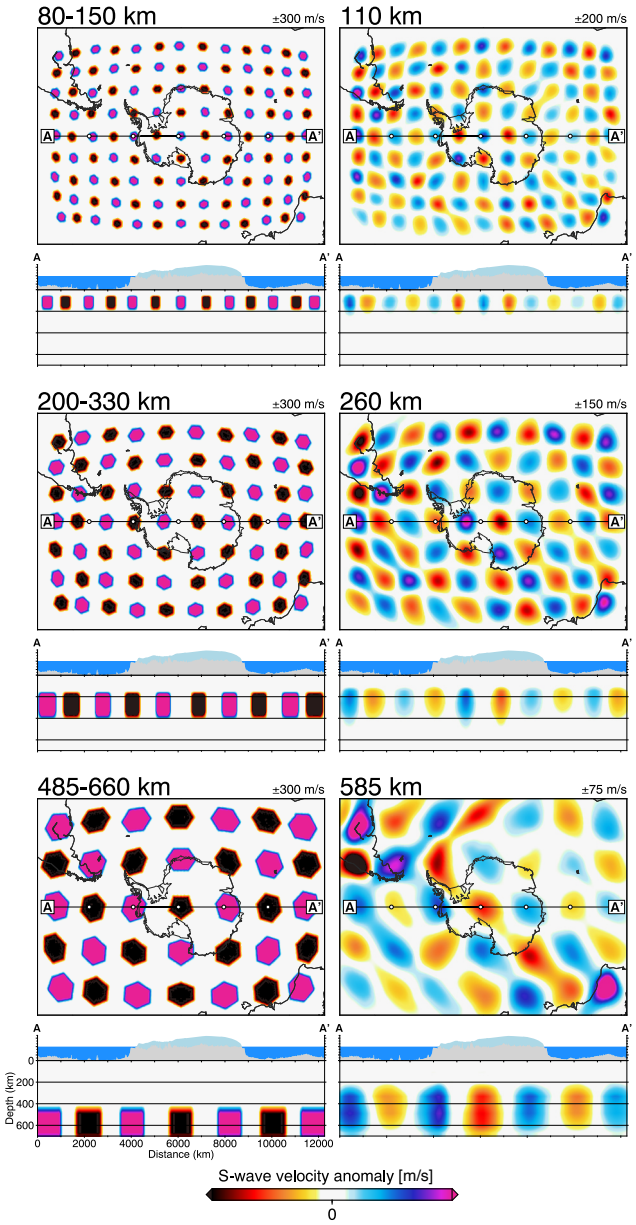


Figure 3.5: Three resolution tests with sparsely distributed spikes at the depth intervals of 80–150 km, 200–300 km and 485–660 km. The left column shows the map views of the input models. Cross sections along the great circle paths shown in the maps are plotted below. The right column shows the map views of the output models at the depths of a model knot within the depth interval of the input anomalies, with cross-sections below at the same locations as in the left column. The limits of the colour scale for each frame are shown above its top right corner.

anomalies are well constrained. The 1–2% amplitude loss, with respect to the reference velocities, is specific to the small size of the anomalies, and the sufficiently large anomalies in the lithospheric depth range (broader than the half-width of the spread of the spikes in the top row of Fig. 4) can be retrieved with accurate amplitude (Schaeffer & Lebedev, 2013; Celli et al., 2020b; de Laat et al., 2023). In

the deep upper mantle, the lateral resolution decreases and the amplitudes are underestimated, due to the decreasing data sampling with depth.

3.4.3 Comparison with other S-wave tomographic models

We compare our model to the most recent S-wave velocity model of the entire Antarctic continent and to four global S-wave models. Fig. 3.5 shows the 6 models at 110 km, 330 km and 485 km depth, plotted with respect to their own reference velocities.

The single continental scale model of Antarctica is ANT-20, a Voigt average S-wave velocity model computed using adjoint waveform tomography (Lloyd et al., 2020). SPiRaL is a joint P- and S-wave velocity model constructed using the joint inversion of P- and S-wave travel times and surface wave phase and group velocities (Simmons et al., 2021). SL2013 is a global, azimuthally anisotropic upper mantle Sv-wave velocity model, the predecessor of AP2024, constructed with the same techniques but on a coarser grid and with substantially less data (Schaeffer & Lebedev, 2013). 3DLGL is a global upper mantle S-wave velocity model computed by multi-mode Rayleigh wave tomography (Debayle et al., 2016). SEMum2 is a global radially anisotropic S-wave velocity model of the upper mantle constrained by multimode Rayleigh and Love waveforms, long-period body waves and group-velocity dispersion maps (French et al., 2013).

In the shallow upper mantle, the first order features of the S-wave velocity models are consistent across all models, with predominantly low and high S-wave velocity anomalies underlying WANT and EANT, respectively. Heterogeneity within the cratonic EANT is present in most models but its patterns are less consistent across them. Other regional-scale features differ across different models as well, including the patterns of low velocity anomalies in the WARS and the presence of strong low velocity anomalies beneath the Upper Scott Glacier region, seen in AP2024 (Fig. 3.6), ANT-20 and a number of regional models (Graw et al., 2016; Heeszel et al., 2016; Brenn et al., 2017; Shen et al., 2018a; Lloyd et al., 2020).

The large-scale structure of the oceanic upper mantle of the Antarctic Plate is consistent across the models, with the thinner lithosphere of the western sector indicated by low velocity anomalies at 110 km depth (Fig. 3.5). By contrast, the thicker, older oceanic lithosphere beneath the Indian Ocean sector of the Southern Ocean is seen as a high-velocity feature in all of the models, albeit with differences in regional-scale heterogeneity. The consistency across the different models decreases with increasing depth. For example, AP2024 shows predominantly low velocities beneath the western sector of the oceans at 330 km depth, in contrast

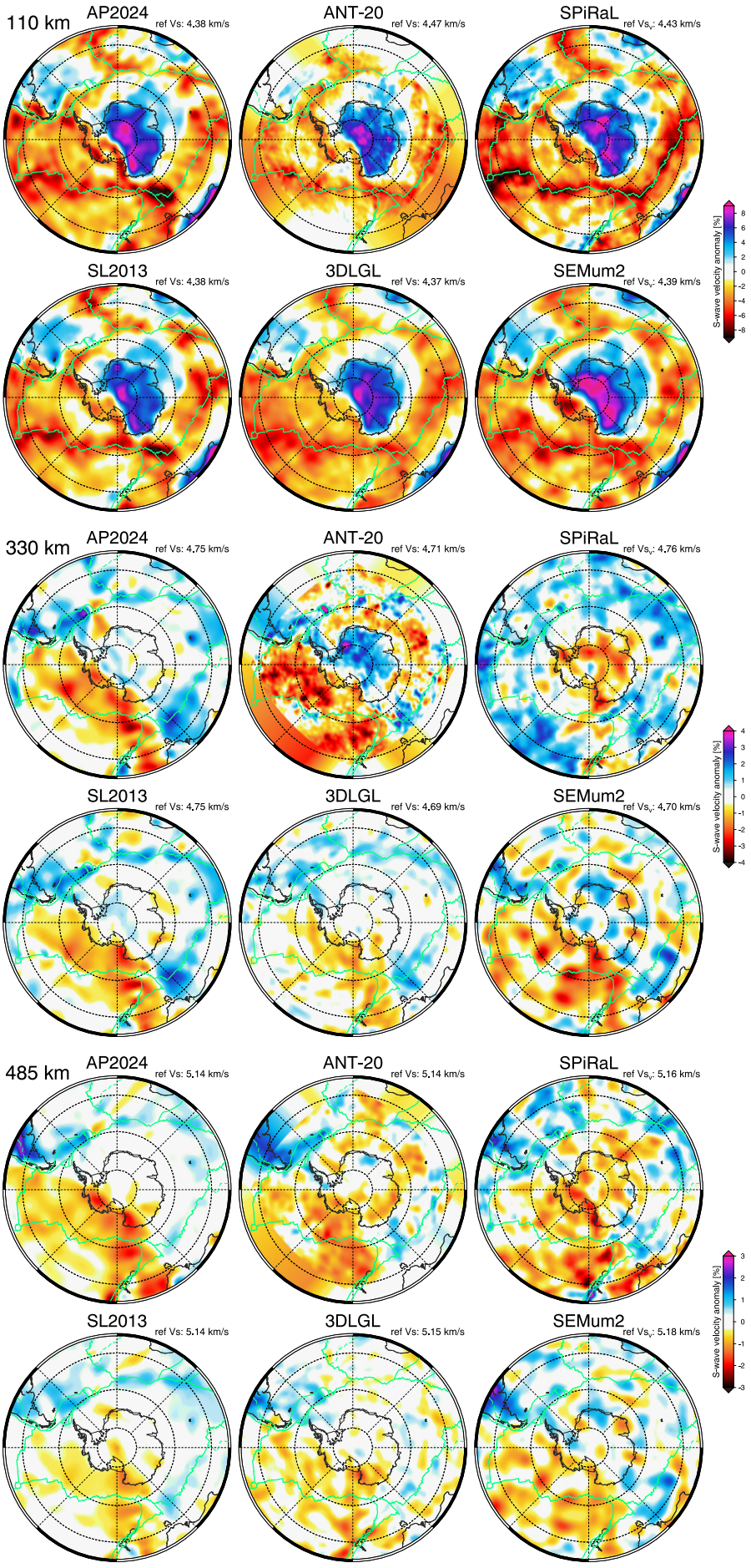

110 km
AP2024
ref Vs: 4.38 km/s
ANT-20
ref Vs: 4.47 km/s
SPiRaL
ref Vs$_v$: 4.43 km/s
SL2013
ref Vs: 4.38 km/s
3DLGL
ref Vs: 4.37 km/s
SEMum2
ref Vs$_v$: 4.39 km/s
S-wave velocity anomaly [%]
330 km
AP2024
ref Vs: 4.75 km/s
ANT-20
ref Vs: 4.71 km/s
SPiRaL
ref Vs$_v$: 4.76 km/s
SL2013
ref Vs: 4.75 km/s
3DLGL
ref Vs: 4.69 km/s
SEMum2
ref Vs$_v$: 4.70 km/s
S-wave velocity anomaly [%]
485 km
AP2024
ref Vs: 5.14 km/s
ANT-20
ref Vs: 5.14 km/s
SPiRaL
ref Vs$_v$: 5.16 km/s
SL2013
ref Vs: 5.14 km/s
3DLGL
ref Vs: 5.15 km/s
SEMum2
ref Vs$_v$: 5.18 km/s
S-wave velocity anomaly [%]

Figure 3.5: A comparison between the AP2024 model and five other S-wave velocity models at 110 km, 330 km and 485 km depths. The models are ANT-20 (Lloyd et al., 2020), SPiRaL (Simmons et al., 2021), SL2013 (Schaeffer & Lebedev, 2013), 3DLGL (Debayle et al., 2016) and SEMum2 (French et al., 2013).

with the high-to-average velocities in SPiRaL. The models 3DLGL and SEMum2 show scattered low-velocity features that are patchy and inconsistent between the two models.

Both at the lithospheric depths (110 km) and in the transition zone (485 km), AP2024, ANT-20 and SPiRaL show the greatest mutual consistency at both large and small scales, as well as consistency with known tectonic features. We consider them to represent the current state of the art regarding the continent-scale seismic velocity structure of Antarctic upper mantle. In mid-upper mantle (330 km), ANT-20 and SPiRaL show unexpected oscillatory features—clusters of short wavelength velocity anomalies of different signs—that are very different in the two models. Such features are absent in AP2024, which shows, in particular, high-velocity cratonic lithosphere anomalies that are consistent with observations beneath stable cratons elsewhere around the world and with the structure of known cratonic geotherms — i.e., high-velocity anomalies decreasing in amplitude with depth and extending down to 200-300 km (e.g., McKenzie et al., 2005; Lebedev et al., 2009; Ravenna et al., 2018; Goes et al., 2020). We infer that AP2024 provides a useful advance in the resolution of the upper mantle imaging beneath the Antarctic Plate.

3.5 Discussion

Seismic velocities are our main source of information on the variations of temperature in the Earth's mantle (e.g., Goes et al., 2000; Fullea et al., 2021; Lebedev et al., 2024). Common compositional variations in the upper mantle change seismic velocities by less than 1%, at most 2% (e.g., Sobolev, 1996; Goes et al., 2000; Cammarano et al., 2003; Schutt & Lesher, 2006). By contrast, the total shear-wave speed variations observed in tomographic models are around $\pm$10% at the scales of a few hundred kilometres, with most of that due to temperature variations (Schaeffer & Lebedev, 2015). High-velocity anomalies that we observe in the lithospheric depth range beneath eastern Antarctica indicate low temperatures and are a proxy for the lithospheric thickness, with the highest velocities indicating the thickest, coldest cratonic lithosphere (McKenzie et al., 2005; Fullea et al., 2021; Lebedev et al., 2024). Low velocity anomalies are most commonly due to relatively high temperature, with partial melting and volatiles also lowering seis-

mic velocities (e.g., Goes et al., 2000; Fullea et al., 2021; Bonadio et al., 2018). The distribution of seismic velocity variations can then be used to constrain temperature and viscosity in the mantle as well as lithospheric thicknesses, which are crucial to better understand the impact of GIA and GHF in Antarctica.

3.5.1 East Antarctic Lithosphere

What is the lateral extent of the Antarctic cratonic lithosphere, concealed nearly everywhere by the ice sheet? Seismic tomography resolves high-velocity anomalies at lithospheric depths that are indicative of cold, thick lithosphere characteristic of cratons. Positive S-wave velocity anomalies exceeding 4.5–5% at 80–150 km depths can be interpreted as regions with cratonic lithosphere (Celli et al., 2020a; de Laat et al., 2023). We empirically define the outlines of the thick and intermediate-thickness cratonic lithosphere. Thick lithosphere is inferred where the S-wave velocity anomaly exceeds 5.2% anywhere in the 110–150 km depth range (Fig. 3.6). Intermediate lithosphere is inferred where S-wave velocity anomaly exceeds 4% but does not reach 5.2% in the same depth range. The definition of the contours is ad hoc, but the difference between the two of them illustrates the effect of the threshold choice.

Thick and intermediate lithosphere underlies most of EANT, with thinner, apparently non-cratonic lithosphere found only in a few areas close to the coast. High S-wave velocities indicate thick cratonic lithosphere in the central part of the continent, including the elongated proposed Mawson Continent (Boger, 2011), stretching across Antarctica from the Weddell Embayment to the Victoria Land, Wilkes Land coast and the areas to the east. The high velocities are consistent with the Archean–Paleoproterozoic cratonic nucleus of the continent comprising most of EANT (Wiens et al., 2023).

At 80 km depth, the highest S-wave velocity anomalies (∼7%) are observed beneath Victoria Land (Fig. 3.4). High velocity anomalies of ∼5% are found within central EANT, Terre Adelié and the Aurora subglacial basin in Wilkes Land. At 110–150 km, strong S-wave velocity anomalies of ∼5–7% are observed within central EANT, Enderby Land, across Wilkes Land and Victoria Land. Anomalies exceeding 7% at 110–150 km are observed adjacent to the Weddell Embayment and the Southern TAM and regions adjacent to the Central and Northern TAM and the TAM hinterland in EANT. Archean–Proterozoic outcrops found in Central TAM (Goodge & Fanning, 2016; Goodge, 2020) in addition to Neoproterozoic (Goodge, 2020) and Paleoproterozoic samples (Will et al., 2009) found in the southern TAM are consistent with the presence of Precambrian cratonic lithosphere. Strong high S-wave velocities indicative of thick cratonic lithosphere also

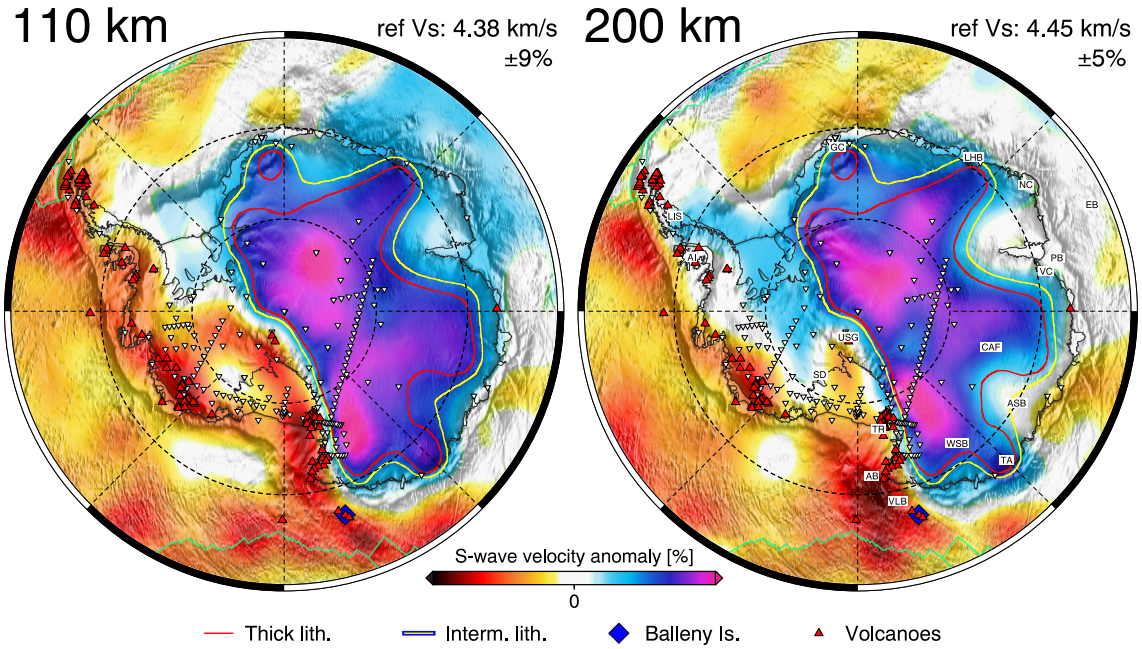


Figure 3.6: Map views of the model at 110 and 200 km depths, with the estimated boundaries of thick and intermediate cratonic lithosphere drawn in red and yellow, respectively. Quaternary volcanoes (https://volcano.si.edu/) are plotted as red triangles and the hotspot at the Balleny Islands is marked with the blue diamond. The stations located on Antarctica, and included in this study are shown as inverted triangles. Abbreviations: AB — Adare Basin, AI — Alexander Island , ASB — Aurora Subglacial Basin, CAF — Coompana/Albany-Fraser Province, EB — Enderby Basin, GC — Grunehogna Complex, LHB — Lützow-Holm Bay, LIS — Larsen Ice Shelf, NC — Napier Complex, PB — Pyrdz Bay, SD — Siple Dome, TA — Terre Adelié, TR — Terror Rift, USG — Upper Scott Glacier, VC — Vestfold Complex, VLB — Victoria Land Basin, WSB — Wilkes Subglacial Basin.

extend from Central EANT toward Enderby Land, across the GSM, as was also seen in central EANT in other recent tomographic studies (Heeszel et al., 2013; An et al., 2015a,b; Lloyd et al., 2020; Wiens et al., 2023). The high S-wave velocity anomalies of greater than 6% at 110 km, extending to below 150 km in depth, below Wilkes Land and the southern section of the Coompana/Albany-Fraser province, were also observed previously (An et al., 2015a; Lloyd et al., 2020).

Strong high velocity anomalies found beneath cratonic terranes along the coastline that were once contiguous with other cratonic provinces. The locations of the high S-wave velocities are consistent with geological and geochronological data EANT and its conjugate cratonic margins, including the Grunehogna complex in DML that was contiguous with the Archean Kalahari Craton (e.g., Marschall et al., 2010; Grantham et al., 2019), now in southern Africa, and Terre Adelié that was contiguous with the Gawler Craton, now in southern Australia (e.g., Baranov & Bobrov, 2018).

Lithospheric thinning along the coast of East Antarctica

Thick lithosphere, indicated by high S-wave velocities that extend to below 200 km, underlies most of EANT. By contrast, several areas with thinner lithosphere—where the high S-wave velocities only extend to ∼100 km depth—are found along the coastal regions of EANT. At 110–200 km depths, S-wave velocities are ∼3–4% lower along the DML coast (between 0–30°E) than in the cratonic core regions (Fig. 3.6). This thinner-lithosphere area stretches ∼700 km inland from the coastline. Another region of thinner lithosphere extending ∼700 km inland from the coast is beneath the Prydz Bay and Kemp Land sector. Lastly, Wilkes Land shows two separate regions of thinner lithosphere beneath the Aurora subglacial basin and the Wilkes subglacial basin. The velocity anomalies beneath Aurora Basin are 2% lower than the surrounding regions, and this area extends ∼300 km inland (Fig. 3.6). A smaller region of thinner lithosphere is also seen under the Wilkes subglacial basin. Both regions are underlain by low S-wave velocity anomalies at 260 km and below, and the modelling of the deglaciated topography of the region suggests the region has been dynamically uplifted since the mid-Pliocene (Austermann et al., 2015).

We observe that segments of the DML coastline (0–20°E) are underlain by average S-wave velocities at 80–200 km depths (Fig. 3.6), consistent with the previous observations (e.g., Lloyd et al., 2020; Wiens et al., 2023). Comparing Fig. 3.6 and the lithospheric thicknesses derived from ANT-20 by Wiens et al. (2023), we find a striking similarity between the two models across the thinned regions in DML, Enderby Land and Kemp Land. A pre-Cenozoic lithospheric delamination event has been invoked to explain this thinning (Lloyd et al., 2020), with either a Cambrian magmatic province associated with the East African-Antarctic Orogen (e.g., Jacobs et al., 2008) or the mid-Jurassic Karoo Plume (e.g., Sirevaag et al., 2018) events being the proposed candidates. We suggest that the rifting between Africa and Antarctica could also have triggered the thinning of the DML lithosphere, as was proposed by Lloyd et al. (2020).

The broad region of thin lithosphere along Enderby Land and Kemp Land could have similar origins—the rifting between India and Antarctica. Rifting between EANT and East India was initiated at approximately 136 Ma in the eastern Enderby Basin, propagating westward (counterclockwise) with low spreading rates (e.g., Gibbons et al., 2013; Davis et al., 2019; Rao & Radhakrishna, 2021; Jokat et al., 2021). Reconstructions of the beginning of the Kerguelen Plume activity and the subsequent rifting between India and Antarctica suggest the detachment between Sri Lanka and EANT at the Lützow-Holm Bay at ∼112 Ma (Jokat et al., 2021). The long-lived interactions between the EANT-Indian margin

(∼20 myr) (Jokat et al., 2021), in addition to the flow and impingement of hot asthenospheric material from the plume may have further increased the extent of the lithospheric thinning and delamination in Enderby Land and Kemp Land (e.g., Celli et al., 2020a).

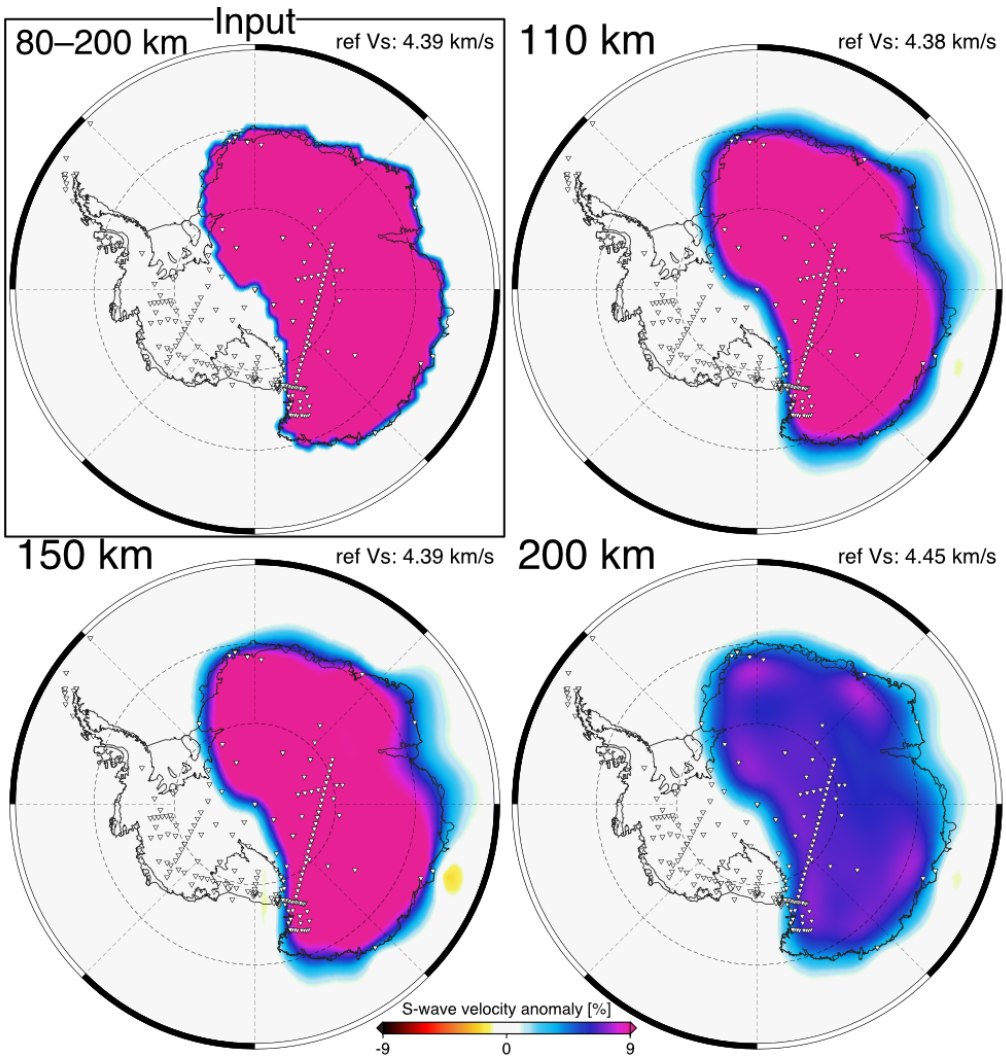


Figure 3.7: Synthetic model simulating the lithospheric structure in East Antarctica. The input model is bound by the approximate grounding lines along the East Antarctic coast and the contour of Fig. 3.6 to the south, between 80–200 km. Top left: Map view of the input model. The other panels show the map views of the output synthetic model at lithospheric depths. Stations are shown as inverted triangles.

The lithospheric mantle beneath the Aurora Basin in Wilkes Land shows a significant transition between intermediate and thick cratonic lithosphere (Fig. 3.6), similar to previous observations (Lloyd et al., 2020; Wiens et al., 2023; Hazzard & Richards, 2024). The AN-1 model (An et al., 2015b) similarly shows a thinning of the Wilkes Land lithosphere beneath the Aurora Basin, consistent with our observations.

Both in the older (e.g., Ritzwoller et al., 2001; An et al., 2015a) and newer (e.g., Lloyd et al., 2020) models of Antarctica, the thick lithosphere underlying EANT extends to the coastline or continental shelf in some regions, whereas in other regions the lithosphere is thin up to several hundred kilometres inland. The patterns of this heterogeneity are different in different models. To verify that the thinned-lithosphere features in AP2024 are real, we perform a targeted synthetic test for the EANT lithosphere. The input model is a thick lithospheric block with high velocities between 80 and 200 km, bounded by the approximate coastlines in the north and the approximate cratonic lithosphere extent from Fig. 3.6 in the south. Fig. 3.7 shows the input model and output of the synthetic test at three different depths. At 110 km and 150 km, the synthetic output recovers the input well with no loss of amplitudes along any of the regions of lithospheric thinning. At 200 km, we observe some station-location dependence for the recovery of amplitudes—the regions where the stations are located show better amplitude retrieval. The synthetic test shows that the features, such as thinned lithosphere in DML, Enderby Land, Kemp Land and Wilkes Land is, indeed, resolved and is not a model artefacts.

3.5.2 West Antarctica

The WANT upper mantle shows lower than average S-wave velocities at 80–110 km depths nearly everywhere. A sharp boundary with the high-velocity EANT closely follows TAM. The lowest S-wave velocities are imaged beneath the Bellingshausen Sea, MBL dome, Erebus volcanic province and between the Balleny Islands and the Macquarie Triple Junction. Moderately high velocity anomalies of between 2–3% are observed at 100–150 km depth beneath the Weddell Embayment, the Larsen Ice Shelf and between the Siple Dome and MBL (Figs 3.5, 3.6 and 3.8). The high velocity anomalies have been associated previously with lithospheric fragments that were not thermally modified during the Cenozoic rifting in the WARS (White-Gaynor et al., 2019; Lucas et al., 2020) and attributed to the compositional signature of ancient continental fragments (O'Donnell et al., 2019a). Proterozoic lithospheric mantle has also been proposed to underlie the younger crustal material there Handler et al. (2003, 2022).

Prominent, -5% low velocity anomalies at 36–56 km are observed beneath the MBL dome, southern TAM, the Whitmore Mountains and the Antarctic Peninsula (Fig. 3.4). At the same depth interval, high velocity anomalies are imaged between the Ellsworth and Pensacola Mountains, between the Ross and Amundsen Seas along the MBL coast and beneath the Larsen Ice Shelf in the Antarctic Peninsula. At 80–150 km, low velocity anomalies are prevalent across WANT,

with the most prominent ones, ranging from ∼-6 to -7%, located beneath MBL and the southern margin of the WARS. Low velocity anomalies of -2 to -3% connect the various low velocity structures in WANT, extending from the Antarctic Peninsula, across the WANT sector and north-westwards in the direction of the Macquaire Triple Junction and Southeast Indian Ridge (Figs 3.4, 3.5 and 3.8). At 150 km, high velocity anomalies in WANT increase in amplitude and lateral extent — the anomaly north of the Siple Dome extends in the east-west direction, separating MBL and southern WARS low velocity anomaly regions, and the high velocity anomalies beneath the Weddell Embayment extend further inland, encompassing the EWM and connecting with the Siple Dome anomaly. Below 200 km, the western portions of the Antarctic continent and Antarctic Plate are underlain by low velocity anomalies.

Marie Byrd Land and the West Antarctic Rift System

At depths shallower than 110 km, low S-wave velocity anomalies of -4 to -5% connect MBL to the other tectonic provinces in WANT (Figs 3.6 and 3.8). At 150 km and deeper, the low velocity anomalies beneath the AP and EWM give way to average to high velocity anomalies. By contrast, low velocity anomalies beneath MBL extend to the deep upper mantle, with the low velocity province stretching in an east-west direction toward Thurston Island and the Bellingshausen Sea. The locations of the low velocity anomalies coincide with the locations of Cenozoic volcanoes in MBL and Thurston Island (Wilch et al., 2021) (Fig. 3.6) and show the areas of thin lithosphere and, probably, partial melting in the asthenosphere that gives rise to the magmatism (Ball et al., 2021; El-Sharkawy et al., 2024). The lowest S-wave velocity anomalies beneath the MBL occur within the shallow upper mantle. At 330 km depth and deeper, the anomaly broadens laterally and tilts towards the southern TAM. The low velocity anomalies extend into the deep upper mantle, including the transition zone, where they show reduced amplitudes and laterally broadened structures. The resolution of the model decreases in the deep upper mantle, so that the averaging length of the imaging increases. The anomaly amplitudes are likely to be underestimated in the transition zone, and another reason for their reduced strength is the decrease of the sensitivity of seismic velocities to temperature with depth (e.g., Cammarano et al., 2003).

Cenozoic magmatic activity above and below the West Antarctic Ice Sheet(Wilch et al., 2021; Geyer et al., 2023) and the presence of partial melting in the crust beneath MBL (Ramirez et al., 2017) indicate the presence of thin lithosphere and warm mantle material beneath the region. The crust beneath MBL is relatively thin, 28–32 km (Chaput et al., 2014; Ramirez et al., 2017). The absence of a thick

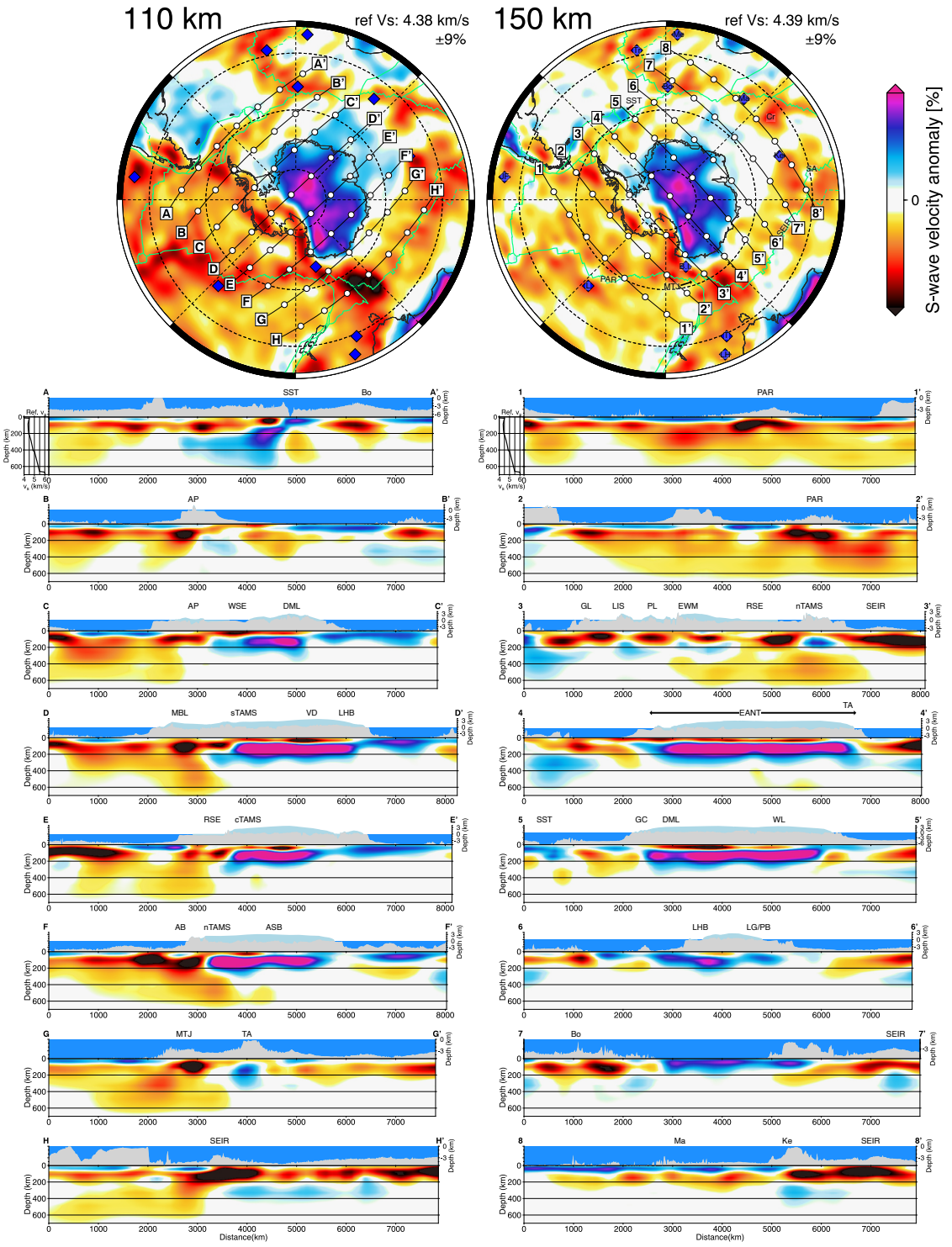


Figure 3.8: Northeast-southwest (A-H) and northwest-southeast (1-8) cross sections through the model. The cross sections are plotted with respect to the reference velocities at each depth and are saturated at ±5%. Hotspots and the corresponding locations are adapted from McNutt & Caress (2007), and are shown as blue diamonds on the map views. Plate boundaries are plotted in green. Abbreviations: AB — Adare Basin, ASB — Aurora Subglacial Basin, B.I. — Balleny Islands, Bo — Bouvet hotspot, Cr — Crozet Islands, DML — Dronning Maud Land, EANT — East Antarctica, EWM — Ellsworth-Whitmore Mountains, GC — Grunehogna Craton, GL — Graham Land, JF — Juan Fernandez hotspot, Ke — Kerguelen hotspot, L — Louisville hotspot,

Figure 3.8: *continued from previous page*
LG/PB — Lambert Graben/ Pyrdz Bay, LHB — Lützow-Holm Bay, LIS — Larsen Ice Shelf, Ma — Marion hotspot, Me — Meteor hotspot, MTJ — Macquarie Triple Junction, PAR — Pacific-Antarctic Ridge, PL — Palmer Land, RSE — Ross Sea Embayment, SA — St. Paul and Amsterdam Islands, SEIR — Southeast Indian Ridge, SST — South Sandwich Trench, T — Tasmanid hotspot, TAMS — Transantarctic Mountains, Tr — Tristan hotspot, WL — Wilkes Land, WSE — Weddell Sea Embayment.

buoyant crust suggests that the high elevations of MBL may not be supported isostatically (Chaput et al., 2014; Pappa et al., 2019), with an alternate, dynamic mechanics, at work. A mantle plume has been proposed to explain the elevated topography and Cenozoic volcanism in MBL (LeMasurier & Landis, 1996; Behrendt, 1999), with Seroussi et al. (2017) suggesting that the presence of a weak plume underlying the WANT was compatible with the basal conditions of the West Antarctic Ice Sheet. Previous tomographic studies have reported low velocity anomalies beneath MBL and the WARS (Hansen et al., 2014; Lloyd et al., 2015, 2020; Shen et al., 2018a). The widespread presence of low velocity mantle material extending down to the transition zone further supports the mantle plume hypothesis (Sieminski et al., 2003; An et al., 2015b; Lloyd et al., 2020).

We image a prominent low velocity structure adjacent to the southern front of the WARS above 200 km in depth. The lowest S-wave velocity anomalies are located beneath Victoria Land, along the Terror rift and the southern TAM (Fig. 3.6). The approximately 1900 km long channel-like structure conterminous with the TAM is 200–250 km wide and connects the low velocity anomalies beneath the Adare and Victoria Land Basins, the volcanic fields in Victoria Land, Terror Rift and the Upper Scott Glacier, before waning in amplitude and terminating at the EWM terrane boundary. The structure also appears to extend northward from the Adare Basin towards the Macquarie Triple Junction, the Southeast Indian Ridge and the Pacific-Antarctic Ridge. We observe a decrease in amplitude and lateral extent of the low velocity anomalies beneath the southern TAM at the southern end of the low velocity structure with increasing depth, as well as an increasing amplitude and northward migration of the low velocity anomalies at Adare Basin. At 260 km, the low velocity anomalies beneath WARS are confined to the Ross Sea, while the mantle beneath southern TAM transition to near average–high velocities. The low velocity anomalies below the Ross Sea region extends below 260 km and through to the deep upper mantle. Previous tomographic studies have reported a similar low velocity belt along the WARS front in the shallow upper mantle (Heeszel et al., 2016; Shen et al., 2018a; White-Gaynor et al., 2019; Lloyd et al., 2020).

The locations of the lowest-velocity anomalies match closely with those of Cenozoic volcanism, in agreement with other recent studies (e.g., Lloyd et al., 2020). The Adare Trough was the location of a spreading ridge active at the time of the TAM uplift in the Eocene (Cande et al., 2000; Whittaker & Müller, 2006). The Terror Rift, a separate extinct spreading ridge that was active between the Neogene to Pleistocene (Henrys et al., 2007; Rilling et al., 2007; Sauli et al., 2021) is located along the low velocity structure. The volcanic provinces along the western margin of the WARS, between the central and northern TAM—the Erebus, Melbourne and Hallett volcanic provinces—have seen extensive volcanic activity occurring within the region from the Eocene (LeMasurier, 1990; Smellie et al., 2021; Panter & Martin, 2022).

The amplitude of the low velocity anomalies shows a qualitative correlation with the amount of volcanic activity observed across the region. The lowest amplitudes are observed in the south, beneath the southern TAM, and the highest — beneath the Terror Rift, Adare Basin and adjacent volcanic provinces. The low velocity structure most likely reflects thin lithosphere due to the multiple Cenozoic extensional events within the WARS and the warm asthenospheric material coming laterally from the Balleny Plume and vertically from the deep-mantle upwelling(s) below WANT. We infer that the thin lithosphere and hot asthenosphere can account for both the high topography and Cenozoic magmatism in MBL.

Antarctic Peninsula

We image low velocity anomalies of -2 to -4% throughout most of the AP at depths shallower than 110 km, peaking below Alexander Island, northern Graham Land and the Bellingshausen Sea. A prominent high velocity anomaly beneath the southern Larsen Ice Shelf increases in amplitude and lateral extent with increasing depth, expanding southwest towards Palmer Land and the Weddell Sea at 150 km and connecting with the high velocity structure beneath the Weddell Embayment at 200 km. The low velocity anomalies underlying the AP at 80–150 km connect to the low velocity anomalies underlying MBL, the WARS and the offshore subantarctic west of the AP. Below 150km, high velocity anomalies are observed, extending down to the transition zone.

Plate reconstructions suggest that subduction of the Phoenix Plate under eastern Gondwana began as early as the Paleozoic (Müller et al., 2022) and continued through the Neogene, ceasing at about ∼3.3 Ma due to the ridge-trench collision south of the Hero Fracture Zone (Larter & Barker, 1991; McCarron & Larter, 1998; Livermore et al., 2000; Jin et al., 2009). The formation of a slab window spanning most of the AP (e.g., Breitsprecher & Thorkelson, 2009) introduced warm,

low seismic velocity asthenospheric material. The cessation of subduction and subsequent detachment and subduction of the leading plate has been proposed as origin of the post-subduction volcanism in the AP (Hole et al., 1994). The widespread low S-wave velocities underlying the AP extending to ∼150 km can thus be attributed to both the slab window and the decompression melting of upwelling asthenosphere (LeMasurier, 1990; Smellie et al., 2021; Geyer et al., 2023). Following An et al. (2015a) and Lloyd et al. (2020), who imaged similar high seismic velocities extending into the deep upper mantle, we interpret that the high velocity anomalies beneath the AP as fragments of the subducted oceanic lithosphere of the Phoenix Plate.

Low S-wave velocity anomalies of -1 to -2% are imaged in the shallow mantle beneath the Drake Passage and are likely to be partly asssociated to the warm, buoyant material from the subducted section of the Antarctic-Phoenix ridge in the upper mantle (e.g., Zhang et al., 2009). Reconstructions of the Pacific margin of the AP and Antarctic-Phoenix subduction system place the subducted ridge sections close to the locations of the imaged low-velocity anomalies (Breitsprecher & Thorkelson, 2009; Burton-Johnson et al., 2023). Alternatively, the low velocity anomalies could, instead, be associated with the unsubducted segments of the Antarctic-Phoenix ridge, where the bathymetry of the former spreading ridge are in the region overlying the low velocity anomalies. The peculiar structure of the AP upper mantle is likely a result of the Antarctic-Phoenix subduction system, with segments of stalled subducting oceanic lithosphere and a subducted spreading ridge system.

3.5.3 Southern and surrounding oceans

At depths <56 km, the oceanic lithosphere of the Antarctic Plate shows high velocity anomalies of 0 to 3%. Low velocity anomalies are observed under the spreading ridges circumnavigating the Antarctic Plate and volcanic areas — the Weddell Sea, the Balleny and Kergeuelen Islands. At 80 km, a bimodal contrast stands out between high velocity anomalies beneath the eastern oceanic sector of the plate and low velocity anomalies beneath the western oceanic sector of the plate. At the same depths, prominent low velocity anomalies are also imaged beneath the Bouvet, Marion, Crozet, Kerguelen, St Paul and Amsterdam, Balleny and Scott volcanic islands located on the eastern sector of the plate.

High velocity anomalies extending from the Enderby Kemp Land coast toward the Indian Ocean are observed down to 110 km depth. At greater depths, average mantle velocities are observed. The younger oceanic lithosphere between Antarctica and eastern Indian Ocean (e.g., Müller et al., 2008) shows lower seis-

mic velocities. The western sector of the plate shows anomalously low velocities from the asthenosphere down to the transition zone.

The bimodal nature of the oceanic domain reflects the difference in the ages of the oceanic lithosphere, with the dividing line extending approximately in a northwest-southeast direction between the AP and Wilkes Land (Figs 3.4 and 3.8). Rifting around Antarctica was initiated at the Weddell Sea rift in the mid–late Jurassic, progressing in a predominantly clockwise direction around EANT and subsequently WANT before culminating in the opening of the Drake Passage in the early-mid Cenozoic (e.g., Reeves & De Wit, 2000; Livermore et al., 2005; Lagabrielle et al., 2009; Boger, 2011; Williams et al., 2019; Jokat et al., 2021). The eastern sector is covered by notably older oceanic crust, with ages of up to 147 Ma in the Weddell Sea and about 50 Ma older than the oldest oceanic crustal regions in the western sector (König & Jokat, 2006; Müller et al., 2008). The high velocity structures beneath the eastern sector of the oceans at depths shallower than 150 km, closely match the outlines of the regions of the Cretaceous or older oceanic crust (Müller et al., 2008).

3.6 Conclusions

AP2024 is an S-wave velocity model of the Antarctic Plate and its boundaries, constrained by a large dataset of 785 thousand waveform-fitted global and regional seismograms. Structural information from surface, S- and multiple S-waves provides resolution in the entire upper mantle depth range and offers the following observations and inferences.

1. The large-scale structure of the continent is bimodal, as observed previously, with high seismic velocities in the east and low velocities in the west. The sharp boundary between the two domains closely follows the Transantarctic Mountains and shows a shear velocity contrast of up to ∼17% at 110 km depth.

2. The structure of the oceanic lithosphere of the Antarctic Plate also differs in its western and eastern parts. The eastern, Indian Ocean section of the Southern Ocean, is underlain by high velocity anomalies down to 150 km in depth, consistent with the older, Cretaceous age of the oceanic crust there. The western, South Pacific section of the Southern Ocean, is underlain by low velocity anomalies throughout the upper mantle, consistent with thin and young (late Cretaceous and younger) oceanic crust.

3. Cratonic lithosphere underlies most of eastern Antarctica. It shows high lateral heterogeneity, with the thickest lithosphere found along the TAM and

in central EANT. The high velocity anomalies under cratons are similar to those in stable cratons elsewhere around the world: shear-velocity anomaly reaches up to ∼10% at 100–150 km and decreases with depth until it vanishes by 300 km depth. The lithospheric thickness decreases in the vicinity of the coastlines, with the central-northern TAM being an exception.

4. Seismic velocities indicate relatively thin lithosphere in the near-coastal parts of Dronning Maud Land and Wilkes Land in eastern Antarctica. Mesozoic rifting associated with Gondwana breakup is likely to have contributed to the lithospheric thinning.

5. A low velocity structure is observed beneath the WARS, connecting the low velocity anomalies between the Macquarire Triple Junction and Upper Scott Volcanic Province. Cenozoic volcanoes are located along or adjacent to the low velocity structure of the WARS rift shoulder.

6. High velocity anomalies are observed beneath the AP and are likely to indicate fragments of the recently subducted Phoenix Plate slab.

7. Deep low-velocity anomalies in the mantle transition zone beneath western Antarctica and adjacent oceans indicate high temperatures and imply active mantle upwellings.

3.7 Acknowledgements

We are grateful to JP O'Donnell, Andrew Lloyd and the Editor, Ian Bastow, for the constructive comments and suggestions that have helped us to improve the manuscript. We thank the operators of the regional and global seismic networks and the international seismic data centres for creating and providing the data used in this study. We are grateful to the creators of the tomographic models that we compared to in this study for making them available. We also thank the IRIS Earth Model Collaboration (EMC) (Incorporated Research Institutions for Seismology, 2011) and Submachine (http://www.earth.ox.ac.uk/~smachine/cgi/index.php) for providing some of these models. All figures were created using PyGMT (Tian et al., 2024) and Generic Mapping Tools (Wessel et al., 2019). This work was supported by the research grant 16/IA/4598 co-funded by the Science Foundation Ireland, the Geological Survey of Ireland and the Marine Institute and by the UK Natural Environment Research Council Grants Number XE/X000060/1 and NE/Y000218/1. The research has been completed in the framework of the projects 3D Earth and 4D Dynamic Earth, funded by the European Space Agency (ESA) as a Support to Science Element (STSE). Additional

support from Project InnerSpace (https://projectinnerspace.org) is gratefully acknowledged.

Chapter 4

Seismic evidence for a deep-mantle origin of the West Antarctic intraplate magmatism

4.1 Abstract

Intraplate volcanism is often attributed to mantle plumes, the hot upwellings from the Earth's core-mantle boundary. Alternatively, it can also be caused by interactions between the lithosphere and the convecting mantle beneath it. Here, we use AP2024, the new S-wave velocity model of the Antarctic Plate upper mantle, complement it with other state-of-the-art tomography models, and investigate the origins of the enigmatic intraplate volcanism in Antarctica. Oceanic hotspots on the plate do not show developed hotspot tracks due to the slow movements of the plate. Low velocity anomalies in the asthenosphere show the areas of partial melting that feed these hotspots' volcanism. Beneath most of West Antarctica, low-velocity anomalies at 100 km depth indicate thin lithosphere and warm asthenosphere. Beneath the Antarctic Peninsula, high-velocity anomalies below 200 km mark the location of the detached subducting slab, and low velocity anomalies in the asthenosphere are observed just below the volcanic areas. This pattern illustrates and confirms the post-subduction origin of the volcanism along the peninsula, proposed previously to be associated with the slab detachment. Marie Byrd Land and the Erebus Volcanic Province are the two largest volcano clusters and show prominent low velocity anomalies at 100-200 km depths beneath them, indicative of the partial melting that feeds the volcanism. The low-velocity anomalies extend continuously down to the bottom of the transition zone. Whole-mantle tomographic models show that the broad low-velocity anomaly continues further down to over 1000 km depth. Below 1200 km,

a complex pattern of interconnected high and low velocity anomalies, seen in the whole-mantle tomography, is consistent with deflections of hot upwellings by descending subducted slabs. Taken together, these observations provide strong evidence for a deep-mantle origin of the West Antarctica intraplate magmatism.

4.2 Introduction

The Antarctic Plate has a unique configuration, encircled almost entirely by spreading ridges and transform faults (Fig. 1). It has remained relatively stationary throughout the Neogene as its boundaries moved primarily northward and the oceanic periphery of the plate grew via seafloor spreading (e.g., LeMasurier et al., 1990).

The Antarctic continent comprises east and west Antarctica, two geologically distinct halves of the continent of Archean-Proterozoic and Phanerozoic ages, respectively, and is surrounded by the Southern Ocean. Volcanism can be found in many locations within the plate, with subduction and arc-related volcanism primarily in and near the Antarctic Peninsula and rift-related volcanism—in the West Antarctic Rift System and Ross Embayment. Intraplate volcanism is also observed elsewhere in western Antarctica, mainly in Marie Byrd Land, and in the oceans.

Intraplate volcanism at hotspots around the world has been attributed to mantle plumes, buoyant upwellings of hot material from the Earth's core-mantle-boundary (CMB) to near the surface (e.g., Morgan, 1971; Davies, 1988; Hill, 1993; Steinberger, 2000; Courtillot et al., 2003; Davies & Davies, 2009). However, there are also many instances of intraplate volcanism that are either not related to mantle plumes or involve complex interactions of the hot upwellings with the lithosphere (e.g., Demidjuk et al., 2007; Conrad et al., 2011; Davies & Rawlinson, 2014; Rawlinson et al., 2017; Hoernle et al., 2020; Mather et al., 2020). In Antarctica, its ice sheet adds challenges to inferring the origins of the magmatism. Many volcanoes in Antarctica are subglacial (van Wyk de Vries et al., 2018), rendering it impossible to analyse and date the basalts. The origin of the intraplate volcanism in Antarctica and, in particular, whether it is deep or shallow, is debated.

4.2.1 Distribution of intraplate volcanism on the Antarctic Plate

Cenozoic intraplate volcanism on the Antarctic Plate is dominated by magmatic centres in West Antarctica, with additional intraplate volcanism at hotspots in the Southern and surrounding oceans. Arc-related volcanism is primarily found along the Antarctic Peninsula and is attributed to the back-arc rifting associated

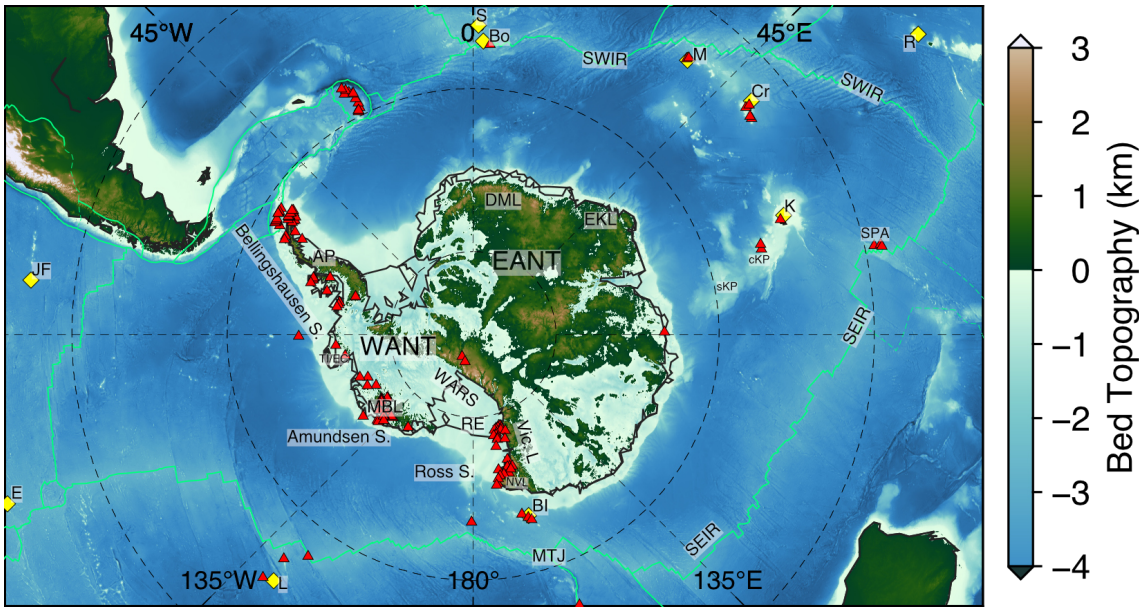


Figure 4.1: Bedrock topography and bathymetry of the Antarctic Plate (NOAA National Centers for Environmental Information, 2022). Quaternary volcanoes (`https://volcano.si.edu/`) are plotted as red triangles. Hotspots locations (Courtillot et al., 2003) are marked with yellow diamonds. Plate boundaries are plotted in green. Abbreviations: AP — Antarctic Peninsula, BI — Balleny Islands and hotspot, Bo — Bouvet hotspot, cKP — Central Kerguelen Plateau, Cr — Crozet hotspot, DML — Dronning Maud Land, E — Easter hotspot, EANT — East Antarctica, EKL — Enderby-Kemp Land, JF — Juan Fernandez hotspot, K — Kerguelen hotspot, L — Louisville hotspot, MTJ — Macquarie Triple Junction, MBL — Marie Byrd Land, M — Marion hotspot, NVL — North Victoria Land, R — Reunion hotspot, RE — Ross Embayment, S — Shona hotspot, SEIR — Southeast Indian Ridge, sKP — South Kerguelen Plateau, SPA — St. Paul and Amsterdam Islands, SWIR — Southwest Indian Ridge, TI/EC — Thurston Island/Eights Coast, Vic. L — Victoria Land, WANT — West Antarctica, WARS — West Antarctic Rift System.

with the opening of the Bransfield Strait and post-subduction volcanism resulting from the opening of slab windows and the decompression melting of upwelling asthenosphere (LeMasurier, 1990; Smellie et al., 2021; Geyer et al., 2023). Arc-related magmatism on the Antarctic Peninsula started before late Triassic, when the peninsula was a part of Gondwana (e.g., Riley et al., 2020a; Bastías et al., 2023). Subduction along the eastern Gondwana margin, between the present-day Antarctic Peninsula and New Caledonia, occurred in the Mesozoic (Luyendyk, 1995; Cande & Stock, 2006; Gardiner et al., 2021), with van de Lagemaat et al. (2023) estimating the convergence at the Zealandia and Antarctic margins to have ceased between 85 and 90 Ma.

Subduction continued further north of the Zealandia margin. The collision of ridge crests with the subduction zone between ~50 and 4 Ma resulted in the gradual cessation of the convergence, which drastically slowed down following the

cessation of the spreading at the Phoenix-Antarctic Ridge (Eagles, 2004; Smellie, 2021b). The cessation of subduction due to the ridge-crest collisions probably resulted in the opening of 'slab windows' and gave rise to decompression melting of the mantle material upwelling across the wedge, forming the series of volcanic fields along the Antarctic Peninsula (Hole, 1988; Hole et al., 1991, 1994; Hole, 2021; Smellie, 2021b).

The West Antarctic Rift System is a massive continental rift zone with widespread alkaline magmatism, containing numerous exposed and subglacial volcanoes beneath the West Antarctic Ice Sheet (e.g., Dunbar et al., 2021; Geyer et al., 2023). Multiple episodes of rifting have occurred in the West Antarctic Rift system from ∼100 to ∼11 Ma, with some faulting continuing into the Quaternary and slow extension continuing up to the present (Spiegel et al., 2016). Widespread Cenozoic magmatism within the West Antarctic Rift System (e.g., LeMasurier & Rex, 1989; Mukasa & Dalziel, 2000; Rilling et al., 2009) has been attributed to a plume origin by some workers (e.g, Kyle et al., 1992; Storey et al., 1999) but to upper-mantle processes, including edge-driven convection, lithospheric extension or slab detachment, by others (e.g., Rocchi et al., 2005; Martin et al., 2021; Panter, 2021; Smellie & Rocchi, 2021).

Several oceanic volcanic islands and provinces are located on the Antarctic Plate, primarily in the Indian Ocean and along the southeast and southwest Indian Ridges. The magmatic activity at the long-lived Kerguelen hotspot may have started before 130 Ma, prior to the separation of India and Antarctica, as evidenced by the magmatic record in eastern Tethyan Himalaya, eastern Lesser Himalaya and Bunbury (Australia) (Peng et al., 2022; Srivastava, 2022). The southern Kergulen Plateau formed as a result of a subsequent episode of volcanic activity starting at 119 Ma (Coffin, 2002; Peng et al., 2022; Srivastava, 2022). The hotspot appears to have remained fairly stationary since the first episode of activity, resulting in a large igneous province with a northwest-ward age progression, reflecting the clockwise rotation of the Antarctic Plate in the early Cenozoic (e.g., Müller et al., 2019, 2022) and northward migration of the southeast Indian Ridge.

The hotspots located along the Southwest Indian Ridge have been linked to the emplacement of large igneous provinces (LIPs): Bouvet—with the Karoo-Ferrar LIP (e.g., Verwoerd et al., 1990; Ballmer et al., 2015), Marion-Prince Edward and Crozet hotspots—with the Madagascar LIP (e.g., Anderson & Schramm, 2005; Ballmer et al., 2015), and Balleny—with the Tasmanian province or Lord Howe Rise (Lanyon et al., 1993; Ballmer et al., 2015). The St. Paul-Amsterdam islands, however, may have formed not due to hostpot activity but due to a young melting anomaly along the southeast Indian Ridge (Ballmer et al., 2015).

Seismic tomography can yield important insights on the mechanisms of in-

traplate volcanism. Images of low seismic velocities beneath major hotspots are considered to be important evidence for deep mantle plumes (e.g., Bijwaard & Spakman, 1999; Montelli et al., 2006; French & Romanowicz, 2015). Other instances of intraplate volcanism, with no clear low velocity conduits and, in some cases, geochemical characteristics not requiring deep mantle origin, motivated development of other models, including decompression melting due to sub-horizontal flow of the asthenosphere or edge-driven convection (e.g., Conrad et al., 2011; Davies & Rawlinson, 2014; Rawlinson et al., 2017; Hoernle et al., 2020; Mather et al., 2020).

Improved understanding of the mechanisms and sources of intraplate volcanism advances our knowledge of the Earth's mantle dynamics and of the origins of catastrophic mass extinctions (e.g., Stadler & Tominaga, 2015). In Antarctica, in particular, intraplate magmatism directly impacts the coupled lithosphere-ice-sheet system, including via the increased heat flux and ice sheet basal heating. A better understanding of intraplate volcanism on the Antarctic continent will also provide better parameters for estimating the Glacial Isostatic Adjustment (GIA) and related sea-level changes.

Seismic tomography provides direct evidence on the current state of the mantle beneath regions of intraplate volcanism. Beneath Antarctica, existing models show substantial disagreements, especially within the sub-lithospheric and deeper mantle. Our new model AP2024 advances the imaging resolution, in particular in the sub-lithospheric upper mantle depth range. The goal of this paper is to combine the new evidence it offers with that from other recent upper-mantle and whole-mantle models and investigate the origins of the intraplate volcanism beneath the Antarctic Plate.

4.3 Methods

AP2024 is an azimuthally anisotropic, Sv velocity model of the Antarctic Plate. It is computed as a global model but with a focus on the Southern Hemisphere, centered at the South Pole. Data sampling is maximised by including seismograms from all openly available databases with either the source, receiver or both located within the Southern Hemisphere. This ensures that the sampling decreases gradually from the equator northwards but is sufficiently complete in the Northern Hemisphere to prevent any boundary effects or erroneous mapping of structures between the hemispheres (Celli et al., 2020b; de Laat et al., 2023).

The model was computed using a very large dataset of 785 thousand waveform-fitted seismograms from over 27,000 events of magnitude 4.5 and above, recorded by 8700 stations between 1982 and 2021. All openly available broad-band seis-

mograms from 1994 onwards were requested from online data centers, including IRIS (https://www.iris.edu/hq/), GFZ (https://geofon.gfz-potsdam.de), IPGP (https://datacenter.ipgp.fr) and ORFEUS (http://www.orfeus-eu.org). Data from stations that were operated only before 1994 were requested for the earlier years. Earthquake source coordinates and moment tensors were obtained from the Global Centroid Moment Tensor (GCMT) catalogue (Dziewonski et al., 1981; Ekström et al., 2012).

Automated Multimode Inversion (AMI) used for the tomography is a three-step process. It first extracts structural information from surface, S and multiple S waves by means of non-linear waveform inversion (Lebedev & Nolet, 2003; Lebedev et al., 2005; Lebedev & van der Hilst, 2008). The information is put in the form of sets of independent linear equations with orthogonal basis functions (Nolet, 1990), which describe the 1-D average S- and P-wave velocity perturbations within the sensitivity volumes between each source and receiver pair with respect to a 3-D reference velocity model (Lebedev & van der Hilst, 2008). The reference velocity model is a 1-D globally-averaged mantle profile computed from a preliminary 3-D model (Lebedev & van der Hilst, 2008), overlain by a 3-D crustal model modified from CRUST2.0 (Bassin, 2000).

The linear equations produced by AMI are combined into a large system and solved for 3-D distributions of P- and S-wave velocity perturbations in the crust and mantle with respect to the reference model and for the π-periodic ("2Ψ") S-wave azimuthal anisotropy (Lebedev & van der Hilst, 2008). The model is parameterised using a global triangular grid with an approximately equal inter-knot spacing of ∼125 km. A finer integration grid with an approximately 25 km inter-knot spacing is used to integrate over the approximate sensitivity volumes (Lebedev & van der Hilst, 2008). Radially, the model is parameterised with a fixed set of 18 (7, 20, 36, 56, 80, 110, 150, 200, 260, 330, 410-, 410+, 485, 585, 660-, 660+, 809, and 1007 km) and 10 (7, 20, 36, 60, 90, 150, 240, 350, 485, and 585 km) knots for S- and P-wave velocity perturbations, respectively. Values between the knots are computed using tri-linear interpolation. P- and S-wave velocity perturbations are damped towards being equal in their absolute values, without imposing a rigid coupling, so as to provide more flexibility if required by the data. Lateral smoothing, radial gradient damping and slight norm damping are applied to stabilise the inversion. The regularisation penalises large changes between neighbouring model knots and large deviations from the reference model.

The final step of the inversion process exploits data redundancy by selecting only the most mutually consistent data through a posteriori outlier analysis. An initial model is computed first, and the most inconsistent data—fit the worst by this model—are identified using an empirical misfit threshold and removed.

A further manual identification process aimed at removing probable artefacts due to instrumentation or source-parameter-related errors is performed. This removes the data with the largest misfits that are likely to be most affected by large source mislocations, instrumentation errors and unaccounted-for diffraction effects (Celli et al., 2020b; Lebedev & van der Hilst, 2008; Legendre et al., 2012).

4.4 Antarctic Mantle Structure

Lateral temperature variations in the Earth's mantle are inferred primarily from seismic velocities (e.g., Goes et al., 2000; Fullea et al., 2021; Lebedev et al., 2024). Typical variations in composition in the upper mantle alter seismic velocities by less than 1%, with the most significant changes reaching up to 2% (e.g., Sobolev, 1996; Goes et al., 2000; Cammarano et al., 2003; Schutt & Lesher, 2006). Tomographic models of the shallow upper mantle display shear-wave speed variations of about $\pm$10% at scales of several hundred kilometres, most of which are due to temperature variations (Schaeffer & Lebedev, 2015; Fullea et al., 2021; Lebedev et al., 2024). The large positive S-velocity anomalies observed at lithospheric depths, for example, beneath the cratons of east Antarctica, are indicative primarily of low temperatures. These high velocity anomalies represent proxies for thick lithosphere, with the highest velocities indicating the locations of the thickest, coldest cratonic lithosphere (McKenzie et al., 2005; Bonadio et al., 2018; Fullea et al., 2021). Conversely, low velocity anomalies are due to relatively high temperature, with partial melting and volatiles also lowering the seismic velocities (Goes et al., 2000; Bonadio et al., 2018; Fullea et al., 2021).

4.4.1 Overview of the upper mantle structure

AP2024 shows a clear distinction between eastern and western Antarctic upper mantle. On the Antarctic continent, high S-wave velocity anomalies of 3% and greater underlie the majority of east Antarctica at 100 km depth, indicative of intermediate-thickness and, for the larger anomalies, thick and cold cratonic lithosphere (McKenzie et al., 2005; Fullea et al., 2021). By contrast, low S-wave velocity anomalies of -3% and lower underlie most of west Antarctica, indicative of thin lithosphere and, in the locations with the lowest asthenospheric S-wave velocities, elevated temperatures and, probably, partial melt in the asthenosphere.

The low-velocity western Antarctica includes the Antarctic Peninsula, Thurston Island, Marie Byrd Land and the West Antarctic Rift System. Along the Antarctic Peninsula, the low velocity anomalies are likely to be subduction-related, but elsewhere their origin is less clear. Pronounced low velocity anomalies of -5%

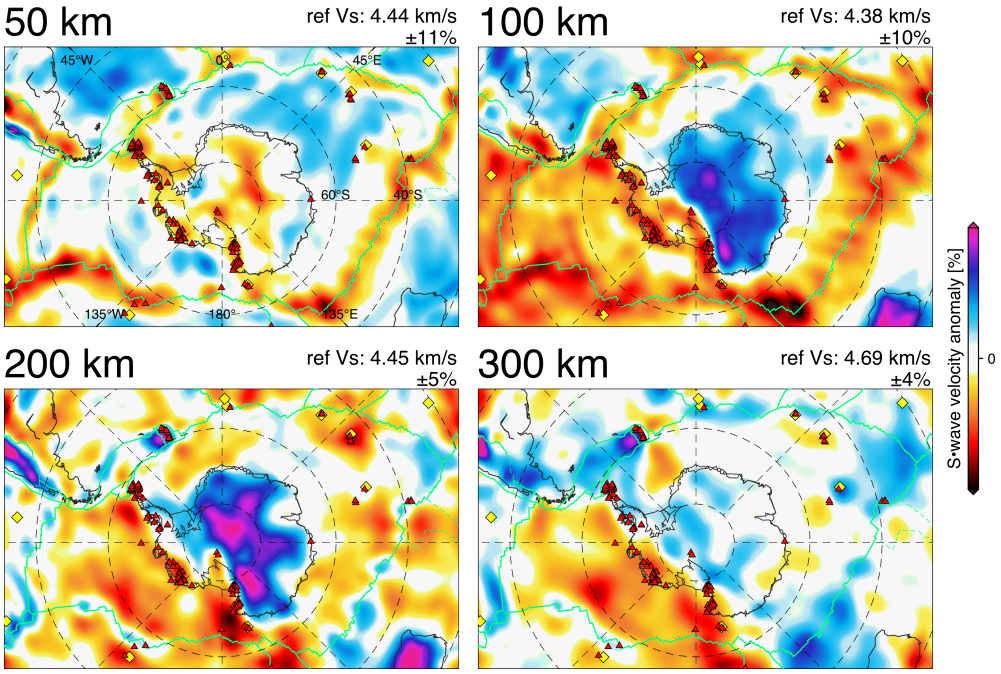


Figure 4.2: Map views of the S-wave velocity model AP2024 at 50, 100, 200 and 300 km depths. The anomalies are plotted relative to the reference velocity at each depth, indicated at the top right of each panel. The colour scale limits decrease with increasing depth and are indicated below the reference velocities of each panel. Plate boundaries are shown in green. Quaternary volcanoes (https://volcano.si.edu/) are plotted as red triangles. Hotspot locations (Courtillot et al., 2003) are marked with yellow diamonds.

and lower form a continuous channel connecting the volcanic provinces along the western Ross Embayment, the Balleny Islands and the Macquarie Triple Junction. An equally low velocity anomaly underlies the Marie Byrd Land Volcanic Province. The low velocity anomalies beneath Marie Byrd Land and the channel-like structure towards the Ross Sea extend deep into the upper mantle (Figures 4.2 and 4.3).

Beneath the oceans, the oldest oceanic crust, offshore of Dronning Maud Land and Enderby-Kemp Land, is underlain by high velocity anomalies of up to 3% at 100 km, indicating the regions of old, thick and cold oceanic mantle lithosphere. Beneath the south Pacific and its sector of the Southern Ocean, low velocity anomalies at 100 km depth reflect the relatively young age and, thus, small lithospheric thickness of the oceanic plates.

Hotspots in the oceans stand out with pronounced low velocity anomalies, which extend to below 300 km depth beneath the Marion and Crozet Hotspots, and to about 250 km depth beneath the Kergeuelen Hotspot. Low velocity anomalies underlying the Balleny and Scott volcanic provinces extend to the deep upper mantle, down to the bottom of the AP2024 model in the lower transition zone.

4.4.2 Comparison with other tomographic models

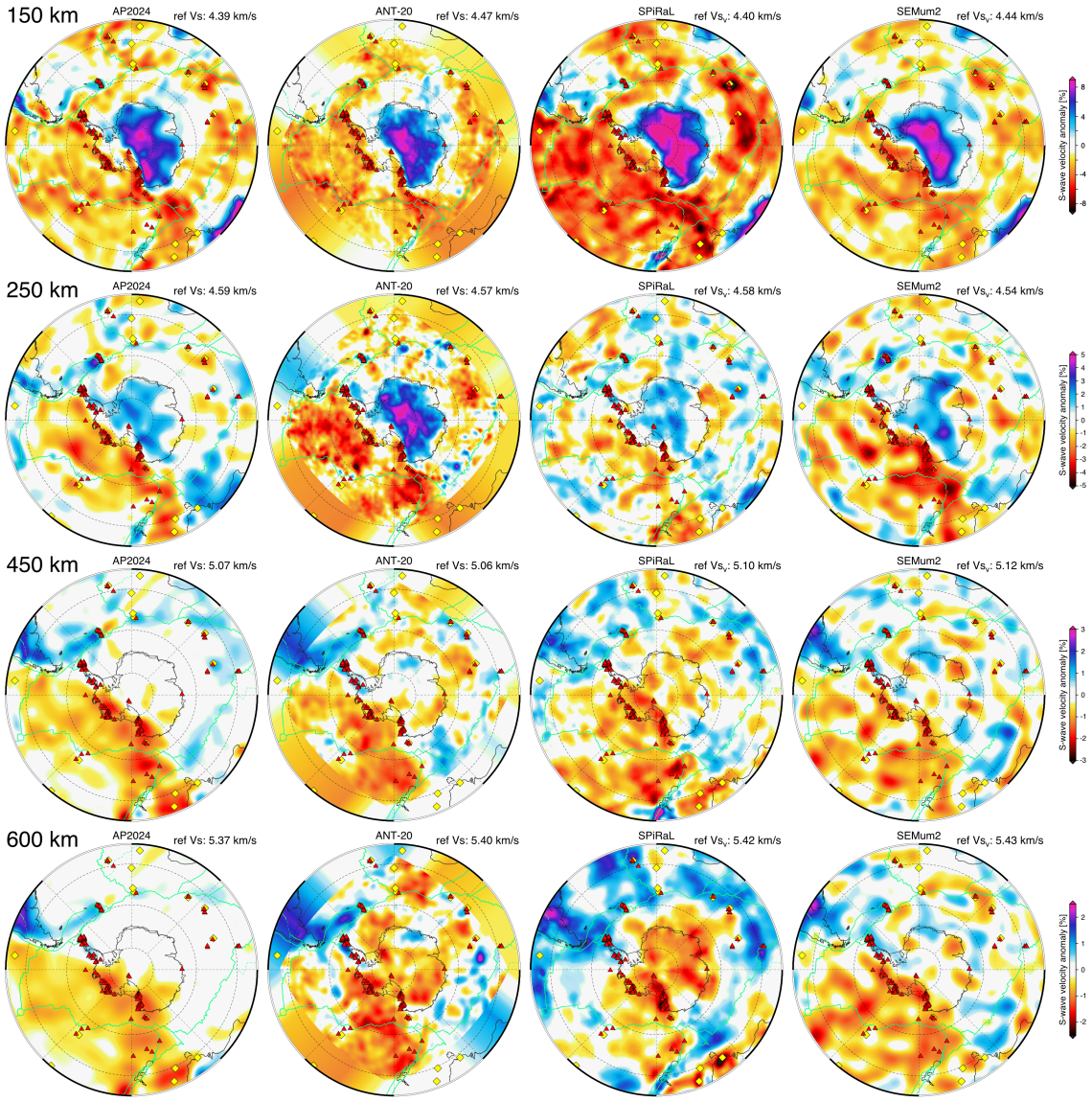


Figure 4.3: A comparison of AP2024 and 3 other S-wave velocity models in the upper mantle at 150 km, 250 km, 450 km and 600 km depths. The models are ANT-20 (Lloyd et al., 2020), the S-wave velocity component of SPiRaL (Simmons et al., 2021) and SEMum2 (French et al., 2013). Reference velocities for each plot are shown on the top right corner of each panel. Locations of Quarternary volcanoes are shown as red triangles, and hotspots are shown as yellow diamonds. Plate boundaries are shown in green. Colour scale limits for each depth are the same across the models and are shown on the right of each row.

AP2024 and other recent regional and global tomographic models show similar large-scale structure at the lithospheric depths in both the continental and oceanic parts of the Antarctic Plate. In Fig. 4.3, we compare AP2024 with 3 other shear-wave velocity models: ANT20 (Lloyd et al., 2020), SPiRaL (Simmons et al., 2021) and SEMum2 (French et al., 2013). Low velocity anomalies at astheno-

spheric depths beneath the locations of Cenozoic intraplate volcanism in western Antarctica and surroundings are present in all the tomographic models.

In the deep upper mantle, especially the transition zone, there is less mutual agreement across different tomographic models, although several key patterns are observed in all of them (Fig. 4.3). In the western sector of the Antarctic Plate, encompassing West Antarctica and the South Pacific, a large-scale pattern of low S-wave velocity is seen in all the 4 models at 250-600 km depths. In particular, low velocity anomalies in the deep upper mantle underlie the locations of intraplate volcanism in western Antarctica.

In the eastern sector—the region beneath east Antarctica and toward the Indian Ocean—there is little consistency among the models in the deep upper mantle. AP2024 shows near-average mantle velocities across most of the sector, with several spots of high velocity anomalies beneath the southeast and southwest Indian Ridge and Kerguelen Plateau. ANT-20, SPiRaL and SEMum2 all show oscillatory and largely mutually inconsistent velocities within the sector. In particular, there is little agreement regarding the velocity structure beneath the hotspots. We note that the eastern sector of the Antarctic Plate—beneath the Indian Ocean sector of the Southern Oceans and southern Indian Ocean—is sparsely sampled by seismic data, which affects all tomographic models. A conservative appraisal of the current state of the art is, thus, that we are unlikely to resolve any plume conduits in the upper mantle with confidence using the present-date data sampling in the region. Although we image clear and prominent low velocity anomalies beneath the Marion, Crozet and Kerguelen hotspots in the shallow upper mantle, current upper-mantle tomography is unlikely to provide conclusive evidence for whether they are a result of deep mantle upwellings or of other mechanisms. By contrast, deep upper mantle structure elsewhere beneath the oceans, for example, beneath the Balleny Hotspot, is sampled better and can be resolved reliably, with important inferences on the origin of volcanism, as discussed below.

Whole mantle tomography models offer evidence on mantle upwellings in the lower mantle, which is complementary to our upper mantle observations. The whole mantle models utilise teleseismic body waves that densely sample the lower mantle and provide resolution there that is sufficient to image large-scale upwellings and downwellings. We plot the locations of Cenozoic volcanoes above the lower mantle map views of 4 whole mantle tomography models—SPiRaL (Simmons et al., 2021), SEMUCB-WM1 (French et al., 2013), GLAD-M25 (Lei et al., 2020) and UU-P07 (Amaru, 2007)—in order to look for evidence for deep mantle upwellings feeding the hot, low-velocity regions mapped by the upper mantle tomography (Fig. 4.4).

All the whole mantle models show low velocity anomalies beneath west Antarc-

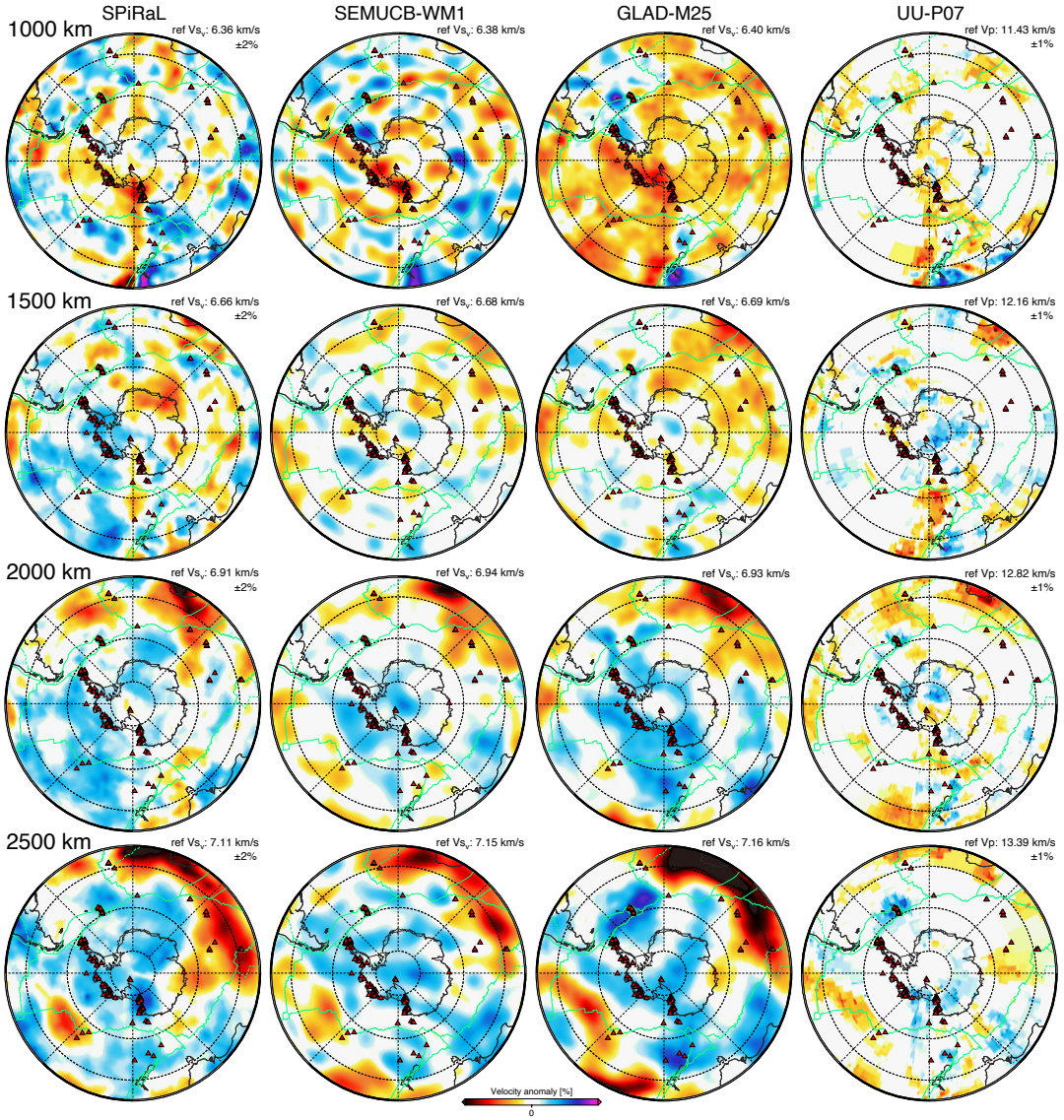


Figure 4.4: A comparison between 4 whole mantle tomography models at 1000, 1500, 2000 and 2500 km depths. The models are the S-wave velocity components of SPiRaL (Simmons et al., 2021), SEMUCB-WM1 (French et al., 2013) and GLAD-M25 (Lei et al., 2020) and the P-wave velocity model UU-P07 (Amaru, 2007). Locations of Quarternary volcanoes are shown as red triangles. Plate boundaries are shown in green

tica and the surrounding oceans extending to about 1000 km depth (Fig. 4.4). This confirms that the low velocities we observe in the upper mantle indicate hot upwellings rising from the lower mantle to the asthenosphere below the volcanic regions. Differences between the models include that the low velocity anomalies in UU-P07 are within the Ross Embayment region and the South Pacific and Southeast Indian Ridge, contrary to the 3 other models. Below 1000 km, the low velocity anomalies beneath west Antarctica taper off. At 1500 km, the models disagree, and at 2000 km and below all of them show high velocity anomalies below West Antarctica. They all show, however, low velocities at 2500 km depth

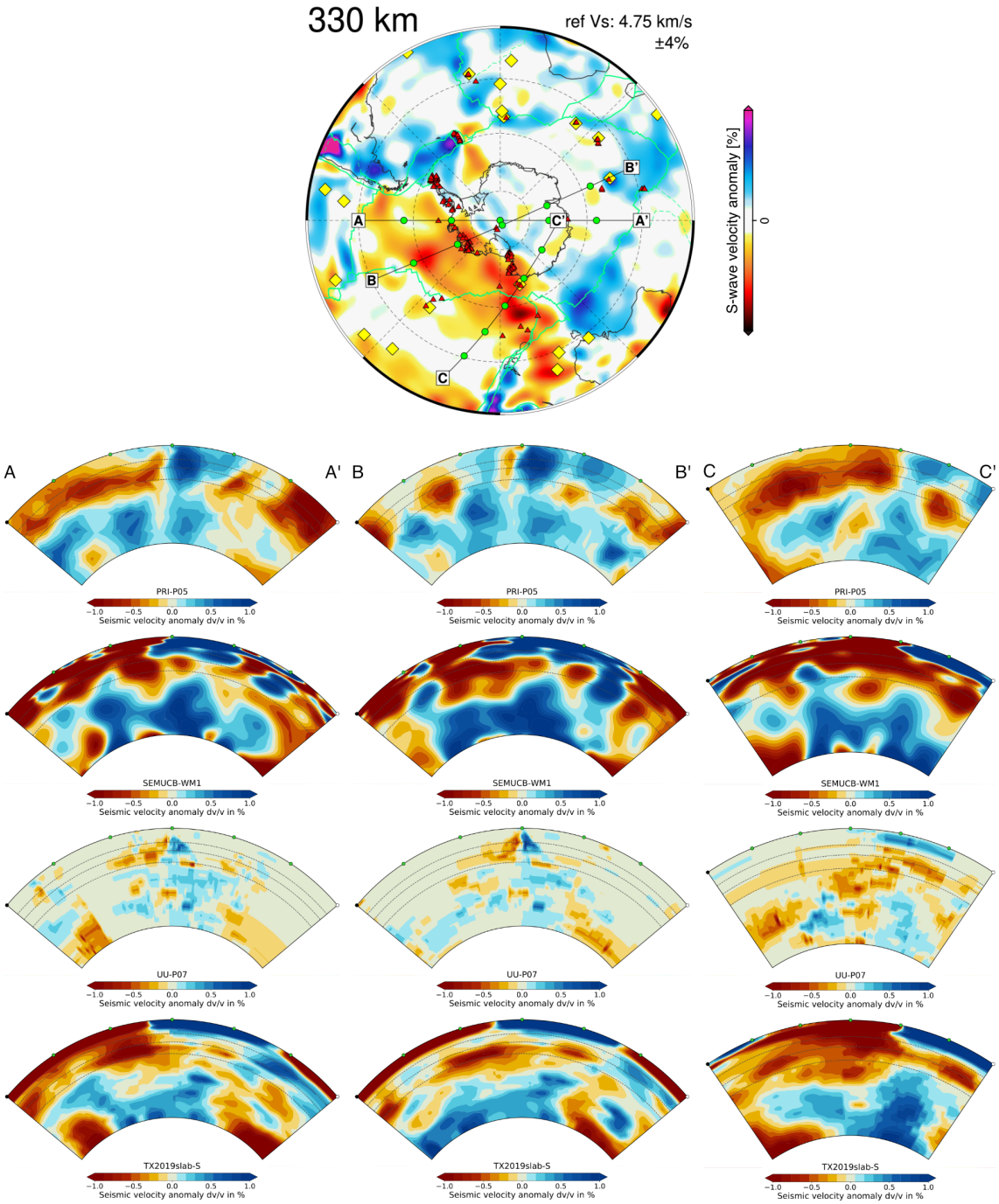


Figure 4.5: Top: AP2024 330-km map view with the cross-section locations indicated. Cross-sections: Whole mantle cross sections across the south Pacific and Antarctica generated by SubMachine (Hosseini et al., 2018). The models shown are PRI-P05 (Montelli et al., 2006), SEMUCB-WM1 (French et al., 2013), UU-P07 (Amaru, 2007) and TX2019slab-S (Lu et al., 2019).

beneath the southern Pacific Ocean, north of western Antarctica, and a region of low velocities at 2500 km depth beneath the margin of east Antarctica. Whole-mantle cross sections show a complex pattern of high and low velocities that is consistent with hot upwellings from the core-mantle boundaries deflected, on their way up, by cold downwellings (Fig. 4.5).

4.4.3 Resolution tests

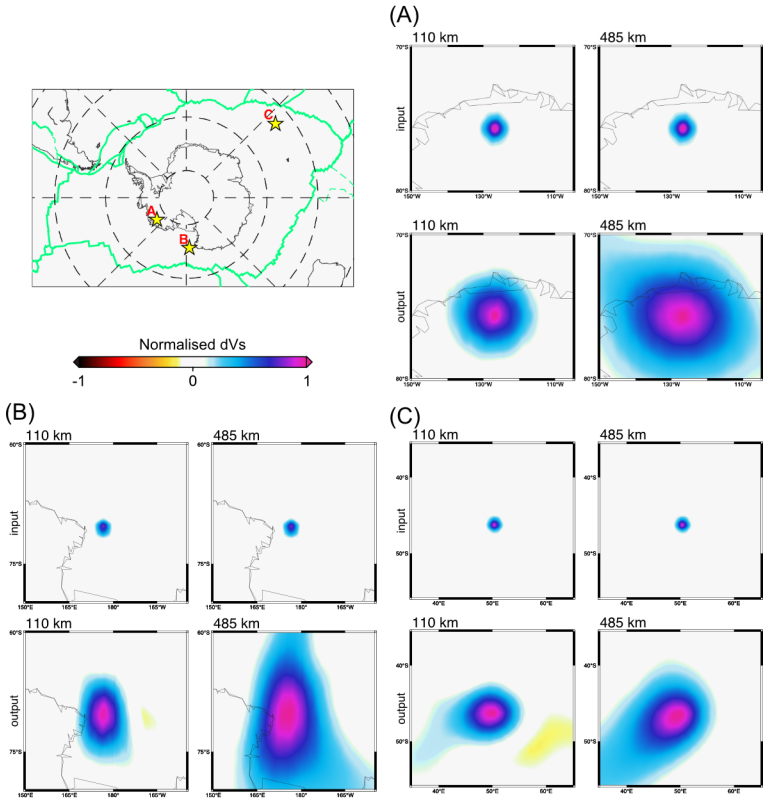


Figure 4.6: Spike resolution tests at 110 km and 485 km depths. The locations of the spikes correspond to those of (A) Marie Byrd Land, (B) the Ross Sea and the (C) Crozet Hotspot. The inversions were performed with the same regularisation as those of the real data.Top left: the positions of the spike anomalies. Map views of the input spikes (above) and output of the tests (below) are plotted together in each set of panels. S-wave velocity anomalies are normalised to the maximum value within each frame.

We performed a series of resolution tests to assess the accuracy of the AP2024 model, with a focus on this study's inferences. Synthetic spike tests were used to estimate the spreading of a narrow input anomaly. Each spike test was performed in a separate inversion in order to prevent interference of the output point-spread patterns (Rawlinson & Spakman, 2016). Spikes at 110 km and 485 km depths were placed at three locations of particular interest, (A) Marie Byrd Land, (B) in the Ross Sea and (C) the Crozet hotspot (Fig. 4.6). The three locations are differently sampled, with Marie Byrd Land being the most densely sampled region and the Crozet hotspot—the most sparsely sampled. The locations of the input spikes are well recovered at shallower depths. At 485 km, the spikes spread laterally more, a consequence of the lower resolution of the model at the greater depth. The spreading in less-sampled parts of the model is also affected, somewhat, by path effects. We observe some elongation of the anomaly in the north-south direction

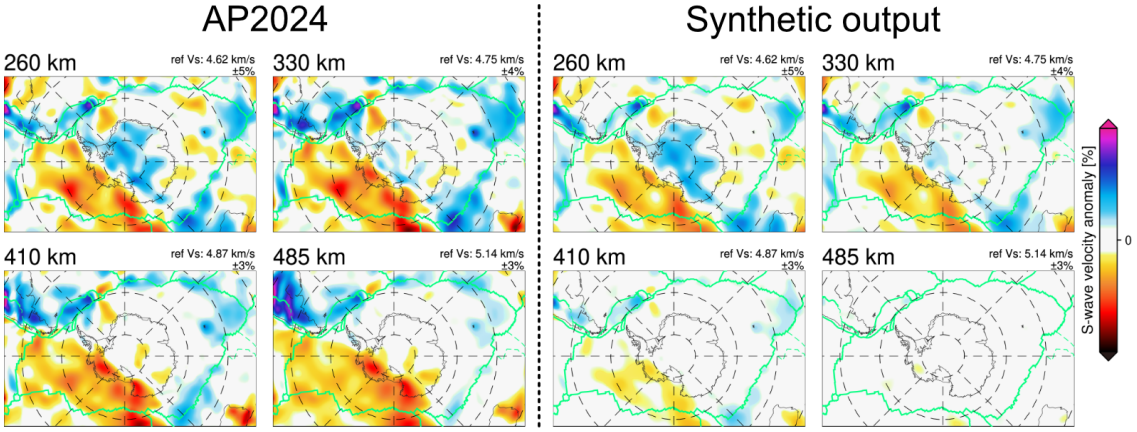


Figure 4.7: Resolution test for the leakage of structure from the upper to the lower half of the AP2024 model. The seismic structure of AP2024 below 330 km is removed, and the remaining structure is taken as the input pattern for a resolution test. The tomographic inversion had the same settings as that of the real data. The 4 panels on the left show the AP2024 models at the depth nodes closest to 330 km and the right panels show the output of the resolution test at these depths. The output of the test is plotted with the same colour saturation used for the AP2024, for a direct comparison. Colour scale limits for each panel are shown at its top right.

in the Ross Sea (spike B), a consequence of the many paths between Antarctica and Australia.

Next, we performed a test where the input pattern was AP2024 with all anomalies below 330 km set to 0. We compare the AP2024 and the output of the test in Fig. 4.7, to make sure that the velocity anomalies observed in the deep upper mantle are not a result of the velocity structure in the shallow upper mantle mapping to greater depths. There is a small decrease in amplitudes at the 260 and 330 km depths in the test output, due to the regularisation of the model causing the anomalies to be averaged radially. The output anomalies seen at 485 km, however, are negligible and disappear at greater depths. This confirms that the main velocity anomalies resolved by AP2024 in the deep upper mantle are, indeed, present in the Earth, and are not artefacts due to vertical smearing.

4.5 Discussion

Quartenary volcanoes on the Antarctic Plate are concentrated predominantly in West Antarctica, all of them underlain by thin lithosphere and low seismic velocity asthenosphere observed in AP2024 (Fig. 4.2). The locations of the volcanoes are concentrated in several regions of prominent low seismic velocity: the Antarctic Peninsula, Marie Byrd Land and the West Antarctic Rift System (Figs. 4.2 and 4.8). We discuss these regions in more detail in Section 4.5.1.

Ball et al. (2021) highlighted the collocation of thin lithosphere and elevated asthenospheric temperatures and intraplate basalts globally, using the SL2013 tomographic model (Schaeffer & Lebedev, 2013), lithospheric thickness estimates derived from it, and magmatic geochemical data. AP2024 advances the resolution of the imaging in the Antarctic Plate and shows a nearly perfect match between the locations of intraplate Cenozoic volcanism on the Antarctic Plate and the locations of low velocity anomalies at asthenospheric depths. This confirms that the intraplate volcanism results from decompression melting of warm asthenospheric material beneath relatively thin lithosphere (Raddick et al., 2002).

4.5.1 West Antarctica

Several explanations can be attributed to the origins of the low seismic velocities beneath the West Antarctic asthenosphere. WINTERC-G (Fullea et al., 2021), a global thermochemical model of the upper mantle, shows partial melting (up to 1–2%) beneath West Antarctica and in the Antarctic Peninsula at ∼80 km depth, as well as elevated temperatures of ∼1450–1600°C at 200 km depth. The magmatism in West Antarctica can be divided into different petrological domains. Post-subduction and arc-related magmatism is observed in the Antarctic Peninsula and results from the subduction of the Aluk Plate beneath East Gondwana and, subsequently, Antarctica (Panter & Martin, 2022). Intraplate magmatism in the Ross Sea and Victoria Land, ongoing since around 50 Ma, may share a common mantle source (Panter & Martin, 2022). Marie Byrd Land magmatism shows rock compositions suggesting a mix of upwelling deep mantle material and partially molten subduction-modified mantle, distinct from the other regions (Panter & Martin, 2022). These observations are consistent with the low seismic velocities observed in AP2024 at asthenospheric depths.

Antarctic Peninsula

We image low velocity anomalies beneath most of the Antarctic Peninsula down to 150 km, whereas high-velocity anomalies are observed in deeper upper mantle (Figs. 4.2 and 4.8 (cross section F–F')). The most prominent low velocity anomalies beneath the Bellingshausen Sea underlie recent (Neogene and later) ridge crests along the remnant of the Aluk Plate, spanning ∼500 km along the extinct margin (Figure 4.2 (∼65–75°W)). Quaternary intraplate volcanism is spread across the Peninsula, with a larger number of volcanoes found at the James Ross Island Volcanic Group located at the northernmost tip of the Antarctic Peninsula (Fig. 4.2 and 4.8). Cenozoic magmatism on the Antarctic Peninsula is primarily characterised by late Neogene and Quaternary volcanism resulting from the

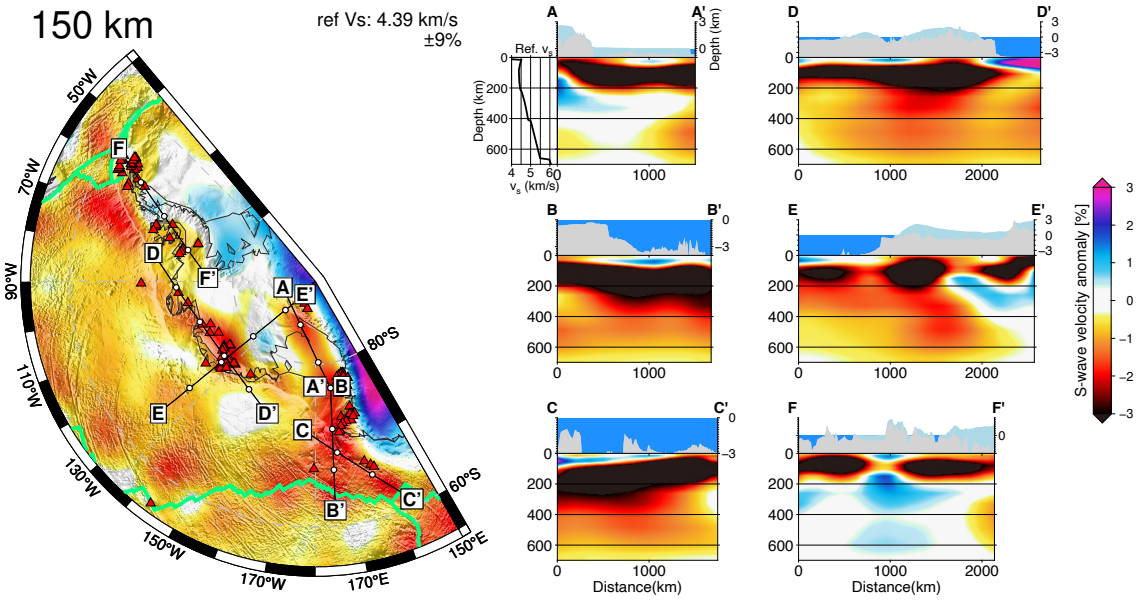


Figure 4.8: Upper mantle cross sections through AP2024 across several regions of Cenozoic volcanism in west Antarctica. The cross sections are plotted with respect to the reference model velocities at each depth and are saturated at ±3%. Cenozoic volcanoes are shown as reg triangles.

collision and subduction of ridge crests and opening of 'slab windows' in the surrounding mantle (between ∼60–80°W, along the Antarctica Peninsula in Fig. 4.8) (Smellie, 2021b). The collision and subduction of ridge-crests occurred between ∼50 and 4 Ma, and eventually resulted in the cessation of subduction (Smellie, 2021b). The continued descent of the subducted lithospheric slab resulted in the opening of 'slab windows' and gave rise to the upwelling of the asthenospheric mantle, decompression melting and emplacement of a series of volcanic fields in the Antarctic Peninsula (Hole, 1988; Hole et al., 1991, 1994; Hole, 2021; Smellie, 2021b). Volcanism in the James Ross Island Volcanic Group, the northernmost tip of the Antarctic Peninsula, is an exception in that it is not post-subduction or slab-window type but, instead, related to a back-arc, formed by the subduction at the South Shetland Trench (Hole et al., 1994; Smellie, 2021a).

The low velocity anomalies transition to high velocity anomalies beneath the Antarctic Peninsula below 150 km depth, and can be attributed to the detached remnant of the subducted Aluk Plate (Figure 4.2 (∼70°W/75°S)). Beyond the domain of the AP2024 model, the high velocity structure can be traced into the lower mantle in the SPiRaL, SEMUCB-WM1 and GLAD-M25 models (Fig. 4.4) where it reaches the depths of ∼1500–2000 km and extends laterally below the entire West Antarctica. Similarly-aged subducted slab material has been found to lie at similar depths elsewhere (van der Meer et al., 2018). Vote maps comparing 33 whole-mantle tomography models indicate that a majority of models show a

high-velocity structure beneath the Antarctic Peninsula at these depths (Fig. 4.9). The locations and depths of the high velocity structure in the upper and lower mantle, and agreement across most tomography models suggest that the structure can indeed be associated with the remnants of the Aluk Plate.

We observe a good agreement between the locations of low seismic velocities and Cenozoic volcanism throughout the Antarctic Peninsula. Both seismic and petrological evidence are consistent with volcanic activity linked to subduction and post-subduction processes in this region.

West Antarctic Rift System and the Ross Embayment

AP2024 resolves a prominent, continuous low velocity structure extending laterally from the spreading ridges at the Macquarie Triple Junction, across the Ross Sea, northern Victoria Land and the southern West Antarctic Rift System (Figs. 4.2 and 4.8 (cross sections A–A′, B–B′ and C–C′)). The approximately 1900 km long and 200–250 km wide low velocity structure is most prominent at asthenospheric depths, which would be consistent with lateral asthenospheric flow along the West Antarctic Rift System. It also extends down to the mantle transition zone and into the lower mantle (Figs. 4.2, 4.3 and 4.4). Quaternary volcanism is found above this structure, mainly along the western Ross Embayment and the Transantarctic Mountains, the rift shoulder of the West Antarctic Rift in Victoria Land (Figs. 4.2 and 4.8).

Shallow melt origins have been put forward for the magmatism, with a common metasomatized lithospheric mantle source for the region proposed (e.g., Hart et al., 1995; Rocchi et al., 2002; Rilling et al., 2009; LeMasurier et al., 2016; Panter & Martin, 2022). This was based on the relative similarity of the isotopic signature of the rocks from different parts of the West Antarctic Rift System (Panter & Martin, 2022). Terror Rift volcanic field (located to the north of the label B in Fig. 4.8 (left)) mantle xenoliths are estimated to have originated at temperatures of ∼1000 °C (Martin, 2022), lending to the lithospheric mantle source, as mantle amphiboles can only reside at temperatures lower than 1150 °C (Mandler & Grove, 2016) and can, thus, only exist within the lithosphere (Panter & Martin, 2022). The HIMU signature of the Ross Island magmatism (located to the south of the Terror Rift volcanic field), however, are consistent with deep-mantle sources for it, different from the metasomatized mantle.

With the different origins proposed from petrological observations, it is possible that localised processes modified the mantle differently at distinct segments along the ∼1900 km long channel. However, the low seismic velocities imaged by AP2024 and other upper mantle models throughout the upper mantle, in addi-

tion to the deep (extending to at least ∼1200 km in depth) low velocity anomalies imaged by whole mantle models (Figs. 4.3, 4.4 and 4.5) suggest a deep mantle upwelling causing the volcanism (Phillips et al., 2018).

Marie Byrd Land, Thurston Island and Eights Coast

Deep seated low velocity anomalies underlie Marie Byrd Land, with its numerous volcanoes. The low velocity anomalies are most prominent beneath the Marie Byrd Land dome near the coast (Fig. 4.1), and is approximately 400 km long and 200 km wide, extends laterally northwards beneath the Amundsen Sea (Figs. 4.2, 4.3, 4.4 and 4.8 (cross sections D–D' and E–E')). Low velocity anomalies extend vertically down to the bottom of our model in the lower mantle transition zone (Fig. 4.3) and, then, to about 1200 km in the lower mantle (Fig. 4.4).

The P-wave receiver function study by Emry et al. (2015) reported the mantle transition zone beneath Marie Byrd Land to be thinner in two spots, with an inference of two separate thermal upwellings. Emry et al. (2015) further proposed that the mantle transition zone showed signs of partial hydration, with the remnant subducted Aluk Plate being the source of the hydration.

The uppermost mantle beneath Eights Coast is compositionally similar to oceanic ridges but is less depleted than below AP, which would be consistent with a contribution from a mantle upwelling (Leat et al., 2022). Studies of Chatham Rise, the Cretaceous conjugate margin of Marie Byrd Land, have suggested that the HIMU-like compositions of Cenzoic magmatism within Zealandia result from a mixing of plume-like and subduction-modified mantle material (e.g., Hoernle et al., 2020; Riefstahl et al., 2020). Hoernle et al. (2020) also proposed that the mixing arose from the deep mantle upwelling flowing along the subducting lithosphere under Zealandia, prior to rising through the slab windows formed from slab tears and slab detachment.

The thin mantle transition zone is consistent with observations of low seismic velocities, and often associated with mantle upwellings (e.g., Montelli et al., 2006; French et al., 2013). The HIMU-like signatures and proposed interactions of upwelling and subducting material observed at the conjugate margins, provide strong evidence for the deep origins of volcanism in the region, which we discuss in the next subsection.

Deep origins of volcanism in west Antarctica

Is there a deep mantle upwelling beneath west Antarctica, feeding the magmatism, or are there, perhaps, more than one upwellings? Or, alternatively, is the magmatism caused by lithospheric dynamics and small-scale convection within

the upper mantle (e.g., Rocchi et al., 2005; Martin et al., 2021; Panter, 2021; Smellie & Rocchi, 2021)?

Tomographic models of the west Antarctic mantle reveal an extensive low velocity area in the asthenosphere beneath nearly the entire West Antarctica region. Interestingly, the low velocity area extends continuously into the deep upper mantle and indicates a vast area of anomalously high temperature in the mantle transition zone (Figs. 4.2,4.3). The anomalies continue further down into the lower mantle down to over 1000 km depth (Fig. 4.4).

A mantle plume or plumes have been proposed to cause the magmatism beneath both Marie Byrd Land (e.g., Kyle et al., 1994; LeMasurier & Landis, 1996; Behrendt, 1999; Emry et al., 2015; Seroussi et al., 2017) and the Erebus Volcanic Province (e.g., Kyle et al., 1992; Storey et al., 1999; Bredow et al., 2022). Distinct magmatic compositions including HIMU basaltic components, commonly associated with mantle plumes, have been observed in both the Erebus Volcanic Province (e.g., Aviado et al., 2015; Phillips et al., 2018; Martin et al., 2021) and Marie Byrd Land (e.g., Panter, 2021). Compositional differences between the magmatism in the two provinces have also been reported and would be consistent with different sources for each (e.g., Panter & Martin, 2022; Geyer et al., 2023).

Alternative, no-plume models postulate decompression melting caused by edge-driven convection, possibly related to slab detachment (e.g., Rocchi et al., 2005; Martin et al., 2021; Panter, 2021; Smellie & Rocchi, 2021) and giving rise to the emplacement of a diffuse alkaline magmatic province (DAMP). It has also been proposed that a plume with HIMU signatures could have initiated the breakup of Gondwana in the region (e.g., Weaver et al., 1994; Hart et al., 1997; Storey et al., 1999), with the migration of the plume head material beneath the lithosphere and underplating resulting in a similar HIMU-like signature in the magamatism observed in the region since then. The lack of flood basalts has been attributed to the proximity to the Aluk-Gondwana convergent margin and the thick cratonic lithosphere (Kipf et al., 2014).

Here, we observe two anomalies that stand out with particularly low velocities in the upper mantle. They are located beneath the two main volcanic provinces with the densest clusters of magmatism, Marie Byrd Land and the Erebus Volcanic Province. Both anomalies extend vertically from the asthenosphere down to the bottom of the transition zone. The anomalies we observe are consistent with those in other recent tomographic models but come in focus more clearly in AP2024 (Figs. 4.2, 4.3).

Further evidence is yielded by tomographic images of the lower mantle. Recent whole-mantle models show that the extensive low-velocity feature we ob-

serve in the transition zone continues down to over 1000 km depth in the lower mantle (Figs. 4.4, 4.5 and 4.9). At greater depths, tomographic models show high seismic velocities, probably associated with cold, subducted lithospheric slabs (Figs. 4.4, 4.5 4.9). The deep slab remnants appear to deflect the upwelling material and create a complex pattern of interactions of the upwellings and downwellings (Figs. 4.4, 4.5).

Interpreted together, the different tomography models thus offer convincing evidence for the existence of a major high-temperature anomaly that extends vertically from the asthenosphere to over 1000 km depth, which is direct evidence for a major hot upwelling. On its way from the CMB to the upper 1000 km of the mantle, the upwelling appears to be deflected and deformed by cold, sinking slab material in the deep lower mantle. In the upper mantle, the upwelling is focussed within two columns with particularly high temperature beneath Marie Byrd Land and the Erebus Volcanic Province.

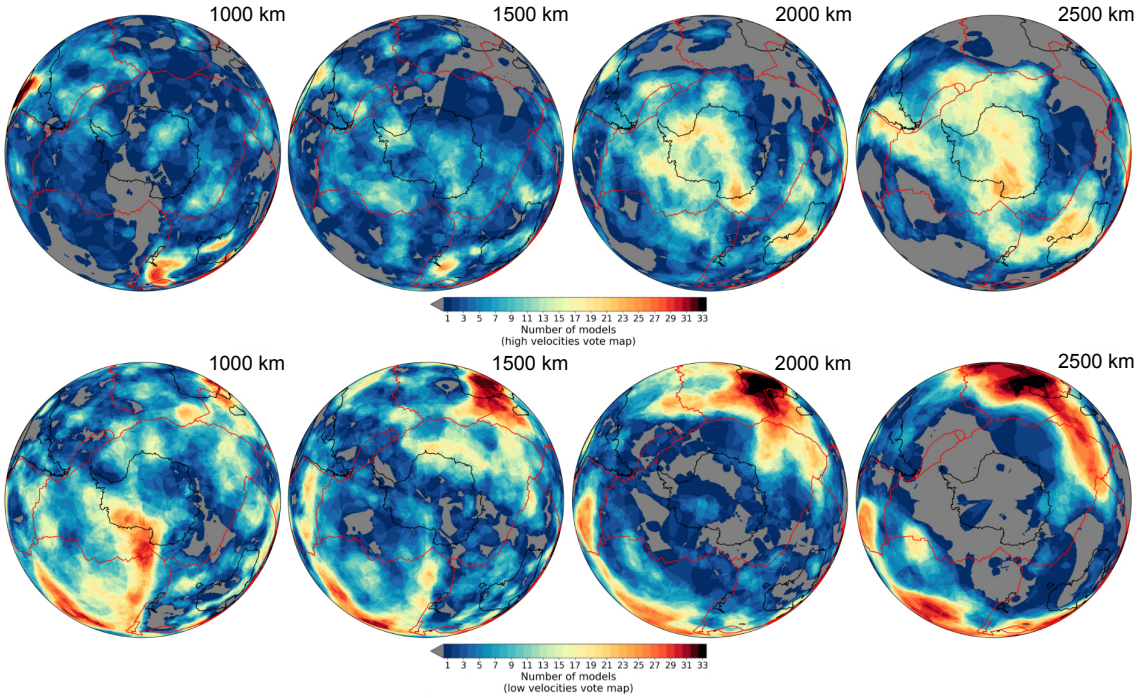


Figure 4.9: Vote maps of the 33 whole-mantle global tomography models available on SubMachine (Hosseini et al., 2018), centred at the South Pole. The vote maps show regions where the models show high seismic velocities (top row) and low seismic velocities (bottom row), with respect to each model's mean at 1000 km, 1500, 2000 and 2500 km depths. Colour scales are based on vote counts. In the top row, for example, blues indicate poor agreement and reds—good agreement of the models regarding the presence of higher than average seismic velocities, whereas grey means no models with higher than average velocity. Plate boundaries are shown in red.

4.5.2 Volcanism in the Southern and surrounding oceans

The Antarctic Plate is almost entirely surrounded by oceanic ridges, all of which are underlain by low velocity anomalies in the asthenosphere, indicating the presence of thin lithosphere, warm asthenosphere and partial melting beneath the ridges (Figs. 4.1 and 4.2). The Amsterdam–St. Paul Islands, Bouvet, Marion-Prince Edward, Crozet, Kerguelen-Heard and Balleny Hotspots (e.g., Anderson & Schramm, 2005; Steinberger & Antretter, 2006; McNutt & Caress, 2007; Ballmer et al., 2015; Bao et al., 2022) are all located above low velocity anomalies in the asthenosphere. In the deep upper mantle, tomographic models show low mutual agreement regarding the presence of low velocities beneath the locations of these hotspots (Fig. 4.3).

Low velocity anomalies underlie parts of the Indian Ocean in the lower mantle (Fig. 4.4), but it is not possible to trace continuous low velocity upwellings beneath the hotspots in today's tomographic models. The southern Indian Ocean is one of the least sampled regions of the upper mantle and, thus, poorly resolved in all current models. Improvements in data sampling would be required in order to resolve the structure of mantle upwellings in the deep upper mantle beneath the hotspots in this region.

Oceanic hotspot tracks and mantle structure

We compare the hotspot tracks of the Marion-Prince Edward, Crozet, Kerguelen-Heard and Balleny hotspots (Fig. 4.1) with the shallow upper-mantle structure in order to see if there are any indications for anomalously thin lithosphere or hot asthenosphere beneath the tracks. The 3 different plate reconstruction models used include those of Matthews et al. (2016), Müller et al. (2019) and Müller et al. (2022). The motions of the hotspots are relative to the Antarctic Plate (Fig. 4.10) and are shown in intervals of 5 Ma, up to 90 Ma. For the Kerguelen-Heard Hotspot, the locations of seamounts and Cenozoic volcanism do not overlap with the estimated hotspot tracks (Fig. 4.10b). The Matthews et al. (2016) plate model shows a fairly good correspondence between the location of seamounts and the hotspot track of the Marion-Prince Edward Hotspot, until about 40 Ma (Fig. 4.10a). The locations of the Cenozoic volcanism and seamounts of the Crozet Hotspot best fit the Müller et al. (2022) model until about 30 Ma. The Balleny Hotspot and seamounts appear to fit most closely with the Müller et al. (2019) reconstruction model in the past 5-10 million years (Fig. 4.10c). Because the Antarctic Plate has remained relatively stationary since the Cretaceous, the movements of the hotspots were slow, which is why it is difficult to reconstruct the hotspot tracks accurately. Lateral movements of the hotspots or lateral flow of asthenospheric

material—guided, for example, by thin lithosphere channels—are other possible reasons for the mismatches.

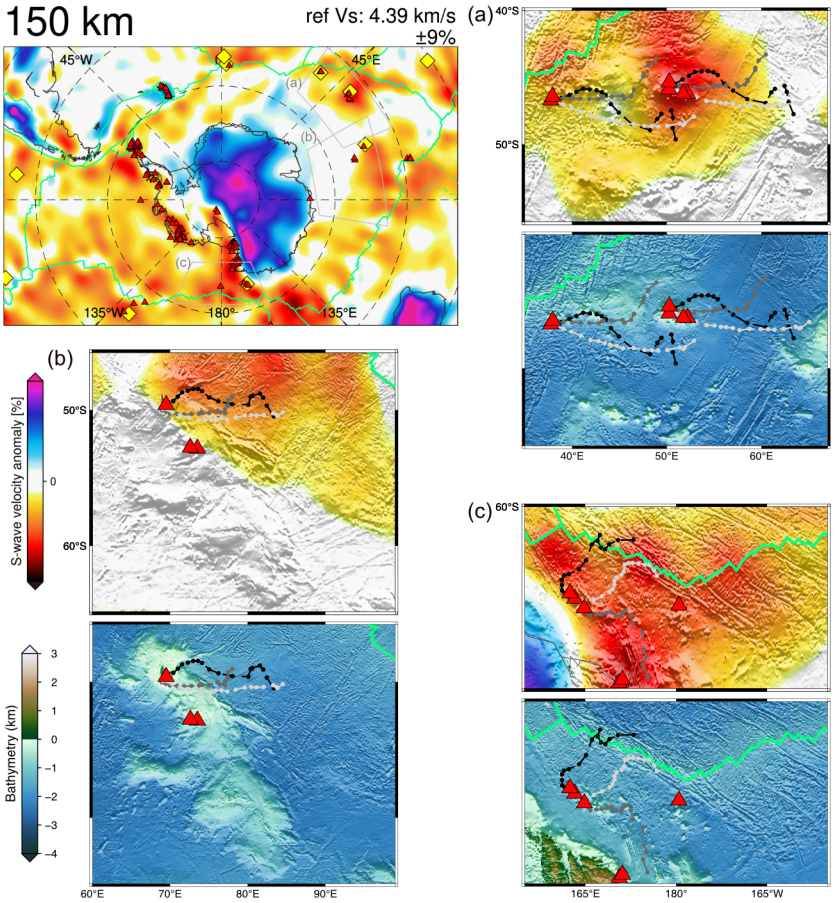


Figure 4.10: Intraplate hotspots and hotspot tracks on the Antarctic Plate. The (a) Marion/Prince Edward and Crozet hotspots, (b) Kergeuelen-Heard hotspot and (c) Balleny hotspot are shown on the 150 km depth map view of AP2024, with bathymetry from NOAA National Centers for Environmental Information (2022). Hotspot locations are from McNutt & Caress (2007). Hotspot tracks are plotted in 5 Ma intervals and extend to 90 Ma. The 3 different plate reconstruction models used for the hotspot tracks are plotted in black (Matthews et al., 2016), grey (Müller et al., 2019) and light grey (Müller et al., 2022). Plate boundaries are shown in green.

The Kergeuelen-Heard Hotspot is linked to a large igneous province and a prolonged period of volcanism (e.g., Coffin, 2002; Ballmer et al., 2015). Low velocity anomalies underlie only the Northern Kerguelen Plateau, which is the plateau's youngest (∼0.1 Ma) and most recently active part (e.g., Coffin, 2002; Ballmer et al., 2015; Srivastava, 2022) (Fig. 4.10b) . The oldest basalts on the Kerguelen Plateau have been dated to be about 120 Ma (Coffin, 2002), which is when the southern Kerguelen Plateau and the Rajmahal Traps in India were emplaced (Coffin, 2002; Kent, 2002). A subsequent event between 110 and 95 Ma led to the formation of the central Kerguelen Plateau and the Broken Ridge (Frey

et al., 2000; Coffin, 2002; Duncan, 2002). The hotspot remained close to the Indian-Antarctic spreading centre between 82–43 Ma, as the Ninetyeast Ridge formed on recent oceanic crust, finally separating and forming the Southeast Indian Ridge at about 40 Ma (e.g., Frey et al., 2000; Ballmer et al., 2015). Evidence of subaerial environments on the plateau in the Cretaceous, which are now lying at average depths for similarly aged oceanic crust, suggests dynamic uplift of the region in the past (Coffin, 1993). The long-lived plume was active for over 100 Ma and has been suggested to have played a role in the breakup of eastern Gondwana (e.g., Storey et al., 2013; Peng et al., 2022). The prolonged localised igneous activity on a relatively stationary plate suggests that the Kerguelen Hotspot is approximately fixed laterally. Declining volcanic activity in the Quarternary suggests that mantle plume, which was active through the Cretaceous and Cenozoic, is waning.

The Balleny Hotspot underlies the Balleny Islands, a late Cenozoic chain of volcanic islands lying in the Ross Sea, off the coast of North Victoria Land (e.g., Wright & Kyle, 1990; Lanyon et al., 1993) (Fig. 4.10c). Prominent low velocity anomalies underlie the region throughout the upper and lower mantle to ∼1500 km (Figs. 4.2, 4.3 and 4.4). The low velocity anomalies beneath the region are connected to the low velocity channel connecting the Southeast Indian Ridge and the West Antarctic Rift System (Figs. 4.2 and 4.8). Low velocity anomalies beneath the region extend deeper in the mantle in the southwest direction, from the Balleny Islands towards East Antarctica, suggesting that the deep mantle source originates away from the Southeast Indian Ridge (Fig. 4.2 and 4.3). The basalts on the Balleny Islands have been found to contain HIMU signatures (e.g., Lanyon et al., 1993; Berg et al., 1997; Merle et al., 2022), commonly linked to mantle plumes, although alternative suggestions attributed the origin of the HIMU signature to metasomatised lithospheric mantle (e.g., Berg et al., 1997; Merle et al., 2022). The magmatism is also fairly recent, and the age progression of volcanism in the Balleny volcanic province is ∼7 cm/year, similar to the spreading rate of the Southeast Indian Ridge in this region (Berg et al., 1997). The age progression is consistent with a stationary plume being passed over by the Southeast Indian Ridge, although lateral flow of the plume material could also affect the age progression (e.g., Berg et al., 1997; de Laat et al., 2023). The deep seated and continuous low velocity anomaly suggests a deep rooted upwelling from the mantle as the cause of the Balleny Hotspot.

The Bouvet Hotspot is marked by the Bouvet Island, a solitary volcanic island located along the Southwest Indian Ridge, and has been linked to the Karoo-Ferrar Plume, which may have assisted the breakup of Gondwana (Verwoerd et al., 1990; Ballmer et al., 2015) (Figs. 4.1 and 4.10). Low seismic velocities are

present beneath the Bouvet Island in the shallow upper mantle, with amplitudes similar to those at the neighbouring ridges and triple junction (Fig. 4.2). A thermochemical plume originating from the core-mantle beneath South Africa and the African LLSVP has been proposed to be the cause of the hotspot (Ballmer et al., 2015; Kirdyashkin et al., 2023). Low velocity anomalies northeast of the Bouvet Island in the lower mantle and mantle transition zone are consistent with a deep upwelling from the African LLSVP as the source of the hotspot (Figs. 4.3 and 4.4).

The Crozet and Marion-Prince Edward Hotspots are adjacent and located in the Indian Ocean (Figs. 4.1 and 4.10b). Low seismic velocities underlie both hotspots in the shallow upper mantle, the elongated ($\sim$700 km long) low velocity anomaly extends from the hotspots towards the Southwest Indian Ridge with the peak of low seismic velocities observed at about 200 km (Fig. 4.2). The seismic velocity structure in the mantle transition zone is inconsistent across the upper mantle models, with no agreement even on the sign of the anomalies (Fig. 4.3). In the deep lower mantle, the region beneath the hotspots and to the north are underlain by low seismic velocities due to their proximity to the African LLSVP (Fig. 4.4). The Marion and Prince Edward islands are primarily Pleistocene volcanic islands (Verwoerd et al., 1990). The Crozet Islands are located on a submarine plateau that is formed $\sim$54 Ma (Verwoerd et al., 1990). Both the Crozet and Marion-Prince Edward Hotspots have been linked to the Madagascar large igneous province (e.g., Anderson & Schramm, 2005; Ballmer et al., 2015). The origins of the hotspots are unable to be clearly traced, due the inconsistencies across the upper mantle and whole mantle tomography models.

The St. Paul-Amsterdam Islands are underlain by low seismic velocities only in the asthenosphere, with the anomaly amplitudes similar to those beneath the adjacent Southeast Indian Ridge (Fig. 4.1 and 4.10). It has been suggested that the islands are unrelated to a deep mantle upwelling and are a result of upper mantle material recycling within the past $\leq$5 Ma (e.g., Graham et al., 1999; Doucet et al., 2004; Ballmer et al., 2015).

4.6 Conclusions

The AP2024 tomographic model offers new evidence on the origins of intraplate volcanism on the Antarctic Plate. Low seismic velocities indicative of thin lithosphere underlie regions of intraplate volcanic activity, as observed previously in Antarctica and elsewhere around the world. Beneath West Antarctica, low-velocity anomalies at greater depths, consistent with deep-mantle origin of the volcanism, are also resolved by AP2024 and other recent models. Among oceanic

hotspots, the Balleny Hotspot shows a particularly prominent low-velocity anomaly beneath it throughout the upper mantle.

1. Volcanism in the Antarctic Peninsula has been attributed previously to subduction, post-subduction and arc-related processes. The cessation of subduction, in part due to the ridge-crest subduction, is thought to have opened slab windows along the margin, and the detachment of the slab gave rise to post-subduction volcanism along the peninsula. We observe low-velocity anomalies in the shallow asthenosphere beneath the volcanic areas indicative of decompression melting that feeds the volcanism. In mid-upper mantle, we detect high velocity anomalies that show the locations of the detached subducted slab.

2. West Antarctica hosts many volcanic areas and the West Antarctic Rift System. All across it, it is underlain by low seismic velocities indicative of thin lithosphere and, at least in some locations, partial melting in the asthenosphere. The low velocities extend continuously into the deep upper mantle, down to the bottom of the transition zone. Recent whole-mantle tomographic models show that the broad low-velocity anomaly continues further down to over 1000 km depth, below which it is interrupted of high-velocity anomalies. The complex pattern of interconnected high and low velocity anomalies in the lower mantle and the vertically continuous low velocity anomaly in the top 1000 km of the mantle suggest a deep mantle upwelling as the origin of the West Antarctica intraplate magmatism. The complex morphology and deflections in the lower mantle are likely to be due to the interaction of the upwelling with descending subducted slabs.

3. Marie Byrd Land, Thurston Island and Eights Coast in West Antarctica form a major volcanic area and show particularly low seismic velocities in the asthenosphere beneath them. The Erebus Volcanic Province-West Antarctic Rift system-Ross Embayment is the other dominant region of intraplate volcanism and also stands out with particularly low velocities in the asthenosphere. In both locations, the prominent low velocity anomalies are probably due to the partial melting that feeds the volcanism. AP2024 shows that the anomalies beneath the two locations extend down and stand out in the transition zone as well. These observations suggest the presence of two localised, hot, deep-mantle upwellings beneath Marie Byrd Land and the Erebus Volcanic Province.

Chapter 5

The Peculiar Anisotropy of the Antarctic Plate

5.1 Abstract

Azimuthal seismic anisotropy—the dependence of seismic wave velocities on the azimuth of their propagation—is caused primarily by the fabric within the rock at depth. Multi-mode surface wave constrain anisotropy in the lithosphere and asthenosphere and provide essential evidence on the deformation of the lithosphere and flow in the underlying mantle. Here, we use AP2024, a new azimuthally anisotropic S-wave velocity model of the Antarctic-Plate upper mantle, to investigate the evolution of deformation and flow within and beneath the plate. The older oceanic lithosphere surrounding the East Antarctica displays fast-propagation directions oriented E-W, in a surprising circular pattern around the continent. The orientation of the fast-propagation axes is parallel to Antarctica's coasts and appears perpendicular to the paleo-spreading, in contrast with the spreading-parallel orientations in the younger oceanic lithosphere in the Antarctic Plate and elsewhere around the world. We attribute this unusual orientation of anisotropy to the pervasive shear between the Antarctica, Africa, India and Australia in the early stages of the continental breakup and to the slow, oblique spreading in the early stages of Southern Ocean opening. Complex anisotropy within the cratonic East Antarctica indicates layering of deformation in the course of the craton formation. Strong azimuthal anisotropy is detected under the Weddell Sea and Sandwich Plate; we interpret it as a result of pressure-driven flow, generated by the subduction of the Phoenix and South American Plate slabs.

5.2 Introduction

Seismic anisotropy in the upper mantle offers important insights into the structure and evolution of the lithosphere, asthenosphere. Seismic anisotropy describes the directional or polarisation dependence of seismic wave velocity, and is commonly split into azimuthal and radial anisotropies. Azimuthal anisotropy describes the dependence of seismic velocities on the propagation azimuth, whereas radial anisotropy describes the difference of the velocities of seismic waves with the horizontal and vertical polarisations. Measurements of anisotropy span a wide range of length and depth scales, from local measurements obtained from shear wave splitting to regional and global scale anisotropy mapping utilising regional and global surface and body waves. Surface waves are highly suitable for the study of the upper mantle anisotropy due to their frequency- and mode-dependent sensitivity to different depth ranges in the upper mantle.

Anisotropy in the Earth arises, firstly, from the lattice or crystallographic preferred orientation (LPO or CPO, used interchangeably) of elastically anisotropic minerals. Secondly, it can be caused by the shape-preferred orientation (SPO) of at depth structures or aligned cracks near the surface. Anisotropy in the upper mantle, predominantly composed of olivine and pyroxenes, can primarily be attributed to the LPO of olivine. Olivine has high intrinsic anisotropy, and preferentially aligns in the direction of shear or direction of flow (e.g., Nicolas & Christensen, 1987; Karato, 1989; Mainprice, 2007; Karato et al., 2008).

Azimuthal anisotropy in the oceanic lithosphere and asthenosphere record past and ongoing deformation and flow. In the oceanic lithosphere, the alignment of the fast-propagation directions of azimuthal anisotropy (fast axes or fast-propagating axes), is typically parallel to the paleo-spreading direction, because of the preferential alignment of the olivine crystals with the direction of flow and shear away from thr ridge segment are frozen-in as the lithosphere cools (e.g., Nicolas & Christensen, 1987; Karato, 1989; Karato et al., 2008; Mainprice, 2007). Asthenospheric anisotropy is related to the olivine LPO due to recent and present-day deformation in the asthenosphere, and aligns parallel to the direction of the absolute plate motion (APM) in hotspot or seafloor-spreading-aligned reference frames (e.g., Becker et al., 2003; Debayle et al., 2005; Yuan & Romanowicz, 2010; Debayle & Ricard, 2013; Becker et al., 2014, 2015; Beghein et al., 2014; Schaeffer et al., 2016).

The Antarctic Plate has a uniquely configuration, encircled almost entirely by spreading ridges (Fig. 5.1). The Antarctic continent in the central part of the plate is surrounded by oceanic lithosphere of varying ages, ranging from old lithosphere along the Weddell Rift in the Weddell Sea (∼183 Ma) close to Antarctica

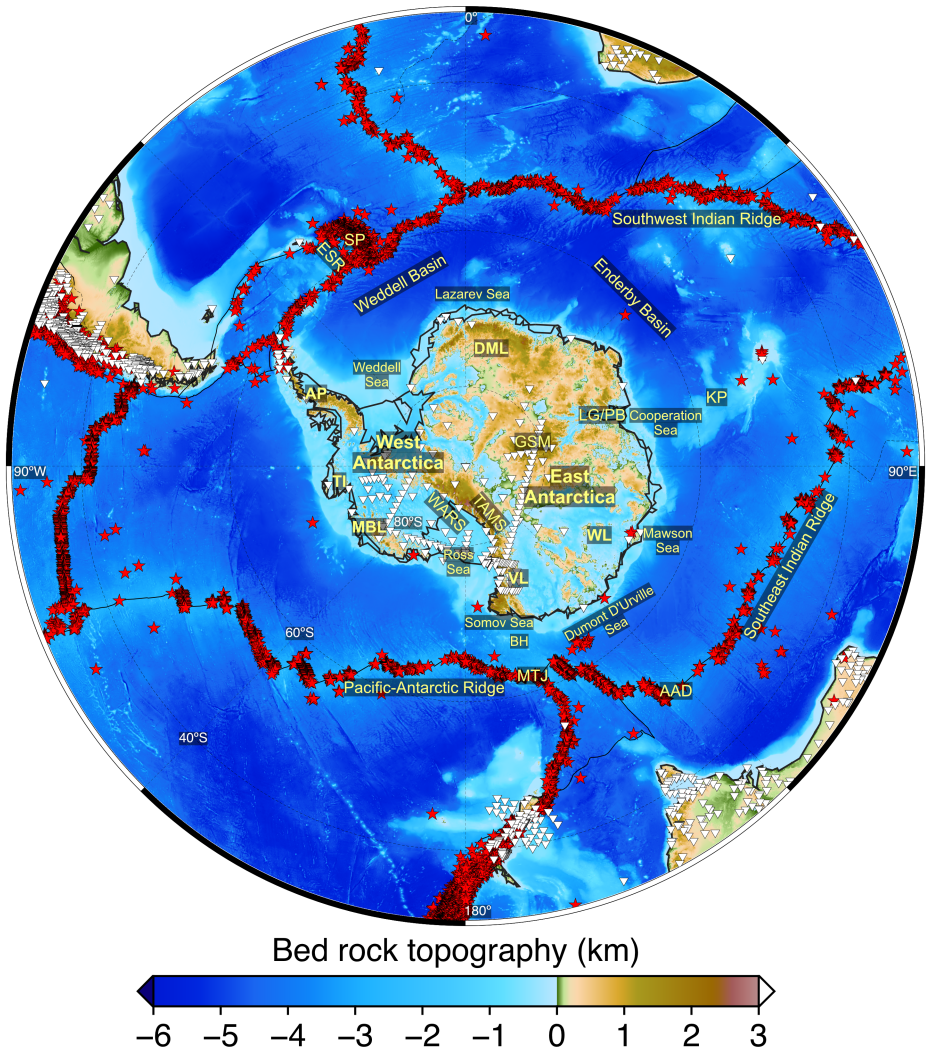


Figure 5.1: Bed rock topography and bathymetry from the NOAA National Centers for Environmental Information (2022) dataset. Broadband seismic stations and events used to compute the AP2024 model are plotted as inverted white triangles and red stars, respectively. Abbreviations: AAD — Australian-Antarctic Discordance, AP — Antarctic Peninsula, BH — Balleny Hotspot, DML — Dronning Maud Land, ESR — East Scotia Ridge, GSM — Gamburtsev Subglacial Mountains, KP — Kerguelen Plateau, LG/PB — Lambert Graben and Pyrdz Bay, MTJ — Macquarie Triple Junction, MBL — Marie Byrd Land, SP — Sandwich Plate, TAMS — Transantarctic Mountains, TI — Thurston Island, VL — Victoria Land, WARS — West Antarctic Rift System, WL — Wilkes Land.

(Svensen et al., 2012; Burgess et al., 2015; Riley et al., 2020b) to the young oceanic lithosphere along the the currently spreading ridges at the plate's periphery (Fig. 5.2).

Anisotropy of the Antarctic lithosphere and asthenosphere has been poorly constrained due to the lack of data sampling. Recently, a number of anisotropy studies used newly available data to map anisotropy on the Antarctic continent (Fig. 5.1), including studies of radial anisotropy beneath the continent (O'Donnell

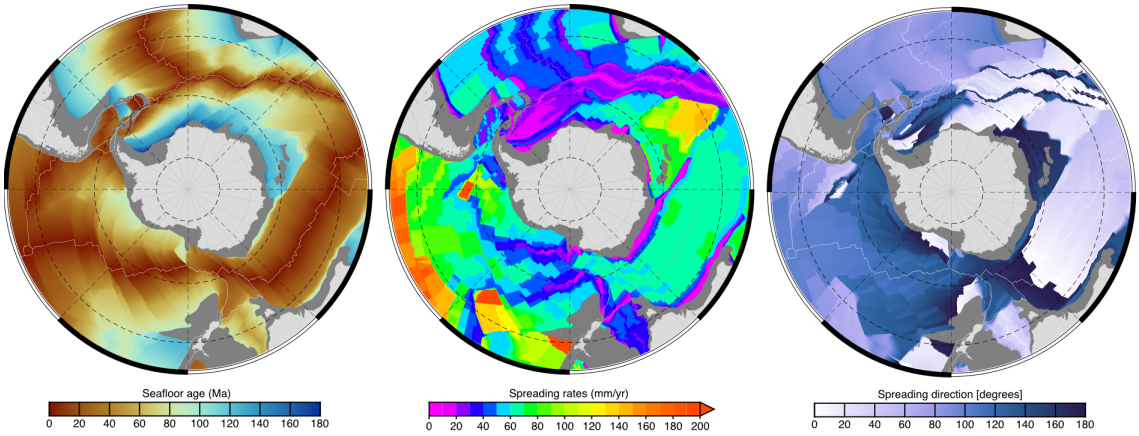


Figure 5.2: Left: Age of the oceanic crust of the Antarctic Plate. Middle: Sea floor spreading rates. Right: Paleo-spreading direction with respect to the north. The data used in the plots were taken from Seton et al. (2020), who derived it from a combination of magnetic anomalies and other geophysical data.

et al., 2019b; Cheng et al., 2021; Zhou et al., 2022). Studies of azimuthal anisotropy have been largely limited to those of shear wave splitting (Reading & Heintz, 2008; Barklage et al., 2009; Accardo et al., 2014; Lucas et al., 2022). Most recently, Zhou et al. (2024) used ambient noise surface-wave measurements and reported azimuthal anisotropy varied with depth from the upper-middle crust to the uppermost mantle.

There is a gap in the current understanding of the anisotropic structure of the Antarctic Plate because the current models and measurements either do not span the lithosphere-asthenosphere depth range or do not have vertical resolution within it. In this study, we fill this gap and present AP2024, an azimuthally anisotropic shear-wave velocity tomographic model of the Antarctic Plate upper mantle, spanning the depth range from the crust down to the mantle transition zone. With the improved sampling and vertical resolution provided by AP2024, we identify and discuss the peculiar anisotropy of the Antarctic Plate.

5.3 Anisotropic waveform tomography

AP2024 is an azimuthally anisotropic Sv velocity model of the Antarctic Plate upper mantle. The model was computed using all openly available broad-band seismograms with either the station, or the event, or both located within the Southern Hemisphere. This maximised the data sampling of the model region (Fig. 5.1) and ensured that the sampling in the Northern Hemisphere was reduced gradually towards the North Pole an was sufficient to prevent erroneous mapping of structures between the hemispheres or any boundary effects (Celli et al., 2020b; de Laat et al., 2023). In other words, AP2024 was built as a global model with a

focus on the Southern Hemisphere.

The model was computed using Automated Multimode Inversion (AMI), which first extracted structural information from surface, S- and multiple S-waves with non-linear waveform inversion (Lebedev & Nolet, 2003; Lebedev et al., 2005; Lebedev & van der Hilst, 2008). The linear equations produced by AMI were then solved, using LSQR, for the 3-D distributions of P and S velocity perturbations with respect to a 3-D reference model and for the π-periodic ("2Ψ")) S-wave azimuthal anisotropy (Lebedev & van der Hilst, 2008). The reference model was a 1-D global-average mantle profile computed from a 3-D tomography model (Lebedev & van der Hilst, 2008) combined with a 3-D crustal model modified from CRUST2.0 (Bassin, 2000) by smoothing at the cell boundaries and applying a 1-D correction that brought its average close to the global average (Lebedev & van der Hilst, 2008). A posteriori outlier analysis was used to remove the least mutually consistent data, affected by the largest errors. A further manual error-control process targeted the causes of probable errors and artefacts in preliminary modeld and completed the selection of the dataset, used for the final tomographic inversion.

5.3.1 Anisotropy parameterisation

Azimuthal anisotropy of surface waves in a smooth, weakly anisotropic medium can be expressed as a series of small π-periodic and $\pi/2$-periodic terms, which describe perturbations from the isotropic-average velocity (Smith & Dahlen, 1973):

$$\begin{aligned} C(\omega,\Psi,\theta,\phi) = & A_0(\omega,\theta,\phi) \\ & + A_1(\omega,\theta,\phi)cos2\Psi + A_2(\omega,\theta,\phi)sin2\Psi \\ & + A_3(\omega,\theta,\phi)cos4\Psi + A_4(\omega,\theta,\phi)cos4\Psi \quad , \end{aligned} \tag{5.1}$$

where $C(\omega,\Psi,\theta,\phi)$ is the phase velocity at the azimuth Ψ, $A_0(\omega,\theta,\phi)$ is the isotropic-average phase speed, A_1 and A_2 are the coefficients for the π-periodic azimuthal variations, A_3 and A_4 are the coefficients for the $\pi/2$-periodic azimuthal variations, ω is the angular frequency, θ is the longitude and ϕ is the latitude. Love and Rayleigh anisotropy of the upper mantle has been mapped using this approach in a number of studies (e.g., Montagner & Tanimoto, 1991; Trampert & Woodhouse, 2003; Ekström, 2011; Adam & Lebedev, 2012). In the olivine and pyroxene rich upper mantle, nearly all of the directional variations in Sv seismic velocities can probably be described by the 2Ψ terms Smith & Dahlen (1973); Montagner & Nataf (1986), although small non-zero 4Ψ terms have also been reported (Trampert & Woodhouse, 2003). We thus simplify eq. 5.1 by only

retaining the A0, A1 and A2 terms. The studies show that in vertically polarised shear-wave velocity models constrained by Rayleigh waves, such as AP2024, the A_1 and A_2 terms describing π-periodic ('2Ψ') anisotropy are dominant, while Love waves are sensitive to $\pi/2$-periodic ('4Ψ') anisotropy described by the A_3 and A_4 terms. We thus simplify eq. 5.1 by only retaining the A_0, A_1 and A_2 terms.

The A_1 and A_2 parameter pairs are projected onto a geographical coordinate system as vectors, with the *cosine* and *sine* terms representing the N-S and E-W components of azimuthal anisotropy respectively (Lebedev & van der Hilst, 2008). This results in a linear inverse problem, which we can then solve for the spatial distribution of the parameters $A_i(r, \theta, \phi)$. We parameterise the model on a set of triangular grid knots (Wang & Dahlen, 1995a), with an inter-knot spacing of approximately 125 km. A lateral smoothing operator is applied to the anisotropic terms A_1 and A_2, as well as to the isotropic Vs varriations. Radial gradient damping and slight norm damping are also applied, in order to stablise the inversion. The regularisation parameters were specifically tuned to more accurately resolve the seismic structure and anisotropy in the model region.

5.3.2 Upper mantle anisotropy of the Antarctic Plate

We observe the amplitude of anisotropy to generally decrease with increasing depth, from up to ∼3.5% in the top 100 km to up to ∼1% in the mantle transition zone. At 100–200 km depths, the cratonic lithosphere beneath Eat Antarctica shows smaller anisotropy than the asthenosphere beneath the tectonic Wset Antarctica and oceanic basins. At 36–110 km depths, large anisotropy amplitudes are observed beneath the spreading ridges encircling the Antarctic Plate and beneath older oceanic regions including the Weddell, Lazarev, Dumont D'Urville and Somov Sea basins close to the East Antarctica coast. The fast-propagation directions beneath the ridges are parallel to the spreading directions. Under older oceanic lithosphere, the highest amplitudes of anisotropy are generally found at greater depths.

In contrast to the generally north-south, spreading-parallel anisotropy at the currently active ridges, the older oceanic lithosphere closer to Antarctica shows a circular pattern of E-W anisotropy orientations, nearly perpendicular to the current spreading directions. Notable exceptions are the Dumont D'Urville and Somov Seas, offshore East Antarctica at 120–170E, where strong N-S oriented azimuthal anisotropy is observed at both the lithospheric and asthenospheric depths (Fig. 5.3). This high amplitude, N-S anisotropy feature extends north to beneath the Australian-Antarctic-Discordance (AAD) between the two continents. At 150-200 km beneath the Southeast Indian Ridge (SEIR), east of the AAD

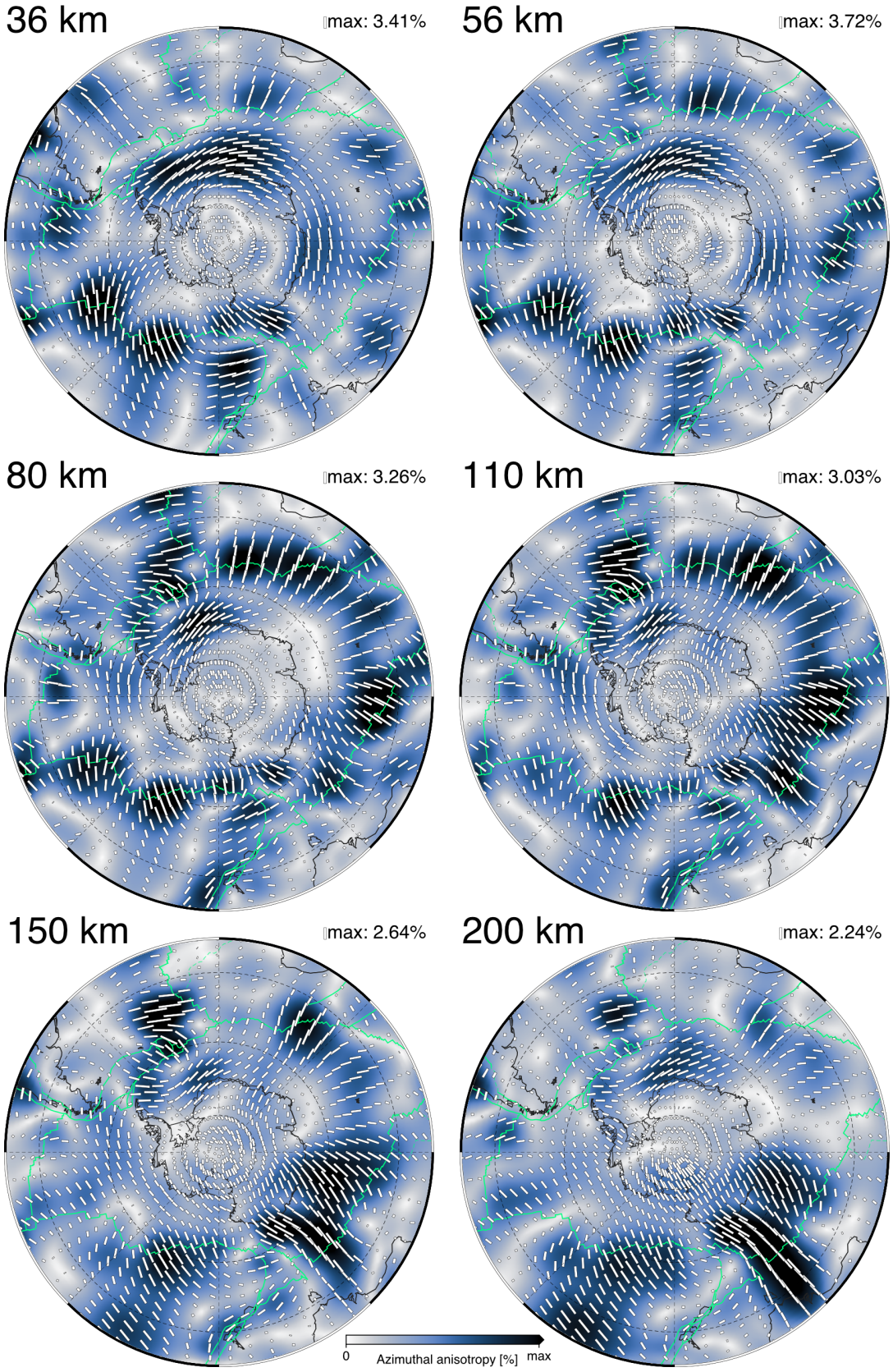


Figure 5.3: Azimuthal anisotropy of the Antarctic Plate and underlying mantle down to 200 km according to AP2024. The colour scale shows the amplitude of anisotropy. The orientations of the white sticks indicate the fast-propagation directions, and their lengths are proportional to the amplitude of anisotropy. The maximum azimuthal anisotropy at each depth is indicated at the top right corner of each panel.

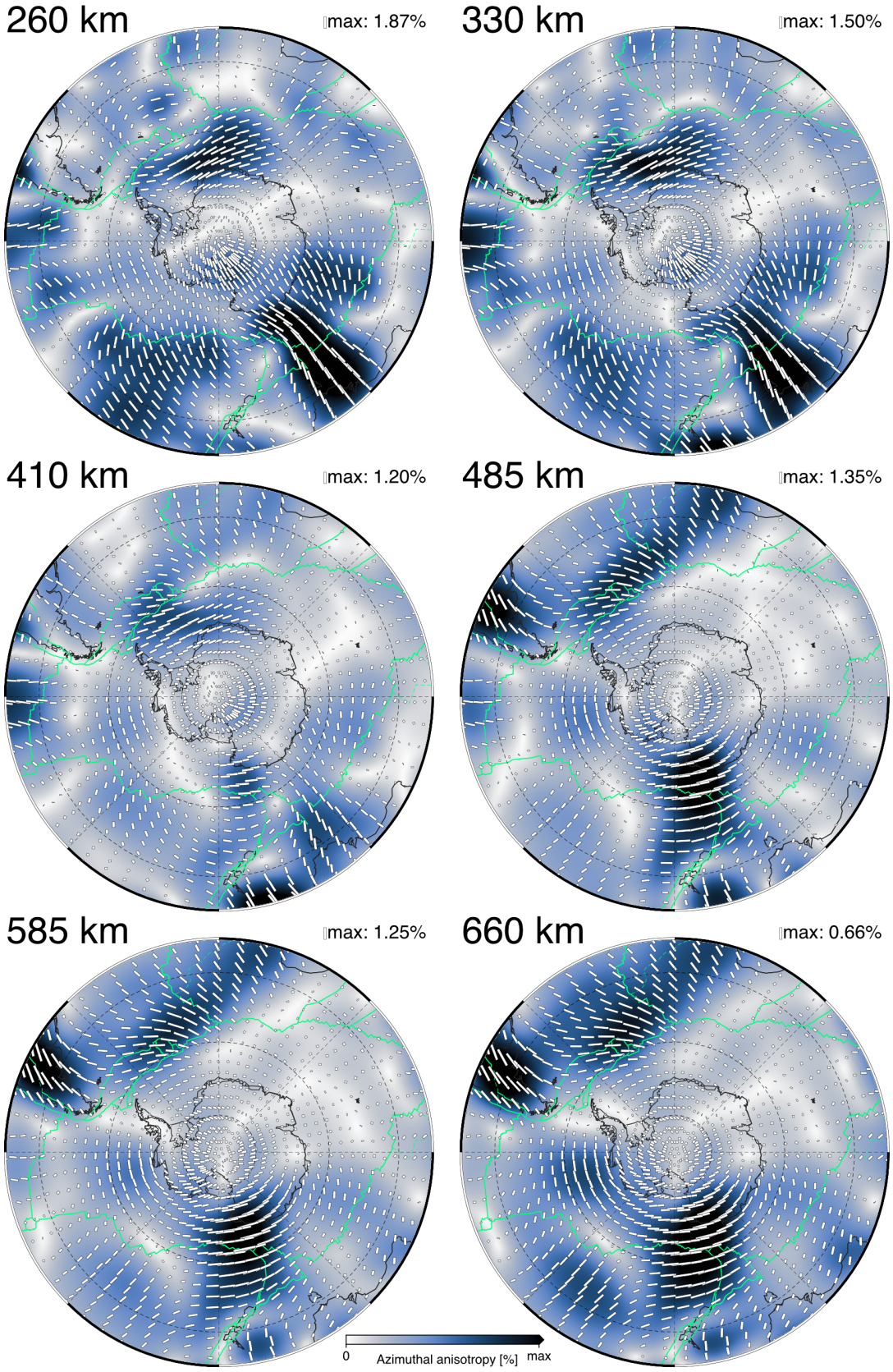


Figure 5.4: Azimuthal anisotropy below the Antarctic Plate in the mid upper mantle and mantle transition zone. The colour scale shows the amplitude of anisotropy. The orientations of the white sticks indicate the fast-propagation directions, and their lengths are proportional to the amplitude of anisotropy. The maximum azimuthal anisotropy at each depth is indicated at the top right corner of each panel.

and close to the Macquaire Triple Junction and the Balleny Hotspot, we observe anisotropy oriented roughly parallel to the ridge.

5.3.3 Resolution testing

In order to assess the robustness of the anisotropy and fast axis orientations in the AP2024 model, shown in Figs. 5.3 and 5.4, we test the model using a synthetic 90°rotation test (e.g., Zhang et al., 2009; Endrun et al., 2011; Schaeffer et al., 2016). The input model of the test is comprises the original isotropic component of AP2024 and anisotropy modified from AP2024 such that the fast axis orientation of the anisotropy is rotated by 90°at every point. This test is effective because it detects where the anisotropy patterns may be affected by the leakage from the isotropic component into the anisotropic component of the model. If the nominal resolution of tomography is too high and cannot be achieved with the data sampling available, then the fast orientation directions mapped are likely to be dictated by the isotropic structure and how it is sampled by the source-station paths in the dataset (e.g., Darbyshire & Lebedev, 2009). In this case, the resolution test with the actual isotropic structure and 90°-rotated anisotropy will show the anisotropy rotating back to the false directions, dictated by the isotropic structure. If, instead, the data sampling is sufficient to map anisotropy with the resolution of the tomographic model, then the rotated anisotropy will be resolved as in the input, at 90°from that in the actual model. The output of our test inversion was, thus, evaluated by comparing the fast-propagation directions in the input and output of the test and in the AP2024 model.

The results of this test are shown in Fig. 5.5, for four depths within the lithosphere and asthenosphere. The input model is shown in the left column, the output of the test in the middle column and AP2024 is shown on the right. The anisotropy sticks in the test-output column of Fig. 5.5 are colour-coded according to the deviation of the direction of anisotropy with respect to the input model. Blue sticks indicate locations where the fast axis orientations are resolved with reasonable accuracy (<25°angular difference with the input model), orange sticks indicate locations where the angular difference is between 25°and 45°and red sticks show locations where the model and data coverage is not able to robustly recover anisotropy and where the angular difference is greater than 45°and, thus, where the model cannot be guaranteed to recover anisotropy, and where anisotropy in AP2024 may or may not be accurate. We note that anisotropy at the red-stick locations is not necessarily wrong in the model, but that the orientation of the fast-propagation azimuth will always be biased toward the same orientation regardless of the actual orientation of anisotropy in the Earth.

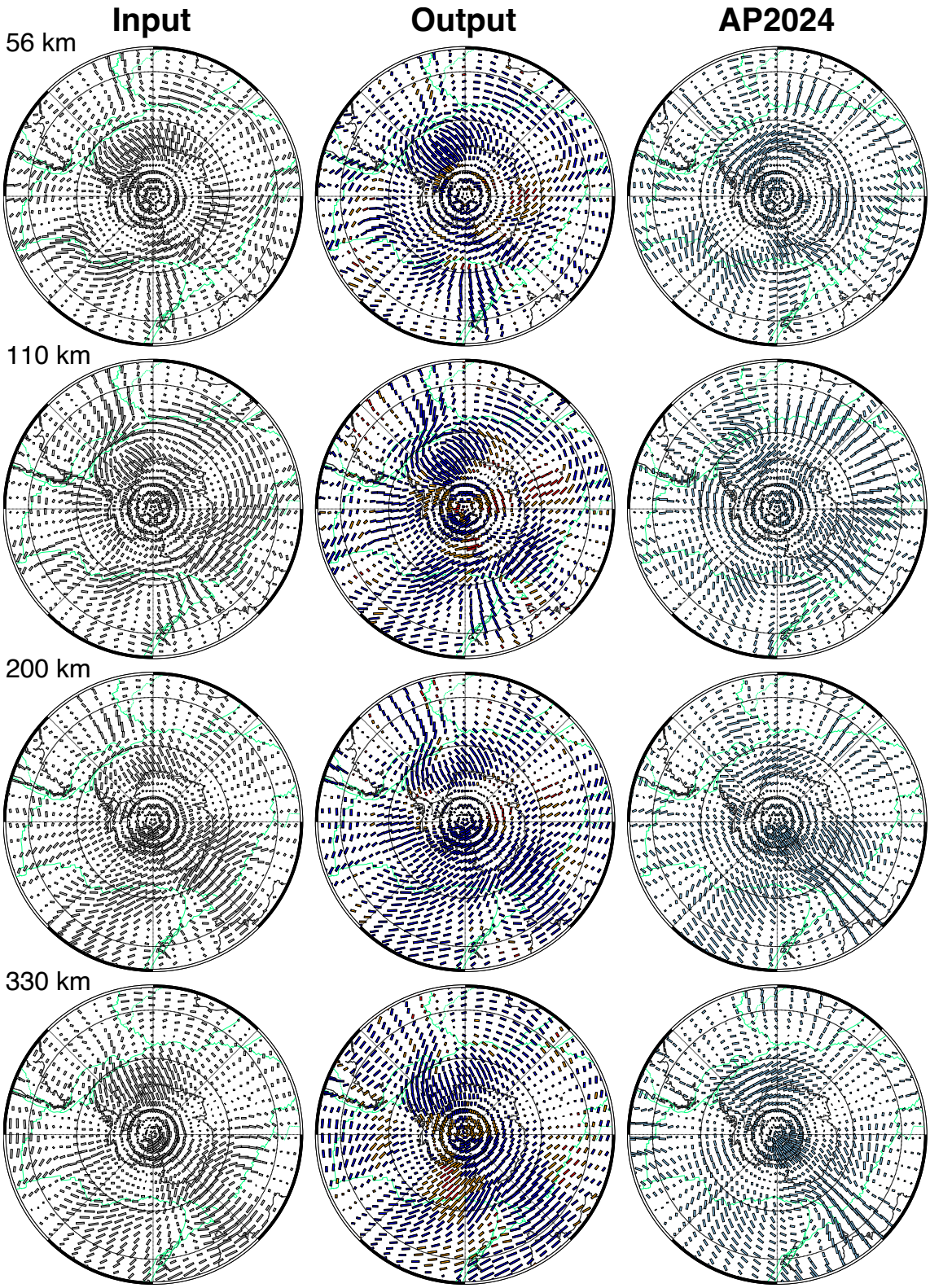


Figure 5.5: Anisotropy resolution test of the AP2024 model. Left: The input pattern of the anisotropy test. The azimuthal anisotropy of the AP2024 model was rotated 90 degrees to obtain the input model, with the isotropic heterogeneity (not shown) exactly as in AP2024. Middle: Output of the anisotropy test. The sticks are colour-coded to indicate the deviation of the fast axis orientation from that in the input model. Blue: fast axes of the input and output deviate by less than 25°, orange: fast axes deviate by between 25°and 45°, red: orientation of the fast axes deviate by greater than 45°. Right: Anisotropy of the Antarctic plate according to AP2024.

Anisotropy is reliably recovered across most depths and locations, with several exceptions. The model is most poorly sampled in the Cooperation Sea and the southern Indian Ocean, and aniostropy in this region is relatively poorly resolved at asthenospheric depths compared to the other oceanic regions. Anisotropy in parts of the cratonic core of East Antarctica is also poorly resolved, despite the nominally good coverage in the region. Anisotropy is best resolved in the shallow upper mantle, down to 200 km, with the resolution decreasing with the increasing depth further down.

5.4 Discussion

5.4.1 The unique anisotropy of the Antarctic Plate

The most surprising feature of anisotropy of the Antarctic Plate is the circular pattern of E-W orient anisotropy around East Antarctica (Fig. 5.3, 36–80 km). The amplitude of this anisotropy is not small and is similar to that beneath active spreading ridges. The E-W orientation of fast azimuths beneath near-coastal regions of the Southern Oceans around East Antarctica are almost ridge-parallel, contrary to the global trend of paleo-spreading-parallel fast azimuths of anisotropy observed nearly everywhere in oceanic lithosphere (e.g., Becker et al., 2014; Schaeffer et al., 2016). Anisotropy in the younger oceanic lithosphere near the periphery of the Antarctic Plate is different from that in the inner parts and does, indeed, display spreading-parallel, ridge-perpendicular fast-propagation directions (Fig. 5.3).

Reconstructions of the Antarctic and neighbouring plates by Müller et al. (2022) reveal extended periods of rift-parallel and, then, ridge-parallel shear between the East Antarctica and its conjugates, just prior to and through the early stages of rifting (Fig. 5.6). Brune et al. (2018) pointed out the prevalence of oblique rifts since the Mesozoic, including the India-Australo-Antarctica and Australia-Antarctica rifts and, in particular, the oblique Africa-Antarctic rift. Rifting at what is now the boundaries of East Antarctica began in the Jurassic, and proceeded in a primarily eastward direction. This resulted in the old oceanic lithosphere getting younger clockwise (eastward) around East Antarctica (Reeves & De Wit, 2000; Boger, 2011; Williams et al., 2019; Jokat et al., 2021) (Fig. 5.2). The anisotropy observed in the older oceanic regions in the eastern Antarctic Plate deviates from the global observations of ridge-perpendicular fast-propagation directions (with respect to present-day spreading ridges), and is most prominent in the 3 ridges segements outlined below.

The 90–180 Ma section of seafloor between 55°W to 25°E recorded very low

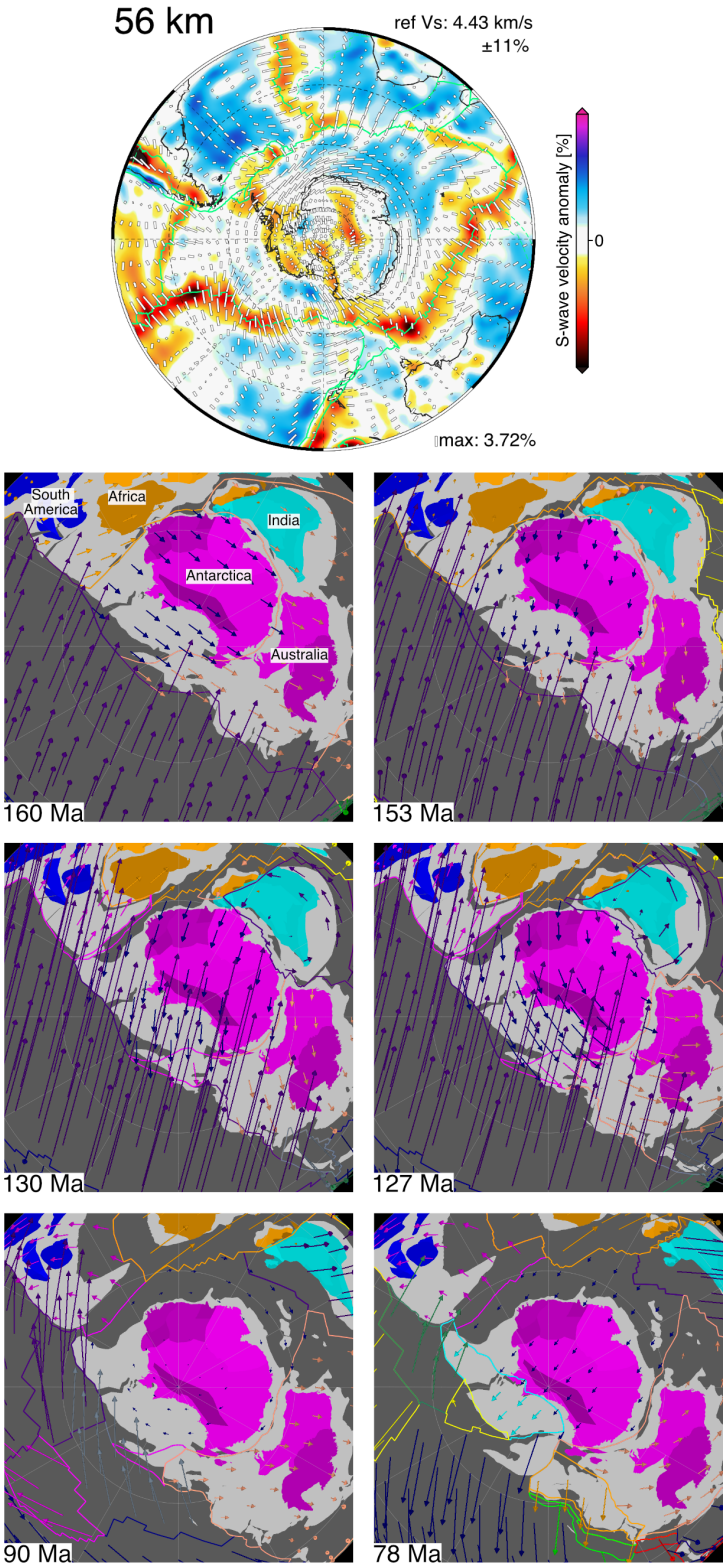


Figure 5.6: Top: Azimuthal anisotropy at oceanic-lithospheric depths plot over the isotropic structure of AP2024 at 56 km. Bottom panels: Paleo-plate reconstructions of the Antarctic and surrounding plates at several time windows showing the plate configurations and velocity vectors of the plates at each time window. The reconstructions were plot in GPlates (Müller et al., 2018) using the SEEM1000 by Müller et al. (2022).

spreading rates, ranging between 0–40 mm/yr, with oblique spreading directions prevalent across the segment (Fig. 5.2). The spreading directions also deviated from N-S. In the Larazrev Sea (between 5°E to 30°E), in particular, the spreading direction was nearly E-W (Fig. 5.2) (e.g., Seton et al., 2020; Müller et al., 2022). Africa-East Antarctic rifting was initiated at the Weddell Sea rift at approximately 180 Ma at relatively low spreading rates (e.g., Svensen et al., 2012; Burgess et al., 2015; Riley et al., 2020b). The eastward propagating rift connected with the extensional margin between present-day Somalia and Madagascar, eventually resulting in the present-day Southwest Indian Ridge (e.g., Phethean et al., 2016; Rao & Radhakrishna, 2021; Roche & Ringenbach, 2022). The relative motions of the plates at the early stages of the break-up showed a complex pattern, with a substantial amount of transtension.

The 80–120 Ma section of the seafloor in the Enderby Basin (between 30°E to 110°E) recorded relatively faster spreading rates of up to 90 mm/yr, which are nonetheless very slow compared to global spreading rates (Fig. 5.2). Sections of the seafloor similar record spreading directions that deviate from N-S, in addition to oblique spreading directions recorded along most of the segment Fig. 5.2). Rifting between the East Antarctica and East India was initiated at approximately 136 Ma in the eastern Enderby Basin before propagating westward, with similar relatively low spreading rates (e.g., Gibbons et al., 2013; Davis et al., 2019; Rao & Radhakrishna, 2021; Jokat et al., 2021). The rifting between India and Australo-Antarctica was accompanied by shear along the margin (Brune et al., 2018). The progression of the early India-Antarctica rifting was also complex, with multiple rifting phases, rift jumps (e.g., Gaina et al., 2007) and multiple spreading ridges initiated at different times (Jokat et al., 2021).

The final section of seafloor lies between 110°E and 140°E, and is the youngest aged at between 40–90 Ma (Fig. 5.2). Initial spreading rates were very low, below 20 mm/yr with prevalent oblique spreading, that gradually increased to about 70 mm/yr as spreading directions transitioned to be predominantly N-S (Fig. 5.2 (middle and right)). Initial Antarctic-Australian rifting began in the Late Jurassic (Powell et al., 1988; Ball et al., 2013), and the continental breakup started at about 83 Ma in the Late Cretaceous, with estimated spreading rates of below 10 mm/yr for the first 10–15 Ma (e.g., Royer & Rollet, 1997; Whittaker et al., 2013; Jacob et al., 2014; Jacob & Dyment, 2014; Williams et al., 2019).

The initial stages of rifting between East Antarctica and the surrounding continents saw oblique, ultra-slow spreading with rates below 10 mm/yr, with the relatively slow spreading rates persisting until today along the Antarctic-African margin (Fig. 5.2). Becker et al. (2014) showed that pattern of spreading-parallel anisotropy is most clearly dominant at high spreading rates (>50 mm/yr), By

contrast, mantle deformation at slow-spreading ridges is often more complex. For example, Russell & Gaherty (2021) reported rift-parallel azimuthal anisotropy along the Eastern North American margin where the spreading rates were low ($\leq$20 mm/yr) and proposed that the rift-parallel azimuthal anisotropy in the regions of ultra-slow spreading is a record of the direction of past APM rather than paleo-spreading direction along the ultra-slow spreading ridge.

We propose that the E-W oriented fast-propagation axis of anisotropy, predominantly ridge-parallel in orientation, originates from the frozen-in structure that records the lateral shear and transtension between the Antarctic and adjacent plates. The shear and transtension occurred in the course of the continental breakup and in the early stages of seafloor spreading (Fig. 5.6).

In itself, the frozen-in pattern of the ridge-parallel anisotropy is not unique to the Antarctic Plate. Importantly, E-W oriented fast-propagation azimuths were detected in the oceanic lithosphere near the conjugate, southern margin of Australia (de Laat et al., 2023). This confirms our inference on the character of the Cretaceous deformation between Antarctica and Australia, made on the basis of anisotropy offshore Antarctica. Elsewhere, the observations of Russell & Gaherty (2021) offshore eastern North America provides further evidence on the occurrence of ridge-parallel fabric formed during slow early stages of ocean-basin opening.

What makes the Antarctic Plate unique is that the transtension and, then, slow, oblique spreading occurred along most of the coastlines of the continent in the course of the break-up of Gondwana. This deformation pattern has created the spectacular circular pattern of anisotropy fast directions that now envelopes East Antarctica along its perimeter.

5.4.2 Comparison with shear wave splitting and other observations

Can we combine and reconcile our observations of anisotropy with shear-wave splitting measurements, which offer another useful line of evidence? The splitting measurements are typically obtained from teleseismic SKS waves and provide direct observations within the Fresnel zones of the waves (e.g., Becker et al., 2012). As the Fresnel zones in the upper mantle are relatively narrow ($\sim$100 km), the splitting measurements have high lateral resolution, compared to the continent-scale, surface-wave tomography resolution of a few hundred kilome tres (e.g., Celli et al., 2020b). Waveform tomography, by contrast, yields greater vertical resolution, as it benefits from the depth-sensitivity of surface wave dispersion, whereas SKS waves integrate anisotropy along nearly-vertical paths from

the CMB to the surface. Direct comparisons of anisotropy distributions from waveform tomography and shear-wave splitting have shown agreement once the splitting measurements were smoothed laterally to the scales of tomographic models (Becker et al., 2012).

Shear-wave splitting shows substantial variability across Antarctica (Fig. 5.7). At the same time, it displays a prevalence of fast propagation directions in the 15–45E azimuth range. Azimuths in this range are not parallel to the plate motion direction in any standard reference frame (Fig. 5.7; Becker et al. (2015) and references therein). This is in contrast to the observations in the stable eastern North America, for example, where a similarly large-scale pattern of consistent SKS splitting aligns with the plate motion (e.g., Becker et al., 2012). Such alignment suggests that the splitting reflects predominantly the shear and the resulting olivine crystal alignment in the asthenosphere below the moving plate. Similarly, waveform tomography shows a dominant pattern of plate-motion-parallel fast directions in the asthenosphere beneath a large majority of oceanic areas (Becker et al., 2014; Schaeffer et al., 2016).

Regardless of the reference frame, Antarctica moves very slowly, which can probably explain why the current plate motion may not create sufficient strain in the asthenosphere to generate observable LPO. The 15–45E fast azimuth may, instead, be due to the motion of the Antarctic Plate in the past. In the Cretaceous, the plate moved at azimuths within this window during at least two periods of time, including an extended period between 78–69 Ma (Müller et al., 2022) (Fig. 5.6). More recently, between 10–19 Ma, the lower half of the Antarctic Plate on the maps (Fig. 5.8)—that is the region lying west of 90W and east of 90E, spanning between Thurston Island and Wilkes Land and extending into the oceans—has moved at azimuths within the window (Fig. 5.8). If the shear in the asthenosphere due to past plate motions has created strong mineral alignment, and if the asthenosphere has deformed little since that time, then the ancient fabric could survive in the asthenosphere to this day.

Alternatively, the prevalence of the 15–45E fast azimuth in SKS splitting measurements may reflect the pressure-driven flow of asthenosphere at present and in the recent past. Presently, most of East Antarctica is moving within this azimuth window, albeit extremely slowly. The isotropic component of AP2024 and other tomographic models provide strong evidence for upwelling of hot material from the deep mantle beneath West Antarctica. This upwelling is likely to be a major driver of pressure-driven flow in the asthenosphere.

We also note that these interpretations of past plate motions were made based on the optimised reference frame of Müller et al. (2022), and that the direction of motion may change significantly depending on the chosen reference frame. How-

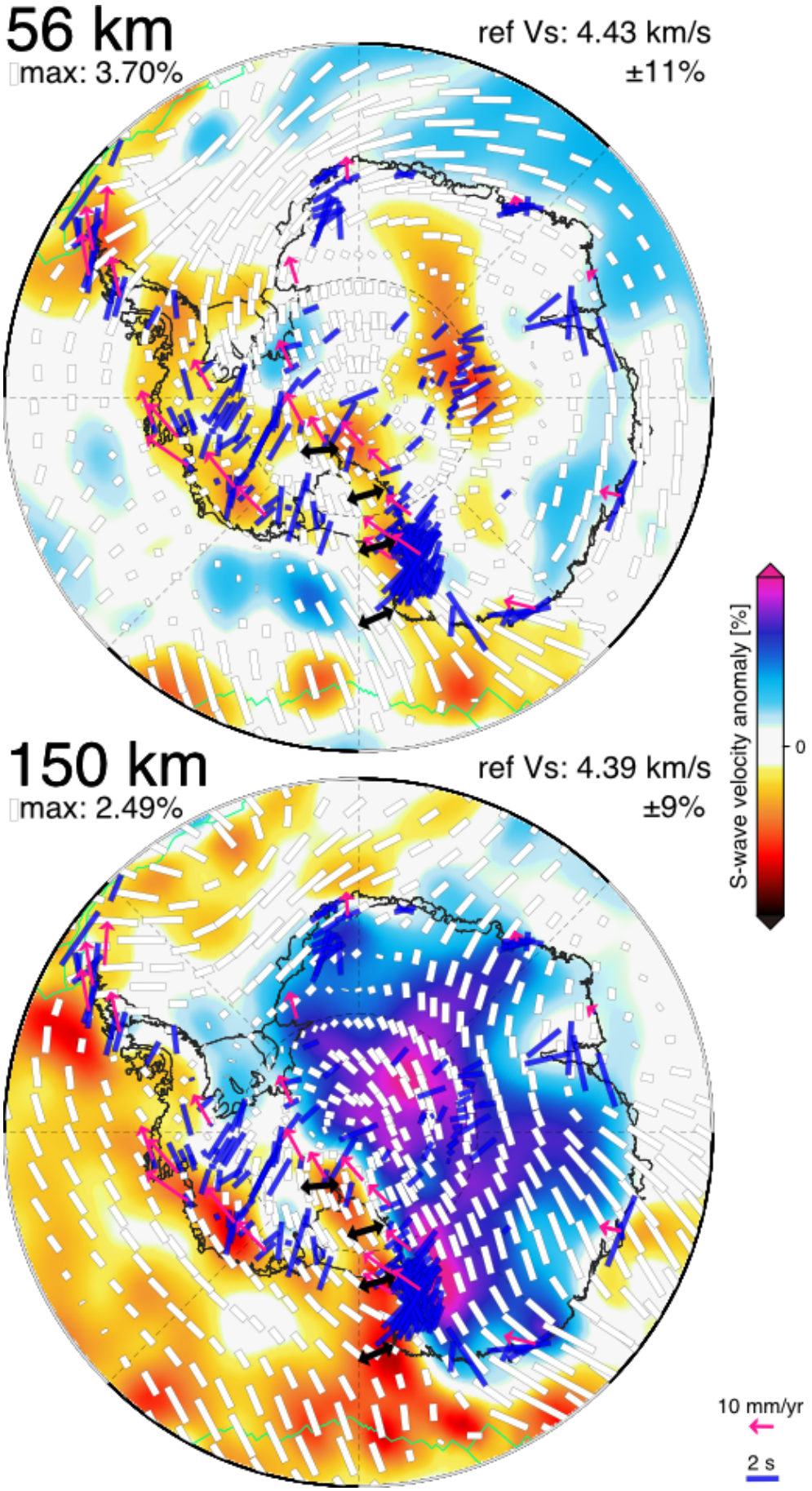


Figure 5.7: Anisotropy, structure and deformation of Antarctica.

Figure 5.7: *continued from previous page*
The fast-propagation directions of azimuthal anisotropy at 56 and 150 km depths according to AP2024 (white sticks) are plotted on the background of the isotropic velocity structure at the same depths. Shear wave splitting measurements (Lucas et al., 2022) are plotted as blue sticks. APM velocity vectors (Savchyn et al., 2023) in the ITRF2014/IGS14 reference frame (Altamimi et al., 2017) are plotted as pink arrows at the locations of selected GNSS stations. The direction of extension in the West Antarctic Rift System in the Ross Sea region is indicated by the black arrows. It was adapted from Müller et al. (2007) and showed agreement with other models for the Ross Sea region (e.g., Cande et al., 2000; Davey et al., 2006, 2016).

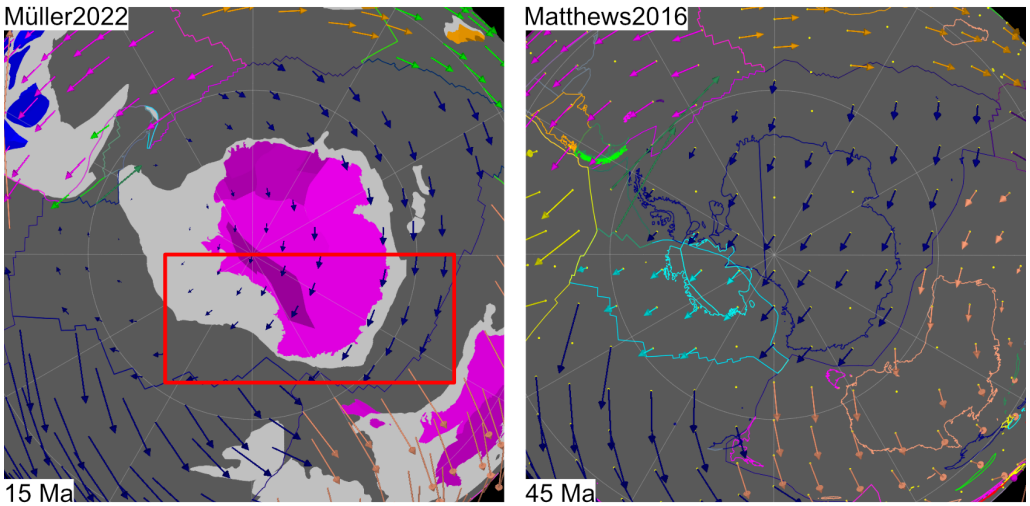


Figure 5.8: Paleo-APM velocity vectors of Müller et al. (2022) and Matthews et al. (2016) at different time intervals, where the paleo-APM of the Antarctic Plate (or sesctions of it) lie within the 15–45E window. Left: The Müller et al. (2022) at 15 Ma. Right: The Matthews et al. (2016) model at 45 Ma. Note that the velocity vectors are not scaled to the same values for both plots.

ever, if our interpretations hold true, and that the strong asthensopheric shear in the past or present pressure driven flow in the asthenosphere, there will be a mantle reference frame where the motion of the Antarctic Plate falls within the 15–45E window. An instance of an extended period, between 47–39 Ma, where the Antarctic Plate is moving in a direction within the 15–45E window can be found in the Matthews et al. (2016) model (Fig. 5.8). This applies, even more, to the very slow current and recent plate motion. It is very likely that there is a plate-motion reference frame that has the recent motion of the Antarctic Plate falls within the 15–45E window and that fits the other data chosen to constrain it, for example, fixed hotspot or ridge-perpendicular oceanic plate motions.

Anisotropy mapped by our waveform tomography at 150 km depth shows fast-propagation directions close to those from SKS splitting in most locations in West Antarctica. Most differences can be accounted for by the SKS splitting

integrating the anisotropy in the asthenosphere with that in the lithosphere (Fig. 5.3, 36 and 56 km depths).

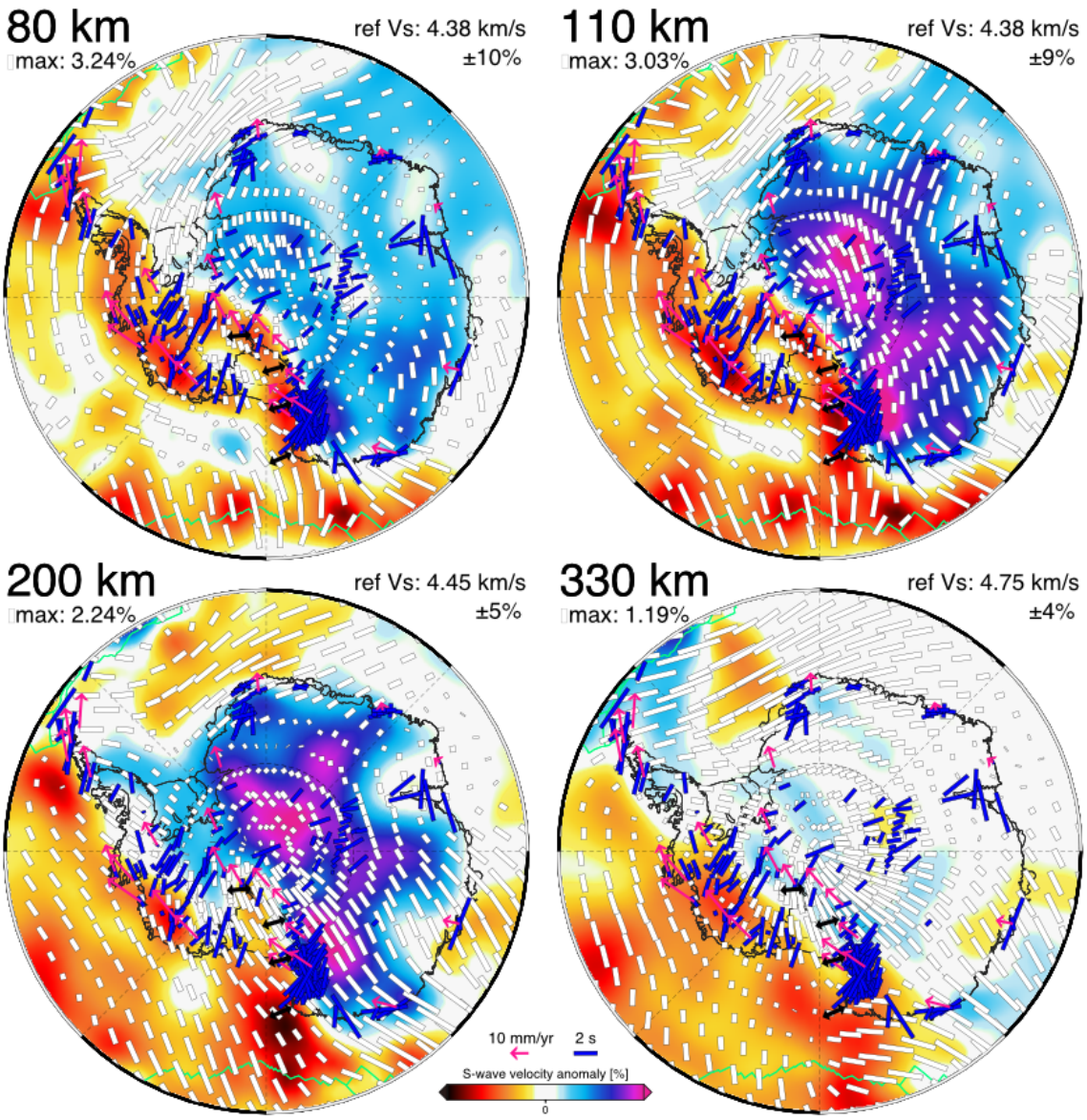


Figure 5.9: The fast-propagation directions of azimuthal anisotropy at four depths according to AP2024 (white sticks) are plotted on the background of the isotropic velocity structure at the same depths. Shear wave splitting measurements (Lucas et al., 2022) are plotted as blue sticks. APM velocity vectors (Savchyn et al., 2023) in the ITRF2014/IGS14 reference frame (Altamimi et al., 2017) are plotted as pink arrows at the locations of selected GNSS stations. The direction of extension in the West Antarctic Rift System in the Ross Sea region is indicated by the black arrows. It was adapted from Müller et al. (2007) and showed agreement with other models for the Ross Sea region (e.g., Cande et al., 2000; Davey et al., 2006, 2016).

We observe E-W oriented fast directions from SKS splitting along most of the coast of Antarctica, clockwise from 90W to 150E (Dronning Maud Land, Pyrdz Bay, the Lambert Graben and Wilkes Land) (Fig. 5.7). This matches the circular

pattern of the E-W orientation of anisotropy seen in AP2024 in the lithosphere (56 km) at the locations. In the Lambert Graben in the east and in the 0–90W segment in the west, the orientation of anisotropy is the same in the asthenosphere as well. Reading & Heintz (2008) proposed that the E-W alignment of splitting orientations in the Lambert Graben/Pyrdz Bay region is related to remnant structures of rifting. Another possibility is that the orientation of the SKS splitting fast-propagation directions parallel to the rift inland—and perpendicular to the rift, and parallel to the coast near the coast—reflects rift-related deformation inland and transpression associated with the continental breakup near the coast.

Near the western coast of the Ross Sea, along the southern margin of the WARS adjacent to the Transantarctic Mountains, Victoria Land, the splitting measurements are sub-parallel to the direction of lithospheric extension in the West Antarctic Rift System (WARS) (Fig. 5.7). There is, however, no agreement between the SKS splitting and AP2024 anisotropy in this location. The presence of strong low velocity channel structure beneath the region suggests elevated temperatures in the asthenosphere (Figs. 5.7 and 5.9), according to AP2024 and other recent tomographic studies (e.g., Heeszel et al., 2016; Shen et al., 2018a; White-Gaynor et al., 2019; Lloyd et al., 2020). The low seismic velocities connects the WARS with the low velocity anomalies underlying the Balleny Hotspot and nearby Pacific-Antarctic and Southeast Indian Ridges (PAR and SEIR, respectively), consistent with lateral flow of hot asthenospheric material beneath the region. The layering of anisotropy due to the flow of hot asthenospheric material and the frozen-in anisotropy from the extension in the WARS, along with lateral averaging over strong, small-scale heterogeneity, may account for the apparent mismatch.

Beneath East Antarctica, AP2024 and other tomographic models resolve high velocity anomalies extending to 200–250 km, indicative of thick cratonic lithosphere (Ritzwoller et al., 2001; An et al., 2015a; Lloyd et al., 2020). The anisotropic AP2024 shows layered anisotropy beneath the craton, as has been observed in other cratons previously (e.g., Yuan & Romanowicz, 2010; Adam & Lebedev, 2012; de Laat et al., 2023). Beneath the Gamburtsev Subglacial Mountains in central East Antarctica, Vs fast-propagation directions are N-S in the upper lithosphere (36–80 km) and sub-cratonic asthenosphere (330 km) (Figs. 5.3, 5.7 and 5.9). This is parallel to the SKS splitting fast azimuth, which indicates that the splitting is dominated by the signal from the upper lithosphere and asthenosphere. In the lower cratonic lithosphere (110–200 km), the orientation of anisotropy is nearly orthogonal (E-W), which reveals the layering of the deformation of the lithosphere during the formation and stabilisation of the craton.

The AP2024 fast-propagation directions of anisotropy within and near the low

velocity channel along the West Antarctica side of the Transantarctic Mountains (the East Antarctica-West Antarctica boundary) are parallel to this major boundary and consistent with flow of hot asthenospheric material along the channel. Holt & Royden (2020) modelled the pressure fields around the Pacific Plate subduction zones and predicted negative dynamic pressure on the upper side of subducting slabs. Strong anisotropy at asthenospheric depths under the Weddell-Lazarev Sea and Sandwich Plate (Fig. 5.3) correspond to the locations of the subducting Phoenix and South American Plate slabs. Geodynamic studies have shown that Poiseuille flow associated with subducting slabs significantly contributes to the asthenospheric flow field (e.g., Höink & Lenardic, 2008, 2010; Höink et al., 2011, 2012; Wang et al., 2023). The strong negative pressure, giving rise to pressure driven flow, could explain the strong anisotropy beneath this region, in addition to the presence of ridge-parallel anisotropy at the East Scotia Ridge.

The orientation of the strong anisotropy underlying the AAD and the Balleny Hotspot suggest asthenospheric flow along the SEIR (Fig. 5.3). de Laat et al. (2023) made a similar observation of ridge-parallel anisotropy along the SEIR and suggested the flow of hot plume material from the Balleny Hotspot as the source of the strong anisotropy, which our observations are also consistent with.

5.5 Conclusions

The AP2024 tomographic model reveals highly unusual azimuthal anisotropy within the Antarctic Plate. The fast-propagation axes in young oceanic lithosphere are aligned with the directions of spreading or paleo-spreading, as observed elsewhere around the world. Within old oceanic lithosphere closer to Antarctica, however, a circular pattern of E-W oriented anisotropy envelopes East Antarctica. Comparing the anisotropy with plate-tectonic reconstructions, we suggest that this unusual pattern originated from a combination of (i) lateral shear between Antarctica and adjacent continents in the early stages of the continental breakup between them and (ii) the oblique, ultra-slow spreading in the early stages of the opening of the Southern Ocean. Anisotropy within the East Antarctica cratonic lithosphere displays stratification that indicates layered deformation during the formation and stabilisation of the cratons. The heterogeneous pattern of published shear-wave splitting measurements is generally consistent with the layered anisotropy structure of the upper mantle. We suggest that the alignment of fast propagation directions in the asthenosphere with some shear wave splitting measurements in both East and West Antarctica in the 15–45E azimuth range are indicative of the past APM of the Antarctic Plate. Strong anisotropy is observed in the asthenosphere overlying the subducting Phoenix

and South Atlantic slabs. We suggest that this is due to the pressure-driven flow generated by the subduction.

Chapter 6

Conclusions

Antarctica is an integral part of the global climate system. By improving our understanding of the processes occurring within the lithosphere and mantle beneath the continent, we can more accurately predict how changes in Antarctica will influence the broader global climate system. We do this by leveraging the improved seismic coverage brought about by the increase in permanent and seasonal deployments, both on Antarctica and globally, over the past two decades. We applied the AMI of surface, S and multiple S waves on all openly available broadband seismic data and obtained a very large dataset of over 1.8 million waveform fits. We use a subset of almost 0.8 million waveform fits, selected to maximise data sampling in the model area while providing sufficient sampling in the antipodal regions, to generate a high resolution seismic tomography model of the Antarctic Plate and its boundaries.

In chapter 2, we discussed the AMI, outlined the advantages of the AMI algorithm and the 3-D tomographic inversion procedure used to produce the a tomography model. In the subsequent chapters, we present more detail on the parameters of the tomographic inversion, and present the azimuthally anisotropic Sv model of the Antarctic Plate, AP2024. We provide an overview of the structure underlying the Antarctic Plate in chapter 3, review the origins of intraplate magmatism in West Antarctica in chapter 4 and review the interesting azimuthal anisotropy pattern on the Antarctic Plate in chapter 5.

6.1 Lithospheric structure

The new tomography model AP2024 revealed the large-scale bimodal structure of the continent. We find the bimodality of the lithosphere of Antarctica extends into the Oceanic lithosphere. The older oceanic region between the Weddell Sea and the Kerguelen Plateau is underlain by high seismic velocities, while the younger

oceanic lithosphere along periphery of the plate and the southern Pacific Ocean is underlain by low seismic velocities. A sharp boundary between East Antarctica and West Antarctica bisects the two subcontinents, with velocity contrasts of up approximately 17% across the boundary. We find that the cratonic lithosphere underlying most of East Antarctica is highly heterogeneous, and comprised of several distinct blocks. The high-velocity anomalies under cratons in East Antarctica are similar to those in stable cratons elsewhere around the world, and lithospheric thickness decreases in the vicinity of coastlines, with the Transantarctic Mountains being the exception. Significant lithospheric thinning along the Dronning Maud Land and Wilkes Land coastline are likely to have been eroded in process of the continental breakup.

6.2 Intraplate magmatism and hotspots

In chapters 3 and 4, we image the presence of widespread low seismic velocities underlying West Antarctica. We confirm the observations of the spatial distribution of intraplate volcanism by Ball et al. (2021), finding that the regions of intraplate volcanic activity are underlain by low seismic velocities. These regions of low seismic velocities are indicative of thin lithosphere and elevated asthenospheric temperatures, and partial melting in at least some regions. Two major volcanic areas are located in West Antarctica, the Marie Byrd Land-Thurston Island-Eights Coast region and the Erebus Volcanic Province-West Antarctic Rift System-Ross Embayment region. Particularly low seismic velocities are imaged in the asthenosphere underlying these regions, indicative of partial melting feeding the volcanic activity within the region. AP2024 shows that the low seismic velocities beneath the two locations extended down to and are prominent in the mantle transition zone as well.

Beneath West Antarctica, low velocity anomalies at greater depths, consistent with deep-mantle origin of the volcanism, are also resolved by AP2024 and other recent models. Tracing the low velocity anomalies underlying the two major volcanic areas into the lower mantle, we find that a region of high velocity anomalies in the lower mantle at over 1000 km interupts the low velocity anomaly, as revealed by recent whole-mantle tomographic models. The complex pattern of interconnected high and low velocity anomalies in the lower mantle and the vertically continuous low velocity anomaly in the top 1000 km of the mantle suggest a deep mantle upwelling is likely the source of West Antarctic intraplate magmatism. The interaction between a deep mantle and a descending subducted slab is likely the cause of the complex morphology and deflections imaged by the whole-mantle models in the lower mantle.

Current magmatism along the Antarctic Peninsula is of post-subduction origin. High seismic velocities imaged beneath the peninsula are the fragments of the recently subducted Phoenix Plate. The opening of slab windows along the margin and detachment of the leading slab is likely the cause of the volcanism along the peninsula. Hotspots in the Antarctic Plate do not show clear tracks due to the slow movement of the plate. We find that the Balleny hotspot is the only hotspot located within the plate to have prominent low seismic velocities extending into the transition zone.

6.3 Azimuthal anisotropy

In chapter 5, we discuss the anisotropic parameterisation of the AP2024 and the azimuthal anisotropy found in the Antarctic Plate, bridging a knowledge gap in the anisotropic structure in the Antarctic Plate. A highly unusual E-W oriented anisotropy encircles East Antarctica. This circular pattern differs from the young oceanic lithosphere of the Antarctic Plate and elsewhere in the world, where the azimuthal anisotropy are aligned with the directions of spreading or paleo-spreading. Analysing the model in conjunction with plate tectonic reconstructions, we propose that this pattern originated from a combination of (i) relative lateral shear between Antarctica and the conjugate continents and (ii) the oblique, ultra-slow spreading rates observed during the early stages of continental breakup. The anisotropy within the cratons in East Antarctica is highly complex and stratified, suggesting layered deformation during the formation of the cratons. The alignment of the azimuthal anisotropy in the asthenosphere and some shear wave splitting directions in the 15–45E azimuth range could be reconciled with past absolute plate motion of the Antarctic Plate. We propose that pressure driven-flow triggered by the negative pressure generated by the subducting Phoenix and South Atlantic slabs could explain the strong anisotropy is observed in the region above the slabs.

6.4 Future work

The AP2024 has answered some interesting questions about the region, we were able to explore the deep mantle origins of West Antarctic intraplate volcanism and the intriguing anisotropy pattern surrounding Antarctica. However, the model also opens up new questions and a number of possibilities for future projects.

Improving the resolution of tomographic models

In our comparisons, we have noticed that AP2024 and the other state-of-the-art Antarctic regional models are lacking in resolution compared to contemporary regional models of other continents. There is a need to improve the resolution of the Antarctic models, however, it is difficult to do so due to the comparatively poor data sampling within the region. Though there are a decent number of stations (Fig. 5.1), particularly in West Antarctica, many of the stations are seasonal deployments that are only active for 1–2 years, while East Antarctica is still remains extremely sparsely sampled. The most straightforward solution is to deploy more stations, however, the location and conditions make it a challenging and costly endeavour. Thus, apart from improving physical station coverage, we should also consider improving the methodology to extract as much information as we possibly can from the seismograms. There are many ways to improve the current algorithm, but we will only outline a few of the key improvements that can be made.

The global centroid-moment tensor (GCMT; Dziewonski et al., 1981; Ekström et al., 2012) project is a widely used CMT catalogue in the seismology communit. However, studies have shown that the GCMT algorithm is biased (Hjörleifsdóttir & Ekström, 2010) and are the sources are at times mislocated. AMI uses the CMT solutions from the catalogue to compute source eigenfunctions since the CMT solutions are similarly generated using PREM, to reduce the errors in the waveform fits, however, the errors from the CMT solutions propagate into the tomographic models. Some adjoint tomographic models perform a refinement of the CMT parameters before using them (e.g., Bozdağ et al., 2016; Zhu et al., 2015), however, they are computationally costly and are only performed on the small number of events carefully selected for each study. Recently, a catalogue of over 9000 refined CMT solutions was presented by Sawade et al. (2022), which is a good start working towards the initiative of producing better CMT solutions. But this is still insufficient for the needs of the AMI algorithm as we have a massive database of waveform fits recorded from over 27 000 events. Having an updated catalogue of well located earthquakes will reduce the errors propagated into the waveform fits and the resulting tomographic model.

The crustal reference model used in AMI is a modified CRUST2.0 (Bassin, 2000). Although the modified model sufficiently describes the Earth on a global scale, it lacks resolution in regional models. In Antarctica, the complex crustal structure and thick ice cover, is not accurately represented by the current model. There is currently ongoing work to implement CRUST1.0 (Laske et al., 2013) as the background crustal model for AMI, with the final goal of including regional

crustal models to more accurately account for the crust in regional models. An improved and accurate crustal model will improve the quality and quantity of waveform fits and tomographic models.

Anisotropy measurements

We identified a circular anisotropy pattern enveloping East Antarctica in chapter 5, and were only able to compare our observations with a handful of SKS splitting measurements along the near-coastal regions of the continent. The lack of splitting measurements, largely due to the lack of sampling in Antarctica, has largely restricted our ability to analyse and compare and validate the anisotropy outside of West Antarctica, leaving East Antarctica almost entirely without and measurements. An improvement in the quantity and distribution of splitting measurements will provide the evidence to better reconcile our anisotropy measurements with past and present asthenospheric deformation, allowing us to make inferences on the geodynamic implications of the anisotropy observations.

Thermodynamic and petrological inversions

Throughout the thesis, we have made various inferences about temperatures and lithospheric thickness from the seismic velocity structure of the model. Thermodynamic and petrological inversions can quantitatively estimate these parameters from our tomography models, with certain underlying assumptions. This can be a useful tool to identify regions of elevated temperatures, and better reconcile our velocity structure observations with geochemical observations such as xenolith samples. The lack of accurate and reliable thermobarometers such as diamondiferous kimberlites, with only a single instance reported in Antarctica thus far (Yaxley et al., 2013) likely stemming from the thick ice sheets overlaying the continent, has hindered us in our interpretation and analysis of still mysterious cratonic East Antarctica. Accurate, quantitative estimates of the lithospheric and mantle parameters will also provide better input parameters to models of the geothermal heat flow and rates of glacial isostatic adjustment in Antarctica, which in turn leads to better predictions of the potential impact to the global climate system.

Final thoughts and future directions

Antarctica is a key component to the global climate system, the interest it has garnered over the past decade is reflected in the increasing number of studies focusing on better understanding the continent and the processes on and beneath it. Most work is performed at small regional scales, with short-term deployments

over the summer being the main contributors to the increasing number of studies. There is a critical need to reconcile the different observations and information from these studies into a larger, integrated knowledge base that can provide a more accurate overview of the processes occurring in the continent. Future work will likely focus on integrating datasets from various methodologies to compensate for each other's limitations, for example, joint inversions with magnetic or gravity and seismic data, and petrochemical or thermochemical inversions. However, seismology and tomography will still play a critical role in the equation as it is the best method to study the deep Earth, and to reconcile our observations and the processes occurring in the deep Earth.

Bibliography

Accardo, N. J., Wiens, D. A., Hernandez, S., Aster, R. C., Nyblade, A., Huerta, A., Anandakrishnan, S., Wilson, T., Heeszel, D. S., & Dalziel, I. W. D., 2014. Upper mantle seismic anisotropy beneath the West Antarctic Rift System and surrounding region from shear wave splitting analysis, *Geophysical Journal International*, **198**(1), 414–429. doi:10.1093/gji/ggu117.

Adam, J. M.-C. & Lebedev, S., 2012. Azimuthal anisotropy beneath southern Africa from very broad-band surface-wave dispersion measurements: Azimuthal anisotropy beneath southern Africa, *Geophysical Journal International*, **191**(1), 155–174. doi:10.1111/j.1365-246X.2012.05583.x.

Aki, K. & Lee, W. H. K., 1976. Determination of three-dimensional velocity anomalies under a seismic array using first P arrival times from local earthquakes: 1. A homogeneous initial model, *Journal of Geophysical Research*, **81**(23), 4381–4399. doi:10.1029/JB081i023p04381.

Aki, K., Christoffersson, A., Husebye, E., & Powell, C., 1974. Three-dimensional seismic velocity anomalies in the crust and upper-mantle under the USGS, California seismic array, *Eos Trans. AGU*, **56**, 1145.

Aki, K., Christoffersson, A., & Husebye, E. S., 1977. Determination of the three-dimensional seismic structure of the lithosphere, *Journal of Geophysical Research*, **82**(2), 277–296, Publisher: Wiley Online Library.

Altamimi, Z., Métivier, L., Rebischung, P., Rouby, H., & Collilieux, X., 2017. ITRF2014 plate motion model, *Geophysical Journal International*, **209**(3), 1906–1912. doi:10.1093/gji/ggx136.

Amaru, M., 2007. *Global travel time tomography with 3-D reference models*, Ph.D. thesis, Faculteit Geowetenschappen Univ. Utrecht, Utrecht, OCLC: 1074524912.

Ammon, C. J., Velasco, A. A., Lay, T., & Wallace, T. C., 2021. Earth structure, in *Foundations of Modern Global Seismology*, pp. 269–301, Elsevier.

An, M., Wiens, D. A., Zhao, Y., Feng, M., Nyblade, A. A., Kanao, M., Li, Y., Maggi, A., & Lévêque, J.-J., 2015a. S-velocity model and inferred Moho topography beneath the Antarctic Plate from Rayleigh waves: Antarctic S-velocities and Moho, *Journal of Geophysical Research: Solid Earth*, **120**(1), 359–383. doi:10.1002/2014JB011332.

An, M., Wiens, D. A., Zhao, Y., Feng, M., Nyblade, A. A., Kanao, M., Li, Y., Maggi, A., & Lévêque, J.-J., 2015b. Temperature, lithosphere-asthenosphere boundary, and heat flux beneath the Antarctic Plate inferred from seismic velocities, *Journal of Geophysical Research: Solid Earth*, **120**(12), 8720–8742. doi:10.1002/2015JB011917.

Anandakrishnan, S., Voigt, D. E., Burkett, P. G., Long, B., & Henry, R., 2000. Deployment of a broadband seismic network in west Antarctica, *Geophysical Research Letters*, **27**(14), 2053–2056. doi:10.1029/1999GL011189, _eprint: https://onlinelibrary.wiley.com/doi/pdf/10.1029/1999GL011189.

Anderson, D. L., 1961. Elastic wave propagation in layered anisotropic media, *Journal of Geophysical Research*, **66**(9), 2953–2963. doi:10.1029/JZ066i009p02953.

Anderson, D. L. & Schramm, K. A., 2005. Global hotspot maps, in *Plates, plumes and paradigms*, Geological Society of America.

Austermann, J., Pollard, D., Mitrovica, J. X., Moucha, R., Forte, A. M., DeConto, R. M., Rowley, D. B., & Raymo, M. E., 2015. The impact of dynamic topography change on Antarctic ice sheet stability during the mid-Pliocene warm period, *Geology*, **43**(10), 927–930. doi:10.1130/G36988.1.

Aviado, K. B., Rilling-Hall, S., Bryce, J. G., & Mukasa, S. B., 2015. Submarine and subaerial lavas in the West Antarctic Rift System: Temporal record of shifting magma source components from the lithosphere and asthenosphere, *Geochemistry, Geophysics, Geosystems*, **16**(12), 4344–4361. doi:10.1002/2015GC006076, _eprint: https://onlinelibrary.wiley.com/doi/pdf/10.1002/2015GC006076.

Baker, M. G., Aster, R. C., Anthony, R. E., Chaput, J., Wiens, D. A., Nyblade, A., Bromirski, P. D., Gerstoft, P., & Stephen, R. A., 2019. Seasonal and spatial variations in the ocean-coupled ambient wavefield of the Ross Ice Shelf, *Journal of Glaciology*, **65**(254), 912–925. doi:10.1017/jog.2019.64.

Ball, P., Eagles, G., Ebinger, C., McClay, K., & Totterdell, J., 2013. The spatial and temporal evolution of strain during the separation of Australia and Antarctica, *Geochemistry, Geophysics, Geosystems*, **14**(8), 2771–2799. doi:10.1002/ggge.20160, _eprint: https://onlinelibrary.wiley.com/doi/pdf/10.1002/ggge.20160.

Ball, P. W., White, N. J., Maclennan, J., & Stephenson, S. N., 2021. Global influence of mantle temperature and plate thickness on intraplate volcanism, *Nature Communications*, **12**(1), 2045. doi:10.1038/s41467-021-22323-9, Number: 1 Publisher: Nature Publishing Group.

Ballmer, M., van Keken, P., & Ito, G., 2015. Hotspots, Large Igneous Provinces, and Melting Anomalies, in *Treatise on Geophysics*, pp. 393–459, Elsevier.

Bannister, S., Yu, J., Leitner, B., & Kennett, B. L. N., 2003. Variations in crustal structure across the transition from West to East Antarctica, Southern Victoria Land, *Geophysical Journal International*, **155**(3), 870–880. doi:10.1111/j.1365-

246X.2003.02094.x.

Bao, X., Lithgow-Bertelloni, C. R., Jackson, M. G., & Romanowicz, B., 2022. On the relative temperatures of Earth's volcanic hotspots and mid-ocean ridges, *Science*, **375**(6576), 57–61. doi:10.1126/science.abj8944, Publisher: American Association for the Advancement of Science.

Baranov, A. & Bobrov, A., 2018. Crustal structure and properties of Archean cratons of Gondwanaland: similarity and difference, *Russian Geology and Geophysics*, **59**(5), 512–524. doi:10.1016/j.rgg.2018.04.005.

Baranov, A., Tenzer, R., & Morelli, A., 2021. Updated Antarctic crustal model, *Gondwana Research*, **89**, 1–18. doi:10.1016/j.gr.2020.08.010.

Barklage, M., Wiens, D. A., Nyblade, A., & Anandakrishnan, S., 2009. Upper mantle seismic anisotropy of South Victoria Land and the Ross Sea coast, Antarctica from SKS and SKKS splitting analysis, *Geophysical Journal International*, **178**(2), 729–741. doi:10.1111/j.1365-246X.2009.04158.x.

Barletta, V. R., Bevis, M., Smith, B. E., Wilson, T., Brown, A., Bordoni, A., Willis, M., Khan, S. A., Rovira-Navarro, M., Dalziel, I., Smalley, R., Kendrick, E., Konfal, S., Caccamise, D. J., Aster, R. C., Nyblade, A., & Wiens, D. A., 2018. Observed rapid bedrock uplift in Amundsen Sea Embayment promotes ice-sheet stability, *Science*, **360**(6395), 1335–1339. doi:10.1126/science.aao1447.

Bassin, C., 2000. The current limits of resolution for surface wave tomography in North America, *Eos Trans. AGU*, **81**, 897.

Bastias, J., Spikings, R., Riley, T., Chew, D., Grunow, A., Ulianov, A., Chiaradia, M., & Burton-Johnson, A., 2023. Cretaceous magmatism in the Antarctic Peninsula and its tectonic implications, *Journal of the Geological Society*, **180**(1), jgs2022–067. doi:10.1144/jgs2022-067.

Bastías, J., Chew, D., Villanueva, C., Riley, T., Manfroi, J., Trevisan, C., Leppe, M., Castillo, P., Poblete, F., Tetzner, D., Giuliani, G., López, B., Chen, H., Zheng, G.-G., Zhao, Y., Gao, L., Rauch, A., & Jaña, R., 2023. The South Shetland Islands, Antarctica: Lithostratigraphy and geological map, *Frontiers in Earth Science*, **10**.

Becker, T. W., Kellogg, J. B., Ekström, G., & O'Connell, R. J., 2003. Comparison of azimuthal seismic anisotropy from surface waves and finite strain from global mantle-circulation models, *Geophysical Journal International*, **155**(2), 696–714. doi:10.1046/j.1365-246X.2003.02085.x.

Becker, T. W., Lebedev, S., & Long, M. D., 2012. On the relationship between azimuthal anisotropy from shear wave splitting and surface wave tomography, *Journal of Geophysical Research: Solid Earth*, **117**(B1), 2011JB008705. doi:10.1029/2011JB008705.

Becker, T. W., Conrad, C. P., Schaeffer, A. J., & Lebedev, S., 2014. Origin of azimuthal seismic anisotropy in oceanic plates and mantle, *Earth and Planetary*

Science Letters, **401**, 236–250. doi:10.1016/j.epsl.2014.06.014.

Becker, T. W., Schaeffer, A. J., Lebedev, S., & Conrad, C. P., 2015. Toward a generalized plate motion reference frame, *Geophysical Research Letters*, **42**(9), 3188–3196. doi:10.1002/2015GL063695.

Beghein, C., Yuan, K., Schmerr, N., & Xing, Z., 2014. Changes in Seismic Anisotropy Shed Light on the Nature of the Gutenberg Discontinuity, *Science*, **343**(6176), 1237–1240. doi:10.1126/science.1246724.

Behrendt, J. C., 1999. Crustal and lithospheric structure of the West Antarctic Rift System from geophysical investigations — a review, *Global and Planetary Change*, **23**(1-4), 25–44.

Bell, R. E., 2008. The role of subglacial water in ice-sheet mass balance, *Nature Geoscience*, **1**(5), 297–304. doi:10.1038/ngeo186.

Bentley, C. R., 1973. Crustal structure of Antarctica, *Tectonophysics*, **20**(1-4), 229–240. doi:10.1016/0040-1951(73)90112-1.

Berg, J. H., Weis, D., McIntosh, W. C., & Cameron, B. I., 1997. AGE AND ORIGIN OF HIMU VOLCANISM IN THE BALLENY ISLANDS: MELTING OF PLUME-DELIVERED DEEP MANTLE OR SHALLOW ASTHENOSPHERIC.

Beyreuther, M., Barsch, R., Krischer, L., Megies, T., Behr, Y., & Wassermann, J., 2010. ObsPy: A Python Toolbox for Seismology, *Seismological Research Letters*, **81**(3), 530–533. doi:10.1785/gssrl.81.3.530.

Bijwaard, H. & Spakman, W., 1999. Tomographic evidence for a narrow whole mantle plume below Iceland, *Earth and Planetary Science Letters*, **166**(3-4), 121–126. doi:10.1016/S0012-821X(99)00004-7.

Block, A. E., Bell, R. E., & Studinger, M., 2009. Antarctic crustal thickness from satellite gravity: Implications for the Transantarctic and Gamburtsev Subglacial Mountains, *Earth and Planetary Science Letters*, **288**(1-2), 194–203. doi:10.1016/j.epsl.2009.09.022.

Boger, S. D., 2011. Antarctica — Before and after Gondwana, *Gondwana Research*, **19**, 335–371.

Bonadio, R., Geissler, W. H., Lebedev, S., Fullea, J., Ravenna, M., Celli, N. L., Jokat, W., Jegen, M., Sens-Schönfelder, C., & Baba, K., 2018. Hot Upper Mantle Beneath the Tristan da Cunha Hotspot From Probabilistic Rayleigh-Wave Inversion and Petrological Modeling, *Geochemistry, Geophysics, Geosystems*, **19**(5), 1412–1428. doi:10.1002/2017GC007347, _eprint: https://onlinelibrary.wiley.com/doi/pdf/10.1002/2017GC007347.

Borghi, A., 2022. Moho depths for Antarctica Region by the inversion of ground-based gravity data, *Geophysical Journal International*, **231**(2), 1404–1420. doi:10.1093/gji/ggac249.

Bozdağ, E., Peter, D., Lefebvre, M., Komatitsch, D., Tromp, J., Hill, J., Podhorszki,

N., & Pugmire, D., 2016. Global adjoint tomography: first-generation model, *Geophysical Journal International*, **207**(3), 1739–1766. doi:10.1093/gji/ggw356.

Bredow, E., Steinberger, B., Gassmöller, R., & Dannberg, J., 2022. Mantle convection and possible mantle plumes beneath Antarctica – insights from geodynamic models and implications for topography, *Geological Society, London, Memoirs*, **56**(1), M56–2020–2. doi:10.1144/M56-2020-2.

Breitsprecher, K. & Thorkelson, D. J., 2009. Neogene kinematic history of Nazca–Antarctic–Phoenix slab windows beneath Patagonia and the Antarctic Peninsula, *Tectonophysics*, **464**(1-4), 10–20. doi:10.1016/j.tecto.2008.02.013.

Brenn, G. R., Hansen, S. E., & Park, Y., 2017. Variable thermal loading and flexural uplift along the Transantarctic Mountains, Antarctica, *Geology*, **45**(5), 463–466. doi:10.1130/G38784.1.

Brune, S., Williams, S. E., & Müller, R. D., 2018. Oblique rifting: the rule, not the exception, *Solid Earth*, **9**(5), 1187–1206. doi:10.5194/se-9-1187-2018.

Burgess, S., Bowring, S., Fleming, T., & Elliot, D., 2015. High-precision geochronology links the Ferrar large igneous province with early-Jurassic ocean anoxia and biotic crisis, *Earth and Planetary Science Letters*, **415**, 90–99. doi:10.1016/j.epsl.2015.01.037.

Burton-Johnson, A., Black, M., Fretwell, P. T., & Kaluza-Gilbert, J., 2016. An automated methodology for differentiating rock from snow, clouds and seain Antarctica from Landsat 8 imagery: a new rock outcrop map and areaestimation for the entire Antarctic continent, *The Cryosphere*, **10**(4), 1665–1677. doi:10.5194/tc-10-1665-2016.

Burton-Johnson, A., Dziadek, R., & Martin, C., 2020. Review article: Geothermal heat flow in Antarctica: current and future directions, *The Cryosphere*, **14**(11), 3843–3873. doi:10.5194/tc-14-3843-2020, Publisher: Copernicus GmbH.

Burton-Johnson, A., Bastias, J., & Kraus, S., 2023. Breaking the Ring of Fire: How Ridge Collision, Slab Age, and Convergence Rate Narrowed and Terminated the Antarctic Continental Arc, *Tectonics*, **42**(5), e2022TC007634. doi:10.1029/2022TC007634, _eprint: https://onlinelibrary.wiley.com/doi/pdf/10.1029/2022TC007634.

Cammarano, F., Goes, S., Vacher, P., & Giardini, D., 2003. Inferring upper-mantle temperatures from seismic velocities, *Physics of the Earth and Planetary Interiors*, **138**(3), 197–222. doi:10.1016/S0031-9201(03)00156-0.

Cande, S. C. & Stock, J. M., 2004. Cenozoic reconstructions of the Australia-New Zealand-South Pacific sector of Antarctica, in *Geophysical Monograph Series*, vol. 151, pp. 5–17, eds Exon, N. F., Kennett, J. P., & Malone, M. J., American Geophysical Union, Washington, D. C.

Cande, S. C. & Stock, J. M., 2006. Constraints on the Timing of Extension in

the Northern Basin, Ross Sea, in *Antarctica*, pp. 319–326, eds Fütterer, D. K., Damaske, D., Kleinschmidt, G., Miller, H., & Tessensohn, F., Springer-Verlag, Berlin/Heidelberg.

Cande, S. C., Stock, J. M., Müller, R. D., & Ishihara, T., 2000. Cenozoic motion between East and West Antarctica, *Nature*, **404**(6774), 145–150. doi:10.1038/35004501.

Celli, N. L., Lebedev, S., Schaeffer, A. J., & Gaina, C., 2020a. African cratonic lithosphere carved by mantle plumes, *Nature Communications*, **11**(1), 92. doi:10.1038/s41467-019-13871-2.

Celli, N. L., Lebedev, S., Schaeffer, A. J., Ravenna, M., & Gaina, C., 2020b. The upper mantle beneath the South Atlantic Ocean, South America and Africa from waveform tomography with massive data sets, *Geophysical Journal International*, **221**(1), 178–204. doi:10.1093/gji/ggz574.

Celli, N. L., Lebedev, S., Schaeffer, A. J., & Gaina, C., 2021. The tilted Iceland Plume and its effect on the North Atlantic evolution and magmatism, *Earth and Planetary Science Letters*, **569**, 117048. doi:10.1016/j.epsl.2021.117048.

Chagas De Melo, B., Lebedev, S., Celli, N. L., de Laat, J. I., & Assumpcao, M., 2024. The lithosphere of South America from seismic tomography: Structure, evolution, and control on tectonics and magmatism, *Gondwana Research*, **GR Focus - Invited Review, (in review)**.

Chagas de Melo, B., Lebedev, S., Celli, N. L., Gibson, S., de Laat, J. I., & Assumpção, M., 2025. The lithosphere of South America from seismic tomography: Structure, evolution, and control on tectonics and magmatism, *Gondwana Research*, **138**, 139–167. doi:10.1016/j.gr.2024.10.012.

Chaput, J., Aster, R. C., Huerta, A., Sun, X., Lloyd, A., Wiens, D., Nyblade, A., Anandakrishnan, S., Winberry, J. P., & Wilson, T., 2014. The crustal thickness of West Antarctica: CRUSTAL THICKNESS OF WEST ANTARCTICA, *Journal of Geophysical Research: Solid Earth*, **119**(1), 378–395. doi:10.1002/2013JB010642.

Chatterjee, S., Debnath, A., Samantaray, S., Arora, D., Dey, S., Gupta, S., & Pant, N. C., 2023. Thermotectonic evolution of the Rauer Group and Vestfold Hills in Prydz Bay: implications for Neoproterozoic assembly of the East Antarctic Shield, *Polar Science*, p. 101015. doi:10.1016/j.polar.2023.101015.

Chen, B., Haeger, C., Kaban, M. K., & Petrunin, A. G., 2018. Variations of the effective elastic thickness reveal tectonic fragmentation of the Antarctic lithosphere, *Tectonophysics*, **746**, 412–424. doi:10.1016/j.tecto.2017.06.012.

Cheng, W., Hu, X. G., & Liu, L. T., 2021. Anisotropy Gradients in the Middle of the Ross Sea Embayment, West Antarctica: Evidence From QL Scattered Surface Waves, *Geophysical Research Letters*, **48**(6), e2020GL091232. doi:10.1029/2020GL091232,

https://onlinelibrary.wiley.com/doi/pdf/10.1029/2020GL091232.

Coffin, M. F., 1993. Emplacement and subsidence of Indian Ocean plateaus and submarine ridges, *GEOPHYSICAL MONOGRAPH-AMERICAN GEOPHYSICAL UNION*, **70**, 115–115.

Coffin, M. F., 2002. Kerguelen Hotspot Magma Output since 130 Ma, *Journal of Petrology*, **43**(7), 1121–1137. doi:10.1093/petrology/43.7.1121.

Conrad, C. P., Bianco, T. A., Smith, E. I., & Wessel, P., 2011. Patterns of intraplate volcanism controlled by asthenospheric shear, *Nature Geoscience*, **4**(5), 317–321. doi:10.1038/ngeo1111.

Courtillot, V., Davaille, A., Besse, J., & Stock, J., 2003. Three distinct types of hotspots in the Earth's mantle, *Earth and Planetary Science Letters*, **205**(3-4), 295–308. doi:10.1016/S0012-821X(02)01048-8.

Cui, C., Lei, W., Liu, Q., Peter, D., Bozdağ, E., Tromp, J., Hill, J., Podhorszki, N., & Pugmire, D., 2024. GLAD-M35: a joint P and S global tomographic model with uncertainty quantification, *Geophysical Journal International*, **239**(1), 478–502. doi:10.1093/gji/ggae270.

Curtis, M. L. & Storey, B. C., 1996. A review of geological constraints on the pre-break-up position of the Ellsworth Mountains within Gondwana: implications for Weddell Sea evolution, *Geological Society, London, Special Publications*, **108**(1), 11–30. doi:10.1144/GSL.SP.1996.108.01.02.

Dahlen, F. A. & Tromp, J., 1998. *Theoretical global seismology*, Princeton University Press, Princeton, N.J.

Dahlen, F. A., Hung, S.-H., & Nolet, G., 2000. Fréchet kernels for finite-frequency traveltimes—I. Theory, *Geophysical Journal International*, **141**(1), 157–174. doi:10.1046/j.1365-246X.2000.00070.x, _eprint: https://onlinelibrary.wiley.com/doi/pdf/10.1046/j.1365-246X.2000.00070.x.

Dalziel, I. W., Lawver, L. A., Norton, I. O., & Gahagan, L. M., 2013. The Scotia Arc: Genesis, Evolution, Global Significance, *Annual Review of Earth and Planetary Sciences*, **41**(1), 767–793. doi:10.1146/annurev-earth-050212-124155.

Dalziel, I. W. D. & Elliot, D. H., 1982. West Antarctica: Problem child of Gondwanaland, *Tectonics*, **1**(1), 3–19. doi:10.1029/TC001i001p00003, _eprint: https://onlinelibrary.wiley.com/doi/pdf/10.1029/TC001i001p00003.

Danesi, S. & Morelli, A., 2001. Structure of the upper mantle under the Antarctic Plate from surface wave tomography, *Geophysical Research Letters*, **28**(23), 4395–4398. doi:10.1029/2001GL013431.

Darbyshire, F. A. & Lebedev, S., 2009. Rayleigh wave phase-velocity heterogeneity and multilayered azimuthal anisotropy of the Superior Craton, Ontario, *Geophysical Journal International*, **176**(1), 215–234. doi:10.1111/j.1365-246x.2008.03982.x, Publisher: Oxford University Press (OUP).

Davey, F. J., Cande, S. C., & Stock, J. M., 2006. Extension in the western Ross Sea region-links between Adare Basin and Victoria Land Basin, *Geophysical Research Letters*, **33**(20), 2006GL027383. doi:10.1029/2006GL027383.

Davey, F. J., Granot, R., Cande, S. C., Stock, J. M., Selvans, M., & Ferraccioli, F., 2016. Synchronous oceanic spreading and continental rifting in West Antarctica, *Geophysical Research Letters*, **43**(12), 6162–6169. doi:10.1002/2016GL069087, _eprint: https://onlinelibrary.wiley.com/doi/pdf/10.1002/2016GL069087.

Davies, D. & Davies, J., 2009. Thermally-driven mantle plumes reconcile multiple hot-spot observations, *Earth and Planetary Science Letters*, **278**(1-2), 50–54. doi:10.1016/j.epsl.2008.11.027.

Davies, D. R. & Rawlinson, N., 2014. On the origin of recent intraplate volcanism in Australia, *Geology*, **42**(12), 1031–1034. doi:10.1130/G36093.1.

Davies, G. F., 1988. Ocean bathymetry and mantle convection: 1. Large-scale flow and hotspots, *Journal of Geophysical Research: Solid Earth*, **93**(B9), 10467–10480. doi:10.1029/JB093iB09p10467.

Davis, J. K., Lawver, L. A., Norton, I. O., Dalziel, I. W. D., & Gahagan, L. M., 2019. The crustal structure of the Enderby Basin, East Antarctica, *Marine Geophysical Research*, **40**(1), 1–16. doi:10.1007/s11001-018-9356-5.

Debayle, E. & Ricard, Y., 2013. Seismic observations of large-scale deformation at the bottom of fast-moving plates, *Earth and Planetary Science Letters*, **376**, 165–177. doi:10.1016/j.epsl.2013.06.025.

Debayle, E., Kennett, B., & Priestley, K., 2005. Global azimuthal seismic anisotropy and the unique plate-motion deformation of Australia, *Nature*, **433**(7025), 509–512. doi:10.1038/nature03247.

Debayle, E., Dubuffet, F., & Durand, S., 2016. An automatically updated *S* -wave model of the upper mantle and the depth extent of azimuthal anisotropy, *Geophysical Research Letters*, **43**(2), 674–682. doi:10.1002/2015GL067329.

Demidjuk, Z., Turner, S., Sandiford, M., George, R., Foden, J., & Etheridge, M., 2007. U-series isotope and geodynamic constraints on mantle melting processes beneath the Newer Volcanic Province in South Australia, *Earth and Planetary Science Letters*, **261**(3-4), 517–533. doi:10.1016/j.epsl.2007.07.006.

de Laat, J. I., Lebedev, S., Celli, N. L., Bonadio, R., Chagas de Melo, B., & Rawlinson, N., 2023. Structure and evolution of the Australian plate and underlying upper mantle from waveform tomography with massive data sets, *Geophysical Journal International*, **234**(1), 153–189. doi:10.1093/gji/ggad062.

Dou, H., Xu, Y., Lebedev, S., Chagas De Melo, B., Van Der Hilst, R. D., Wang, B., & Wang, W., 2024. The upper mantle beneath Asia from seismic tomography, with inferences for the mechanisms of tectonics, seismicity, and magmatism, *Earth-Science Reviews*, **255**, 104841. doi:10.1016/j.earscirev.2024.104841.

Doucet, S., Weis, D., Scoates, J. S., Debaille, V., & Giret, A., 2004. Geochemical and Hf–Pb–Sr–Nd isotopic constraints on the origin of the Amsterdam–St. Paul (Indian Ocean) hotspot basalts, *Earth and Planetary Science Letters*, **218**(1-2), 179–195. doi:10.1016/S0012-821X(03)00636-8.

Dunbar, N. W., Iverson, N. A., Smellie, J. L., McIntosh, W. C., Zimmerer, M. J., & Kyle, P. R., 2021. Chapter 7.4 Active volcanoes in Marie Byrd Land, *Geological Society, London, Memoirs*, **55**(1), 759–783. doi:10.1144/M55-2019-29.

Duncan, R. A., 2002. A Time Frame for Construction of the Kerguelen Plateau and Broken Ridge, *Journal of Petrology*, **43**(7), 1109–1119. doi:10.1093/petrology/43.7.1109.

Dziewonski, A. M., Hager, B. H., & O'Connell, R. J., 1977. Large-scale heterogeneities in the lower mantle, *Journal of Geophysical Research*, **82**(2), 239–255. doi:10.1029/JB082i002p00239.

Dziewonski, A. M., Chou, T.-A., & Woodhouse, J. H., 1981. Determination of earthquake source parameters from waveform data for studies of global and regional seismicity, *Journal of Geophysical Research: Solid Earth*, **86**(B4), 2825–2852. doi:10.1029/JB086iB04p02825.

Eagles, G., 2004. Tectonic evolution of the Antarctic–Phoenix plate system since 15 Ma, *Earth and Planetary Science Letters*, **217**(1-2), 97–109. doi:10.1016/S0012-821X(03)00584-3.

Eagles, G., Livermore, R., & Morris, P., 2006. Small basins in the Scotia Sea: The Eocene Drake Passage gateway, *Earth and Planetary Science Letters*, **242**(3-4), 343–353. doi:10.1016/j.epsl.2005.11.060.

Ekström, G., 2011. A global model of Love and Rayleigh surface wave dispersion and anisotropy, 25-250 s: Global dispersion model GDM52, *Geophysical Journal International*, **187**(3), 1668–1686. doi:10.1111/j.1365-246X.2011.05225.x.

Ekström, G., Nettles, M., & Dziewoński, A., 2012. The global CMT project 2004–2010: Centroid-moment tensors for 13,017 earthquakes, *Physics of the Earth and Planetary Interiors*, **200-201**, 1–9. doi:10.1016/j.pepi.2012.04.002.

El-Sharkawy, A., Hansteen, T. H., Clemente-Gomez, C., Fullea, J., Lebedev, S., & Meier, T., 2024. Cenozoic Volcanic Provinces and Shallow Asthenospheric Volumes in the Circum-Mediterranean: Evidence From Magmatic Geochemistry, Seismic Tomography, and Integrated Geophysical-Petrological Thermochemical Inversion, *Geochemistry, Geophysics, Geosystems*, **25**(9), e2023GC011017. doi:10.1029/2023GC011017, _eprint: https://onlinelibrary.wiley.com/doi/pdf/10.1029/2023GC011017.

Emry, E. L., Nyblade, A. A., Julià, J., Anandakrishnan, S., Aster, R. C., Wiens, D. A., Huerta, A. D., & Wilson, T. J., 2015. The mantle transition zone beneath West Antarctica: Seismic evidence for hydration and thermal upwellings,

Geochemistry, Geophysics, Geosystems, **16**(1), 40–58. doi:10.1002/2014GC005588, _eprint: https://onlinelibrary.wiley.com/doi/pdf/10.1002/2014GC005588.

Endrun, B., Lebedev, S., Meier, T., Tirel, C., & Friederich, W., 2011. Complex layered deformation within the Aegean crust and mantle revealed by seismic anisotropy, *Nature Geoscience*, **4**(3), 203–207. doi:10.1038/ngeo1065, Publisher: Springer Science and Business Media LLC.

Evison, F. F., Ingham, C. E., Orr, R. H., & Fort, J. H. L., 1960. Thickness of the Earth's Crust in Antarctica and the Surrounding Oceans, *Geophysical Journal International*, **3**(3), 289–306. doi:10.1111/j.1365-246X.1960.tb01704.x.

Fanning, C., Flint, R., Parker, A., Ludwig, K., & Blissett, A., 1988. Refined Proterozoic evolution of the Gawler Craton, South Australia, through U-Pb zircon geochronology, *Precambrian Research*, **40-41**, 363–386. doi:10.1016/0301-9268(88)90076-9.

Faure, G., Bowman, J., & Elliot, D., 1979. The initial 87Sr86Sr ratios of the Kirwan volcanics of Dronning Maud Land: Comparison with the Kirkpatrick Basalt, Transantarctic Mountains, *Chemical Geology*, **26**(1-2), 77–90. doi:10.1016/0009-2541(79)90031-7.

Fichtner, A., Kennett, B. L. N., Igel, H., & Bunge, H.-P., 2009. Full seismic waveform tomography for upper-mantle structure in the Australasian region using adjoint methods, *Geophysical Journal International*, **179**(3), 1703–1725. doi:10.1111/j.1365-246X.2009.04368.x.

Fichtner, A., Kennett, B. L. N., Tsai, V. C., Thurber, C. H., Rodgers, A. J., Tape, C., Rawlinson, N., Borcherdt, R. D., Lebedev, S., Priestley, K., Morency, C., Bozdağ, E., Tromp, J., Ritsema, J., Romanowicz, B., Liu, Q., Golos, E., & Lin, F.-C., 2024. Seismic Tomography 2024, *Bulletin of the Seismological Society of America*, **114**(3), 1185–1213. doi:10.1785/0120230229.

Fielding, C. R., Whittaker, J., Henrys, S. A., Wilson, T. J., & Naish, T. R., 2008. Seismic facies and stratigraphy of the Cenozoic succession in McMurdo Sound, Antarctica: Implications for tectonic, climatic and glacial history, *Palaeogeography, Palaeoclimatology, Palaeoecology*, **260**(1-2), 8–29. doi:10.1016/j.palaeo.2007.08.016.

Fitzsimons, I. C. W., 2003. Proterozoic basement provinces of southern and southwestern Australia, and their correlation with Antarctica, *Geological Society, London, Special Publications*, **206**(1), 93–130. doi:10.1144/GSL.SP.2003.206.01.07.

Flowerdew, M., Millar, I., Curtis, M., Vaughan, A., Horstwood, M., Whitehouse, M., & Fanning, C., 2007. Combined U-Pb geochronology and Hf isotope geochemistry of detrital zircons from early Paleozoic sedimentary rocks, Ellsworth-Whitmore Mountains block, Antarctica, *Geological Society of America Bulletin*, **119**(3-4), 275–288. doi:10.1130/B25891.1.

Flöttmann, T. & Oliver, R., 1994. Review of Precambrian-Palaeozoic relationships at the craton margins of southeastern Australia and adjacent Antarctica, *Precambrian Research*, **69**(1-4), 293–306. doi:10.1016/0301-9268(94)90093-0.

Forsyth, D. & Uyedat, S., 1975. On the Relative Importance of the Driving Forces of Plate Motion.

Fowler, C. M. R., 2005. *The solid earth: an introduction to global geophysics*, Cambridge University Press, Cambridge, UK ; New York, 2nd edn.

French, S., Lekic, V., & Romanowicz, B., 2013. Waveform Tomography Reveals Channeled Flow at the Base of the Oceanic Asthenosphere, *Science*, **342**(6155), 227–230. doi:10.1126/science.1241514.

French, S. W. & Romanowicz, B., 2015. Broad plumes rooted at the base of the Earth's mantle beneath major hotspots, *Nature*, **525**(7567), 95–99. doi:10.1038/nature14876.

Fretwell, P., Pritchard, H. D., Vaughan, D. G., Bamber, J. L., Barrand, N. E., Bell, R., Bianchi, C., Bingham, R. G., Blankenship, D. D., Casassa, G., Catania, G., Callens, D., Conway, H., Cook, A. J., Corr, H. F. J., Damaske, D., Damm, V., Ferraccioli, F., Forsberg, R., Fujita, S., Gim, Y., Gogineni, P., Griggs, J. A., Hindmarsh, R. C. A., Holmlund, P., Holt, J. W., Jacobel, R. W., Jenkins, A., Jokat, W., Jordan, T., King, E. C., Kohler, J., Krabill, W., Riger-Kusk, M., Langley, K. A., Leitchenkov, G., Leuschen, C., Luyendyk, B. P., Matsuoka, K., Mouginot, J., Nitsche, F. O., Nogi, Y., Nost, O. A., Popov, S. V., Rignot, E., Rippin, D. M., Rivera, A., Roberts, J., Ross, N., Siegert, M. J., Smith, A. M., Steinhage, D., Studinger, M., Sun, B., Tinto, B. K., Welch, B. C., Wilson, D., Young, D. A., Xiangbin, C., & Zirizzotti, A., 2013. Bedmap2: improved ice bed, surface and thickness datasets for Antarctica, *The Cryosphere*, **7**(1), 375–393. doi:10.5194/tc-7-375-2013.

Frey, F., Coffin, M., Wallace, P., Weis, D., Zhao, X., Wise, S., Wähnert, V., Teagle, D., Saccocia, P., Reusch, D., Pringle, M., Nicolaysen, K., Neal, C., Müller, R., Moore, C., Mahoney, J., Keszthelyi, L., Inokuchi, H., Duncan, R., Delius, H., Damuth, J., Damasceno, D., Coxall, H., Borre, M., Boehm, F., Barling, J., Arndt, N., & Antretter, M., 2000. Origin and evolution of a submarine large igneous province: the Kerguelen Plateau and Broken Ridge, southern Indian Ocean, *Earth and Planetary Science Letters*, **176**(1), 73–89. doi:10.1016/S0012-821X(99)00315-5.

Fullea, J., Lebedev, S., Martinec, Z., & Celli, N. L., 2021. WINTERC-G: mapping the upper mantle thermochemical heterogeneity from coupled geophysical–petrological inversion of seismic waveforms, heat flow, surface elevation and gravity satellite data, *Geophysical Journal International*, **226**(1), 146–191. doi:10.1093/gji/ggab094.

Gaina, C., Müller, R. D., Brown, B., Ishihara, T., & Ivanov, S., 2007. Breakup and early seafloor spreading between India and Antarctica, *Geophysical Journal International*, **170**(1), 151–169. doi:10.1111/j.1365-246X.2007.03450.x.

Gardiner, N. P., Hall, M. W. D., & Cawood, P. A., 2021. A Forearc Stratigraphic Response to Cretaceous Plateau Collision and Slab Detachment, South Island, New Zealand, *Tectonics*, **40**(10), e2021TC006806. doi:10.1029/2021TC006806, _eprint: https://onlinelibrary.wiley.com/doi/pdf/10.1029/2021TC006806.

Garrett, S. W., 1990. Interpretation of reconnaissance gravity and aeromagnetic surveys of the Antarctic Peninsula, *Journal of Geophysical Research: Solid Earth*, **95**(B5), 6759–6777. doi:10.1029/JB095iB05p06759, _eprint: https://onlinelibrary.wiley.com/doi/pdf/10.1029/JB095iB05p06759.

Geyer, A., Di Roberto, A., Smellie, J. L., Van Wyk de Vries, M., Panter, K. S., Martin, A. P., Cooper, J. R., Young, D., Pompilio, M., Kyle, P. R., & Blankenship, D., 2023. Volcanism in Antarctica: An assessment of the present state of research and future directions, *Journal of Volcanology and Geothermal Research*, **444**, 107941. doi:10.1016/j.jvolgeores.2023.107941.

Gibbons, A. D., Whittaker, J. M., & Müller, R. D., 2013. The breakup of East Gondwana: Assimilating constraints from Cretaceous ocean basins around India into a best-fit tectonic model, *Journal of Geophysical Research: Solid Earth*, **118**(3), 808–822. doi:10.1002/jgrb.50079.

Goes, S., Govers, R., & Vacher, P., 2000. Shallow mantle temperatures under Europe from P and S wave tomography, *Journal of Geophysical Research: Solid Earth*, **105**(B5), 11153–11169. doi:10.1029/1999JB900300, _eprint: https://onlinelibrary.wiley.com/doi/pdf/10.1029/1999JB900300.

Goes, S., Hasterok, D., Schutt, D. L., & Klöcking, M., 2020. Continental lithospheric temperatures: A review, *Physics of the Earth and Planetary Interiors*, **306**, 106509. doi:10.1016/j.pepi.2020.106509.

Golledge, N. R., Kowalewski, D. E., Naish, T. R., Levy, R. H., Fogwill, C. J., & Gasson, E. G. W., 2015. The multi-millennial Antarctic commitment to future sea-level rise, *Nature*, **526**(7573), 421–425. doi:10.1038/nature15706.

Gomez, N., Pollard, D., & Holland, D., 2015. Sea-level feedback lowers projections of future Antarctic Ice-Sheet mass loss, *Nature Communications*, **6**(1), 8798. doi:10.1038/ncomms9798, Publisher: Nature Publishing Group.

Goodge, J. W., 2020. Geological and tectonic evolution of the Transantarctic Mountains, from ancient craton to recent enigma, *Gondwana Research*, **80**, 50–122. doi:10.1016/j.gr.2019.11.001.

Goodge, J. W. & Fanning, C. M., 2016. Mesoarchean and Paleoproterozoic history of the Nimrod Complex, central Transantarctic Mountains, Antarctica: Stratigraphic revisions and relation to the Mawson Continent in East Gondwana,

Precambrian Research, **285**, 242–271. doi:10.1016/j.precamres.2016.09.001.

Graham, D., Johnson, K., Priebe, L., & Lupton, J., 1999. Hotspot–ridge interaction along the Southeast Indian Ridge near Amsterdam and St. Paul islands: helium isotope evidence, *Earth and Planetary Science Letters*, **167**(3-4), 297–310. doi:10.1016/S0012-821X(99)00030-8.

Granot, R. & Dyment, J., 2018. Late Cenozoic unification of East and West Antarctica, *Nature Communications*, **9**(1), 3189. doi:10.1038/s41467-018-05270-w.

Granot, R., Cande, S. C., Stock, J. M., Davey, F. J., & Clayton, R. W., 2010. Postspreading rifting in the Adare Basin, Antarctica: Regional tectonic consequences, *Geochemistry, Geophysics, Geosystems*, **11**(8). doi:10.1029/2010GC003105, _eprint: https://onlinelibrary.wiley.com/doi/pdf/10.1029/2010GC003105.

Grantham, G. H., Kramers, J. D., Eglington, B., & Burger, E. P., 2019. The Ediacarian-Cambrian uplift history of western Dronning Maud Land: New 40Ar-39Ar and Sr/Nd data from Sverdrupfjella and Kirwanveggan, the source of the Urfjell Group and tectonic evolution of Dronning Maud Land within the Kuunga Orogeny and Gondwana amalgamation, *Precambrian Research*, **333**, 105444. doi:10.1016/j.precamres.2019.105444.

Graw, J. H., Adams, A. N., Hansen, S. E., Wiens, D. A., Hackworth, L., & Park, Y., 2016. Upper mantle shear wave velocity structure beneath northern Victoria Land, Antarctica: Volcanism and uplift in the northern Transantarctic Mountains, *Earth and Planetary Science Letters*, **449**, 48–60. doi:10.1016/j.epsl.2016.05.026.

Grunow, A. M., Kent, D. V., & Dalziel, I. W. D., 1987. Mesozoic evolution of West Antarctica and the Weddell Sea Basin: new paleomagnetic constraints, *Earth and Planetary Science Letters*, **86**(1), 16–26. doi:10.1016/0012-821X(87)90184-1.

Grunow, A. M., Kent, D. V., & Dalziel, I. W. D., 1991. New paleomagnetic data from Thurston Island: Implications for the tectonics of west Antarctica and Weddell Sea opening, *Journal of Geophysical Research: Solid Earth*, **96**(B11), 17935–17954. doi:10.1029/91JB01507, _eprint: https://onlinelibrary.wiley.com/doi/pdf/10.1029/91JB01507.

Gutenberg, B. & Richter, C., 1934a. On seismic waves (first paper), *Beitr. Geophys*, **43**(56), 2.

Gutenberg, B. & Richter, C., 1934b. *On seismic waves (second paper)*, Akademische Verlagsgesellschaft, mbH.

Gutenberg, B. & Richter, C., 1936. On seismic waves (third paper), *Gerlands Beitr. Geophys*, **47**, 73–131.

Gutenberg, B. & Richter, C., 1939. On seismic waves (fourth paper), *Gerlands Beitrgge Geophysik*, **54**, 94–136.

Haas, P., Ebbing, J., & Szwillus, W., 2023. Cratonic crust illuminated by global gravity gradient inversion, *Gondwana Research*, **121**, 276–292. doi:10.1016/j.gr.2023.04.012.

Haeger, C., Kaban, M. K., Tesauro, M., Petrunin, A. G., & Mooney, W. D., 2019. 3-D Density, Thermal, and Compositional Model of the Antarctic Lithosphere and Implications for Its Evolution, *Geochemistry, Geophysics, Geosystems*, **20**(2), 688–707. doi:10.1029/2018GC008033.

Handler, M. R., Wysoczanski, R. J., & Gamble, J. A., 2003. Proterozoic lithosphere in Marie Byrd Land, West Antarctica: Re–Os systematics of spinel peridotite xenoliths, *Chemical Geology*, **196**(1-4), 131–145. doi:10.1016/S0009-2541(02)00410-2.

Handler, M. R., Wysoczanski, R. J., & Gamble, J. A., 2022. Marie Byrd Land lithospheric mantle: a review of the xenolith record, *Geological Society, London, Memoirs*, **56**(1), M56–2020–17. doi:10.1144/M56-2020-17.

Hansen, S. E., Julià, J., Nyblade, A. A., Pyle, M. L., Wiens, D. A., & Anandakrishnan, S., 2009. Using S wave receiver functions to estimate crustal structure beneath ice sheets: An application to the Transantarctic Mountains and East Antarctic craton, *Geochemistry, Geophysics, Geosystems*, **10**(8). doi:10.1029/2009GC002576, _eprint: https://onlinelibrary.wiley.com/doi/pdf/10.1029/2009GC002576.

Hansen, S. E., Nyblade, A. A., Heeszel, D. S., Wiens, D. A., Shore, P., & Kanao, M., 2010. Crustal structure of the Gamburtsev Mountains, East Antarctica, from S-wave receiver functions and Rayleigh wave phase velocities, *Earth and Planetary Science Letters*, **300**(3-4), 395–401. doi:10.1016/j.epsl.2010.10.022.

Hansen, S. E., Graw, J. H., Kenyon, L. M., Nyblade, A. A., Wiens, D. A., Aster, R. C., Huerta, A. D., Anandakrishnan, S., & Wilson, T., 2014. Imaging the Antarctic mantle using adaptively parameterized P-wave tomography: Evidence for heterogeneous structure beneath West Antarctica, *Earth and Planetary Science Letters*, **408**, 66–78. doi:10.1016/j.epsl.2014.09.043.

Hansen, S. E., Reusch, A. M., Parker, T., Bloomquist, D. K., Carpenter, P., Graw, J. H., & Brenn, G. R., 2015. The Transantarctic Mountains Northern Network (TAMNNET): Deployment and Performance of a Seismic Array in Antarctica, *Seismological Research Letters*, **86**(6), 1636–1644. doi:10.1785/0220150117.

Harris, C., Marsh, J. S., Duncan, A. R., & Erlank, A. J., 1990. The Petrogenesis of the Kirwan Basalts of Dronning Maud Land, Antarctica, *Journal of Petrology*, **31**(2), 341–369. doi:10.1093/petrology/31.2.341.

Harry, D. L., Anoka, J. L., & Jha, S., 2018. Geodynamic models of the West Antarctic Rift System: Implications for the mantle thermal state, *Geosphere*, **14**(6), 2407–2429. doi:10.1130/GES01594.1.

Hart, S. R., Blijsztajn, J., & Craddock, C., 1995. Cenozoic volcanism in Antarctica: Jones Mountains and Peter I Island, *Geochimica et Cosmochimica Acta*, **59**(16), 3379–3388. doi:10.1016/0016-7037(95)00212-I.

Hart, S. R., Blusztajn, J., LeMasurier, W. E., & Rex, D. C., 1997. Hobbs Coast Cenozoic volcanism: Implications for the West Antarctic rift system, *Chemical Geology*, **139**(1-4), 223–248. doi:10.1016/S0009-2541(97)00037-5.

Hazzard, J. A. N. & Richards, F. D., 2024. Antarctic Geothermal Heat Flow, Crustal Conductivity and Heat Production Inferred From Seismological Data, *Geophysical Research Letters*, **51**(7), e2023GL106274. doi:10.1029/2023GL106274, _eprint: https://onlinelibrary.wiley.com/doi/pdf/10.1029/2023GL106274.

Heeszel, D. S., Wiens, D. A., Nyblade, A. A., Hansen, S. E., Kanao, M., An, M., & Zhao, Y., 2013. Rayleigh wave constraints on the structure and tectonic history of the Gamburtsev Subglacial Mountains, East Antarctica, *Journal of Geophysical Research: Solid Earth*, **118**(5), 2138–2153. doi:10.1002/jgrb.50171, _eprint: https://onlinelibrary.wiley.com/doi/pdf/10.1002/jgrb.50171.

Heeszel, D. S., Wiens, D. A., Anandakrishnan, S., Aster, R. C., Dalziel, I. W. D., Huerta, A. D., Nyblade, A. A., Wilson, T. J., & Winberry, J. P., 2016. Upper mantle structure of central and West Antarctica from array analysis of Rayleigh wave phase velocities, *Journal of Geophysical Research: Solid Earth*, **121**(3), 1758–1775. doi:10.1002/2015JB012616.

Henrys, S., Wilson, T., Whittaker, J. M., Fielding, C., Hall, J., & Naish, T., 2007. Tectonic history of mid-Miocene to present southern Victoria Land Basin, inferred from seismic stratigraphy in McMurdo Sound, Antarctica, in *Antarctica: A Keystone in a Changing World – Online Proceedings of the 10th ISAES, edited by A.K. Cooper and C.R. Raymond et al.*, California, U.S.A. doi:doi:10.3133/of2007-1047.srp049, Series: Open-File Report.

Hersir, G. P., Guðnason, E. , & Flóvenz, G., 2022. Geophysical Exploration Techniques, in *Comprehensive Renewable Energy*, pp. 26–79, Elsevier.

Hess, H. H., 1964. Seismic Anisotropy of the Uppermost Mantle under Oceans, *Nature*, **203**(4945), 629–631. doi:10.1038/203629a0.

Hill, R. I., 1993. Mantle plumes and continental tectonics, *Lithos*, **30**(3-4), 193–206. doi:10.1016/0024-4937(93)90035-B.

Hjörleifsdóttir, V. & Ekström, G., 2010. Effects of three-dimensional Earth structure on CMT earthquake parameters, *Physics of the Earth and Planetary Interiors*, **179**(3-4), 178–190. doi:10.1016/j.pepi.2009.11.003.

Hoernle, K., Timm, C., Hauff, F., Tappenden, V., Werner, R., Jolis, E., Mortimer, N., Weaver, S., Riefstahl, F., & Gohl, K., 2020. Late Cretaceous (99-69 Ma) basaltic intraplate volcanism on and around Zealandia: Tracing upper mantle geodynamics from Hikurangi Plateau collision to Gondwana breakup and beyond,

Earth and Planetary Science Letters, **529**, 115864. doi:10.1016/j.epsl.2019.115864.

Hole, M. J., 1988. Post-subduction alkaline volcanism along the Antarctic Peninsula, *Journal of the Geological Society*, **145**(6), 985–998. doi:10.1144/gsjgs.145.6.0985.

Hole, M. J., 2021. Chapter 4.1b Antarctic Peninsula: petrology, *Geological Society, London, Memoirs*, **55**(1), 327–343. doi:10.1144/M55-2018-40.

Hole, M. J., Rogers, G., Saunders, A. D., & Storey, M., 1991. Relation between alkalic volcanism and slab-window formation, *Geology*, **19**(6), 657. doi:10.1130/0091-7613(1991)019<0657:RBAVAS>2.3.CO;2.

Hole, M. J., Saunders, A. D., Rogers, G., & Sykes, M. A., 1994. The relationship between alkaline magmatism, lithospheric extension and slab window formation along continental destructive plate margins, *Geological Society, London, Special Publications*, **81**(1), 265–285. doi:10.1144/GSL.SP.1994.081.01.15.

Holt, A. F. & Royden, L. H., 2020. Subduction Dynamics and Mantle Pressure: 2. Towards a Global Understanding of Slab Dip and Upper Mantle Circulation, *Geochemistry, Geophysics, Geosystems*, **21**(7), e2019GC008771. doi:10.1029/2019GC008771.

Hosseini, K., Matthews, K. J., Sigloch, K., Shephard, G. E., Domeier, M., & Tsekhmistrenko, M., 2018. SubMachine: Web-Based Tools for Exploring Seismic Tomography and Other Models of Earth's Deep Interior, *Geochemistry, Geophysics, Geosystems*, **19**(5), 1464–1483. doi:10.1029/2018GC007431, _eprint: https://onlinelibrary.wiley.com/doi/pdf/10.1029/2018GC007431.

Höink, T. & Lenardic, A., 2008. Three-dimensional mantle convection simulations with a low-viscosity asthenosphere and the relationship between heat flow and the horizontal length scale of convection, *Geophysical Research Letters*, **35**(10), 2008GL033854. doi:10.1029/2008GL033854.

Höink, T. & Lenardic, A., 2010. Long wavelength convection, Poiseuille–Couette flow in the low-viscosity asthenosphere and the strength of plate margins, *Geophysical Journal International*, **180**(1), 23–33. doi:10.1111/j.1365-246X.2009.04404.x.

Höink, T., Jellinek, A. M., & Lenardic, A., 2011. Viscous coupling at the lithosphere-asthenosphere boundary: VISCOUS COUPLING AT THE LAB, *Geochemistry, Geophysics, Geosystems*, **12**(10), n/a–n/a. doi:10.1029/2011GC003698.

Höink, T., Lenardic, A., & Richards, M., 2012. Depth-dependent viscosity and mantle stress amplification: implications for the role of the asthenosphere in maintaining plate tectonics: Asthenosphere and mantle stress amplification, *Geophysical Journal International*, **191**(1), 30–41. doi:10.1111/j.1365-246X.2012.05621.x.

Incorporated Research Institutions for Seismology, 2011. Data Services Products: EMC. Incorporated Research Institutions for Seismology. doi:10.17611/DP/EMC.1.

Ivins, E. R., van der Wal, W., Wiens, D. A., Lloyd, A. J., & Caron, L., 2022. Antarctic upper mantle rheology, *Geological Society, London, Memoirs*, **56**(1), M56–2020–19. doi:10.1144/M56-2020-19.

Jacob, J. & Dyment, J., 2014. Early opening of Australia and Antarctica: New inferences and regional consequences, *Tectonophysics*, **636**, 244–256. doi:10.1016/j.tecto.2014.08.020.

Jacob, J., Dyment, J., & Yatheesh, V., 2014. Revisiting the structure, age, and evolution of the Wharton Basin to better understand subduction under Indonesia, *Journal of Geophysical Research: Solid Earth*, **119**(1), 169–190. doi:10.1002/2013JB010285, _eprint: https://onlinelibrary.wiley.com/doi/pdf/10.1002/2013JB010285.

Jacobs, J., Bingen, B., Thomas, R. J., Bauer, W., Wingate, M. T. D., & Feitio, P., 2008. Early Palaeozoic orogenic collapse and voluminous late-tectonic magmatism in Dronning Maud Land and Mozambique: insights into the partially delaminated orogenic root of the East African–Antarctic Orogen?, *Geological Society, London, Special Publications*, **308**(1), 69–90. doi:10.1144/SP308.3.

Jeffreys, H. & Bullen, K., 1940. Seismological Tables, British Association for the Advancement of Science Gray-Mllne Trust. London.

Jin, Y. K., Lee, J., Hong, J. K., & Nam, S. H., 2009. Is subduction ongoing in the South Shetland Trench, Antarctic Peninsula?: new constraints from crustal structures of outer trench wall, *Geosciences Journal*, **13**(1), 59–67. doi:10.1007/s12303-009-0005-5.

Jokat, W., Altenbernd, T., Eagles, G., & Geissler, W. H., 2021. The early drift of the Indian plate, *Scientific Reports*, **11**(1), 10796. doi:10.1038/s41598-021-90172-z, Publisher: Nature Publishing Group.

Jordan, T. A., Ferraccioli, F., Ross, N., Corr, H. F., Leat, P. T., Bingham, R. G., Rippin, D. M., Le Brocq, A., & Siegert, M. J., 2013. Inland extent of the Weddell Sea Rift imaged by new aerogeophysical data, *Tectonophysics*, **585**, 137–160. doi:10.1016/j.tecto.2012.09.010.

Jordan, T. A., Riley, T. R., & Siddoway, C. S., 2020. The geological history and evolution of West Antarctica, *Nature Reviews Earth & Environment*, **1**(2), 117–133. doi:10.1038/s43017-019-0013-6.

Jordan, T. A., Ferraccioli, F., & Forsberg, R., 2022. An embayment in the East Antarctic basement constrains the shape of the Rodinian continental margin, *Communications Earth & Environment*, **3**(1), 52. doi:10.1038/s43247-022-00375-z.

Kaminuma, K. & Aki, K., 1963. 14. Crustal Structure in Japan from the Phase

Velocity of Rayleigh Waves. Rayleigh Waves from the Aleutian Shock of March 9, 1957, *Bulletin of the Earthquake Research Institute*.

Karato, S., 1989. Grain growth kinetics in olivine aggregates, *Tectonophysics*, **168**(4), 255–273. doi:10.1016/0040-1951(89)90221-7.

Karato, S.-i., Jung, H., Katayama, I., & Skemer, P., 2008. Geodynamic Significance of Seismic Anisotropy of the Upper Mantle: New Insights from Laboratory Studies, *Annual Review of Earth and Planetary Sciences*, **36**(1), 59–95. doi:10.1146/annurev.earth.36.031207.124120.

Kaufmann, G. & Wolf, D., 2002. Effects of lateral viscosity variations on postglacial rebound: an analytical approach: Lateral viscosity variations and postglacial rebound, *Geophysical Journal International*, **137**(2), 489–500. doi:10.1046/j.1365-246X.1999.00804.x.

Kennett, B. L. N. & Engdahl, E. R., 1991. Traveltimes for global earthquake location and phase identification, *Geophysical Journal International*, **105**(2), 429–465. doi:10.1111/j.1365-246X.1991.tb06724.x, _eprint: https://onlinelibrary.wiley.com/doi/pdf/10.1111/j.1365-246X.1991.tb06724.x.

Kennett, B. L. N., Engdahl, E. R., & Buland, R., 1995. Constraints on seismic velocities in the Earth from traveltimes, *Geophysical Journal International*, **122**(1), 108–124. doi:10.1111/j.1365-246X.1995.tb03540.x.

Kent, R. W., 2002. 40Ar/39Ar Geochronology of the Rajmahal Basalts, India, and their Relationship to the Kerguelen Plateau, *Journal of Petrology*, **43**(7), 1141–1153. doi:10.1093/petrology/43.7.1141.

Kipf, A., Hauff, F., Werner, R., Gohl, K., Van Den Bogaard, P., Hoernle, K., Maicher, D., & Klügel, A., 2014. Seamounts off the West Antarctic margin: A case for non-hotspot driven intraplate volcanism, *Gondwana Research*, **25**(4), 1660–1679. doi:10.1016/j.gr.2013.06.013.

Kirdyashkin, A., Kirdyashkin, A., Simonov, V., Buslov, M., & Kotlyarov, A., 2023. The Bouvet Plume: Parameters, Evolution, and Interaction with the Triple Junction of Midocean Ridges in the South Atlantic, *Russian Geology and Geophysics*, **64**(10), 1251–1261. doi:10.2113/RGG20234568.

Konrad, H., Sasgen, I., Pollard, D., & Klemann, V., 2015. Potential of the solid-Earth response for limiting long-term West Antarctic Ice Sheet retreat in a warming climate, *Earth and Planetary Science Letters*, **432**, 254–264. doi:10.1016/j.epsl.2015.10.008.

Kovach, R. L. & Press, F., 1961. Surface wave dispersion and crustal structure in Antarctica and the Surrounding Oceans, *Annals of Geophysics*, **14**(2). doi:10.4401/ag-5296.

Kuchar, J. & Milne, G. A., 2015. The influence of viscosity structure in the litho-

sphere on predictions from models of glacial isostatic adjustment, *Journal of Geodynamics*, **86**, 1–9. doi:10.1016/j.jog.2015.01.002.

Kyle, P. R., Moore, J. A., & Thirlwall, M. F., 1992. Petrologic Evolution of Anorthoclase Phonolite Lavas at Mount Erebus, Ross Island, Antarctica, *Journal of Petrology*, **33**(4), 849–875. doi:https://doi.org/10.1093/petrology/33.4.849.

Kyle, P. R., Pankhurst, R. J., Mukasa, S. B., Panter, K. S., & McIntosh, W. C., 1994. Sr, Nd and Pb Isotopic Variations in the Marie Byrd Plume, West Antarctica.

König, M. & Jokat, W., 2006. The Mesozoic breakup of the Weddell Sea, *Journal of Geophysical Research: Solid Earth*, **111**(B12), 2005JB004035. doi:10.1029/2005JB004035.

Lagabrielle, Y., Goddéris, Y., Donnadieu, Y., Malavieille, J., & Suarez, M., 2009. The tectonic history of Drake Passage and its possible impacts on global climate, *Earth and Planetary Science Letters*, **279**(3-4), 197–211. doi:10.1016/j.epsl.2008.12.037.

Lanyon, R., Varne, R., & Crawford, A. J., 1993. Tasmanian Tertiary basalts, the Balleny plume, and opening of the Tasman Sea (southwest Pacific Ocean), *Geology*, **21**(6), 555. doi:10.1130/0091-7613(1993)021<0555:TTBTBP>2.3.CO;2.

Larter, R. D. & Barker, P. F., 1991. Effects of ridge crest-trench interaction on Antarctic-Phoenix Spreading: Forces on a young subducting plate, *Journal of Geophysical Research: Solid Earth*, **96**(B12), 19583–19607. doi:10.1029/91JB02053.

Laske, G., Masters, G., Ma, Z., & Pasyanos, M., 2013. Update on CRUST1. 0—A 1-degree global model of Earth's crust, in *Geophysical research abstracts*, vol. 15, p. 2658, Issue: 15.

Lawrence, J. F., Wiens, D. A., Nyblade, A. A., Anandakrishan, S., Shore, P. J., & Voigt, D., 2006a. Upper mantle thermal variations beneath the Transantarctic Mountains inferred from teleseismic S-wave attenuation, *Geophysical Research Letters*, **33**(3). doi:10.1029/2005GL024516, _eprint: https://onlinelibrary.wiley.com/doi/pdf/10.1029/2005GL024516.

Lawrence, J. F., Wiens, D. A., Nyblade, A. A., Anandakrishnan, S., Shore, P. J., & Voigt, D., 2006b. Rayleigh wave phase velocity analysis of the Ross Sea, Transantarctic Mountains, and East Antarctica from a temporary seismograph array, *Journal of Geophysical Research: Solid Earth*, **111**(B6). doi:10.1029/2005JB003812, _eprint: https://onlinelibrary.wiley.com/doi/pdf/10.1029/2005JB003812.

Leat, P. T., Scarrow, J. H., & Millar, I. L., 1995. On the Antarctic Peninsula batholith, *Geological Magazine*, **132**(4), 399–412. doi:10.1017/S0016756800021464.

Leat, P. T., Ross, A. J., & Gibson, S. A., 2022. Ultramafic mantle xenoliths in the Late Cenozoic volcanic rocks of the Antarctic Peninsula and Jones Moun-

tains, West Antarctica, *Geological Society, London, Memoirs*, **56**(1), M56–2019–44. doi:10.1144/M56-2019-44.

Lebedev, S. & Nolet, G., 2003. Upper mantle beneath Southeast Asia from *S* velocity tomography: UPPER MANTLE BENEATH SE ASIA, *Journal of Geophysical Research: Solid Earth*, **108**(B1). doi:10.1029/2000JB000073.

Lebedev, S. & van der Hilst, R. D., 2008. Global upper-mantle tomography with the automated multimode inversion of surface and *S* -wave forms, *Geophysical Journal International*, **173**(2), 505–518. doi:10.1111/j.1365-246X.2008.03721.x.

Lebedev, S., Nolet, G., Meier, T., & van der Hilst, R. D., 2005. Automated multimode inversion of surface and *S* waveforms, *Geophysical Journal International*, **162**(3), 951–964. doi:10.1111/j.1365-246X.2005.02708.x.

Lebedev, S., Boonen, J., & Trampert, J., 2009. Seismic structure of Precambrian lithosphere: New constraints from broad-band surface-wave dispersion, *Lithos*, **109**(1-2), 96–111. doi:10.1016/j.lithos.2008.06.010.

Lebedev, S., Schaeffer, A. J., Fullea, J., & Pease, V., 2018. Seismic tomography of the Arctic region: inferences for the thermal structure and evolution of the lithosphere, *Geological Society, London, Special Publications*, **460**(1), 419–440. doi:10.1144/SP460.10.

Lebedev, S., Fullea, J., Xu, Y., & Bonadio, R., 2024. Seismic Thermography, *Bulletin of the Seismological Society of America*, **114**(3), 1227–1242. doi:10.1785/0120230245.

Legendre, C. P., Meier, T., Lebedev, S., Friederich, W., & Viereck-Götte, L., 2012. A shear wave velocity model of the European upper mantle from automated inversion of seismic shear and surface waveforms, *Geophysical Journal International*, **191**(1), 282–304. doi:10.1111/j.1365-246X.2012.05613.x.

Lehmann, I., 1936. P', *Publ. Bur. Cent. Seismol. Int. A*, **14**, 87–115.

Lei, W., Ruan, Y., Bozdağ, E., Peter, D., Lefebvre, M., Komatitsch, D., Tromp, J., Hill, J., Podhorszki, N., & Pugmire, D., 2020. Global adjoint tomography—model GLAD-M25, *Geophysical Journal International*, **223**(1), 1–21. doi:10.1093/gji/ggaa253.

Lekić, V. & Romanowicz, B., 2011. Inferring upper-mantle structure by full waveform tomography with the spectral element method: SEM based global tomography, *Geophysical Journal International*, **185**(2), 799–831. doi:10.1111/j.1365-246X.2011.04969.x.

LeMasurier, W., 1990. Late Cenozoic volcanism on the Antarctic Plate: An overview, in *Antarctic Research Series*, vol. 48, pp. 1–17, eds LeMasurier, W., Thomson, J., Baker, P., Kyle, P., Rowley, P., Smellie, J., & Verwoerd, W., American Geophysical Union, Washington, D. C.

eds LeMasurier, W., Thomson, J., Baker, P., Kyle, P., Rowley, P., Smellie, J., &

Verwoerd, W., 1990. *Volcanoes of the Antarctic Plate and Southern Oceans*, vol. 48 of **Antarctic Research Series**, American Geophysical Union, Washington, D. C.

LeMasurier, W. E. & Landis, C. A., 1996. Mantle-plume activity recorded by low-relief erosion surfaces in West Antarctica and New Zealand, *Geological Society of America Bulletin*, **108**(11), 1450–1466. doi:10.1130/0016-7606(1996)108<1450:MPARBL>2.3.CO;2.

LeMasurier, W. E. & Rex, D. C., 1989. Evolution of linear volcanic ranges in Marie Byrd Land, West Antarctica, *Journal of Geophysical Research: Solid Earth*, **94**(B6), 7223–7236. doi:10.1029/JB094iB06p07223.

LeMasurier, W. E., Choi, S. H., Hart, S. R., Mukasa, S., & Rogers, N., 2016. Reconciling the shadow of a subduction signature with rift geochemistry and tectonic environment in Eastern Marie Byrd Land, Antarctica, *Lithos*, **260**, 134–153. doi:10.1016/j.lithos.2016.05.018.

Li, C., Van Der Hilst, R. D., Engdahl, E. R., & Burdick, S., 2008. A new global model for *P* wave speed variations in Earth's mantle, *Geochemistry, Geophysics, Geosystems*, **9**(5), 2007GC001806. doi:10.1029/2007GC001806.

Li, X. & Romanowicz, B., 1996. Global mantle shear velocity model developed using nonlinear asymptotic coupling theory, *Journal of Geophysical Research: Solid Earth*, **101**(B10), 22245–22272. doi:10.1029/96JB01306.

Liu, Y., Li, Z.-X., Pisarevsky, S. A., Kirscher, U., Mitchell, R. N., Stark, J. C., Clark, C., & Hand, M., 2018. First Precambrian palaeomagnetic data from the Mawson Craton (East Antarctica) and tectonic implications, *Scientific Reports*, **8**(1), 16403. doi:10.1038/s41598-018-34748-2, Number: 1 Publisher: Nature Publishing Group.

Livermore, R., Balanyá, J. C., Maldonado, A., Martínez, J. M., Rodríguez-Fernández, J., Sanz De Galdeano, C., Zaldívar, J. G., Jabaloy, A., Barnolas, A., Somoza, L., Hernández-Molina, J., Suriñach, E., & Viseras, C., 2000. Autopsy on a dead spreading center: The Phoenix Ridge, Drake Passage, Antarctica, *Geology*, **28**(7), 607. doi:10.1130/0091-7613(2000)28<607:AOADSC>2.0.CO;2.

Livermore, R., Nankivell, A., Eagles, G., & Morris, P., 2005. Paleogene opening of Drake Passage, *Earth and Planetary Science Letters*, **236**(1-2), 459–470. doi:10.1016/j.epsl.2005.03.027.

Lloyd, A. J., Wiens, D. A., Nyblade, A. A., Anandakrishnan, S., Aster, R. C., Huerta, A. D., Wilson, T. J., Dalziel, I. W. D., Shore, P. J., & Zhao, D., 2015. A seismic transect across West Antarctica: Evidence for mantle thermal anomalies beneath the Bentley Subglacial Trench and the Marie Byrd Land Dome, *Journal of Geophysical Research: Solid Earth*, **120**(12), 8439–8460. doi:10.1002/2015JB012455.

Lloyd, A. J., Wiens, D. A., Zhu, H., Tromp, J., Nyblade, A. A., Aster, R. C., Hansen, S. E., Dalziel, I. W. D., Wilson, T., Ivins, E. R., & O'Donnell, J. P.,

2020. Seismic Structure of the Antarctic Upper Mantle Imaged with Adjoint Tomography, *Journal of Geophysical Research: Solid Earth*, **125**(3), 2019JB017823. doi:10.1029/2019JB017823.

Lough, A. C., Wiens, D. A., Grace Barcheck, C., Anandakrishnan, S., Aster, R. C., Blankenship, D. D., Huerta, A. D., Nyblade, A., Young, D. A., & Wilson, T. J., 2013. Seismic detection of an active subglacial magmatic complex in Marie Byrd Land, Antarctica, *Nature Geoscience*, **6**(12), 1031–1035. doi:10.1038/ngeo1992.

Lu, C., Grand, S. P., Lai, H., & Garnero, E. J., 2019. TX2019slab: A New P and S Tomography Model Incorporating Subducting Slabs, *Journal of Geophysical Research: Solid Earth*, **124**(11), 11549–11567. doi:10.1029/2019JB017448, _eprint: https://onlinelibrary.wiley.com/doi/pdf/10.1029/2019JB017448.

Lucas, E. M., Soto, D., Nyblade, A. A., Lloyd, A. J., Aster, R. C., Wiens, D. A., O'Donnell, J. P., Stuart, G. W., Wilson, T. J., Dalziel, I. W., Winberry, J. P., & Huerta, A. D., 2020. P- and S-wave velocity structure of central West Antarctica: Implications for the tectonic evolution of the West Antarctic Rift System, *Earth and Planetary Science Letters*, **546**, 116437. doi:10.1016/j.epsl.2020.116437.

Lucas, E. M., Nyblade, A. A., Accardo, N. J., Lloyd, A. J., Wiens, D. A., Aster, R. C., Wilson, T. J., Dalziel, I. W., Stuart, G. W., O'Donnell, J. P., Winberry, J. P., & Huerta, A. D., 2022. Shear Wave Splitting Across Antarctica: Implications for Upper Mantle Seismic Anisotropy, *Journal of Geophysical Research: Solid Earth*, **127**(4), e2021JB023325. doi:10.1029/2021JB023325.

Luttinen, A. V. & Furnes, H., 2000. Flood Basalts of Vestfjella: Jurassic Magmatism Across an Archaean–Proterozoic Lithospheric Boundary in Dronning Maud Land, Antarctica, *Journal of Petrology*, **41**(8), 1271–1305. doi:10.1093/petrology/41.8.1271.

Luyendyk, B., Cisowski, S., Smith, C., Richard, S., & Kimbrough, D., 1996. Paleomagnetic study of the northern Ford Ranges, western Marie Byrd Land, West Antarctica: Motion between West and East Antarctica, *Tectonics*, **15**(1), 122–141. doi:10.1029/95TC02524.

Luyendyk, B. P., 1995. Hypothesis for Cretaceous rifting of east Gondwana caused by subducted slab capture, *Geology*, **23**(4), 373. doi:10.1130/0091-7613(1995)023<0373:HFCROE>2.3.CO;2.

Lösing, M., Ebbing, J., & Szwillus, W., 2020. Geothermal Heat Flux in Antarctica: Assessing Models and Observations by Bayesian Inversion, *Frontiers in Earth Science*, **8**, 105. doi:10.3389/feart.2020.00105.

Mainprice, D., 2007. Seismic Anisotropy of the Deep Earth from a Mineral and Rock Physics Perspective, in *Treatise on Geophysics*, pp. 437–491, Elsevier.

Mandler, B. E. & Grove, T. L., 2016. Controls on the stability and composition

of amphibole in the Earth's mantle, *Contributions to Mineralogy and Petrology*, **171**(8-9), 68. doi:10.1007/s00410-016-1281-5.

Marschall, H. R., Hawkesworth, C. J., Storey, C. D., Dhuime, B., Leat, P. T., Meyer, H.-P., & Tamm-Buckle, S., 2010. The Annandagstoppane Granite, East Antarctica: Evidence for Archaean Intracrustal Recycling in the Kaapvaal-Grunehogna Craton from Zircon O and Hf Isotopes, *Journal of Petrology*, **51**(11), 2277–2301. doi:10.1093/petrology/egq057.

Martin, A. P., 2022. A review of the composition and chemistry of peridotite mantle xenoliths in volcanic rocks from Antarctica and their relevance to petrological and geophysical models for the lithospheric mantle, *Geological Society, London, Memoirs*, **56**(1), M56–2021–26. doi:10.1144/M56-2021-26.

Martin, A. P., Cooper, A. F., Price, R. C., Kyle, P. R., & Gamble, J. A., 2021. Chapter 5.2b Erebus Volcanic Province: petrology, *Geological Society, London, Memoirs*, **55**(1), 447–489. doi:10.1144/M55-2018-80.

Masters, G., Jordan, T. H., Silver, P. G., & Gilbert, F., 1982. Aspherical Earth structure from fundamental spheroidal-mode data, *Nature*, **298**(5875), 609–613. doi:10.1038/298609a0.

Masters, G., Laske, G., Bolton, H., & Dziewonski, A., 2000. The Relative Behavior of Shear Velocity, Bulk Sound Speed, and Compressional Velocity in the Mantle: Implications for Chemical and Thermal Structure, in *Earth's Deep Interior: Mineral Physics and Tomography From the Atomic to the Global Scale*, pp. 63–87, American Geophysical Union (AGU), _eprint: https://onlinelibrary.wiley.com/doi/pdf/10.1029/GM117p0063.

Mather, B. R., Müller, R. D., Seton, M., Ruttor, S., Nebel, O., & Mortimer, N., 2020. Intraplate volcanism triggered by bursts in slab flux, *Science Advances*, **6**(51), eabd0953. doi:10.1126/sciadv.abd0953, Publisher: American Association for the Advancement of Science.

Matthews, K. J., Maloney, K. T., Zahirovic, S., Williams, S. E., Seton, M., & Müller, R. D., 2016. Global plate boundary evolution and kinematics since the late Paleozoic, *Global and Planetary Change*, **146**, 226–250. doi:10.1016/j.gloplacha.2016.10.002.

McCarron, J. J. & Larter, R. D., 1998. Late Cretaceous to early Tertiary subduction history of the Antarctic Peninsula, *Journal of the Geological Society*, **155**(2), 255–268. doi:10.1144/gsjgs.155.2.0255.

McEvilly, T. V., 1964. Central U.S. crust—Upper mantle structure from Love and Rayleigh wave phase velocity inversion, *Bulletin of the Seismological Society of America*, **54**(6A), 1997–2015. doi:10.1785/BSSA05406A1997.

McFadden, R. R., Siddoway, C. S., Teyssier, C., & Fanning, C. M., 2010. Cretaceous oblique extensional deformation and magma accumulation in the

Fosdick Mountains migmatite-cored gneiss dome, West Antarctica: CRETACEOUS EXTENSION WEST ANTARCTICA, *Tectonics*, **29**(4), n/a–n/a. doi:10.1029/2009TC002492.

McKenzie, D., Jackson, J., & Priestley, K., 2005. Thermal structure of oceanic and continental lithosphere, *Earth and Planetary Science Letters*, **233**(3), 337–349. doi:10.1016/j.epsl.2005.02.005.

McNutt, M. & Caress, D., 2007. Crust and Lithospheric Structure - Hot Spots and Hot-Spot Swells, in *Treatise on Geophysics*, pp. 453–478, Elsevier.

Merle, R. E., Jiang, Q., Jourdan, F., & Olierook, H., 2022. The age and origin of the Balleny and Scott volcanic provinces, Ross Sea, Antarctica, *Geochemistry*, **82**(4), 125904. doi:10.1016/j.chemer.2022.125904.

Mikhalsky, E. V., 2008. Age of the Earth's crust and the Nd isotopic composition of the mantle sources of East Antarctic complexes, *Geochemistry International*, **46**(2), 168–174. doi:10.1134/S0016702908020067.

Millar, I. L. & Pankhurst, R. J., 1987. Rb-Sr Geochronology of the Region Between The Antarctic Peninsula and The Transantarctic Mountains: Haag Nunataks and Mesozoic Granitoids, in *Gondwana Six: Structure, Tectonics, and Geophysics*, vol. 40 of **Geophysical Monograph Series**, pp. 151–160, ed. Mckenzie, American Geophysical Union, Washington, D. C.

Millar, I. L., Pankhurst, R. J., & Fanning, C. M., 2002. Basement chronology of the Antarctic Peninsula: recurrent magmatism and anatexis in the Palaeozoic Gondwana Margin, *Journal of the Geological Society*, **159**(2), 145–157. doi:10.1144/0016-764901-020.

Mitrovica, J. X., Tamisiea, M. E., Davis, J. L., & Milne, G. A., 2001. Recent mass balance of polar ice sheets inferred from patterns of global sea-level change, *Nature*, **409**(6823), 1026–1029. doi:10.1038/35059054, Publisher: Nature Publishing Group.

Mohanty, S., 2015. Precambrian continent assembly and dispersal events of South Indian and East Antarctic Shields, *International Geology Review*, **57**(16), 1992–2027. doi:10.1080/00206814.2015.1048751.

Mohorovicic, A., 1910. Das Beben vom 8. x. 1909, *Jahrbuch Meterologie Observatorie Zagrab*, **9**, 1–63, Publisher: Zagreb University Zagreb, Yugoslavia.

Montagner, J. & Nataf, H., 1986. A simple method for inverting the azimuthal anisotropy of surface waves, *Journal of Geophysical Research: Solid Earth*, **91**(B1), 511–520. doi:10.1029/JB091iB01p00511.

Montagner, J. & Tanimoto, T., 1991. Global upper mantle tomography of seismic velocities and anisotropies, *Journal of Geophysical Research: Solid Earth*, **96**(B12), 20337–20351. doi:10.1029/91JB01890.

Montagner, J.-P. & Nataf, H.-C., 1988. Vectorial tomography–I. Theory, *Geophysi-*

cal Journal International, **94**(2), 295–307. doi:10.1111/j.1365-246X.1988.tb05903.x.

Montelli, R., Nolet, G., Dahlen, F. A., Masters, G., Engdahl, E. R., & Hung, S.-H., 2004. Finite-Frequency Tomography Reveals a Variety of Plumes in the Mantle, *Science*, **303**(5656), 338–343. doi:10.1126/science.1092485.

Montelli, R., Nolet, G., Dahlen, F. A., & Masters, G., 2006. A catalogue of deep mantle plumes: New results from finite-frequency tomography: DEEP MANTLE PLUME CATALOGUE, *Geochemistry, Geophysics, Geosystems*, **7**(11), n/a–n/a. doi:10.1029/2006GC001248.

Morgan, W. J., 1971. Convection Plumes in the Lower Mantle, *Nature*, **230**(5288), 42–43. doi:10.1038/230042a0.

Mukasa, S. B. & Dalziel, I. W. D., 2000. Marie Byrd Land, West Antarctica: Evolution of Gondwana's Pacific margin constrained by zircon U-Pb geochronology and feldspar common-Pb isotopic compositions, *Geological Society of America Bulletin*, **112**(4), 611–627. doi:10.1130/0016-7606(2000)112<611:MBLWAE>2.0.CO;2.

Mégnin, C. & Romanowicz, B., 2000. The three-dimensional shear velocity structure of the mantle from the inversion of body, surface and higher-mode waveforms, *Geophysical Journal International*, **143**(3), 709–728. doi:10.1046/j.1365-246X.2000.00298.x.

Müller, R. D., Gohl, K., Cande, S. C., Goncharov, A., & Golynsky, A. V., 2007. Eocene to Miocene geometry of the West Antarctic Rift System, *Australian Journal of Earth Sciences*, **54**(8), 1033–1045. doi:10.1080/08120090701615691.

Müller, R. D., Sdrolias, M., Gaina, C., & Roest, W. R., 2008. Age, spreading rates, and spreading asymmetry of the world's ocean crust, *Geochemistry, Geophysics, Geosystems*, **9**(4), 2007GC001743. doi:10.1029/2007GC001743.

Müller, R. D., Cannon, J., Qin, X., Watson, R. J., Gurnis, M., Williams, S., Pfaffelmoser, T., Seton, M., Russell, S. H. J., & Zahirovic, S., 2018. GPlates: Building a Virtual Earth Through Deep Time, *Geochemistry, Geophysics, Geosystems*, **19**(7), 2243–2261. doi:10.1029/2018gc007584, Publisher: American Geophysical Union (AGU).

Müller, R. D., Zahirovic, S., Williams, S. E., Cannon, J., Seton, M., Bower, D. J., Tetley, M. G., Heine, C., Le Breton, E., Liu, S., Russell, S. H. J., Yang, T., Leonard, J., & Gurnis, M., 2019. A Global Plate Model Including Lithospheric Deformation Along Major Rifts and Orogens Since the Triassic, *Tectonics*, **38**(6), 1884–1907. doi:10.1029/2018TC005462.

Müller, R. D., Flament, N., Cannon, J., Tetley, M. G., Williams, S. E., Cao, X., Bodur, F., Zahirovic, S., & Merdith, A., 2022. A tectonic-rules-based mantle reference frame since 1 billion years ago – implications for supercontinent cycles and plate–mantle system evolution, *Solid Earth*, **13**(7), 1127–1159. doi:10.5194/se-

13-1127-2022.

Nettles, M. & Dziewoński, A. M., 2008. Radially anisotropic shear velocity structure of the upper mantle globally and beneath North America, *Journal of Geophysical Research: Solid Earth*, **113**(B2), 2006JB004819. doi:10.1029/2006JB004819.

Nicolas, A. & Christensen, N. I., 1987. Formation of anisotropy in upper mantle peridotites: A review, in *Geodynamics Series*, vol. 16, pp. 111–123, eds Fuchs, K. & Froidevaux, C., American Geophysical Union, Washington, D. C.

Nield, G. A., Barletta, V. R., Bordoni, A., King, M. A., Whitehouse, P. L., Clarke, P. J., Domack, E., Scambos, T. A., & Berthier, E., 2014. Rapid bedrock uplift in the Antarctic Peninsula explained by viscoelastic response to recent ice unloading, *Earth and Planetary Science Letters*, **397**, 32–41. doi:10.1016/j.epsl.2014.04.019.

Nield, G. A., Whitehouse, P. L., van der Wal, W., Blank, B., O'Donnell, J. P., & Stuart, G. W., 2018. The impact of lateral variations in lithospheric thickness on glacial isostatic adjustment in West Antarctica, *Geophysical Journal International*, **214**(2), 811–824. doi:10.1093/gji/ggy158.

NOAA National Centers for Environmental Information, 2022. ETOPO 2022 15 Arc-Second Global Relief Model. NOAA National Centers for Environmental Information. doi:10.25921/FD45-GT74.

Nolet, G., 1987. Waveform tomography, in *Seismic tomography: With applications in global seismology and exploration geophysics*, pp. 301–322, Springer.

Nolet, G., 1990. Partitioned waveform inversion and two-dimensional structure under the network of autonomously recording seismographs, *Journal of Geophysical Research*, **95**(B6), 8499. doi:10.1029/JB095iB06p08499.

Nolet, G., 2008. A BREVIARY OF SEISMIC TOMOGRAPHY: Imaging the Interior of the Earth and Sun.

Nolet, G., Dost, B., & Paulssen, H., 1986. Intermediate wavelength seismology and the NARS experiment, *Ann. Geophys*, **4**, 305–314.

O'Donnell, J., Stuart, G., Brisbourne, A., Selway, K., Yang, Y., Nield, G., Whitehouse, P., Nyblade, A., Wiens, D., Aster, R., Anandakrishnan, S., Huerta, A., Wilson, T., & Winberry, J., 2019a. The uppermost mantle seismic velocity structure of West Antarctica from Rayleigh wave tomography: Insights into tectonic structure and geothermal heat flow, *Earth and Planetary Science Letters*, **522**, 219–233. doi:10.1016/j.epsl.2019.06.024.

O'Donnell, J. P., Brisbourne, A. M., Stuart, G. W., Dunham, C. K., Yang, Y., Nield, G. A., Whitehouse, P. L., Nyblade, A. A., Wiens, D. A., Anandakrishnan, S., Aster, R. C., Huerta, A. D., Lloyd, A. J., Wilson, T., & Winberry, J. P., 2019b. Mapping Crustal Shear Wave Velocity Structure and Radial Anisotropy Beneath West Antarctica Using Seismic Ambient Noise, *Geochem-*

istry, Geophysics, Geosystems, **20**(11), 5014–5037. doi:10.1029/2019GC008459, https://onlinelibrary.wiley.com/doi/pdf/10.1029/2019GC008459.

Oldham, R. D., 1906. The Constitution of the Interior of the Earth, as Revealed by Earthquakes, *Quarterly Journal of the Geological Society of London*, **62**(1-4), 456–475. doi:10.1144/GSL.JGS.1906.062.01-04.21.

Olivetti, V., Rossetti, F., Balestrieri, M. L., Pace, D., Cornamusini, G., & Talarico, F., 2018. Variability in uplift, exhumation and crustal deformation along the Transantarctic Mountains front in southern Victoria Land, Antarctica, *Tectonophysics*, **745**, 229–244. doi:10.1016/j.tecto.2018.08.017.

Oppenheimer, M., Glavovic, B. C., Hinkel, J., van de Wal, R., Magnan, A. K., Abd-Elgawad, A., Cai, R., Cifuentes-Jara, M., DeConto, R. M., Ghosh, T., Hay, J., Isla, F., Marzeion, B., Meyssignac, B., & Sebesvari, Z., 2019. Sea Level Rise and Implications for Low-Lying Islands, Coasts and Communities., in *IPCC Special Report on the Ocean and Cryosphere in a Changing Climate*, pp. 321–445, The Intergovernmental Panel on Climate Change.

Paige, C. C. & Saunders, M. A., 1982. LSQR: An Algorithm for Sparse Linear Equations and Sparse Least Squares, *ACM Trans. Math. Softw.*, **8**(1), 43–71. doi:10.1145/355984.355989.

Pankhurst, R. J., Weaver, S. D., Bradshaw, J. D., Storey, B. C., & Ireland, T. R., 1998. Geochronology and geochemistry of pre-Jurassic superterranes in Marie Byrd Land, Antarctica, *Journal of Geophysical Research: Solid Earth*, **103**(B2), 2529–2547. doi:10.1029/97JB02605.

Panter, K. S., 2021. Chapter 1.3 Antarctic volcanism: petrology and tectonomagmatic overview, *Geological Society, London, Memoirs*, **55**(1), 43–53. doi:10.1144/M55-2020-10.

Panter, K. S. & Martin, A. P., 2022. West Antarctic mantle deduced from mafic magmatism, *Geological Society, London, Memoirs*, **56**(1), M56–2021–10. doi:10.1144/M56-2021-10.

Pappa, F., 2019. The Lithospheric Structure of Antarctica from Geophysical–Petrological Modelling.

Pappa, F. & Ebbing, J., 2022. Gravity, magnetics and geothermal heat flow of the Antarctic lithospheric crust and mantle, *Geological Society, London, Memoirs*, **56**(1), M56–2020–5. doi:10.1144/M56-2020-5.

Pappa, F., Ebbing, J., & Ferraccioli, F., 2019. Moho Depths of Antarctica: Comparison of Seismic, Gravity, and Isostatic Results, *Geochemistry, Geophysics, Geosystems*, **20**(3), 1629–1645. doi:10.1029/2018GC008111.

Parmentier, E., 2015. The Dynamics and Convective Evolution of the Upper Mantle, in *Treatise on Geophysics*, pp. 319–337, Elsevier.

Peltier, W. R., 1974. The impulse response of a Maxwell Earth, *Re-*

views of Geophysics, **12**(4), 649–669. doi:10.1029/RG012i004p00649, _eprint: https://onlinelibrary.wiley.com/doi/pdf/10.1029/RG012i004p00649.

Peltier, W. R., 1976. Glacial-Isostatic Adjustment—II. The Inverse Problem, *Geophysical Journal International*, **46**(3), 669–705. doi:10.1111/j.1365-246X.1976.tb01253.x.

Peng, W., Yang, T., Shi, Y., Bian, W., Ma, Y., Wang, S., Jiao, X., Ma, J., Kang, Y., Zhang, S., Wu, H., & Li, H., 2022. Role of the Kerguelen mantle plume in breakup of eastern Gondwana: Evidence from early cretaceous volcanic rocks in the eastern Tethyan Himalaya, *Palaeogeography, Palaeoclimatology, Palaeoecology*, **588**, 110823. doi:10.1016/j.palaeo.2021.110823.

Peucat, J., Ménot, R., Monnier, O., & Fanning, C., 1999. The Terre Adélie basement in the East-Antarctica Shield: geological and isotopic evidence for a major 1.7Ga thermal event; comparison with the Gawler Craton in South Australia, *Precambrian Research*, **94**(3-4), 205–224. doi:10.1016/S0301-9268(98)00119-3.

Phethean, J. J., Kalnins, L. M., Van Hunen, J., Biffi, P. G., Davies, R. J., & McCaffrey, K. J., 2016. Madagascar's escape from Africa: A high-resolution plate reconstruction for the Western Somali Basin and implications for supercontinent dispersal, *Geochemistry, Geophysics, Geosystems*, **17**(12), 5036–5055. doi:10.1002/2016GC006624.

Phillips, E. H., Sims, K. W., Blichert-Toft, J., Aster, R. C., Gaetani, G. A., Kyle, P. R., Wallace, P. J., & Rasmussen, D. J., 2018. The nature and evolution of mantle upwelling at Ross Island, Antarctica, with implications for the source of HIMU lavas, *Earth and Planetary Science Letters*, **498**, 38–53. doi:10.1016/j.epsl.2018.05.049.

Phillips, G., Wilson, C. J., Phillips, D., & Szczepanski, S. K., 2007. Thermochronological (^{40} Ar/ ^{39} Ar) evidence of Early Palaeozoic basin inversion within the southern Prince Charles Mountains, East Antarctica: implications for East Gondwana, *Journal of the Geological Society*, **164**(4), 771–784. doi:10.1144/0016-76492006-073.

Polak, E. & Ribiere, G., 1969. Note sur la convergence de méthodes de directions conjuguées, *Revue française d'informatique et de recherche opérationnelle. Série rouge*, **3**(16), 35–43. doi:10.1051/m2an/196903R100351.

Pollard, D., DeConto, R. M., & Nyblade, A. A., 2005. Sensitivity of Cenozoic Antarctic ice sheet variations to geothermal heat flux, *Global and Planetary Change*, **49**(1-2), 63–74. doi:10.1016/j.gloplacha.2005.05.003.

Powell, C., Roots, S., & Veevers, J., 1988. Pre-breakup continental extension in East Gondwanaland and the early opening of the eastern Indian Ocean, *Tectonophysics*, **155**(1-4), 261–283. doi:10.1016/0040-1951(88)90269-7.

Press, F. & Dewart, G., 1959. Extent of the Antarctic Continent, *Science*, **129**(3347),

462–463. doi:10.1126/science.129.3347.462.

Priestley, K., Ho, T., Takei, Y., & McKenzie, D., 2024. The thermal and anisotropic structure of the top 300 km of the mantle, *Earth and Planetary Science Letters*, **626**, 118525. doi:10.1016/j.epsl.2023.118525.

Pyle, M. L., Wiens, D. A., Nyblade, A. A., & Anandakrishnan, S., 2010. Crustal structure of the Transantarctic Mountains near the Ross Sea from ambient seismic noise tomography, *Journal of Geophysical Research: Solid Earth*, **115**(B11). doi:10.1029/2009JB007081, _eprint: https://onlinelibrary.wiley.com/doi/pdf/10.1029/2009JB007081.

Raddick, M. J., Parmentier, E. M., & Scheirer, D. S., 2002. Buoyant decompression melting: A possible mechanism for intraplate volcanism, *Journal of Geophysical Research: Solid Earth*, **107**(B10), ECV 7–1–ECV 7–14. doi:10.1029/2001JB000617, _eprint: https://onlinelibrary.wiley.com/doi/pdf/10.1029/2001JB000617.

Ramirez, C., Nyblade, A., Emry, E., Julià, J., Sun, X., Anandakrishnan, S., Wiens, D., Aster, R., Huerta, A., Winberry, P., & Wilson, T., 2017. Crustal structure of the Transantarctic Mountains, Ellsworth Mountains and Marie Byrd Land, Antarctica: constraints on shear wave velocities, Poisson's ratios and Moho depths, *Geophysical Journal International*, **211**(3), 1328–1340. doi:10.1093/gji/ggx333.

Randall, D. E. & Mac Niocaill, C., 2004. Cambrian palaeomagnetic data confirm a Natal Embayment location for the Ellsworth—Whitmore Mountains, Antarctica, in Gondwana reconstructions, *Geophysical Journal International*, **157**(1), 105–116. doi:10.1111/j.1365-246X.2004.02192.x.

Rao, G. S. & Radhakrishna, M., 2021. India-Elan Bank-East Antarctica Breakup, Crustal Architecture, and Margin Evolution: Results From Constrained Potential Field and Process-Oriented Gravity Modeling of Conjugate Margin Segments, *Tectonics*, **40**(2), e2019TC005804. doi:10.1029/2019TC005804, _eprint: https://onlinelibrary.wiley.com/doi/pdf/10.1029/2019TC005804.

Ravenna, M., Lebedev, S., Fullea, J., & Adam, J. M.-C., 2018. Shear-Wave Velocity Structure of Southern Africa's Lithosphere: Variations in the Thickness and Composition of Cratons and Their Effect on Topography, *Geochemistry, Geophysics, Geosystems*, **19**(5), 1499–1518. doi:10.1029/2017GC007399, _eprint: https://onlinelibrary.wiley.com/doi/pdf/10.1029/2017GC007399.

Rawlinson, N. & Spakman, W., 2016. On the use of sensitivity tests in seismic tomography, *Geophysical Journal International*, **205**(2), 1221–1243. doi:10.1093/gji/ggw084.

Rawlinson, N., Davies, D. R., & Pilia, S., 2017. The mechanisms underpinning Cenozoic intraplate volcanism in eastern Australia: Insights from seismic tomography and geodynamic modeling, *Geophysical Research Letters*, **44**(19),

9681–9690. doi:10.1002/2017GL074911.

Reading, A., 2006. The seismic structure of Precambrian and early Palaeozoic terranes in the Lambert Glacier region, East Antarctica, *Earth and Planetary Science Letters*, **244**(1-2), 44–57. doi:10.1016/j.epsl.2006.01.031.

Reading, A. M., 2004. The Seismic Structure of Wilkes Land/Terre Adelie, East Antarctica and Comparison with Australia: First Steps in Reconstructing the Deep Lithosphere of Gondwana, *Gondwana Research*, **7**(1), 21–30. doi:10.1016/S1342-937X(05)70303-8.

Reading, A. M. & Heintz, M., 2008. Seismic anisotropy of East Antarctica from shear-wave splitting: Spatially varying contributions from lithospheric structural fabric and mantle flow?, *Earth and Planetary Science Letters*, **268**(3-4), 433–443. doi:10.1016/j.epsl.2008.01.041.

Reeves, C. & De Wit, M., 2000. Making ends meet in Gondwana: retracing the transforms of the Indian Ocean and reconnecting continental shear zones, *Terra Nova*, **12**(6), 272–280. doi:10.1046/j.1365-3121.2000.00309.x.

Riefstahl, F., Gohl, K., Davy, B., Hoernle, K., Mortimer, N., Timm, C., Werner, R., & Hochmuth, K., 2020. Cretaceous intracontinental rifting at the southern Chatham Rise margin and initialisation of seafloor spreading between Zealandia and Antarctica, *Tectonophysics*, **776**, 228298. doi:10.1016/j.tecto.2019.228298.

Riley, T. R., Leat, P. T., Curtis, M. L., Millar, I. L., Duncan, R. A., & Fazel, A., 2005. Early–Middle Jurassic Dolerite Dykes from Western Dronning Maud Land (Antarctica): Identifying Mantle Sources in the Karoo Large Igneous Province, *Journal of Petrology*, **46**(7), 1489–1524. doi:10.1093/petrology/egi023.

Riley, T. R., Flowerdew, M. J., & Whitehouse, M. J., 2012. U–Pb ion-microprobe zircon geochronology from the basement inliers of eastern Graham Land, Antarctic Peninsula, *Journal of the Geological Society*, **169**(4), 381–393. doi:10.1144/0016-76492011-142.

Riley, T. R., Flowerdew, M. J., Millar, I. L., & Whitehouse, M. J., 2020a. Triassic magmatism and metamorphism in the Antarctic Peninsula: Identifying the extent and timing of the Peninsula Orogeny, *Journal of South American Earth Sciences*, **103**, 102732. doi:10.1016/j.jsames.2020.102732.

Riley, T. R., Jordan, T. A., Leat, P. T., Curtis, M. L., & Millar, I. L., 2020b. Magmatism of the Weddell Sea rift system in Antarctica: Implications for the age and mechanism of rifting and early stage Gondwana breakup, *Gondwana Research*, **79**, 185–196. doi:10.1016/j.gr.2019.09.014.

Riley, T. R., Burton-Johnson, A., Flowerdew, M. J., Poblete, F., Castillo, P., Hervé, F., Leat, P. T., Millar, I. L., Bastias, J., & Whitehouse, M. J., 2023a. Palaeozoic – Early Mesozoic geological history of the Antarctic Peninsula and correlations with Patagonia: Kinematic reconstructions of the proto-Pacific margin of Gond-

wana, *Earth-Science Reviews*, **236**, 104265. doi:10.1016/j.earscirev.2022.104265.

Riley, T. R., Millar, I. L., Carter, A., Flowerdew, M. J., Burton-Johnson, A., Bastias, J., Storey, C. D., Castillo, P., Chew, D., & Whitehouse, M. J., 2023b. Evolution of an Accretionary Complex (LeMay Group) and Terrane Translation in the Antarctic Peninsula, *Tectonics*, **42**(2), e2022TC007578. doi:10.1029/2022TC007578.

Rilling, S., Mukasa, S., Wilson, T., Lawver, L., & Hall, C., 2009. New determinations of ^{40} Ar/ ^{39} Ar isotopic ages and flow volumes for Cenozoic volcanism in the Terror Rift, Ross Sea, Antarctica, *Journal of Geophysical Research: Solid Earth*, **114**(B12), 2009JB006303. doi:10.1029/2009JB006303.

Rilling, S. E., Mukasa, S. B., Wilson, T. J., & Lawver, L. A., 2007. 40Ar-39Ar Age constraints on volcanism and tectonism in the Terror Rift of the Ross Sea, Antarctica, in *Antarctica: A Keystone in a Changing World – Online Proceedings of the 10th ISAES, edited by A.K. Cooper and C.R. Raymond et al.*, California, U.S.A. doi:10.3133/of2007-1047.srp092.

Ritsema, J., Deuss, A., van Heijst, H. J., & Woodhouse, J. H., 2011. S40RTS: a degree-40 shear-velocity model for the mantle from new Rayleigh wave dispersion, teleseismic traveltime and normal-mode splitting function measurements: S40RTS, *Geophysical Journal International*, **184**(3), 1223–1236. doi:10.1111/j.1365-246X.2010.04884.x.

Ritzwoller, M. H., Shapiro, N. M., Levshin, A. L., & Leahy, G. M., 2001. Crustal and upper mantle structure beneath Antarctica and surrounding oceans, *Journal of Geophysical Research: Solid Earth*, **106**(B12), 30645–30670. doi:10.1029/2001JB000179.

Robertson Maurice, S. D., Wiens, D. A., Shore, P. J., Vera, E., & Dorman, L. M., 2003. Seismicity and tectonics of the South Shetland Islands and Bransfield Strait from a regional broadband seismograph deployment, *Journal of Geophysical Research: Solid Earth*, **108**(B10). doi:10.1029/2003JB002416, _eprint: https://onlinelibrary.wiley.com/doi/pdf/10.1029/2003JB002416.

Rocchi, S., Armienti, P., D'Orazio, M., Tonarini, S., Wijbrans, J. R., & Di Vincenzo, G., 2002. Cenozoic magmatism in the western Ross Embayment: Role of mantle plume versus plate dynamics in the development of the West Antarctic Rift System, *Journal of Geophysical Research: Solid Earth*, **107**(B9). doi:10.1029/2001JB000515.

Rocchi, S., Armienti, P., & Di Vincenzo, G., 2005. No plume, no rift magmatism in the West Antarctic Rift, in *Plates, plumes and paradigms*, Geological Society of America.

Roche, V. & Ringenbach, J.-C., 2022. The Davie Fracture Zone: A recorder of continents drifts and kinematic changes, *Tectonophysics*, **823**, 229188.

doi:10.1016/j.tecto.2021.229188.

Roult, G., Rouland, D., & Montagner, J., 1994. Antarctica II: Upper-mantle structure from velocities and anisotropy, *Physics of the Earth and Planetary Interiors*, **84**(1-4), 33–57. doi:10.1016/0031-9201(94)90033-7.

Royer, J. & Rollet, N., 1997. Plate-tectonic setting of the Tasmanian region, *Australian Journal of Earth Sciences*, **44**(5), 543–560. doi:10.1080/08120099708728336.

Russell, J. B. & Gaherty, J. B., 2021. Lithosphere Structure and Seismic Anisotropy Offshore Eastern North America: Implications for Continental Breakup and Ultra-Slow Spreading Dynamics, *Journal of Geophysical Research: Solid Earth*, **126**(12), e2021JB022955. doi:10.1029/2021JB022955, _eprint: https://onlinelibrary.wiley.com/doi/pdf/10.1029/2021JB022955.

Sauli, C., Sorlien, C., Busetti, M., De Santis, L., Geletti, R., Wardell, N., & Luyendyk, B. P., 2021. Neogene Development of the Terror Rift, Western Ross Sea, Antarctica, *Geochemistry, Geophysics, Geosystems*, **22**(3), e2020GC009076. doi:10.1029/2020GC009076, _eprint: https://onlinelibrary.wiley.com/doi/pdf/10.1029/2020GC009076.

Savchyn, I., Brusak, I., & Tretyak, K., 2023. Analysis of recent Antarctic plate kinematics based on GNSS data, *Geodesy and Geodynamics*, **14**(2), 99–110. doi:10.1016/j.geog.2022.08.004.

Sawade, L., Beller, S., Lei, W., & Tromp, J., 2022. Global centroid moment tensor solutions in a heterogeneous earth: the CMT3D catalogue, *Geophysical Journal International*, **231**(3), 1727–1738. doi:10.1093/gji/ggac280.

Schaeffer, A. & Lebedev, S., 2014. Imaging the North American continent using waveform inversion of global and USArray data, *Earth and Planetary Science Letters*, **402**, 26–41. doi:10.1016/j.epsl.2014.05.014.

Schaeffer, A., Lebedev, S., & Becker, T., 2016. Azimuthal seismic anisotropy in the Earth's upper mantle and the thickness of tectonic plates, *Geophysical Journal International*, **207**(2), 901–933. doi:10.1093/gji/ggw309.

Schaeffer, A. J. & Lebedev, S., 2013. Global shear speed structure of the upper mantle and transition zone, *Geophysical Journal International*, **194**(1), 417–449. doi:10.1093/gji/ggt095.

Schaeffer, A. J. & Lebedev, S., 2015. Global Heterogeneity of the Lithosphere and Underlying Mantle: A Seismological Appraisal Based on Multimode Surface-Wave Dispersion Analysis, Shear-Velocity Tomography, and Tectonic Regionalization, in *The Earth's Heterogeneous Mantle*, pp. 3–46, eds Khan, A. & Deschamps, F., Springer International Publishing, Cham.

Schutt, D. L. & Lesher, C. E., 2006. Effects of melt depletion on the density and seismic velocity of garnet and spinel lherzolite, *Journal of Geophysical Research: Solid Earth*, **111**(B5). doi:10.1029/2003JB002950, _eprint:

https://onlinelibrary.wiley.com/doi/pdf/10.1029/2003JB002950.

Sengupta, M. K. & Toksöz, M. N., 1976. Three dimensional model of seismic velocity variation in the Earth's mantle, *Geophysical Research Letters*, **3**(2), 84–86. doi:10.1029/GL003i002p00084.

Seroussi, H., Ivins, E. R., Wiens, D. A., & Bondzio, J., 2017. Influence of a West Antarctic mantle plume on ice sheet basal conditions, *Journal of Geophysical Research: Solid Earth*, **122**(9), 7127–7155. doi:10.1002/2017JB014423.

Seton, M., Müller, R. D., Zahirovic, S., Williams, S., Wright, N. M., Cannon, J., Whittaker, J. M., Matthews, K. J., & McGirr, R., 2020. A Global Data Set of Present-Day Oceanic Crustal Age and Seafloor Spreading Parameters, *Geochemistry, Geophysics, Geosystems*, **21**(10), e2020GC009214. doi:10.1029/2020GC009214.

Shapiro, N. M. & Ritzwoller, M. H., 2002. Monte-Carlo inversion for a global shear-velocity model of the crust and upper mantle, *Geophysical Journal International*, **151**(1), 88–105. doi:10.1046/j.1365-246X.2002.01742.x.

Shen, W., Wiens, D. A., Anandakrishnan, S., Aster, R. C., Gerstoft, P., Bromirski, P. D., Hansen, S. E., Dalziel, I. W. D., Heeszel, D. S., Huerta, A. D., Nyblade, A. A., Stephen, R., Wilson, T. J., & Winberry, J. P., 2018a. The Crust and Upper Mantle Structure of Central and West Antarctica From Bayesian Inversion of Rayleigh Wave and Receiver Functions, *Journal of Geophysical Research: Solid Earth*, **123**(9), 7824–7849. doi:10.1029/2017JB015346.

Shen, W., Wiens, D. A., Stern, T., Anandakrishnan, S., Aster, R. C., Dalziel, I., Hansen, S., Heeszel, D. S., Huerta, A., Nyblade, A., Wilson, T. J., & Winberry, J. P., 2018b. Seismic evidence for lithospheric foundering beneath the southern Transantarctic Mountains, Antarctica, *Geology*, **46**(1), 71–74. doi:10.1130/G39555.1.

Shen, W., Wiens, D. A., Lloyd, A. J., & Nyblade, A. A., 2020. A Geothermal Heat Flux Map of Antarctica Empirically Constrained by Seismic Structure, *Geophysical Research Letters*, **47**(14), e2020GL086955. doi:10.1029/2020GL086955.

Siddoway, C., 2021. The Geology of West Antarctica, in *The Geology of the Antarctic Continent*, pp. 87–131, ed. Kleinschmidt, G., Borntraeger Science Publishers, Stuttgart, Germany, 2021st edn.

Siddoway, C. S. & Fanning, C. M., 2009. Paleozoic tectonism on the East Gondwana margin: Evidence from SHRIMP U–Pb zircon geochronology of a migmatite–granite complex in West Antarctica, *Tectonophysics*, **477**(3-4), 262–277. doi:10.1016/j.tecto.2009.04.021.

Siddoway, C. S., Baldwin, S. L., Fitzgerald, P. G., Fanning, C. M., & Luyendyk, B. P., 2004. Ross Sea mylonites and the timing of intracontinental extension within the West Antarctic rift system, *Geology*, **32**(1), 57. doi:10.1130/G20005.1.

Sieminski, A., Debayle, E., & Lévêque, J.-J., 2003. Seismic evidence for deep low-velocity anomalies in the transition zone beneath West Antarctica, *Earth and Planetary Science Letters*, **216**(4), 645–661. doi:10.1016/S0012-821X(03)00518-1.

Sigloch, K. & Nolet, G., 2006. Measuring finite-frequency body-wave amplitudes and traveltimes, *Geophysical Journal International*, **167**(1), 271–287. doi:10.1111/j.1365-246X.2006.03116.x.

Simmons, N. A., Myers, S. C., Johannesson, G., & Matzel, E., 2012. LLNL-G3Dv3: Global P wave tomography model for improved regional and teleseismic travel time prediction, *Journal of Geophysical Research: Solid Earth*, **117**(B10). doi:10.1029/2012JB009525, _eprint: https://onlinelibrary.wiley.com/doi/pdf/10.1029/2012JB009525.

Simmons, N. A., Myers, S. C., Morency, C., Chiang, A., & Knapp, D. R., 2021. SPiRaL: a multiresolution global tomography model of seismic wave speeds and radial anisotropy variations in the crust and mantle, *Geophysical Journal International*, **227**(2), 1366–1391. doi:10.1093/gji/ggab277.

Sirevaag, H., Jacobs, J., Ksienzyk, A. K., Dunkl, I., & Marschall, H. R., 2018. Extent, thickness and erosion of the Jurassic continental flood basalts of Dronning Maud Land, East Antarctica: A low-T thermochronological approach, *Gondwana Research*, **61**, 222–243. doi:10.1016/j.gr.2018.04.017.

Smellie, J. L., 2021a. Chapter 3.2a Bransfield Strait and James Ross Island: volcanology, *Geological Society, London, Memoirs*, **55**(1), 227–284. doi:10.1144/M55-2018-58.

Smellie, J. L., 2021b. Chapter 1.2 Antarctic volcanism: volcanology and palaeoenvironmental overview, *Geological Society, London, Memoirs*, **55**(1), 19–42. doi:10.1144/M55-2020-1.

Smellie, J. L. & Rocchi, S., 2021. Chapter 5.1a Northern Victoria Land: volcanology, *Geological Society, London, Memoirs*, **55**(1), 347–381. doi:10.1144/M55-2018-60.

Smellie, J. L., Panter, K. S., & Geyer, A., 2021. Introduction to volcanism in Antarctica: 200 million years of subduction, rifting and continental break-up, *Geological Society, London, Memoirs*, **55**(1), 1–6. doi:10.1144/M55-2020-14.

Smith, M. L. & Dahlen, F. A., 1973. The azimuthal dependence of Love and Rayleigh wave propagation in a slightly anisotropic medium, *Journal of Geophysical Research (1896-1977)*, **78**(17), 3321–3333. doi:10.1029/JB078i017p03321, _eprint: https://onlinelibrary.wiley.com/doi/pdf/10.1029/JB078i017p03321.

Sobolev, A. V., 1996. Melt inclusions in minerals as a source of principle petrological information, *Petrology*, **4**, 209–220.

Spiegel, C., Lindow, J., Kamp, P. J., Meisel, O., Mukasa, S., Lisker, F., Kuhn, G., & Gohl, K., 2016. Tectonomorphic evolution of Marie Byrd Land – Implications

for Cenozoic rifting activity and onset of West Antarctic glaciation, *Global and Planetary Change*, **145**, 98–115. doi:10.1016/j.gloplacha.2016.08.013.

Srivastava, R. K., 2022. Early Cretaceous Greater Kerguelen Large Igneous Province and its plumbing systems: A contemplation on concurrent magmatic records of the eastern Indian Shield and adjoining regions, *Geological Journal*, **57**(2), 681–693. doi:10.1002/gj.4239.

Stadler, T. J. & Tominaga, M., 2015. Intraplate volcanism of the western Pacific: New insights from geological and geophysical observations in the Pigafetta Basin, *Geochemistry, Geophysics, Geosystems*, **16**(9), 3015–3033. doi:10.1002/2015GC005873, _eprint: https://onlinelibrary.wiley.com/doi/pdf/10.1002/2015GC005873.

Steinberger, B., 2000. Plumes in a convecting mantle: Models and observations for individual hotspots, *Journal of Geophysical Research: Solid Earth*, **105**(B5), 11127–11152. doi:10.1029/1999JB900398.

Steinberger, B. & Antretter, M., 2006. Conduit diameter and buoyant rising speed of mantle plumes: Implications for the motion of hot spots and shape of plume conduits, *Geochemistry, Geophysics, Geosystems*, **7**(11). doi:10.1029/2006GC001409, _eprint: https://onlinelibrary.wiley.com/doi/pdf/10.1029/2006GC001409.

Storey, B. C., Leat, P. T., Weaver, S. D., Pankhurst, R. J., Bradshaw, J. D., & Kelley, S., 1999. Mantle plumes and Antarctica-New Zealand rifting: evidence from mid-Cretaceous mafic dykes, *Journal of the Geological Society*, **156**(4), 659–671. doi:10.1144/gsjgs.156.4.0659.

Storey, B. C., Vaughan, A. P. M., & Riley, T. R., 2013. The links between large igneous provinces, continental break-up and environmental change: evidence reviewed from Antarctica, *Earth and Environmental Science Transactions of the Royal Society of Edinburgh*, **104**(1), 17–30. doi:10.1017/S175569101300011X.

Studinger, M., Bell, R. E., Buck, W., Karner, G. D., & Blankenship, D. D., 2004. Sub-ice geology inland of the Transantarctic Mountains in light of new aerogeophysical data, *Earth and Planetary Science Letters*, **220**(3-4), 391–408. doi:10.1016/S0012-821X(04)00066-4.

Su, W.-j., Woodward, R. L., & Dziewonski, A. M., 1992. Deep origin of mid-ocean-ridge seismic velocity anomalies, *Nature*, **360**(6400), 149–152. doi:10.1038/360149a0.

Svensen, H., Corfu, F., Polteau, S., Hammer, , & Planke, S., 2012. Rapid magma emplacement in the Karoo Large Igneous Province, *Earth and Planetary Science Letters*, **325-326**, 1–9. doi:10.1016/j.epsl.2012.01.015.

Szwillus, W., Afonso, J. C., Ebbing, J., & Mooney, W. D., 2019. Global Crustal Thickness and Velocity Structure From Geostatistical Analysis of

Seismic Data, *Journal of Geophysical Research: Solid Earth*, **124**(2), 1626–1652. doi:10.1029/2018JB016593.

Tape, C., Liu, Q., Maggi, A., & Tromp, J., 2009. Adjoint Tomography of the Southern California Crust, *Science*, **325**(5943), 988–992. doi:10.1126/science.1175298, Publisher: American Association for the Advancement of Science.

Tarantola, A. & Valette, B., 1982. Generalized nonlinear inverse problems solved using the least squares criterion, *Reviews of Geophysics*, **20**(2), 219–232. doi:10.1029/RG020i002p00219, _eprint: https://onlinelibrary.wiley.com/doi/pdf/10.1029/RG020i002p00219.

ten Brink, U. S., Bannister, S., Beaudoin, B. C., & Stern, T. A., 1993. Geophysical Investigations of the Tectonic Boundary Between East and West Antarctica, *Science*, **261**(5117), 45–50. doi:10.1126/science.261.5117.45.

ten Brink, U. S., Hackney, R. I., Bannister, S., Stern, T. A., & Makovsky, Y., 1997. Uplift of the Transantarctic Mountains and the bedrock beneath the East Antarctic ice sheet, *Journal of Geophysical Research: Solid Earth*, **102**(B12), 27603–27621. doi:10.1029/97JB02483, _eprint: https://onlinelibrary.wiley.com/doi/pdf/10.1029/97JB02483.

Tian, D., Uieda, L., Leong, W. J., Fröhlich, Y., Schlitzer, W., Grund, M., Jones, M., Toney, L., Yao, J., Magen, Y., Tong, J.-H., Materna, K., Belem, A., Newton, T., Anant, A., Ziebarth, M., Quinn, J., & Wessel, P., 2024. PyGMT: A Python interface for the Generic Mapping Tools. Zenodo. doi:10.5281/zenodo.11062720.

Torsvik, T. H., Gaina, C., & Redfield, T. F., 2008. Antarctica and Global Paleogeography: From Rodinia, Through Gondwanaland and Pangea, to the Birth of the Southern Ocean and the Opening of Gateways, *Antarctica: A keystone in a changing world*.

Trampert, J. & Woodhouse, J. H., 2003. Global anisotropic phase velocity maps for fundamental mode surface waves between 40 and 150 s, *Geophysical Journal International*, **154**(1), 154–165. doi:10.1046/j.1365-246X.2003.01952.x.

van de Lagemaat, S. H. A., Kamp, P. J. J., Boschman, L. M., & van Hinsbergen, D. J. J., 2023. Reconciling the Cretaceous breakup and demise of the Phoenix Plate with East Gondwana orogenesis in New Zealand, *Earth-Science Reviews*, **236**, 104276. doi:10.1016/j.earscirev.2022.104276.

van der Meer, D. G., van Hinsbergen, D. J. J., & Spakman, W., 2018. Atlas of the underworld_ Slab remnants in the mantle, their sinking history, and a new outlook on lower mantle viscosity, *Tectonophysics*, **723**, 309–448. doi:10.1016/j.tecto.2017.10.004.

van Wyk de Vries, M., Bingham, R. G., & Hein, A. S., 2018. A new volcanic province: an inventory of subglacial volcanoes in West Antarctica, *Geological Society, London, Special Publications*, **461**(1), 231–248. doi:10.1144/SP461.7.

Veevers, J., 2012. Reconstructions before rifting and drifting reveal the geological connections between Antarctica and its conjugates in Gondwanaland, *Earth-Science Reviews*, **111**(3-4), 249–318. doi:10.1016/j.earscirev.2011.11.009.

Veevers, J., Saeed, A., & O'Brien, P., 2008. Provenance of the Gamburtsev Subglacial Mountains from U–Pb and Hf analysis of detrital zircons in Cretaceous to Quaternary sediments in Prydz Bay and beneath the Amery Ice Shelf, *Sedimentary Geology*, **211**(1-2), 12–32. doi:10.1016/j.sedgeo.2008.08.003.

Verwoerd, W., Chevallier, L., Thomson, J., Nougier, J., Barling, J., Tingey, R., Wright, A., Kyle, P., & Rowley, P., 1990. F. Oceanic Islands on the Antarctic Plate, in *Antarctic Research Series*, vol. 48, pp. 396–463, eds LeMasurier, W., Thomson, J., Baker, P., Kyle, P., Rowley, P., Smellie, J., & Verwoerd, W., American Geophysical Union, Washington, D. C.

Wang, Z. & Dahlen, F. A., 1995a. Spherical-spline parameterization of three-dimensional earth models, *Geophysical Research Letters*, **22**(22), 3099–3102. doi:10.1029/95GL03080.

Wang, Z. & Dahlen, F. A., 1995b. Validity of surface-wave ray theory on a laterally heterogeneous earth, *Geophysical Journal International*, **123**(3), 757–773. doi:10.1111/j.1365-246X.1995.tb06888.x.

Wang, Z. R., Stotz, I. L., Bunge, H.-P., Vilacís, B., Hayek, J. N., Ghelichkhan, S., & Lebedev, S., 2023. Cenozoic upper mantle flow history of the Atlantic realm based on Couette/Poiseuille models: Towards paleo-mantle-flowgraphy, *Physics of the Earth and Planetary Interiors*, **340**, 107045. doi:10.1016/j.pepi.2023.107045.

Wannamaker, P., Hill, G., Stodt, J., Maris, V., Ogawa, Y., Selway, K., Boren, G., Bertrand, E., Uhlmann, D., Ayling, B., Green, A. M., & Feucht, D., 2017. Uplift of the central transantarctic mountains, *Nature Communications*, **8**(1), 1588. doi:10.1038/s41467-017-01577-2, Number: 1 Publisher: Nature Publishing Group.

Watson, T., Nyblade, A., Wiens, D. A., Anandakrishnan, S., Benoit, M., Shore, P. J., Voigt, D., & VanDecar, J., 2006. P and S velocity structure of the upper mantle beneath the Transantarctic Mountains, East Antarctic craton, and Ross Sea from travel time tomography, *Geochemistry, Geophysics, Geosystems*, **7**(7). doi:10.1029/2005GC001238, _eprint: https://onlinelibrary.wiley.com/doi/pdf/10.1029/2005GC001238.

Weaver, S. D., Storey, B. C., Pankhurst, R. J., Mukasa, S. B., DiVenere, V. J., & Bradshaw, J. D., 1994. Antarctica-New Zealand rifting and Marie Byrd Land lithospheric magmatism linked to ridge subduction and mantle plume activity, *Geology*, **22**(9), 811. doi:10.1130/0091-7613(1994)022<0811:ANZRAM>2.3.CO;2.

Wessel, P., Luis, J. F., Uieda, L., Scharroo, R., Wobbe, F., Smith, W. H. F., & Tian, D.,

2019. The Generic Mapping Tools Version 6, *Geochemistry, Geophysics, Geosystems*, **20**(11), 5556–5564. doi:10.1029/2019GC008515.

White-Gaynor, A. L., Nyblade, A. A., Aster, R. C., Wiens, D. A., Bromirski, P. D., Gerstoft, P., Stephen, R. A., Hansen, S. E., Wilson, T., Dalziel, I. W., Huerta, A. D., Paul Winberry, J., & Anandakrishnan, S., 2019. Heterogeneous upper mantle structure beneath the Ross Sea Embayment and Marie Byrd Land, West Antarctica, revealed by P-wave tomography, *Earth and Planetary Science Letters*, **513**, 40–50. doi:10.1016/j.epsl.2019.02.013.

Whitehouse, P. L., 2018. Glacial isostatic adjustment modelling: historical perspectives, recent advances, and future directions, *Earth Surface Dynamics*, **6**(2), 401–429. doi:10.5194/esurf-6-401-2018.

Whittaker, J. M. & Müller, R. D., 2006. Seismic stratigraphy of the Adare Trough area, Antarctica, *Marine Geology*, **230**(3-4), 179–197. doi:10.1016/j.margeo.2006.05.002.

Whittaker, J. M., Williams, S. E., & Müller, R. D., 2013. Revised tectonic evolution of the Eastern Indian Ocean, *Geochemistry, Geophysics, Geosystems*, **14**(6), 1891–1909. doi:10.1002/ggge.20120, _eprint: https://onlinelibrary.wiley.com/doi/pdf/10.1002/ggge.20120.

Wiens, D. A., Shen, W., & Lloyd, A. J., 2023. The seismic structure of the Antarctic upper mantle, *Geological Society, London, Memoirs*, **56**(1), 195–212. doi:10.1144/M56-2020-18.

Wilch, T. I., McIntosh, W. C., & Panter, K. S., 2021. Chapter 5.4a Marie Byrd Land and Ellsworth Land: volcanology, *Geological Society, London, Memoirs*, **55**(1), 515–576. doi:10.1144/M55-2019-39.

Will, T. M., Zeh, A., Gerdes, A., Frimmel, H. E., Millar, I. L., & Schmädicke, E., 2009. Palaeoproterozoic to Palaeozoic magmatic and metamorphic events in the Shackleton Range, East Antarctica: Constraints from zircon and monazite dating, and implications for the amalgamation of Gondwana, *Precambrian Research*, **172**(1), 25–45. doi:10.1016/j.precamres.2009.03.008.

Williams, S. E., Whittaker, J. M., Halpin, J. A., & Müller, R. D., 2019. Australian-Antarctic breakup and seafloor spreading: Balancing geological and geophysical constraints, *Earth-Science Reviews*, **188**, 41–58. doi:10.1016/j.earscirev.2018.10.011.

Wilson, D. S. & Luyendyk, B. P., 2009. West Antarctic paleotopography estimated at the Eocene-Oligocene climate transition, *Geophysical Research Letters*, **36**(16). doi:10.1029/2009GL039297, _eprint: https://onlinelibrary.wiley.com/doi/pdf/10.1029/2009GL039297.

Winberry, J. P. & Anandakrishnan, S., 2004. Crustal structure of the West Antarctic rift system and Marie Byrd Land hotspot, *Geology*, **32**(11), 977.

doi:10.1130/G20768.1.

Woodhouse, J. H. & Dziewonski, A. M., 1984. Mapping the upper mantle: Three-dimensional modeling of earth structure by inversion of seismic waveforms, *Journal of Geophysical Research: Solid Earth*, **89**(B7), 5953–5986. doi:10.1029/JB089iB07p05953.

Wright, A. & Kyle, P. R., 1990. "Scott Island.", in *Volcanoes of the Antarctic plate and southern oceans*, Antarctic Research Series, pp. 452–453, eds LeMasurier, W. E. & Thomson, J., American Geophysical Union.

Yakymchuk, C., Brown, C. R., Brown, M., Siddoway, C. S., Fanning, C. M., & Korhonen, F. J., 2015. Paleozoic evolution of western Marie Byrd Land, Antarctica, *Geological Society of America Bulletin*, **127**(9-10), 1464–1484. doi:10.1130/B31136.1.

Yaxley, G. M., Kamenetsky, V. S., Nichols, G. T., Maas, R., Belousova, E., Rosenthal, A., & Norman, M., 2013. The discovery of kimberlites in Antarctica extends the vast Gondwanan Cretaceous province, *Nature Communications*, **4**(1), 2921. doi:10.1038/ncomms3921.

Yegorova, T., Bakhmutov, V., Janik, T., & Grad, M., 2011. Joint geophysical and petrological models for the lithosphere structure of the Antarctic Peninsula continental margin: Petrological models of Antarctic Peninsula, *Geophysical Journal International*, **184**(1), 90–110. doi:10.1111/j.1365-246X.2010.04867.x.

Yuan, H. & Romanowicz, B., 2010. Lithospheric layering in the North American craton, *Nature*, **466**(7310), 1063–1068. doi:10.1038/nature09332, Number: 7310 Publisher: Nature Publishing Group.

Zhang, X., Paulssen, H., Lebedev, S., & Meier, T., 2009. 3D shear velocity structure beneath the Gulf of California from Rayleigh wave dispersion, *Earth and Planetary Science Letters*, **279**(3-4), 255–262. doi:10.1016/j.epsl.2009.01.003.

Zhou, Y., Nolet, G., Dahlen, F. A., & Laske, G., 2006. Global upper-mantle structure from finite-frequency surface-wave tomography, *Journal of Geophysical Research: Solid Earth*, **111**(B4). doi:10.1029/2005JB003677, _eprint: https://onlinelibrary.wiley.com/doi/pdf/10.1029/2005JB003677.

Zhou, Z., Wiens, D. A., Shen, W., Aster, R. C., Nyblade, A., & Wilson, T. J., 2022. Radial Anisotropy and Sediment Thickness of West and Central Antarctica Estimated From Rayleigh and Love Wave Velocities, *Journal of Geophysical Research: Solid Earth*, **127**(3), e2021JB022857. doi:10.1029/2021JB022857, _eprint: https://onlinelibrary.wiley.com/doi/pdf/10.1029/2021JB022857.

Zhou, Z., Wiens, D. A., Nyblade, A. A., Aster, R. C., Wilson, T., & Shen, W., 2024. Crustal and Uppermost Mantle Azimuthal Seismic Anisotropy of Antarctica From Ambient Noise Tomography, *Journal of Geophysical Research: Solid Earth*, **129**(1), e2023JB027556. doi:10.1029/2023JB027556.

Zhu, H., Bozdağ, E., & Tromp, J., 2015. Seismic structure of the European upper mantle based on adjoint tomography, *Geophysical Journal International*, **201**(1), 18–52. doi:10.1093/gji/ggu492.

Zielhuis, A. & Nolet, G., 1994. Shear-wave velocity variations in the upper mantle beneath central Europe, *Geophysical Journal International*, **117**(3), 695–715. doi:10.1111/j.1365-246X.1994.tb02463.x.